Controls and Concepts of Operation for Load Balancing with IPWRs in a High Renewables Penetration Grid

A Dissertation Presented for the

Doctor of Philosophy

Degree

The University of Tennessee, Knoxville

Richard Joseph Bisson

May 2021

To my mother and my father

Acknowledgments

I would like to thank everyone in my life who contributed to my growth and development, but I can only enumerate so many people by name. I am eternally grateful to my parents, Cindy and Doug Bisson, for their love and support and letting me know in grade school that grad school is a path I might want to take. My committee members have provided invaluable insight and feedback into many technically challenging aspects of this work. In particular my advisor, Dr. Jamie Coble, has shown me infinite patience.

Abstract

The future of commercial nuclear power in the United States is uncertain in the wake of construction delays and several plant closings, especially in deregulated wholesale electricity markets with cheap natural gas and increasing wind and solar penetration. As a firm low carbon resource, nuclear power plants can serve a key role in climate mitigation strategies by displacing the natural gas generators that provide dispatchable peaking capacity in systems with large and increasing variable renewable energy (VRE) shares. Small modular reactors, or SMRs, are among a suite of new reactor technologies that might alleviate the time and cost overruns facing nuclear industry in the West and offer increased flexibility over the currently operating reactor fleet. Integral pressurized water reactors (IPWRs) will almost certainly be the first such SMRs commercially deployed as of this writing. The goal of this thesis is to develop and evaluate the performance of a control system for an IPWR power plant in a high renewables penetration grid. A reactor similar to the NuScale Integral Pressurized Water Reactor has been chosen as the candidate reactor for these control design and feasibility studies due to the availability of design data and research literature pertaining to the NuScale IPWR module and plant concepts. This reactor concept was modeled in the Modelica language and a fuzzy logic coordinated control system was developed in Simulink to achieve different load profiles that may be typical of an electrical system with a large share of VRE generation. The results of these closed loop control simulations demonstrated the efficacy of load balancing with an IPWR module plant with such a generation mix but with additional notional costs and penalties that are not inherent to baseload operation.

Table of Contents

List of Tables

List of Figures

Chapter 1

Introduction

The increasing penetration of natural gas and renewables in the electric grid and their disruptive effect on markets have spurred lively discussion regarding the future of the generating mix, the uncertain future of coal and nuclear power, and energy policy more generally as it relates to scarce resources and emissions reductions for a growing population. With respect to the prospects of commercial nuclear generation in the West, this discussion includes the unfavorable economics of many currently operating Generation II light water reactor (LWR) plants in the Pennsylvania, Jersey, Maryland Interconnection (PJM) and Midcontinent Independent System Operator (MISO) markets, the struggling Generation III construction project at Vogtle in Georgia, and the cancelled VC Summer project in South Carolina, leading to increased interest in other LWR technology and even advanced (non-LWR) reactor concepts. Such reactors with advanced concepts usually are passively safe, have improved power plant economics, and may operate flexibly. The most mature of these Generation III+ and Generation IV technologies from a commercial perspective are light water small modular reactor (SMR) designs, specifically integral pressurized water reactors (IPWRs); the NuScale 50 MWe IPWR module is undergoing safety review by the NRC as of this writing and has contracted with UAMPS and INL to establish a test site for their reactor design [1].

The practical motivation for this work is primarily one of engineering, clean air, and climate policy concerns. Natural gas and renewable energy are expected to keep growing as a share of electrical generation in the US, but the scenarios with more than 80% renewable penetration are considered extremely difficult, if not impossible, to achieve from both an engineering and economic standpoint. The remaining 20% will still need to be filled by other generation and storage. It would be desirable to replace not only the remaining coal plants but also carbon-emitting natural gas plants with non-emitting nuclear power plants to stay within the carbon budget of various limited warming scenarios. Natural gas plants, especially "peaker" plants, have helped support the renewable energy revolution by serving as fast dispatchable generators when wind and solar generation are not sufficient to meet grid demand while ramping down very quickly (seconds or minutes) when those resources are abundant. It is in this environment of cheap and flexible natural gas fired plants that commercial nuclear generation is struggling economically to provide non-emitting power. This results in a path dependence for the carbon budget such that even if full decarbonization could be achieved regardless of nuclear penetration, that budget could be exhausted.

Typically nuclear power plants are operated in baseload generation mode at full rated power to maximize revenue. However, electrical grids with a large nuclear share or high renewables penetration require that at least some nuclear power plants be able to load follow. A significant body of work has focused on power maneuvering that may be more properly categorized as load shaping, with long time horizons of several hours or even a few days, such as that conducted at Columbia Generating Station near Richland, WA [2]. Greater attention is being given to load following wherein reactor power and generator systems must be able to adapt to more rapidly varying and unpredictable grid power demand. In France and Germany, nuclear power plants operate in load following mode, i.e., they participate in primary and secondary frequency control [3]. European Utilities Requirements (EUR) demand that nuclear power plants be capable of load cycling operation between 50% and 100% rated reactor power with rate of change in electric output of 3-5% per minute [3]. This range of power maneuvering is achieved primarily by movement of various control rod bank types [3].

The current state of deregulated electricity markets and its effect on nuclear power plant economics suggest consideration of alternative paradigms for nuclear reactor design and operation may be in order. A controversial and sometimes misunderstood option, especially in the United States, is load following operation. Load following with nuclear power plants is feasible and conducted in some grids, but it is a nontrivial and sometimes costly endeavor, especially for large reactor power maneuvers [3] [4]. Ramping the reactor and turbine up and down imposes stresses and increases wear and tear on the power plant systems, and power reduction is viewed as “leaving money on the table” by generators because prices are normally (but not always) positive. Nonetheless it is a topic worth exploring deeply as it will likely figure into the long-term future of commercial nuclear generation in the West due to the rapidly evolving energy market conditions and government policy making. In part this merit for research arises from the design of the steam generator systems of many of these new reactors, which require different control strategies and safety considerations than those of conventional reactors of the currently operating nuclear plant fleet. The dynamics of these steam generator systems will require careful attention and consideration in the development and design of controls, perhaps more than the reactor core system itself, under a regime of rapid response to load changes that are not fully predictable (although grid averaging effects can ameliorate these issues). With all this in mind, the goal of this work is to develop controls and concepts of operation for the load following operation of a NuScale-sized IPWR module, or integral PWRs more generally, and associated plant systems in an electrical grid with a high variable renewable energy penetration.

1.1 Small Modular Reactor Designs and Concepts

There are several SMR designs undergoing development or regulatory approval around the world. Many are marketed with a putative load following capability so as to operate flexibly for remote applications or, more germane to this work, operation in the expected high renewables penetration grids of the future [5]. There are several SMR concepts including pressurized water reactors, boiling water reactors (BWRs), high temperature gas-cooled reactors (HTGRs), liquid metal-cooled fast reactors (LMFRs), and molten salt reactors (MSRs). The focus of this work is on land-based PWR technology. Three US-based PWR designs are selected here for further discussion to provide perspective on the kinds of IPWR SMR generating capacities and technologies that have been significantly developed.

1.1.1 IRIS

The International Reactor Innovative and Secure (IRIS) IPWR is a fully integral small modular reactor with rated power of 1000 MWth, or 335 MWe [6]. It has 89 17x17 Westinghouse PWR fuel assemblies using 4.95% enriched fuel and up to a 48-month refueling cycle [5]. It uses 8 spool type reactor coolant pumps to circulate fluid in the primary loop and 8 helical coil steam generators (HTSGs) to supply steam to the secondary loop [5]. A diagram of the IRIS appears in Figure 1.1. Though it is not currently under development, regulatory approval, or construction, the IRIS design has been extensively studied in the open literature and much engineering data and simulation results are available for it [7]. With a rated power higher than that of most other SMRs, the IRIS may be more economically viable than lower power single or dual module SMR concepts and easier to operate in tandem with small but highly variable renewable power sources such as wind farms or solar parks on the order of 10-200 MWe nameplate capacity. In such cases the IRIS plant may operate close to full power most of the time and ramp up or down according to grid operator demand while remaining within Electric Power Research Institute (EPRI) guidelines for ramp rates [3]. IRIS in particular is discussed here because of previous modeling and control development work on IRIS as part of the application and validation of TRANSFORM library modeling components [8] and prior work conducted at the University of Tennessee [7] informs this dissertation.

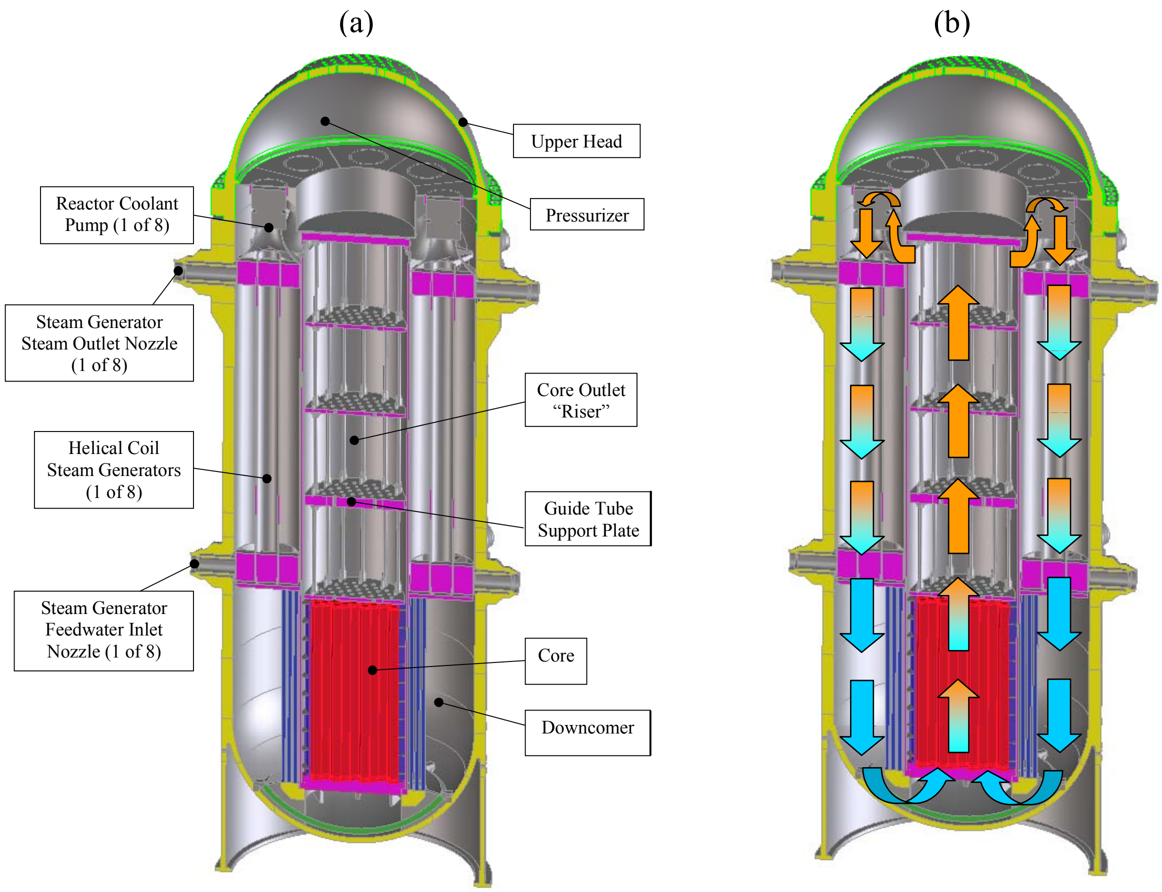

Figure 1.1: Cutaway diagram of the IRIS with key components identified and the direction of circulation mapped [9].

1.1.2 mPower

The mPower SMR is a passively safe 575 MWth/195 MWe IPWR [5]. Its plant concept is a two-module 390 MWe power plant, making it comparable to an IRIS one-module plant in capacity [5]. The mPower has 69 LEU fuel assemblies with a 24-month refueling cycle. It uses eight active reactor coolant pumps to circulate fluid in the primary loop and eight once-through steam generators (OTSG) to generate steam for the secondary loop [5]. The mPower module appears in Figure 1.2.

1.1.3 NuScale

The NuScale Power Module is an IPWR SMR with a design power of 200 MWth/60 MWe [5]. The NuScale module appears in Figure 1.3. The reactor core has 37 17x17 Westinghouse PWR fuel assemblies with LEU fuel and integral burnable poisons and 16 control rod assemblies; it has a refueling cycle of 24 months [5]. One relatively unusual operating principle of the NuScale module is its use of natural convection and gravity for its primary coolant loop circulation rather than active pumps; eight helical coil steam generators (HTSGs) are used to create steam for the secondary [5]. The power plant concept is that of a site that can be staggered in 60 MWe increments, up to 720 MWe produced. Each module in the plant is operated independently and has its own turbine-generator system it feeds into [5]. It is worth showcasing because the SMR plant model used for this work is similar in concept as an IPWR and in design parameters to the older design data for a single NuScale module (160 MWth/50 MWe). Of the three SMR designs looked at in this chapter, NuScale is furthest along to deployment, having recently been approved by the NRC and with planning underway to build and operate at INL.

1.2 Thesis Contribution

The goal of this dissertation work is to develop and evaluate concepts of operation and an integrated control system for IPWR SMRs in an electrical grid system with large variable

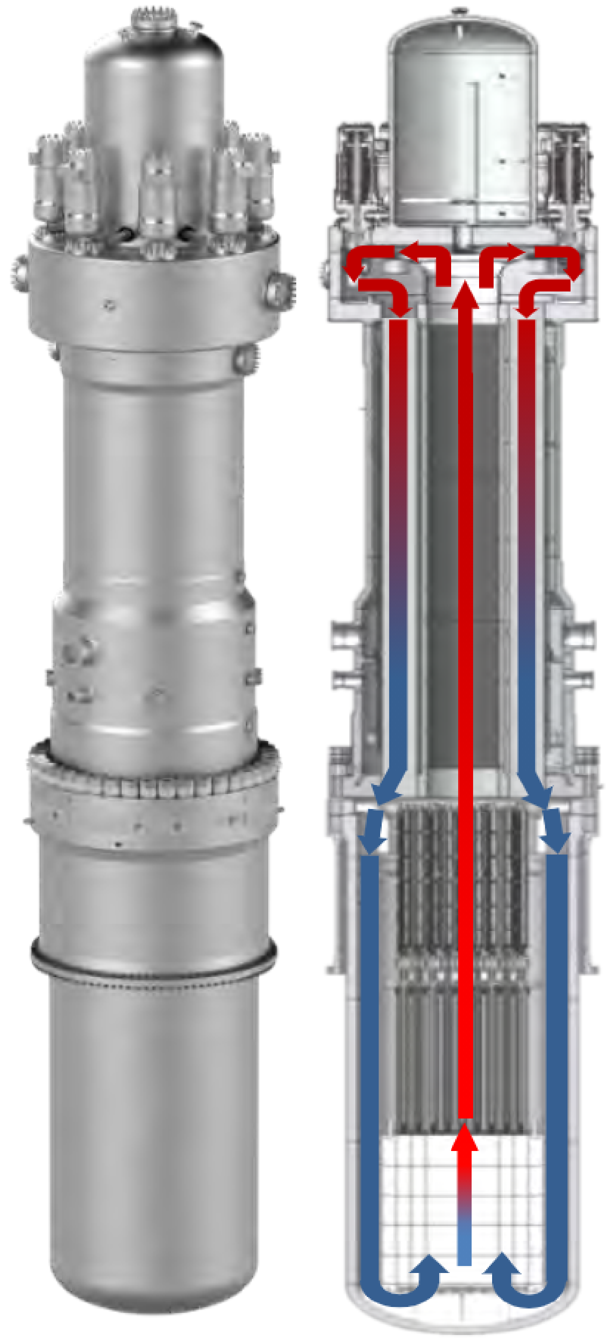

Figure 1.2: Cutaway diagram of the mPower module illustrating fuel and rod assembly and coolant circulation.

Figure 1.3: Cutaway diagram of the NuScale module situated in its pool [5].

renewable generation penetration. This work has been done with the integration of individual reactor and plant models with electrical grid models and unit commitment-economic dispatch (UC-ED) problems of thermal generating units as the ultimate goals in mind. Contributions to facilitate integration with grid and UC-ED models include investigation of the physical limits imposed by xenon and their effect on the UC-ED problem, constructing figures of merit reflecting the effort of actuation that can be fed into future degradation and maintenance models, and the estimation of plant revenues through the collaboration at CURENT. As load following is a solved problem in nuclear power plant operation, the emphasis of this work is placed upon balancing priorities of the plant in a holistic sense. Even more important in continuous load balancing operation than thermal phenomena that originate in the reactor, which evolve slowly, are those that occur in the steam generator and balance of plant, which evolve more quickly. These transients can pose challenges to a plant load following to match rapidly changing power demand from the grid. The efficacy of the controls is evaluated in the context of a high renewables penetration grid using one or more figures of merit such as power mismatch, total electrical energy delivered, metrics for plant degradation based on the amount and type of actuation, or ramp availability, which is of particular interest when a large increase in power is needed following a large decrease. Such operation is approximated using relatively aggressive ideal load profiles as well as synthetic profiles created from daily historical generation data from the California Independent System Operator (CAISO).

1.3 Organization of This Dissertation

Chapter 1 of this dissertation provides motivation for the development of this thesis, brief primers on the topics of flexible nuclear and SMRs, and defines the thesis contribution. Chapter 2 reviews the areas of research pertinent to this effort and discusses what this thesis develops beyond the current state of the literature. Chapter 3 section reviews the physical modeling of the reactor, steam generator, and balance of plant systems in detail. Chapter 4 discusses the relevant plant state variables and figures of merit for evaluation of performance, identifies candidate actuators based on performance under perturbation studies, and provides the motivation for the implemented control system. In Chapter 5 simulation data from the control system studies are presented and discussed. At last in Chapter 6 there is discussion of the conclusions, and possible avenues for future work are identified; a foundation for future studies of IPWR systems as well as other SMRs and advanced nuclear systems more generally is presented.

Chapter 2

Literature Survey

This literature survey reviews distinct but related areas of research and practice in nuclear power generation as they relate to the work of this proposed thesis. The academic literature specifically concerning load following nuclear reactors with a realistic grid demonstration is not very broad, but there exists much operational experience in and a body of regulation for load following operation, especially in continental Europe. The instrumentation and controls for conventional operation, whether baseload operation or scheduled load changes, are used in load following as well. Some controls concepts are applicable across different reactor designs.

2.1 Experience with Load Following and Control of Generation II Reactors

2.1.1 Load Following Operational Experience

Typically nuclear power plants are operated in baseload generation mode at full rated power to maximize sales revenue because capital costs are high whereas fuel costs are very low [3]. In normal baseload operation nuclear power plants are operated at full rated power to maximize revenue; minimize thermal, mechanical, and hydraulic stresses to the core and all plants systems; and maintain a predictable fuel reloading schedule. However, those electrical grids with a large nuclear–as in France–or renewables–as in Germany–share require some nuclear power plants be able to load follow. A significant body of work has focused on power maneuvering that is more properly categorized as load shaping or load scheduling several hours ahead, such as that conducted at Columbia Generating Station (BWR) near Richland, WA, by adjusting reactor coolant recirculation flow and control rod insertion. Greater attention is being given to load following wherein reactor power and generator systems must be able to adapt to more rapidly varying and unpredictable grid power demand [2].

In France and Germany, nuclear power plants operate in load following mode, i.e., participation in both primary and secondary frequency control [3], [10]. European Utilities Requirements (EUR) demand that nuclear power plants be capable of load cycling operation between 50% and 100% rated reactor power with change of electric output between 3-5% per minute [3]. However, the actual rate of maneuver is often lower, at 1-2%/min in the upper 15-30% power range [10]. This range of power maneuvering is achieved primarily by movement of various control rod bank types. However, this is can be nontrivial, requiring a long sequence of rod maneuvers and pump recirculation steps [2]. International experience is mixed; some work suggests frequent operation in load following and automatic frequency control modes leads to poorer plant reliability, worse fuel economy, increased maintenance costs, and shorter plant life [11] while other, more recent work by Morilhat et al. states that flexible operation imposes little to no additional problems due to design decisions taken prior to plant construction and operation [12].

The German nuclear power sector has years of experience load following with PWRs and BWRs [10], [13]. Similar to the load shaping maneuvers at Columbia Generating Station, German operators use a combination of control rod bank shifts and recirculation pump control to control the thermal reactor power level in BWRs [13]. The average coolant temperature is maintained at a constant level over the 40-100% power regime, and the increasing differential between the reactor coolant outlet and inlet temperatures results in a greater power level [13]. The types of load cycling under consideration are not considered demanding by operators due to the relatively low power ramp rates (65 MWe per minute, or 5%/min, for the 1345 MWe

Grafenrheinfeld unit, would be considered strenuous [10]) but leave room for the optimization of fuel loading, control rod movement, and demand look-ahead strategies [13].

2.1.2 Flexible Nuclear Operation Economic Studies

Ponciroli et al. conducted profitability evaluations for flexible nuclear for the Arizona grid [14]. A simple PWR core model including xenon poisoning was coupled to a UC-ED optimization model of the grid. Rules for ramping the nuclear reactor power level up and down were informed by the physical constraints of xenon. The reactivity conditional ($\rho_{margin} > \rho_{Xe}$) to ramp back up to a prior power level informs the work of this thesis, which developed continuous conditional tracking and forms a framework for evaluating ramp rate availability [14]. For an Arizona spring day case study, it is shown that flexible operation, even when constrained by xenon transients, results in slightly lower system costs and slightly great plant profitability (ignoring additional costs due to maintenance) [14]. Jenkins et al. considered the benefits of flexible nuclear for electrical generation systems and found that overall system cost and renewables curtailment were reduced, providing motivation on the operator side for flexible nuclear [15]. The IAEA has also extensively studied the nature and consequences of non-baseload operation of light water reactors across member states [16] [12]. These studies do not firmly account for costs–financial, component degradation, human factors, or otherwise–in an explicit and quantitative way. This motivates the creation of figures of merit which can be used to evaluate the performance of nuclear plant systems and rank the performance of different control actions and schema. Optimization of figures of merit is also a possibility with optimal control techniques or through tuning controller gains for particular control actions.

2.1.3 Advanced Control Concepts for PWRs

There is much academic research focused on the development of novel and robust control schemes for both conventional and new reactors [17] [18] [19], but not necessarily with a particular kind of load following operation in mind, e.g., the kind of aggressive and somewhat unpredictable power maneuvering that is the aim of this work. State feedback control, model predictive control, artificial neural networks, optimal control, and others have all been evaluated throughout the literature on reactor dynamics control [18].

Fuzzy Logic Control

Review articles note fuzzy logic has been applied to nuclear power systems with some promise [18], [20]. In fact, there are several examples of fuzzy logic applied to the control of PWR dynamics, some with the aim of facilitating improved load following capability [21] [22] [23] [24] [25] [26]. Fuzzy logic has also been applied to the control rod systems of research reactors [27] [28]. Because of the ease of implementation in even complex systems and understanding, especially at an intuitive level for a human operator, fuzzy logic control (FLC) developments are discussed at length here. FLC forms the core of the coordinated control development of this dissertation work. Fuzzy logic control methods do not require detailed physical models to work. In a FLC system, the crisp input is "fuzzified" so it may be interpreted with linguistic rules of control, this fuzzified value undergoes "fuzzy computation" in accordance with the rule set, and finally this computed value is "defuzzified" in order to generate a crisp signal [20]. This approach can be advantageous because it can mimic the performance of an experienced operator with a real system instead of developing controllers based on simplified models that suffer with incomplete information regarding the system. The intuitiveness of the controls and rules themselves is also an advantage [20]. Hah and Lee applied the FLC algorithm to the control of the Yonggwang Nuclear Unit 3 with a 5-input, 2-output MIMO system to regulate core power and temperature with boron and control element assemblies [25]. Similar work was conducted by Fodil et al. for the improved control of PWR, wherein a fuzzy rule set regarding power distribution and rod position determined boration or dilution for total reactor power and power distribution control [26]. Akin and Altin used a validated model of the H. B. Robinson nuclear power plant to develop a fuzzy logic controller for fast power regulation (too fast for humans) using steam flow rate, which required the development of a rule set derived from numerical simulations [23]. Heger et al. provide a review of the theory and applications of fuzzy logic control with respect to nuclear reactor systems, especially for power level tracking in an intuitive fashion [29].

2.2 SMRs in Auxiliary Applications and Hybrid Energy Systems

Because of the stringent demands and stresses (thermal, mechanical, etc.) placed upon nuclear power plants in load following operation, much interest has turned toward auxiliary applications of nuclear power in which the reactor can remain near full, constant output, such as district heating with low grade steam, industrial cogeneration (especially for High Temperature Reactors, or HTRs), and desalination. Often these proposed systems are coupled with natural gas plants and renewable generation like solar and wind. These arrangements between nuclear reactors, other power sources, and industrial processes or other applications are usually referred to as nuclear hybrid energy systems (NHES), or simply hybrid energy systems. Some work at the University of Tennessee regarding SMR instrumentation, control, and diagnostics with an IRIS demonstration was connected to auxiliary applications of nuclear power in desalination [30]. A multi-stage flash desalination system was coupled to an IRIS plant which provided the heat for the production of distillate and brine [30].

Work at North Carolina State University (NCSU) has focused on operating a Babcock & Wilcox SMR mPower module (530 MWth, 180 MWe) in concert with thermal energy storage (TES) systems [31] [32] [33] [34]. For this sensible heat storage-SMR coupled system design, the reactor thermal power level moves very little while the TES system and turbine operate to meet grid demand and thermal process needs [34]. By operating at near 100% power the entire time, the stresses on the power plant system are minimized. Drawbacks of the TES system, although likely minor, include the additional capital and operation and maintenance (O&M) costs of the thermal storage system and additional safety precautions related to their function and integration with the reactor and plant systems. However, there is still merit in load following without auxiliary applications, and the problem itself is interesting from a controls perspective. Nuclear heat generation may be desirable in some markets, especially for building or district heating in northern Europe and Russia. However, there still needs to be a customer for the excess heat/steam generated to be used for purposes other than reintroducing steam to the turbine.

Work at Idaho National Laboratory, Argonne National Laboratory, and Oak Ridge National Laboratory has considered NHES with IRIS as a demonstrator in a broad sense and with the hope that integrated systems may have superior performance to isolated components [35]. This multidomain modeling of multiple coupled physical systems, including the IRIS reactor systems, was handled through the development of the TRANSFORM library in the Modelica modeling language [35], [8]. A nuclear reactor is operated in tandem with other power sources and industrial customers who may want process heat or electric energy onsite. The aforementioned thermal energy storage (TES) storage is a special case of this much more general concept. The IRIS was chosen for the NHES demonstration and operated with battery storage, a gas turbine, and an industrial end user [35]. As in the case of the NCSU nuclear-TES system, there is reliance on external customers, which poses practical engineering, regulatory, and economic challenges to the deployment of such a system. NHES modeling with the goal of TES and hydrogen production has also been studied for a NuScale module [36].

The work of this thesis, i.e., load following in a high renewables grid, is related to the works referenced in this section, yet it is fundamentally distinct from them in its focus and concerns. A brief survey of the NHES topical literature regarding SMRs for nuclear generation was necessary to make this distinction in purpose and modeling clear. The only function of the nuclear power plant in this work is its role in electrical generation. So-called auxiliary applications, such as district heating, industrial cogeneration, and hydrogen production, will not be explored in modeling, operation and control, or economic analysis. However, ancillary services, namely frequency regulation and spinning reserves, that are of interest to a grid operator are under consideration. The inclusion of ancillary services in modeling may have ramifications for plant operation and economics beyond those of simple grid demand matching in load scheduling or frequency control.

2.3 PWR Modeling and Control Development

2.3.1 Prior Work at the University of Tennessee

An IRIS SMR model developed at the University of Tennessee was validated against a high-fidelity FORTRAN model developed at North Carolina State University [7]. The model is reviewed in Modeling and Methodology. Some IRIS control concepts were explored by Wood and others at ORNL [9]. The goal of the modeling and simulation efforts at the University of Tennessee were to evaluate the performance of instrumentation and control methods with an IRIS demonstration model, especially for multi-modular control, diagnostics and fault monitoring, and flexible operation. This prior research helps inform the work of this thesis despite being a different, larger SMR concept.

2.3.2 Effects and Control of Xenon Transients

The effect of neutron poisons in fission products, particularly xenon-135, on core reactivity must be managed, for time domains on the order of several hours to a few days. Xenon harms the neutron economy of a reactor by absorbing the neutrons liberated by the fission chain reaction. The absorption cross section of Xe-135 for thermal neutrons ($v = 2200$) m/s is 2.7×10^6 b, whereas that of U-235 is 676 b, so a Xe-135 nucleus much more readily absorbs thermal neutrons than a U-235 nucleus [37]. A decrease in reactor power, or flux, results in a buildup of xenon initially. This buildup of xenon and thus additional negative xenon reactivity has significant implications for load following operation: reducing the power level too much can make ramping back up difficult or even impossible, depending on the desired power level [37]. The burnup of xenon due to a neutron flux increase results in a positive core reactivity insertion and increases the margin required for a shutdown, which should not be an operational or safety concern.

The axially nonuniform distribution of xenon also requires management to avoid excessive localized power peaking or flux tilting. There is much literature on xenon control, especially in load following applications where this factor is more significant than in baseload operation [38] [39] [40] [41]. The control strategy that is typically employed is axial offset (AO) control strategy. This strategy entails using reactivity effects–boron, temperature feedback, control rods–to maintain a relative power differential between the top and bottom regions of the core within an acceptable band based on the overall power level of the core [26], [41]. Implementations of axial offset strategy include sliding mode control [41], fuzzy logic control [26], and feed-forward control [39], with control rod movement actuation and/or boron to control core power and indirectly xenon. The mechanical shim (MSHIM) control strategy can control not only the total reactor power but also the power distribution, managing the xenon spatial distribution axially [39]. It is an important option in reactors where soluble boron control is not used or the primary coolant inventory is so large that it is fairly insensitive to boration and dilution control, as is the case for the IRIS [39]. Stated briefly, MSHIM makes aggressive use of different rod banks for total reactor power control and axial power distribution control.

2.3.3 Effects and Control of Other Transients

The effect of boron concentration transients on core reactivity and steam generator behavior in an IRIS system was evaluated by Magalhaes et al. [42]. In this work a model of IRIS was developed in MATLAB and Simulink with the addition of a linear boron reactivity term:

$$\rho_B = \alpha_B (B - B_0). \tag{2.1}$$

Here ρ_B is the boron reactivity, α_B is the reactivity coefficient, B is the current concentration of boron in the primary coolant loop, and B_0 is the initial boron concentration in the primary coolant loop. The boron from the boric acid solution tank was assumed to mix uniformly in the primary coolant loop, i.e., there are no spatial effects modeled. The observed reactivity transients resulting from boration and dilution were small in magnitude, on the order of 15 pcm, compared to the thermal reactivity from the fuel and coolant or control rod maneuvers [42]. Previously cited and discussed FLC papers also evaluate boron control for PWRs [25] [26]. Boron control is not under consideration at this time due to the large coolant inventory of integral PWRs that requires much more boration or dilution to achieve a desired concentration compared to a conventional PWR. Boron is realistically only useful for long-term reactivity management (several days/months) in these cases.

2.4 Control Strategies in Other Reactors with Advanced Concepts of Operation

The control systems of other advanced reactor designs are under consideration to aid the development of controls in this work. Several control systems have been proposed for the Indian Advanced Heavy Water Reactor (AHWR), including fuzzy logic controllers [43] [44] [45]. Over the course of these modeling and control development efforts for the AHWR, a single-input FLC was developed to handle spatial control of the AHWR with the rod banks [43]. A fuzzy-like PD controller was also developed for the AHWR to accomplish the same goal [44]. Several different control systems for the spatial control of the AHWR were reviewed and compared; fuzzy based controllers had the best performance under transients conditions [45].

Wood and Wilson developed an inherent reactor power control system for another advanced reactor concept, the Advanced Liquid Metal Reactor (ALMR), with the aim of matching load demand [46]. The control system provides active power removal in the balance of plant, direct control of selected primary and secondary coolant temperatures, and passive reactor power control [46]. These implemented concepts of control are similar to the goals of this work regarding an IWPR reactor and power plant control for load following. However, the strongly nonlinear nature and complexity of the steam generator, the balance of plant model, and the large and frequent power maneuvers make system linearization approaches of limited usefulness for analysis and control development.

Work by Ponciroli et al. on the Advanced Lead Fast Reactor European Demonstrator (ALFRED) concept (300 MWth) for grid frequency regulation [47] suggests an approach to modeling and control as well as the overall structure of this thesis. After development of the ALFRED model and its implementation in Modelica, candidate actuators were selected on the basis of feasibility and safety considerations. The ALFRED was operated in a constant reactor power state while the mechanical work in the turbine was varied to meet grid demand because of the thermal inertia of the system [48]. Decoupling the balance of plant from the primary circuit was considered the best approach; operating the steam generator at constant pressure and controlling the turbine bypass and admissions valves to meet fast demand changes prevented these power fluctuations from affecting the primary circuit [48].

The IP200 IPWR (220 MWth) with a once through steam generator (OTSG) was modeled in RELAP5 for the purpose of developing control strategies to achieve load following operation [49] [50]. This work evaluated the load following capability of the RELAP5 IP200 model under a coordination control scheme between the primary and secondary loops, namely the variables of steam flow, feedwater flow, and reactor power (under a constant average primary coolant temperature program). For low load conditions, it was noted that there was a limit to the feasibility of feedwater throttling, requiring the establishment of a minimum flow rate, although Du, Xia, and He remarked that a lower temperature setpoint for the average primary coolant temperature can improve stability in the OTSG [50]. Load following capability using primary coolant temperature control, feedwater control, and OTSG grouping control was demonstrated with some caveats. The work here is instructive due to the similarity of the reactor designs and simulated models.

2.4.1 Load Following with Novel Reactor Designs in a High Renewables Share Grid

Utah Associated Municipal Power Systems (UAMPS) and NuScale Power, LLC., have studied the possibility of very aggressive load following operation with multiple (6-12) 50 MWe NuScale modules in conjunction with variable renewable energy (VRE) sources in a distributed network [2]. In this study the SMR power plant was coupled to the 60 MWe Horse Butte wind farm in the simulations. The power profiles of the wind farm and local grid load are typical 24-hour profiles, appearing in Figure 2.1. Operational decisions include taking SMR modules offline for extended periods of low grid demand and/or sustained wind farm output, reactor power maneuvering over several minutes or hours, and bypassing the turbine to dump steam directly into the condenser for rapid power demand changes. In isolation, these are not considered economical modes of operation because of the waste of the generated steam and the revenue lost from decreased electrical power generation. This fact has motivated interest in the aforementioned hybrid energy systems concepts with additional functions such as storage, industrial process heat, and steam heating that allow for efficient use of fuel, more stable power, and avoiding revenue loss. It is clear from the power plots in Figure 2.1 that load following in a small distributed generation system with one SMR module, especially with a rated power as low as that of the NuScale module, requires several power maneuvers, often on the balance of plant side, that may harm power plant economics. The power plant concept for the NuScale reactor and other similarly sized SMR modules is to operate a number of them together [2]. This concept can significantly reduce stress on the systems as changes in load may be shared across several reactors. For advanced SMRs it is possible a PID control strategy is not sufficient for load following, especially for large and rapid maneuvers [51].

2.5 Summary

Several research areas of modeling and control of reactors (mostly PWRs) for load following operation have been surveyed and discussed. There is a wealth of operational experience of load following and control with Generation II reactors, especially in Europe, but there is an apparent disconnect between the real world experience of operators and the concerns of academic research. This makes sense given the challenges of such operation, the fact that control of older reactor designs has long been a solved problem, and the lack of a large number of reactors with advanced concepts of operation in service. The advanced control systems to be developed and implemented should be sensible to operators and convincing to nuclear regulators. It is also worth noting that there is a marked preference in the literature toward hybrid energy applications over load following for engineering and economic reasons.

The control and operation of reactors with advanced concepts of operation seem relatively open, especially with respect to grid demonstration in a high renewables scenario. Control approaches such as fuzzy logic control, neural network control, feedback linearization, sliding mode control, and gain scheduling are prominent in nonlinear modeling and control research, including for nuclear reactor systems. Fuzzy logic control has a significant body of research demonstrating its efficacy and suitability for a variety of nuclear systems. Thus fuzzy logic control has been selected for intuitive application and mimicking human operator expert behavior for complex nonlinear systems.

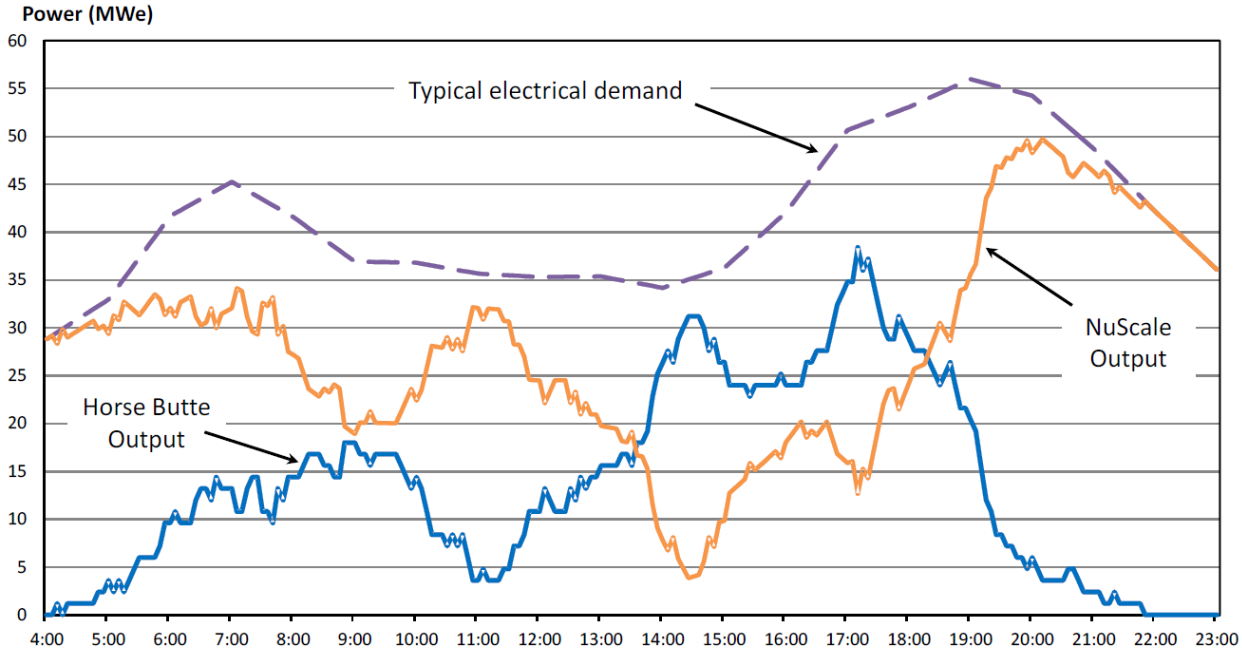

Figure 2.1: Power profiles over the course of a day. The NuScale plant maneuvers to accommodate wind generation and demand variation [2].

Chapter 3

System Modeling and Methodology

The augmented IPWR model is discussed at a high level in this section; greater detail for submodels are discussed in the appendices of this dissertation. The plant system modeled and simulated in this work is a zero dimension lumped parameter nodal model of the reactor core and steam generator coupled to a balance of plant for heat removal and electrical generation. The primary loop of the plant includes the reactor core subdivided into top and bottom halves, an upper plenum control volume for outgoing coolant, a large pressurizer volume, down the shell side of the once through steam generator (OTSG) and back to the lower plenum beneath the reactor core. The diagram level model of the primary system loop appears in Figure 3.1. The secondary loop connects the primary system to the balance of plant (BOP) model. The BOP model is a relatively simple regenerative cycle, with a high pressure stage turbine, a steam bleed to the feedwater heater, a low pressure stage turbine, an ideal condenser maintained at vacuum pressure, a condensate pump, the feedwater heater, and a feedwater pump that returns the heated condensate back to the tube side of the OTSG. The diagram level model of the BOP appears in Figure 3.4.

Modelica was chosen as the modeling language for this system modeling and control design effort. It is suited to acausal modeling of multidomain physical systems and has several open source libraries. The TRANSFORM library developed at ORNL and INL provides the coupled nuclear and thermal hydraulic components that form the basis of this work [8]. The modeling, simulation, and fast prototyping were conducted in the Dymola IDE and then coupled to MATLAB/Simulink via Dymola's proprietary interface for control studies and data visualization.

The models in Modelica are multidomain and physically typed–phenomena such as heat, rigid body dynamics, fluids, and electricity–are predefined in the Modelica Standard Library and have associated "connectors" that link components and establish their boundary conditions. These physical typings are reused in the TRANSFORM library and the model components here. For the power plant model presented and simulated in this work, the entire fluidic network is connected and thermodynamic quantities are calculated for every control volume uses first principles and steam tables. The IF97 standard tables are used to calculate the properties of water–pressure, specific volume, specific enthalpy, specific entropy, temperature, and density–for all flow models and control volumes. For heat transfer, only conductive heat transfer and convective heat transfer, often realized through well-established empirical correlations, are considered. Radiative heat transfer ($P = \sigma T^4$) is neglected due to the low temperature of the reactor system.

3.1 Nuclear Steam Supply System

The Nuclear Steam Supply System (NSSS) consists of the reactor core itself, the liquid single phase primary coolant loop, associated primary system components and control volumes, and the steam generator, which facilitates heat transfer from the primary loop to the secondary loop. Heat energy is generated by the fission chain reaction within the fuel, thus heating it and allowing its energy to be carried away by the primary coolant to the steam generator. This hot primary coolant heats the secondary coolant via contact with the steam generator tube walls. The secondary coolant undergoes a phase change from subcooled water to superheated steam to turn the turbine generator.

3.1.1 Reactor Core

A lumped parameter model of the reactor core was implemented, shown in Figure 3.2. The fission heat power is delivered to the fuel on a volume-weighted basis. The heat transfer model used for the reactor core dynamics is discussed in detail in Appendix A. The fission power level of the core is calculated using the point reactor kinetic equations (PRKE) with six delayed neutron precursor groups:

$$\frac{dP}{dt} = \frac{\rho - \beta}{\Lambda} P + \sum_{i=1}^{6} \lambda_i C_i \tag{3.1}$$

$$\frac{dC_i}{dt} = \frac{\beta_i}{\Lambda} P - \lambda_i C_i. \tag{3.2}$$

The total reactivity including thermal feedback from the fuel and coolant is

$$\rho = \rho_0 + \rho_{CR} + \alpha_F \left(T_F - T_{F0}\right) + \alpha_C (T_C - T_{C0}) + \alpha_X (X - X_0), \tag{3.3}$$

where ρ is the total reactivity of the core including external reactivity and thermal feedback effects. The naught subscripts denote initial steady-state values. These feedback effects arise from density effects in the coolant and fuel as well as a Doppler effect of the relative motion between neutrons and nuclei which alters the microscopic cross sections presented by the nuclei to the neutrons [37]. This reactivity feedback effect due to a change in variable, in this case the temperature of the medium in which the neutrons travel, can be linearly approximated as $\frac{\partial \rho}{\partial T} \cong \frac{\Delta \rho}{\Delta \mathrm{T}} \equiv \alpha_T$. The reactor core nodalization is implemented as an effective average model for state variables, which is considered a homogeneous and well-mixed volume for its individual nodes as discussed in the appendix A. An energy balance is invoked for each control volume node. The reactivity term ρ_0 is the excess reactivity of the fuel and ρ_{CR} feed-forward control associated with control rod insertion or withdrawal; T_F and T_C are the temperatures of the fuel and coolant nodes, respectively, and α_f and α_c are the corresponding temperature feedback coefficients. X is the xenon-135 concentration in the core, and α_X is its reactivity coefficient. Xenon-135 is a strong poison, or absorber, of thermal neutrons. It has a thermal neutron microscopic absorption cross section of $\sigma_X = 2 \times 10^6$ barns (10^{-24} cm^2).

Xenon Feedback Modeling and Control

The reactivity addition due to poisoning is given by the following equation:

$$\Delta\rho = -\frac{\Sigma_{\mathrm{a}}^{\mathrm{P}}}{\Sigma_{\mathrm{a}}} \frac{1}{1 + L^2 B_g^2} \left[1 - L^2 B_g^2 \frac{\Sigma_{tr}^P / \Sigma_a^P}{\Sigma_{tr} / \Sigma_a} \right] \cong \frac{\Sigma_a^P / \Sigma_a}{1 + L^2 B_g^2} \approx \frac{\Sigma_a^P}{\Sigma_a}, \tag{3.4}$$

where the macroscopic cross section $\Sigma_a^P = N_P \sigma_a^P$ [37]. The number density is calculated from the Bateman equations for xenon-135 and iodine-135, enabling the calculation of the instantaneous reactivity worth of xenon, or any other neutron poison, in the core. The Bateman equations for the generation of iodine-135 and xenon-135 are

$$\frac{dI}{dt} = \gamma_I \Sigma_F \phi - \lambda_I I \tag{3.5}$$

$$\frac{dX}{dt} = \gamma_X \Sigma_F \phi + \lambda_I I - \lambda_X X - \sigma_a \phi X. \tag{3.6}$$

The parameters γ_I, γ_X, λ_I, and λ_X are the fission yields and decay constants for iodine-135 and xenon-135, respectively. Here the flux ϕ is calculated from the equation relating thermal power and reaction rate $P = w_F \Sigma_F \phi V$, where w_F is the mean energy liberated per fission event (200 MeV) and V is the active core volume. The addition of xenon feedback may have meaningful consequences for long term reactor operation and ramping over periods of several hours. The inclusion of xenon requires adjustments to control strategies. For simulations on the order of several hours or a few days, xenon transients will affect total power. Even more important is the spatial instability of power/flux introduced by xenon, which must be managed with axial control strategies.

Much contemporary literature regarding xenon measurement, modeling, and control focuses on these xenon oscillations and how to prevent or dampen them to avoid flux tilting. For these reasons the neutron kinetics model has been expanded to have axial geometry, as in Figure 3.1, to capture relevant axial transient phenomena. Multi-node modeling strategies

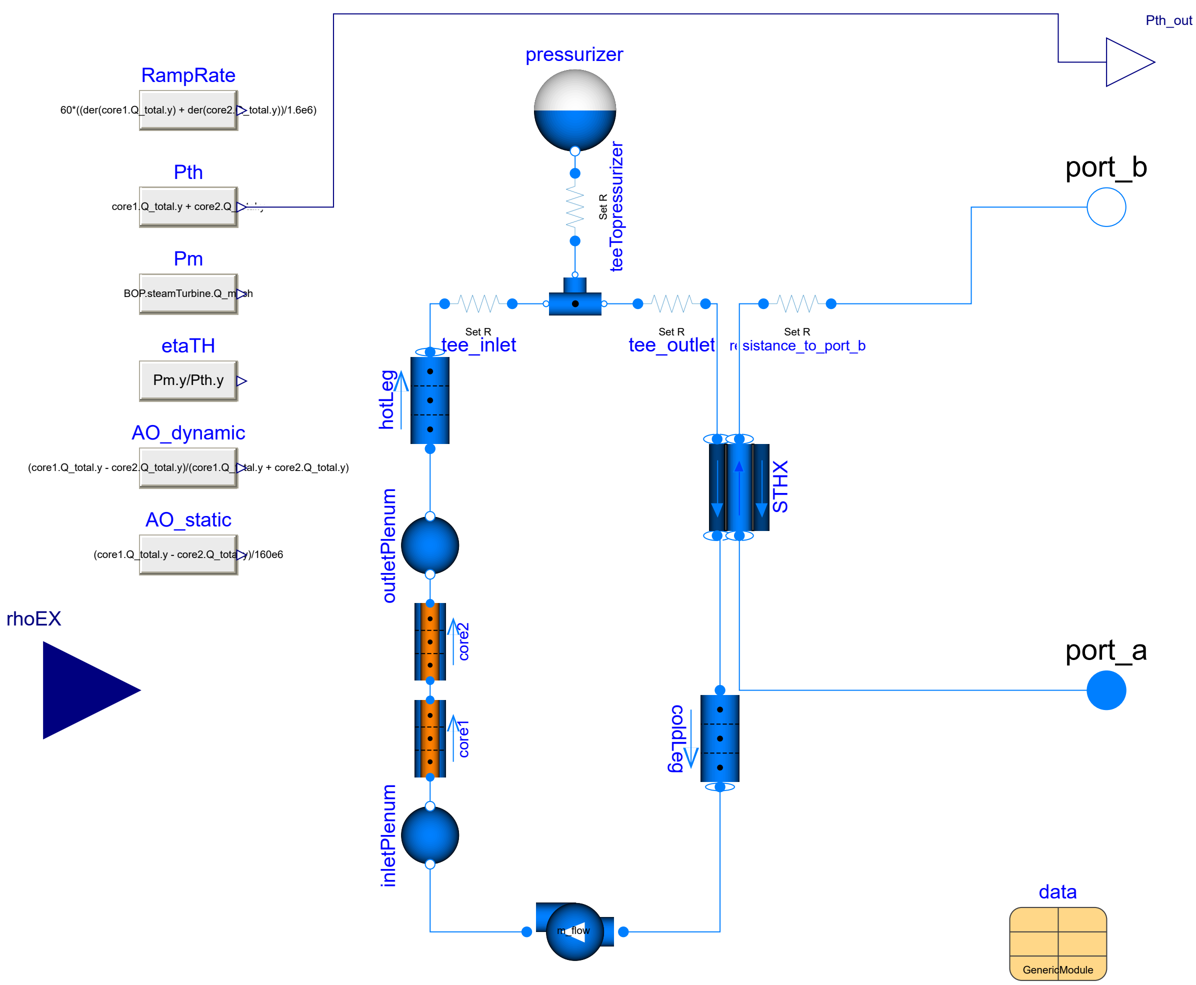

Figure 3.1: Diagram of multipoint core and primary loop system in Dymola environment

have been devised and implemented and assisted the development of this work [17] [18] [19] [38] [52].

Multipoint Kinetics

The reactor core model is augmented to be a 1D axial core to achieve higher fidelity and explore spatial transients associated with xenon. The management of xenon in a single point reactor by itself is generally not very interesting as it only requires excess reactivity and minimum power level monitoring to manage. The risks of xenon buildup primarily arise from xenon oscillations and power peaking in the core that create thermomechanical stresses in the fuel and cladding that damage the structural integrity thereof. The modified neutronics equations for the j-th node are

$$\frac{dP_j}{dt} = \frac{\rho_j - \beta}{\Lambda} P + \sum_{i=1}^{6} \lambda_i C_{ij} + w_{j,j+1}(P_j - P_{j+1}) + w_{j,j-1}(P_j - P_{j-1}) \tag{3.7}$$

$$\frac{dC_{ij}}{dt} = \frac{\beta_i}{\Lambda} P - \lambda_i C_{ij} \tag{3.8}$$

$$\rho_j = \rho_{j,ex} + \alpha_F (T_{Fj} - T_{F0j}) + \alpha_C [(T_{Cj} - T_{C0j})] + \alpha_X (X_j - X_{j0}), \tag{3.9}$$

Here the w's are coupling coefficients between nearest neighbor nodes quantifying the diffusion or leakage between them. The coupling term is given by the following from Wang [53]:

$$w = \frac{Dv}{Hd}. \tag{3.10}$$

Here D is the diffusion coefficient of thermal neutrons in the reactor core, v is the speed of thermal neutrons, H is the active volume height of the node, and d is the distance between node centers. For a symmetric two node system, this reduces to

$$w = \frac{Dv}{H^2}. \tag{3.11}$$

Xenon transients are slow compared to the intervals of load following operation, but they are worth investigating to evaluate xenon management for long simulation periods of 24-48 hours of operation with significant ramping; it is worth noting that, depending on the reactor, the power may not remain below a certain level indefinitely due to xenon buildup. The external reactivity is adjusted to incorporate both excess reactivity associated with the stage of the reactor core life cycle, ρ_0, as well as a control rod reactivity insertion term that is treated as a linear or sigmoid function of rod bank height H, $\rho_{CR}(H)$, which is especially relevant for xenon control and represented in the following modified external reactivity term equation:

$$\rho_{ex} = \rho_0 + \rho_{CR} = \rho_0 + \rho_{CR}(H). \tag{3.12}$$

For this work, the reactivity worth of the rod is taken to be linear over the range of operation.

3.1.2 Outlet Plenum

The outlet plenum is a lumped node parameter volume. Its mass and energy balance equations are

$$\frac{dm_{OP}}{dt} = \dot{m}_{Rx} - \dot{m}_{OP} \tag{3.13}$$

$$\frac{dE_{OP}}{dt} = h_{Rx}\dot{m}_{Rx} - h_{OP}\dot{m}_{OP}, \tag{3.14}$$

where OP designates the outlet plenum and Rx designates the coolant state variables from the reactor. The plenum has an associated hydraulic residence time, which adds thermal inertia to the system. This residence time is

$$\tau_{OP} = V_{OP}/\dot{m}_{OP}, \tag{3.15}$$

where τ_{OP} is the hydraulic residence time of the fluid in the outlet plenum, V_{OP} is the total volume of the outlet plenum, and $\dot{m}_{OP}$ is the mass flow rate through the outlet plenum.

3.1.3 Hot Leg

The hot leg is modeled as a large, one dimensional vertical cylindrical pipe discretized into a finite number of nodes along the z-axis. The mass, energy, and momentum balance equations for each node j are the following:

$$\frac{dm_{HLj}}{dt} = \dot{m}_{HLj-1} - \dot{m}_{HLj} \tag{3.16}$$

$$\frac{dE_{HLj}}{dt} = h_{HLj-1}\dot{m}_{HLj-1} - h_{HLj}\dot{m}_{HLj} \tag{3.17}$$

$$p_{HLj} = p_{HLj} - \rho_{HLj} g \Delta z_j. \tag{3.18}$$

3.1.4 Pressurizer

The pressurizer in a PWR maintains the desired pressure in the primary coolant circuit to prevent boiling of the coolant. Here the pressurizer geometry is slightly simplified and modeled as a cylindrical tank. Its mass, energy, fluid, and pressure level equations are given by

$$\frac{dE_{pzr}}{dt} = \dot{m}_{surge} h_{surge} \tag{3.19}$$

$$\frac{dm_{pzr}}{dt} = \dot{m}_{surge} \tag{3.20}$$

$$L_{pzr} = (V_0 - V_l)/A \tag{3.21}$$

$$p_{pzr} = p_{surface} + \rho_l g L, \tag{3.22}$$

The surface pressure is the pressure in the primary coolant loop, and the $\dot{m}_{surge}$ mass flow "surge" denotes the net fluid mass flow entering or exiting the pressurizer volume from the primary coolant loop. L_{pzr} is the pressurizer level, V_0 is the total presurrizer volume, V_l is the liquid volume, and A is the cross sectional area of the pressurizer. Pressurizer controls, such as relief valves, heaters, and cold sprays are not modeled in this work. Due to the large volume relative to a pressurizer in a typical Generation II PWR loop, the pressurizer for this module is allowed to "ride out" transients.

3.1.5 Cold Leg

The cold leg is modeled similarly to the hot leg, i.e., as an extended 1D cylindrical pipe model with mass, energy, and momentum balances for each node j.

$$\frac{dm_{CLj}}{dt} = m_{CLj-1} - m_{CLj} \tag{3.23}$$

$$\frac{dE_{CLj}}{dt} = h_{CLj-1}m_{CLj-1} - h_{CLj}m_{CLj} \tag{3.24}$$

$$p_{CLj} = p_{CLj} + \rho_{CLj} g \Delta z_j. \tag{3.25}$$

Here the positive convention is used for the pressure since the coolant is flowing downward.

3.1.6 Primary Coolant Pump

Unlike the NuScale reactor, which uses natural convection phenomena (thermally induced coolant density gradient and gravity) for coolant circulation, this model has a primary coolant pump to circulate the fluid through the reactor primary loop. The primary coolant pump is an ideal mass flow regulator that takes in an external control input from the master control to set the mass flow rate. It is maintained at a constant mass flow rate of 700 kg/s for nominal operating conditions.

3.1.7 Inlet Plenum

The primary coolant flows through the lower plenum. The coolant returns to begin the cycle again. Like the outlet plenum, the lower plenum has an associated hydaulic residence time that affects plant dynamics through its inertia.

$$\frac{dm_{IP}}{dt} = \dot{m}_{CL} - \dot{m}_{IP} \tag{3.26}$$

$$\frac{dE_{IP}}{dt} = h_{CL}\dot{m}_{RCL} - h_{IP}\dot{m}_{IP}. \tag{3.27}$$

3.1.8 Steam Generator

The once through steam generator (OTSG) model is a nodalized fixed boundary approximation of the primary loop-tube wall-secondary loop system with three distinct heat transfer coefficient calculation algorithms depending on the phase region in the secondary loop—a subcooled water, a saturated two-phase mixture, and superheated steam. The phase region determines the heat transfer properties between the tube wall and the secondary loop. The nodalization is diagrammed in Figure 3.3. Steam mass flow rate and pressure controllers at the outlet are embedded in the OTSG. The steam generator model and its discretization are discussed in greater detail in Appendix A.

3.2 Balance of Plant

The balance of plant (BOP) in the model features a turbine control valve at the entry, a generic fluid volume steam nozzle chest model, high pressure stage turbine, a low pressure stage turbine, a condenser, a condensate pump, a feedwater heater, and a feedwater pump. The BOP uses the Modelica Media library's IF97 standard for water to calculate the fluid properties of the superheated steam leaving the secondary outlet and subcooled feedwater entering the secondary inlet. The steam flow through the turbine stages is assumed to be isentropic. Some superheated steam is bled from the high pressure stage turbine and directed to the feedwater heater to facilitate the thermal regeneration typical of Rankine cycle plants. The balance of plant appears in Figure 3.4.

3.2.1 Turbine Control Valve

An isentropic steam valve immediately succeeds the secondary (tube) side of the steam generator in the secondary coolant loop. The valve position takes in a real valued input for its fractional opening, which affects the mass flow and pressure drop through the valve. The flow model for the valve treats the medium as a compressible fluid. The equations for the valve are

$$Y = 1 - \frac{|x|}{3F_{xt}} \tag{3.28}$$

$$\dot{m}_{TCV} = f_C(u)A_v Y \sqrt{x\rho p} \tag{3.29}$$

$$F_{xt} = F_{xt0} \tag{3.30}$$

$$x = \Delta p/p. \tag{3.31}$$

Here u is the fractional opening input signal, Δp is the pressure drop over the valve, p is the inlet pressure, f_c is the valve characteristic function (constant for this model), and the TCV acronym denotes it is the turbine control valve.

3.2.2 Nozzle Chest

The first volume beyond the steam generator tubes is the nozzle chest. A valve precedes the nozzle chest, which can throttle flow to the nozzle chest and affect the downstream mass flow rate and the pressure in the superheated region of the steam generator.

$$\frac{dm_{NC}}{dt} = \dot{m}_{TCV} - \dot{m}_{NC} \tag{3.32}$$

$$\frac{dE_{NC}}{dt} = h_{TCV}\dot{m}_{TCV} - h_{NC}\dot{m}_{NC}, \tag{3.33}$$

Here TCV denotes the mass and enthalpy flows arriving from the nozzle chest while NC denotes the outgoing flows from the well-mixed nozzle chest volume.

3.2.3 HP Turbine

The high pressure turbine stage is modeled as simple constant isentropic efficiency turbine. The superheated steam undergoes isentropic expansion through the high pressure turbine stage, meaning it emerges with the same specific entropy and experiences a specific enthalpy associated with the constant entropy and the pressure drop.

$$s_{HPin} = s_{HPout} \tag{3.34}$$

$$h_{HPout} = h(s_{HPout}, p_{HPout}) \tag{3.35}$$

The mechanical efficiency of the shaft is $\eta_{mech} = 0.9$ is isentropic efficiency is taken to be unity ($\eta_{is} = 1$). The turbine is a flow model and does not store fluid, so the outlet mass flow always equals, which is defined as $\dot{m}_{HP}$. The mass flow equation and shaft work equation are

$$\dot{m}_{in} = \dot{m}_{out} = \dot{m}_{HP} = \dot{m}_{HP0}\frac{p_{HP_{in}}}{p_{HP_{in0}}} \tag{3.36}$$

$$\dot{Q}_m = \eta_{mech}\dot{m}_{HP}(h_{HPin} - h_{HPout}). \tag{3.37}$$

The outgoing steam, which is still relatively high pressure at 1 MPa for nominal conditions, is divided between the feedwater heater mixing volume and the low pressure (LP) turbine stage.

3.2.4 LP Turbine

The equations governing the low pressure turbine are the same. The boundary conditions differ as well as the due to steam bleed to the feedwater heater for thermal regeneration of the secondary fluid.The superheated steam undergoes isentropic expansion through the high pressure turbine stage, meaning it emerges with the same specific entropy and experiences a specific enthalpy drop associated with the constant entropy and the pressure drop.

$$s_{LPin} = s_{LPout} \tag{3.38}$$

$$h_{LPout} = h(s_{LPout}, p_{LPout}) \tag{3.39}$$

The mechanical efficiency of the shaft is $\eta_{mech} = 0.9$ is isentropic efficiency is taken to be unity ($\eta_{is} = 1$). The turbine is a flow model and does not store fluid, so the outlet mass flow always equals, which is defined as $\dot{m}_{LP}$. The mass flow equation and shaft work equation are

$$\dot{m}_{in} = \dot{m}_o ut = \dot{m}_{LP} = \dot{m}_{LP0}\frac{p_{LP_{in}}}{p_{LP_{in0}}} \tag{3.40}$$

$$\dot{Q}_m = \eta_{mech}\dot{m}_{LP}(h_{LPin} - h_{LPout}), \tag{3.41}$$

The outgoing steam enters the condenser and undergoes a phase change in the low pressure chamber.

3.2.5 Condenser

The condenser is maintained at a constant vacuum pressure p_0 and is treated as a saturated fluid vessel. Effluent steam from the LP turbine enters the condenser and undergoes a phase change from hot steam to subcooled liquid. For a vacuum pressure of $p_0 = 10$ kPa, the saturation temperature is 45 °C with a specific enthalpy of 1.92×10^5 J/kg. The mass, fluid level, and energy equations for the condenser are

$$p = p_0 \tag{3.42}$$

$$\frac{dm}{dt} = \dot{m}_{LP} - \dot{m}_C \tag{3.43}$$

$$\frac{dE}{dt} = \dot{m}_{LP} h_{LP} - \dot{m}_C h_C - \dot{Q}. \tag{3.44}$$

Here $\dot{Q}$ is the heat removal from the condenser; the value of $\dot{Q}$ is the heat removal required to bring the fluid to saturated liquid condition at the pressure p_0. The subcooled liquid is pumped from the condenser to the feedwater heater by the condensate pump.

3.2.6 Condensate Pump

The condensate pump is treated as an ideal mass flow controller. The condensate pump is controlled so as to maintain the liquid inventory in the condenser; mass flows in and out are equalized. The consequence for the condenser then is

$$\frac{dm_C}{dt} = \dot{m}_{LP} - \dot{m}_C = 0. \tag{3.45}$$

The mass flow $\dot{m}_C$ is delivered to the feedwater heater from the condenser.

3.2.7 Feedwater Heater

The feedwater heater in this model is a well-mixed volume taking in the still superheated steam bleed from the end of the high pressure stage turbine and the liquid effluent from the condenser at liquid saturation condition.

$$\frac{dm_{FWH}}{dt} = \dot{m}_{bleed} + \dot{m}_C - \dot{m}_{FWP} \tag{3.46}$$

$$\frac{dE_{FWH}}{dt} = \dot{m}h_{HPout} + \dot{m}_C h_C - \dot{m}_{FWP} h_{FWH} \dot{m}_{bleed} = \dot{m}_{bleed0} \sqrt{\frac{p_{HP}}{p_{HP0}} \frac{\rho}{\rho_0}} \tag{3.47}$$

For nominal conditions, the bleed fraction is 26%, which compares well to the total bleed across multiple feedwater heaters in the NuScale turbine. The outgoing feedwater temperature at nominal condition is 180°C with a specific enthalpy of 8.3×10^5 J/kg.

3.2.8 Feedwater Pump

The condensate pump is treated as an ideal mass flow controller. The input signal from the external master control determines the mass flow rate through the pump. The feedwater pump is used to pump the reheated secondary fluid from the feedwater heater back to the steam generator inlet. The feedwater pump mass flow rate is simply the variable input $\dot{m}_{FWP}$.

3.3 Model Validation

Data for nominal steady state operation appear in Table 3.1. These values are what one would expect for an integral PWR. The nominal steady state data for the total plant model were also compared to the nominal data for the NuScale NRC Design Certification Application documents for the steam system [54]. Due to the simplification of the balance of plant relative to the NRC Design Certification Application documents for the steam system, assumptions compared to the NRC design certification, some physical quantities differ. The performance does not need to match exactly, but results, especially primary coolant inlet and outlet temperatures, steam properties, and electric power, are comparable between the model and design data. The steady state data presented here are similar to the natural circulation model data from the INL NuScale development effort presented by Frick and Bragg-Sitton [36].

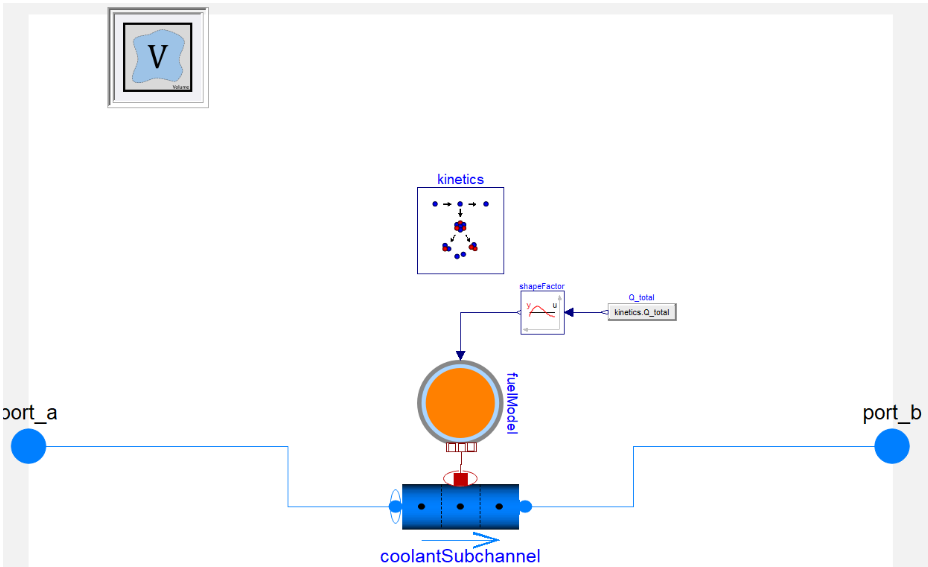

Figure 3.2: Diagram level model of the coupling between fission heat generation and heat transfer from the fuel to the coolant in Dymola.

Table 3.1: Comparison of Modelica results and NuScale design data for nominal conditions

Process Variable	Modelica Model	Design Parameters	INL Model
Reactor Thermal Power (MWth)	159.27	160	160
Electrical Power (MWe)	49.8	50	50
Steam Outlet Temperature (°C)	320	325	308
Steam Flow Rate (kg/s)	0.096	0.095	0.084
Feedwater Flow Rate (kg/s)	0.096	0.095	0.084
Feedwater Temp (°C)	180	191	-
Steam Outlet Pressure (MPa)	3.5	3.5	3.44

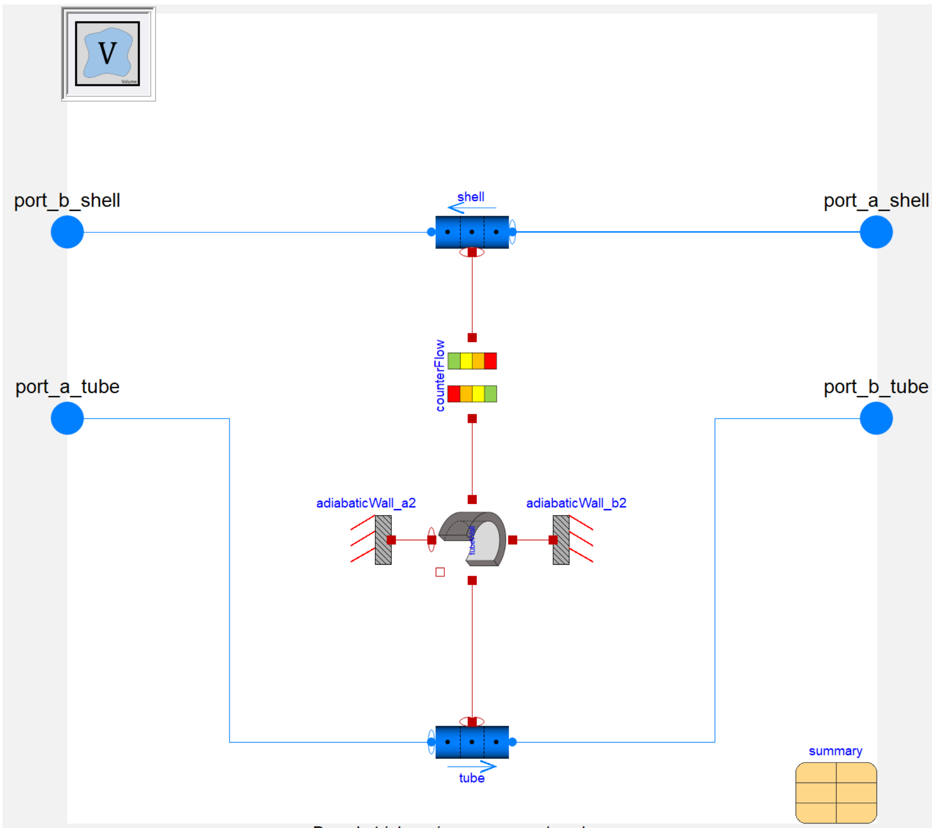

Figure 3.3: Nodalization of the steam generator with primary coolant loop (P), tube wall (W), and secondary coolant loop. The primary coolant from the upper plenum enters through the port_a_shell fluid connector interface while secondary coolant from the feedwater pump enters through the port_a_tube fluid connector interface.

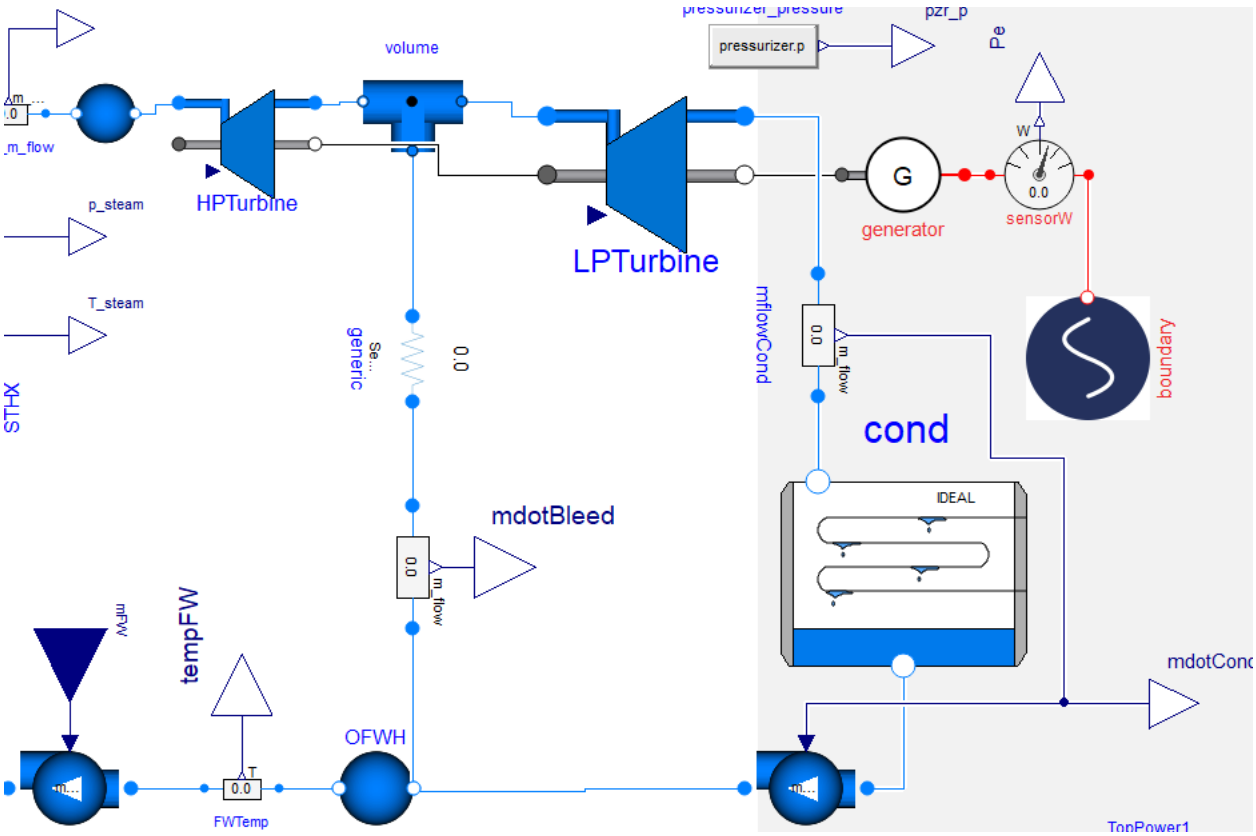

Figure 3.4: Diagram level model of the balance of plant in Dymola.

The open loop response of the total plant model was validated against other published models of IPWRs and SMR PWRs. A NuScale model from Arda and Holbert, including a natural circulation model in the primary and pressurizer control, was presented and its response to different open loop control actions tested [55]. A similar IPWR modeling effort was conducted by Poudel, Joshi, and Gokaraju [56] featuring a natural circulation flow model with both open and cloosed loop response of the system tested. A similarly sized PWR design with a once-through steam generator was presented by Ma and others [57]. Step reactivity insertion results from the other models selected for validation studies appear in Figures 3.5 - 3.9. The results for the same relative perturbation for the model presented in this chapter appear in Figure 3.10. It is important to note the key differences in the models compared to this chapter's model, such as the use of a natural circulation model that determines the primary coolant mass flow rate in [55] and [56] as well as the absence of feedback from their respective balance of plant models. The power response of the model is quite similar to that of [55] both quantitatively and qualitatively as well as [56] to a lesser extent; the general response is still similar to that of [57]. The coolant and fuel temperatures evolve similarly across the models, with the coolant temperatures rising and settling to hire to steady state values whereas the fuel temperatures experience a a rapid increasing before feedback reduces them to a still higher new steady state value. The total core reactivity behaves similarly, with a large spike due to the step insertion and thermal feedback returning the total reactivity to zero. The similarity of the system response of the model presented in this chapter demonstrates the soundness of the model, although some differences exist between steam pressure evolution due to the thermodynamic linkage to the balance of plant and the flow models used for the TCV and the bleed.

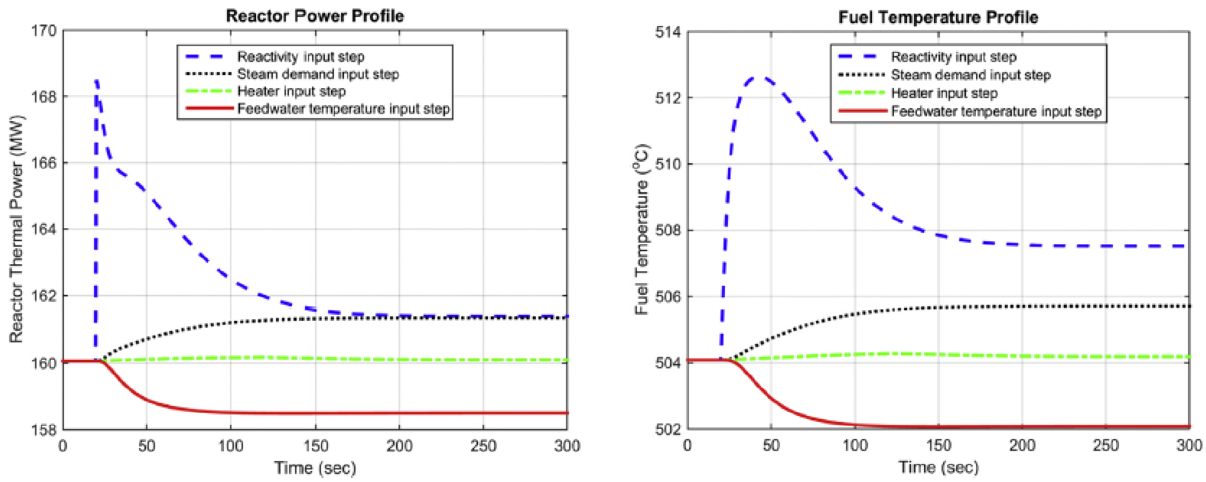

Figure 3.5: The reactor thermal power and fuel temperature response due to a +5¢ reactivity insertion as seen in [55]. The system response to the reactivity step insertion is plotted as the blue dotted line. The power evolves in a fashion similar to the Modelica model used in this dissertation work–a fast rise followed by a short and similarly rapid decrease, followed by a slower, smoother thermal feedback-induced decrease.

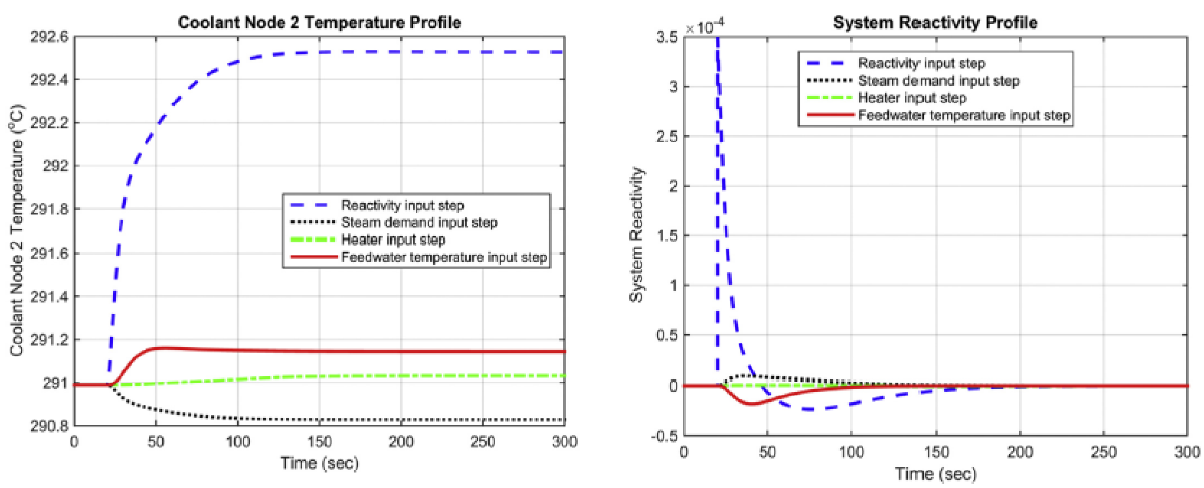

Figure 3.6: The upper coolant node temperature response and total reactivity due to a +5¢ reactivity insertion as seen in [55]. The system response to the reactivity step insertion is plotted as the blue dotted line.

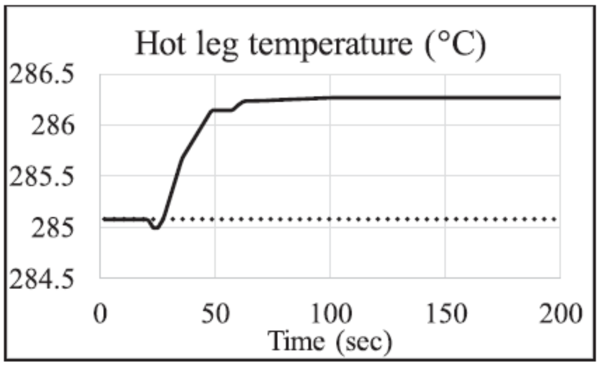

(c) T_{HL}

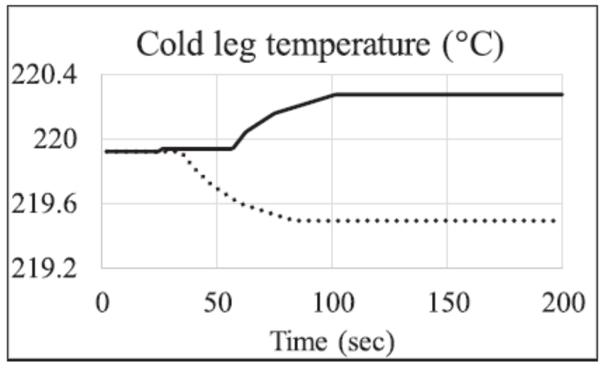

(d) T_{CL}

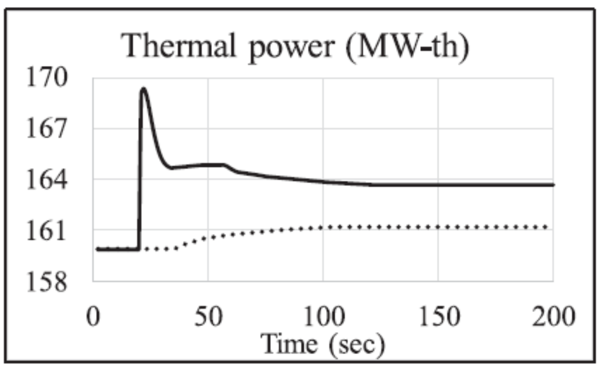

(g) P_{th}

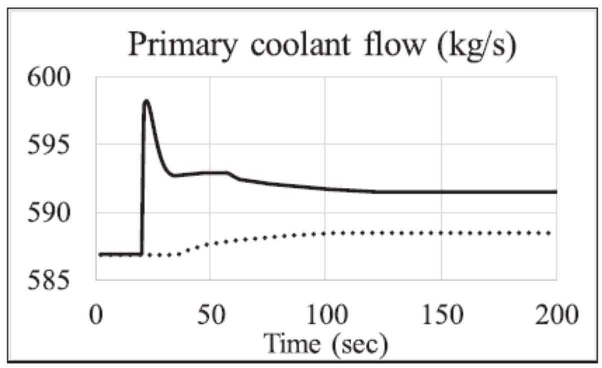

(h) $\dot{m}_{cp}$

Figure 3.7: The primary loop leg temperature, thermal power, and mass coolant flow response due to a +5¢ reactivity step insertion as seen in [56] are plotted as solid black lines. Note the rapid thermal power and coolant flow rise followed by the slower thermal feedback response.

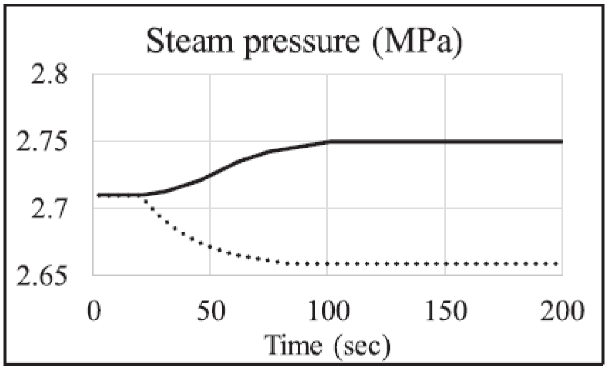

(a) p_{sat}

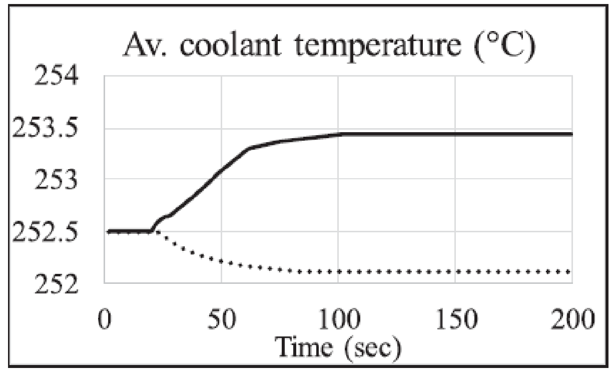

(b) T_p

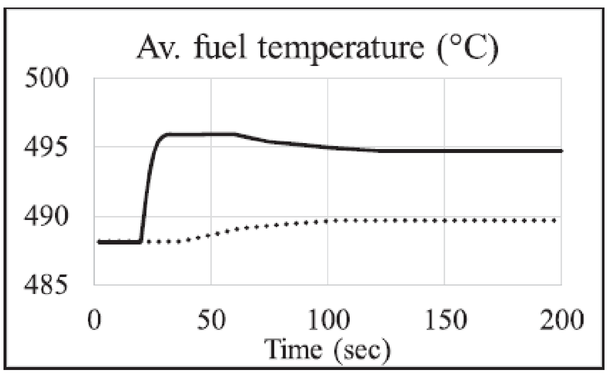

(e) T_f

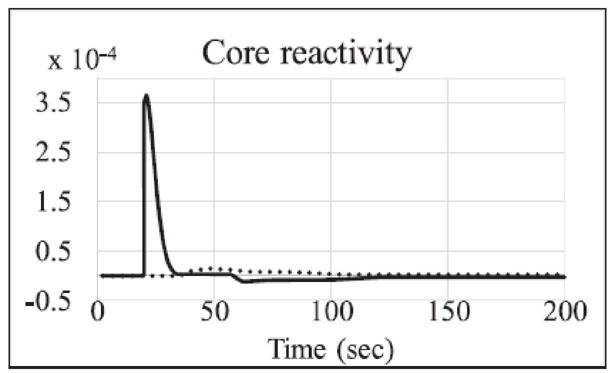

(f) ρ

Figure 3.8: The steam pressure, average temperature, and total reactivity response due to a +5¢ reactivity step insertion as seen in [56] are plotted as solid black lines. The increase in heat generation due to the positive reactivity insertion leads to increases in the primary system temperatures and steam header pressure, which is expected for an increase in the primary loop temperature.

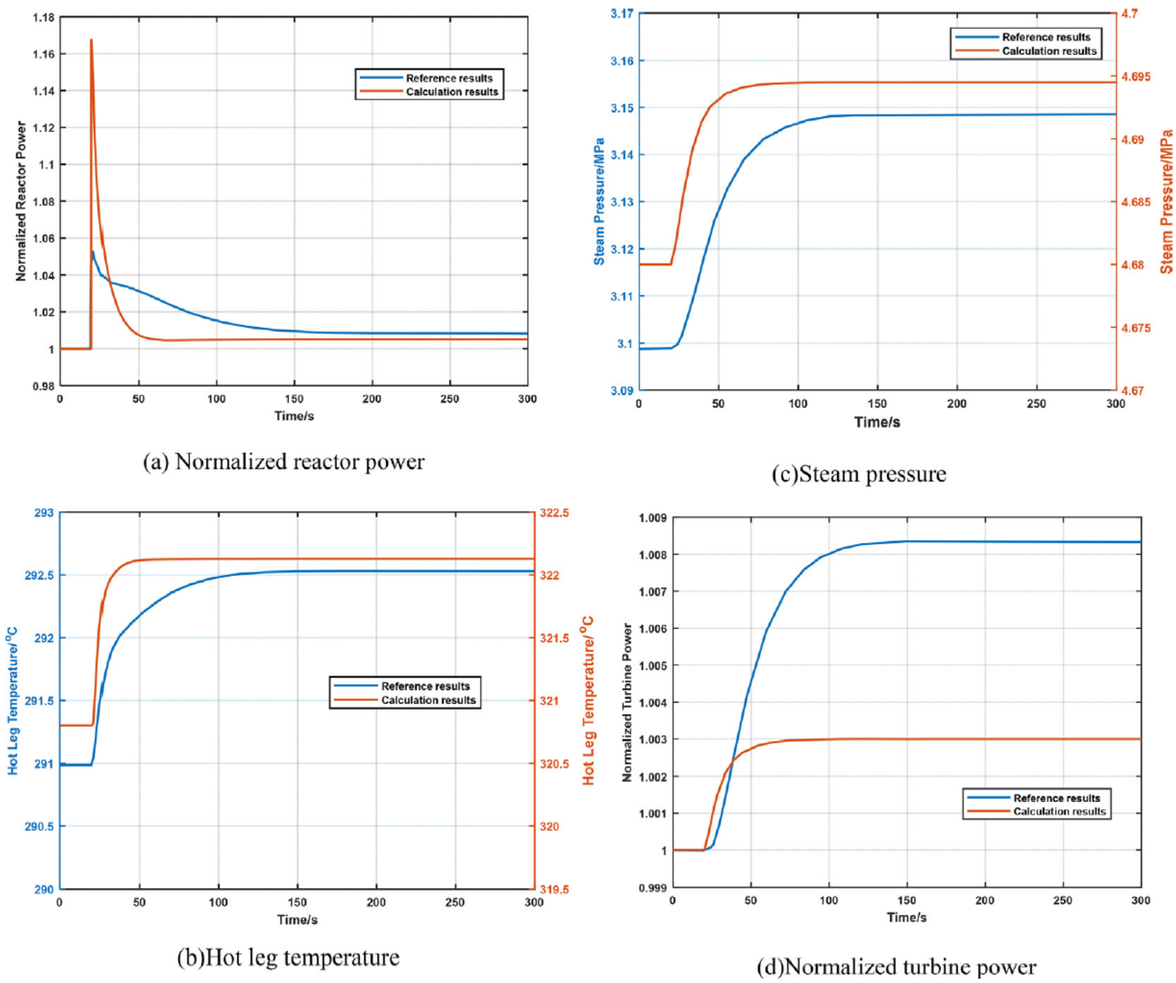

(a) Normalized reactor power

(c)Steam pressure

(b)Hot leg temperature

(d)Normalized turbine power

Figure 3.9: Reactor and turbine power, steam pressure, and hot leg temperature response as seen in [57]. The solid orange lines denote the response of the model developed in [57] whereas the blue lines denote the consulted reference model from Arda and Holbert [55].

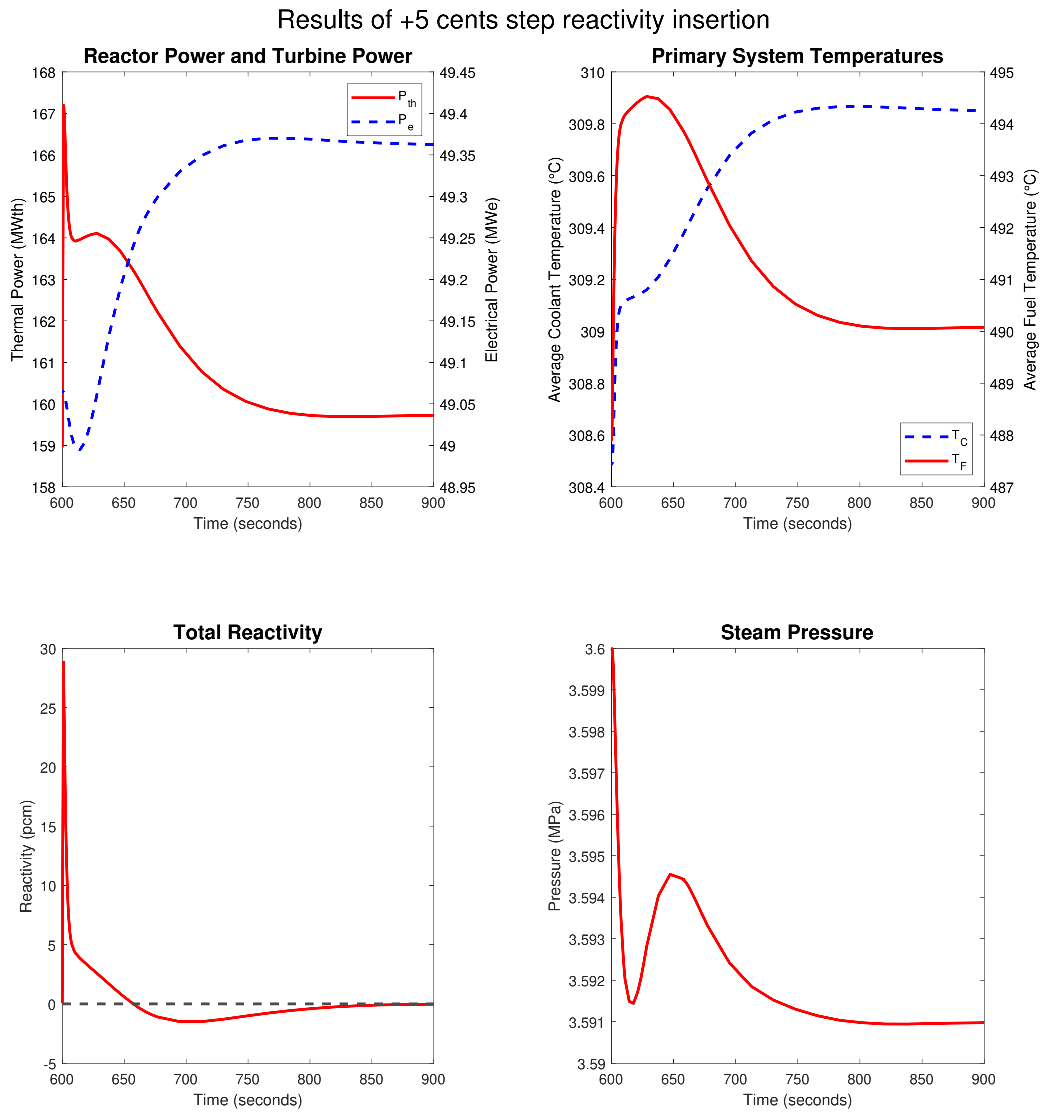

Figure 3.10: The reactor and turbine power, the primary system temperatures, and the net reactivity of the system evolve in a manner similar to the other models in response to a small reactivity insertion of 5 ¢. The steam pressure evolution stands out compared to the other models, but this is due to the linkage with the balance of plant model absent in the cited publications and lack of closed loop control of the feedwater pump.

Chapter 4

Operational Concepts and Motivations for Controls

This chapter motivates the choice of state variables to monitor, choice of actuator variables, figures of merit, and operational concepts. The state variables crucial to understanding the effects and limitations of load balancing operation are identified and the reasons for their relevance discussed. Four key actuator candidates are similarly identified, discussed, and tested for the feasibility and desirability for load balancing operations. Additionally figures of merit are presented and motivated with respect to how they relate to the flexible operation of an SMR power plant. Perturbation studies were conducted and are evaluated to motivate the selection of candidate actuators.

4.1 State Variables

The model presented in Chapter 3 is rather complex when all its constituent components with their respective nodalizations are connected via the fluidic connectors in Modelica. The system of equations is quite large and consists of 11,925 equations before model flattening, translation, and compiling. However, only some of these variables are of particular interest for studying nuclear power plant operation at the systems analysis level and for this dissertation work in particular. Each key state, input, or derived (from the prior two) variable is identified and discussed in turn as it relates to the evaluation of load balancing operational performance. A number of state variables are monitored in simulation, but only the reactor thermal power, electric power, core average temperature, and axial offset are discussed in detail due to their consequences for operation and control. The steam temperature, steam pressure, and feedwater temperature are also monitored since they can affect balance of plant behavior negatively if they operate beyond design parameters.

4.1.1 Reactor Thermal Power

The total reactor thermal power P_{th} is the most important state variable in the primary system since it determines the turbine-generator output power possible and thus its ability to meet grid demand. The thermal powers in the top and bottom halves of the core are monitored, a requirement for tracking the subsequently discussed state variable of the system, the axial offset (AO). In this work, the total reactor thermal power is the variable affected in control strategies for load balancing and for evaluating ramp rate availability.

4.1.2 Axial Offset

The reactor core model was constructed to in order to capture spatial phenomena in the core. In nuclear reactors it is necessary to control spatial gradients and instabilities arising weak spatial coupling, often exacerbated by poisons like xenon. The vertical power distribution in a real nuclear reactor is actually not axially symmetric due to moderator temperature effects as the coolant is heated from the bottom to the top [26], [37], but this is not modeled or explored for axial offset studies here. The axial offset is a measure of the relative difference between the top and bottom halves of the reactor core powers. It is defined mathematically as the following:

$$\text{AO} \equiv \frac{P_T - P_B}{P_T + P_B} \times 100\%. \tag{4.1}$$

Here P_T is the reactor thermal power in the top half of the core, and P_B is the reactor thermal power in the bottom half of the core. Thus the axial offset is the relative difference in percent in thermal power between the top and bottom halves of the core in percent. If this deviation in power levels becomes too large, it can cause thermal gradient stresses or instabilities in a real reactor, although this behavior is not modeled. In the feedforward control results later in this section, it will be demonstrated that an axial control strategy is not necessary for this particular reactor model. This is due to the strong neutronic coupling (Chapter 3) between the top and bottom reactor node halves [58].

4.1.3 Core Average Temperature

The core average temperature is the arithmetic average of the temperatures taken at the cold leg and hot leg of the primary coolant loop. Mathematically this is

$$T_{avg} = \frac{1}{2}(T_{CL} + T_{HL}). \tag{4.2}$$

The T_{avg} temperature offers a way to evaluate the thermal transients imposed on the reactor core. It is important to keep in mind that this measure is *not* a temperature for either of the two reactor core nodes.

4.1.4 Electrical Power

The power P_e is simply the electrical power generated by the rotation of the turbine-generator, the key state variable of interest in the balance of plant. This is the actual power supplied to the electrical grid and is obviously integral to any load balancing operational concept.

4.2 Actuator Variables

There are several possible actuators for the control and safe operation of a nuclear power plant. For the level of complexity and fidelity chosen for this model, the actuators that can be interacted with are the external reactivity applied to the core, $\rho_C R$, the mass flow rate in the primary coolant loop, $\dot{m}_{primary}$, the feedwater mass flow rate in the secondary coolant loop, $\dot{m}_{FW}$, and the steam header pressure to the turbine, p_s. The results presented in this chapter demonstrate the motivations for selecting control rod position and feedwater mass flow rates as the best actuators for the developed model and in particular for selecting and developing a control strategy for the reactor thermal power and turbine electrical power. The primary coolant mass flow rate and steam header pressure are less useful for maneuvering the SMR plant power level for reasons that will be explained in this chapter.

4.3 Controls and Concepts of Operation

4.3.1 Reactor-Leading Mode

In reactor-leads-turbine, or reactor leading, operation, the reactor power is actuated to achieve a setpoint, and other plant systems respond to this reactor thermal power change [59]. This mode is also known as turbine-lagging because the turbine responds to changes in the reactor [59]. Figure 4.1 illustrates this concept for a CANDU reactor, but the concept is similar for PWRs. In the feedforward results section it is made clear that feedforward reactor leading operation is a problematic control strategy for the model due to significant feedback that causes core power to evolve in undesirable ways. A reactor power setpoint control scheme is not feasible due to this feedback, so another setpoint, typically primary coolant average temperature, should be used to regulate the primary loop.

4.3.2 Turbine-Leading Mode

In turbine-leads-reactor, or turbine leading, operation, the turbine generation error is corrected first by actuation on the balance of plant side [59]. The reactor power evolves in response to the changes in the balance of plant until the whole system stabilizes. For this reason it is also known as reactor-lagging operation [59]. This enables very fast response, but it is taxing for the reactor and steam systems as power and temperature evolve rapidly. Ordinarily this

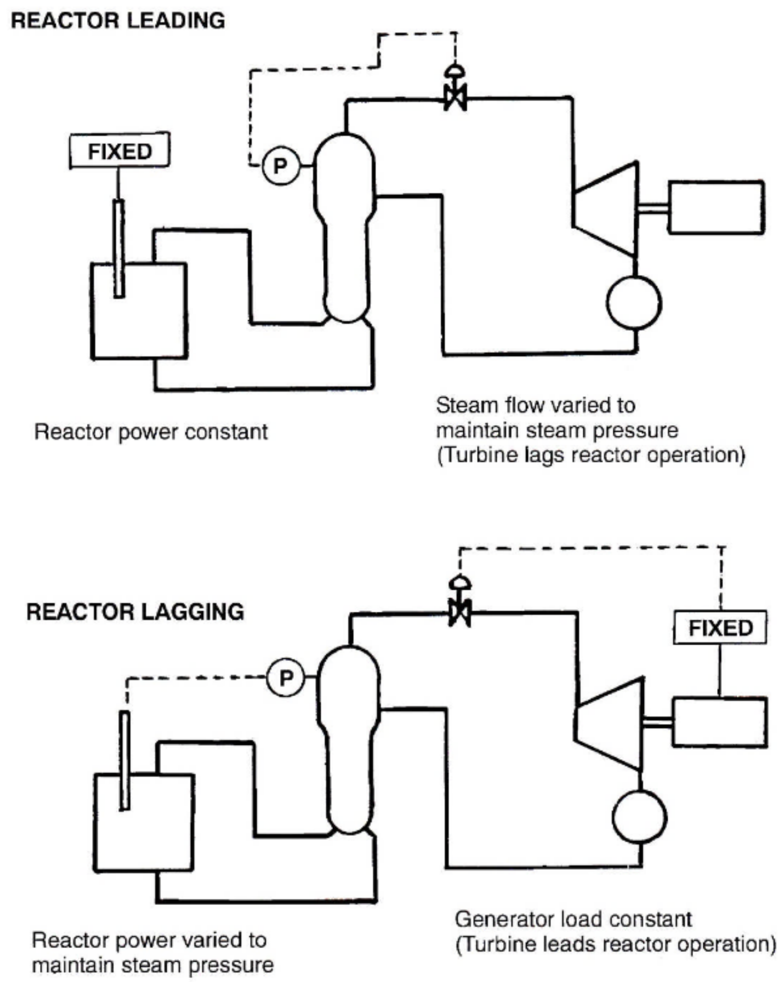

Figure 4.1: Diagram illustrating the concepts of reactor-leading/turbine-lagging and turbine-leading/reactor-lagging operation as it is presented in *The Essential CANDU* [59].

is accomplished through opening or closing the turbine governor valve [59]. The plant model has no governor-generator model, so feedwater control has been used instead to regulate heat removal from the primary and steam mass generation to alter the turbine shaft power and thus electrical power generated.

4.3.3 Towards a Coordinated Control Scheme

More traditional control design concepts typically rely upon separate control systems for each loop, but contemporary design paradigms trend towards a more integrated approach [60] [58]. A system of coordinated control is desirable given the problems with reactor leading and turbine leading operation that may arise under aggressive load following operation of an SMR. Instead of relying on one mode of operation and designing separate control loops for processes in a decoupled fashion, it may be beneficial to develop a system of coordinated control between the primary and secondary plant systems. Ideally such a control system could mimic the behavior of an experienced human operator, which makes fuzzy logic control an attractive option for this effort.

Nuclear power plants are operated in the aforementioned "reactor-leading-turbine" mode or "turbine-leading-reactor" mode, depending on the goals and restrictions of the power plant operator [59]. In fact, "turbine-leading-reactor" is generally the preferred mode of operation for load following and primary frequency control in order to respond rapidly to the demands of the grid [47]. It would be desirable for the reactor and turbine to operate in concert to manage transient phenomena [58].

4.4 Figures of Merit

The figures of merit (FOMs) are the quantitative functions by which the performance of the nuclear power plant system is evaluated. In future work these figures of merit can be used for the motivation and development of optimal control strategies or control systems which are optimal in some fashion. The figures of merit articulated in this thesis work are state variable error, actuator cost, and a notion of ramp availability dependent upon the xenon reactivity defect. The first two are generally transformed into cost functions, which can take the following forms:

$$J = \int_0^t x^T x + u^T u \, d\tau \tag{4.3}$$

$$J = \int_0^t \dot{x}^T \dot{x} + \dot{u}^T \dot{u} \, d\tau \tag{4.4}$$

$$J_i = \frac{1}{t} \int_0^t |u_i| \, d\tau \tag{4.5}$$

$$J_i = \int_0^t |e_i| \, d\tau \, , \tag{4.6}$$

Equation 4.3 is widely referred to as the cost, Equation 4.4 is often referred to as the energy of the system, Equation 4.5 is the integral absolute value time-averaged cost, and Equation 4.6 is the absolute value integral error. It is worth noting that these are not the only possible or valid cost function formulations; these are only some example functions common in the foundational control theory and optimization literature [61] [62]. This work concerns itself primarily with the quadratic error discussed in subsections 4.4.2 and 4.4.3 for evaluating load following performance.

4.4.1 State Variable Error

The state variable error is simply the difference between the particular state variable of the system and the reference signal for that variable. Here a quadratic cost formulation of the error is constructed as a way to evaluate the relative merit of a control strategy, controller gain value, or a controller or weight parameter.

$$e = x - x^* \tag{4.7}$$

$$J_e = \int_0^t e^T(\tau) e(\tau) \, d\tau = \int_0^t e^2(\tau) \, d\tau \tag{4.8}$$

Here e is the error, x is the state variable of interest, x^* is the initial value, the setpoint, or desired target value of x, and J_e is the time-integrated cost function associated with the error e in the state variable x relative to the target x^*. The power error is the primary consideration for control input used in the control studies in Chapter 5.

4.4.2 Energy of State Variable

$$J = \int_0^t \dot{x}^T \dot{x} \, d\tau = \int_0^t \dot{x}^2(\tau) \, d\tau \tag{4.9}$$

This is a measure of the stress the system undergoes due to transient evolution of the system. For instance, a change in the core temperature is a phenomenon that can degrade the integrity of the fuel cladding or rod banks. The formulation of this figure as the derivative of a valuable is designed to penalize evolution in that variable as opposed to deviation from a reference or nominal value. Although the term "energy" is often used to describe this quadratic state variable function, it is generally not energy in the strictly physical sense [61]. Rather, this is a way of quantifying notions of degradation, maintenance cost, or failure rates, which can be fed into models directly concerning those topics. Thus figures of this form provide a quantitative means of evaluating performance but can also facilitate control optimization.

4.4.3 Actuator Cost

The actuator cost is a measure of the control effort exerted to control the system. A quadratic function is used for the actuator cost so as to keep the value positive-definite and monotonically increasing with time. The general function form is the following:

$$J_u = \int_0^t \dot{u}^T(\tau) \dot{u}(\tau) \, d\tau = \int_0^t \dot{u}^2(\tau) \, d\tau \, . \tag{4.10}$$

As previously mentioned, this is often referred to as the "energy" of a control action, but it should not be confused with literal physical energy [61]. The selected actuators are the control rod reactivity insertion, the primary coolant feedwater mass flow rate, the feedwater mass flow rate, and the turbine control valve position.

4.4.4 Electrical Energy

The total electrical energy produced is also a key figure of merit. Although a flexible nuclear plant can earn income from providing ramping and frequency control services, it is primarily paid for the energy it supplies to the grid [14]. The total electrical energy generated is a proxy for energy revenue in this work. Mathematically the electrical energy is simply

$$E_e = \int_0^t P_e(\tau)\, d\tau \,, \tag{4.11}$$

where E_e is the electrical energy, and P_e is the electrical power created by the turbine-generator system.

4.5 Perturbation Studies of the SMR Plant Model

Perturbation studies were conducted to examine system response and evaluate the viability of candidate actuator variables for load following control strategies. All simulations were conducted with the whole plant model, i.e., the reactor core, the steam generator, and the balance of plant systems.

4.5.1 External Reactivity Insertion

Direct reactivity ramp insertions were made to the reactor core to evaluate the performance of the plant using only simple control rod maneuvers. This is in keeping with the usual practice of using regulating rods to adjust the reactor thermal power as in the French and German nuclear power plants [3] [63]. The reactivity perturbation studies here facilitate a quantitative evaluation of plant behavior. All perturbation actions start 600 s into all simulations.

200 pcm ramp insertion

A ramp insertion of 200 pcm was made over a time period of 200 s. The results of this ramp perturbation appear in Figures 4.2-4.7. The thermal power prior to the initiation of the control action is the nominal 160 MWth while the turbine power is 49.4 MWe in Figure 4.2, but thermal feedback in the core pushes the thermal power from a low of 151 MWth up to an intermediate where it remains stable for the duration of the simulation. The electrical power falls to 48.2 MWe, and the axial offset, pressurizer level, and pressurizer pressure also fall. In Figure 4.3 the effective fuel temperatures evolve analogously to the thermal power while the coolant node and coolant loop temperatures fall slightly and stabilize in a manner similar to the electrical power level. Figure 4.4 shows a small transient in the steam pressure that settles back at the nominal operating pressure at the end of the power ramp. It is worth noting this happens without altering the control valve opening. In the same figure the steam temperature drops markedly while the feedwater temperature decreases only slightly. In Figure 4.5 the control rod effort is the only nonzero actuator cost term since this perturbation only has the control rod reactivity as an input. In Figure 4.6 the energy generated grows roughly linearly since the change in electrical power generated was small; the changes in the temperature and steam pressure penalties are also similarly small. Lastly, xenon reactivity evolves slowly (as expected from the Bateman equations) in Figure 4.7; longer simulations for the same perturbation and the discussion in 4.6.2 better illustrate the evolution and effect of xenon as it pertains to reactor operation.

2000 pcm ramp insertion

A ramp insertion of 2000 pcm was made over a time period of 200 s starting at a time of 600 s. The results of this ramp perturbation appear in Figures 4.8-4.13. In Figure 4.8 the reactor thermal power decreases with the ramp negative reactivity insertion of the control rod bank from 159 MWth down to 68 MWth and experiences a small excursion that returns the reactor thermal power to 93 MWth. This excursion is due to the thermal reactivity feedback from the fuel and coolant; such significant feedback must be considered in the control design for flexible operation. The electrical power falls from 49 MWe to 25 MWe due to the decrease in heat generation in the core and thus a reduction of heat transfer from the primary to the secondary loop. The axial offset falls dramatically but remains under

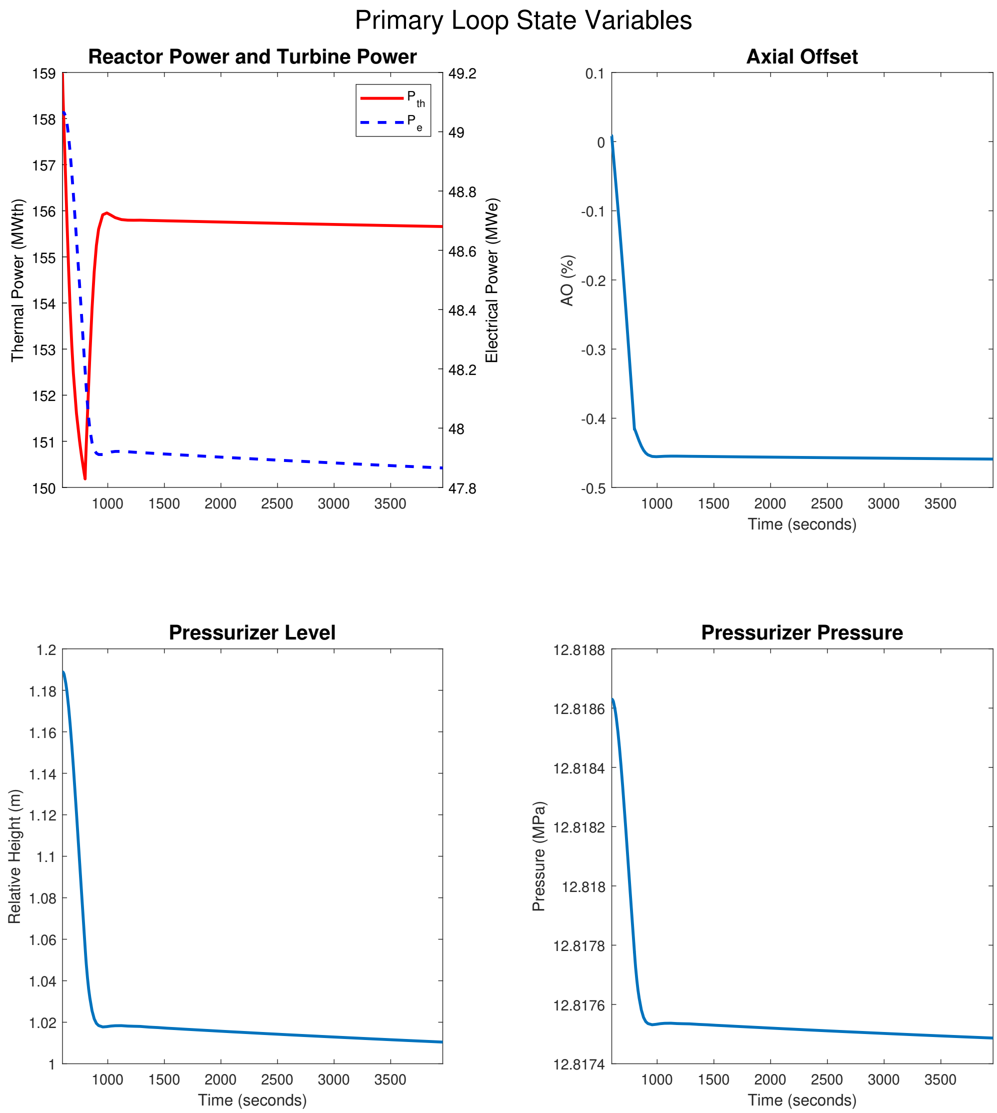

Figure 4.2: The plant state variables of interest are plotted here. Note the feedback in the thermal power and steam pressure transient at the end of the 200 pcm reactivity ramp.

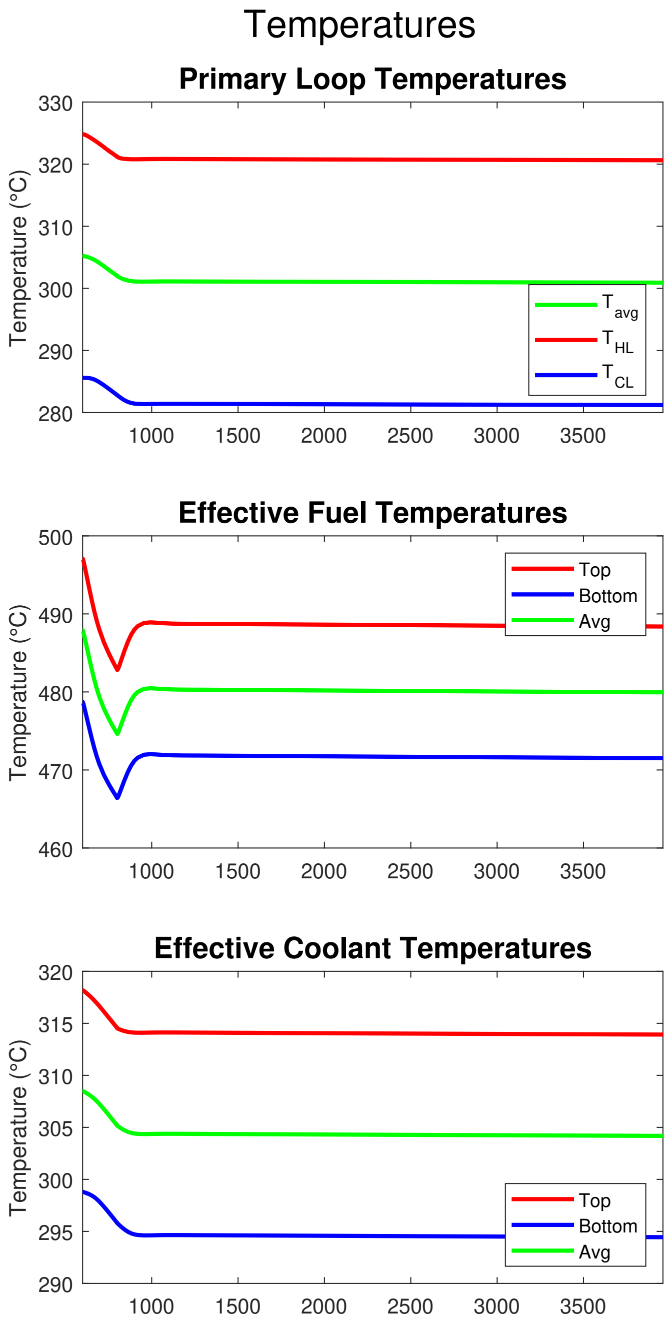

Figure 4.3: Temperature profiles associated with the primary system. Note the dramatic bounce in the fuel temperatures.

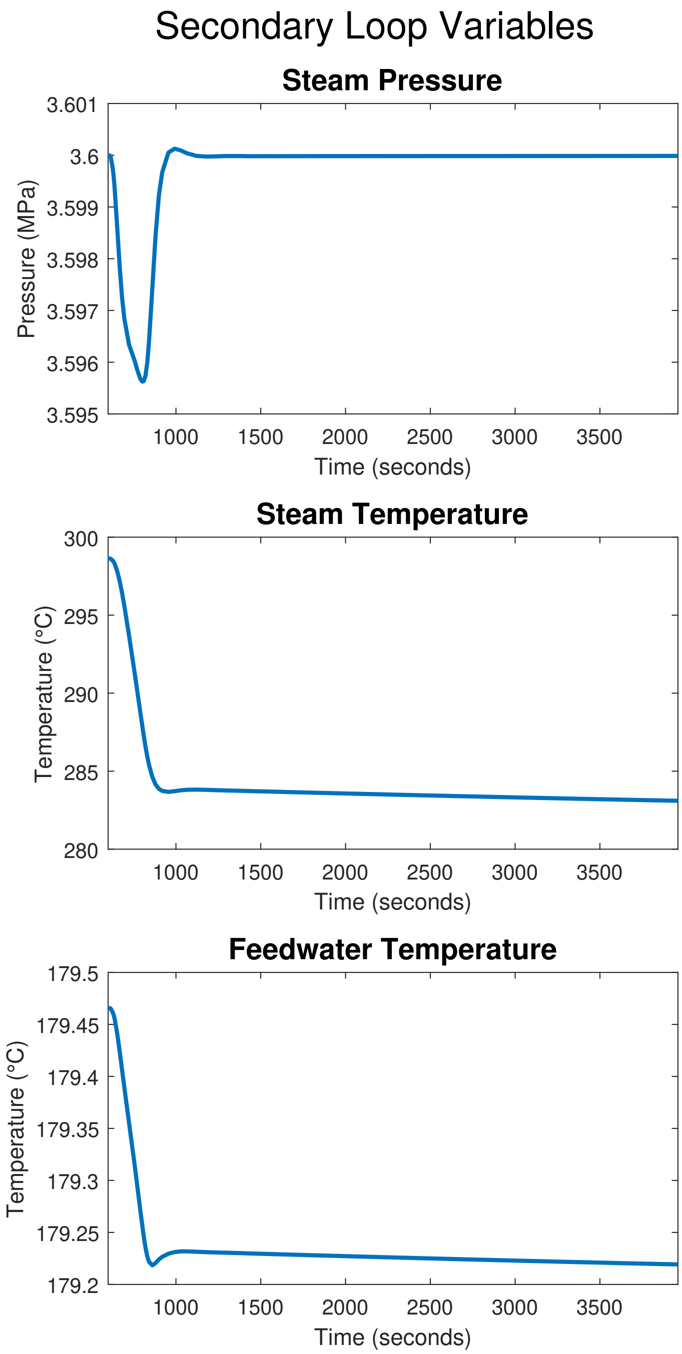

Figure 4.4: The steam pressure stabilizes relatively quickly after a moderate reactivity insertion while the steam temperature falls markedly.

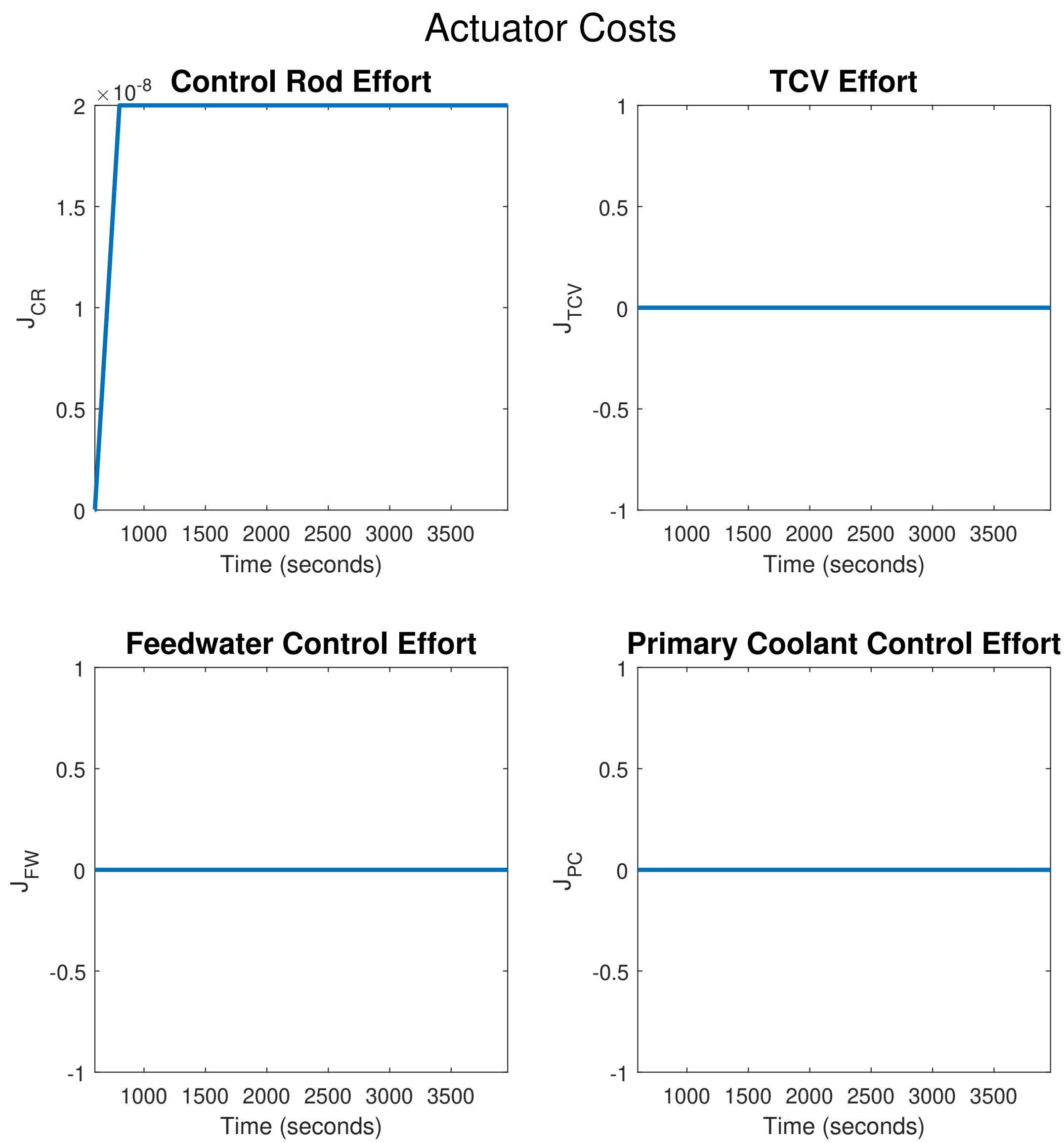

Figure 4.5: The cost of actuation for the 200 pcm ramp maneuver is plotted here. Since this is solely a control rod maneuver, only the control rod cost evolves over time.

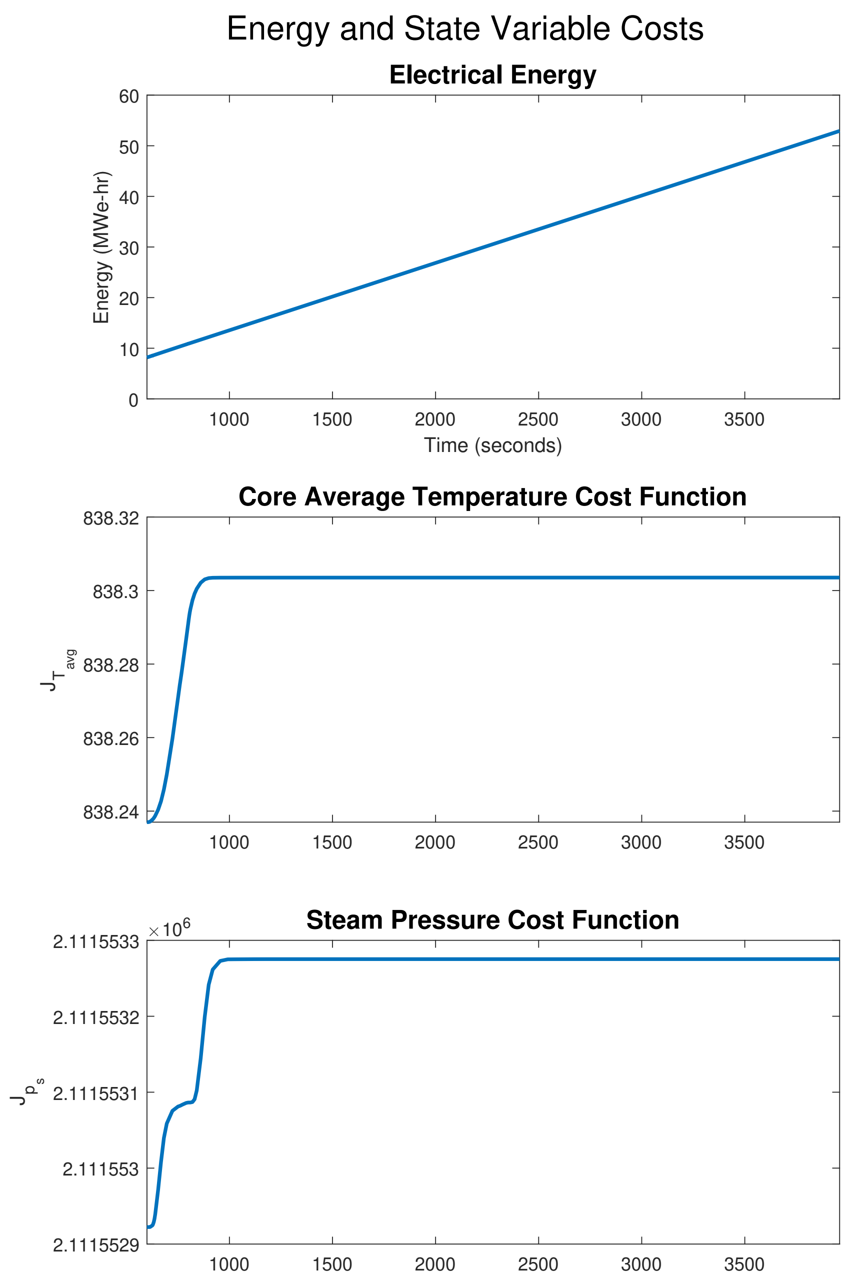

Figure 4.6: The electrical energy and state variable cost functions for the 200 pcm excursion. The large drop in core temperature implies a significant penalty to a control rod maneuver without consideration of maintaining the temperature in the primary circuit. There is a similarly sized penalty for the steam pressure, but it stabilizes relatively quickly.

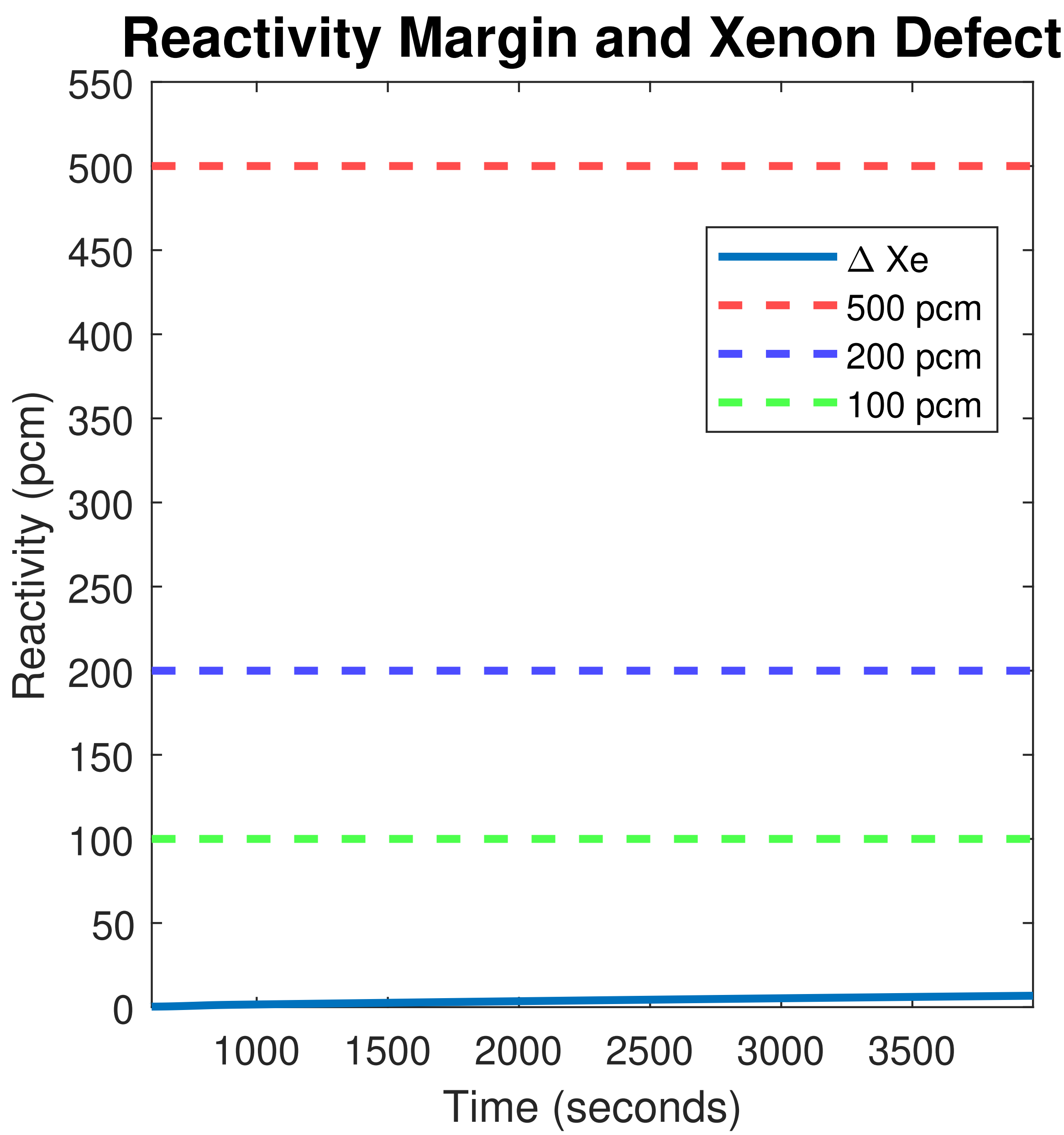

Figure 4.7: Xenon reactivity defect relative to low excess reactivities for the 200 pcm control rod action.

5% due to the strong coupling of the neutronically small core. The relative pressurizer level falls significantly while the pressure decreases slightly in response to the decrease in heat generation. This fall in heat generation causes a rapid drop in fuel temperatures that induces a thermal feedback to the core kinetics that in turn raises the fuel temperatures in Figure 4.9. The coolant temperatures decline somewhat and do not experience the same behavior as the fuel temperatures. The steam pressure experiences a very small relative decline during the ramp action and returns to nominal conditions at the end of the ramp followed by two shorter and smaller deviations in Figure 4.10. The steam and feedwater temperatures decline. The only control cost is that associated with the rod motion in Figure 4.11, and the core temperature cost increases moderately and smoothly in Figure 4.12. The steam pressure cost evolves sharply in response to the small drops later in the simulation; this may seem contrary to intuition, but the sharp drop in pressure implies a large penalty due to the functional form of the cost J_{p_s}. Most dramatic compared to other open loop control simulations in this chapter is the rapid increase in the xenon reactivity defect due to the large and rapid power drop in Figure 4.13.

4.5.2 Primary Coolant Mass Flow Rate

The primary coolant mass rate was perturbed from its nominal value of 700 kg/s by -20% to evaluate the overall effect on the modular plant operating state. The results of this perturbation appear in Figures 4.14-4.19. The low sensitivity of the response of the reactor power to the primary coolant flow rate combined with undesirable transients in temperatures and pressures suggests that it is an unsuitable candidate for power maneuvers in this model by itself. This significant reduction in the primary coolant mass flow rate in Figure 4.14 results in relatively modest reductions in the thermal and electrical power from 160 MWth and 49.2 MWe, respectively, to 154.5 MWth and 47.4 MWe. The axial offset falls modestly, as do the pressurizer level and pressure after a jittery transient during the primary coolant mass flow rate ramp action. In Figure 4.15 the ΔT across the the reactor core increases while the average temperature remains roughly unchanged. Figure 4.16 shows that the steam

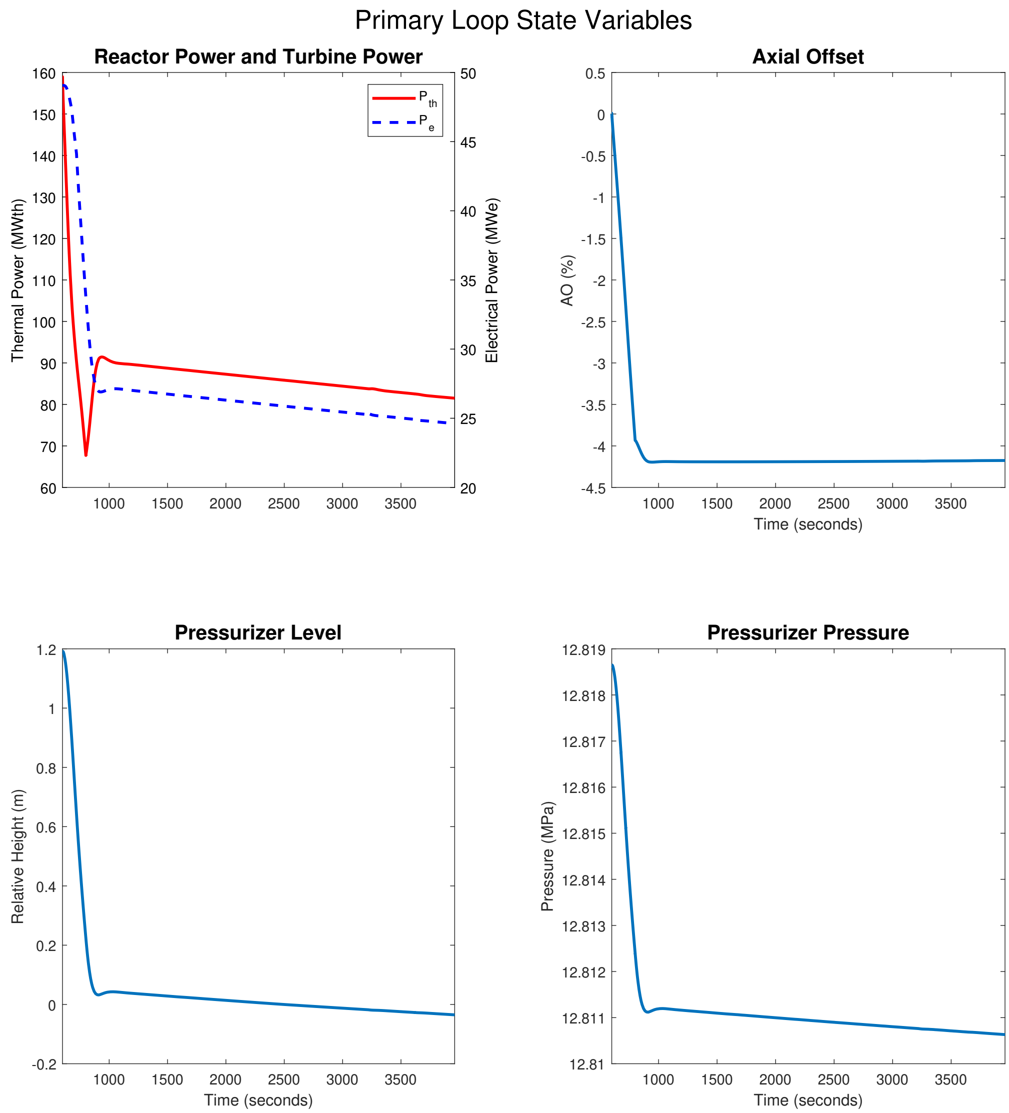

Figure 4.8: The plant state variables of interest are plotted here. Note the strong thermal feedback in the reactor power at the end of the reactivity ramp.

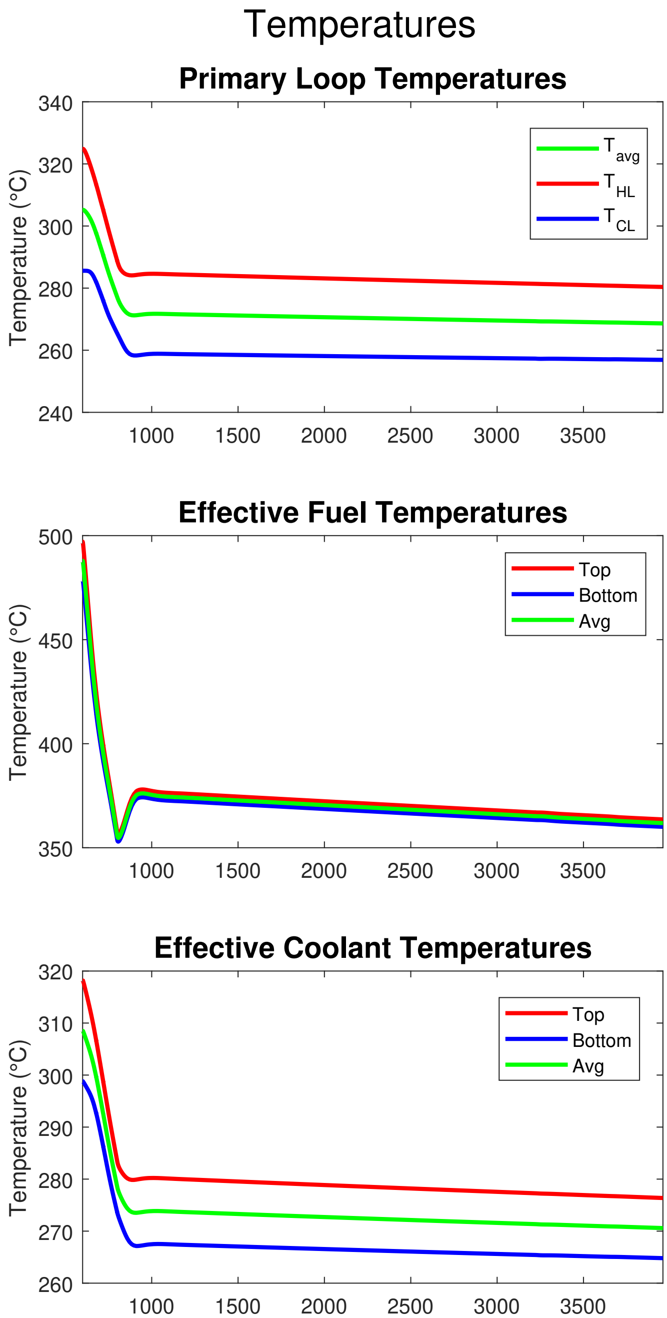

Figure 4.9: The primary temperatures' evolution due to the 2000 pcm ramp maneuver is plotted here. The large reactor power decreases causes a comparably large reduction in the primary loop temperatures.

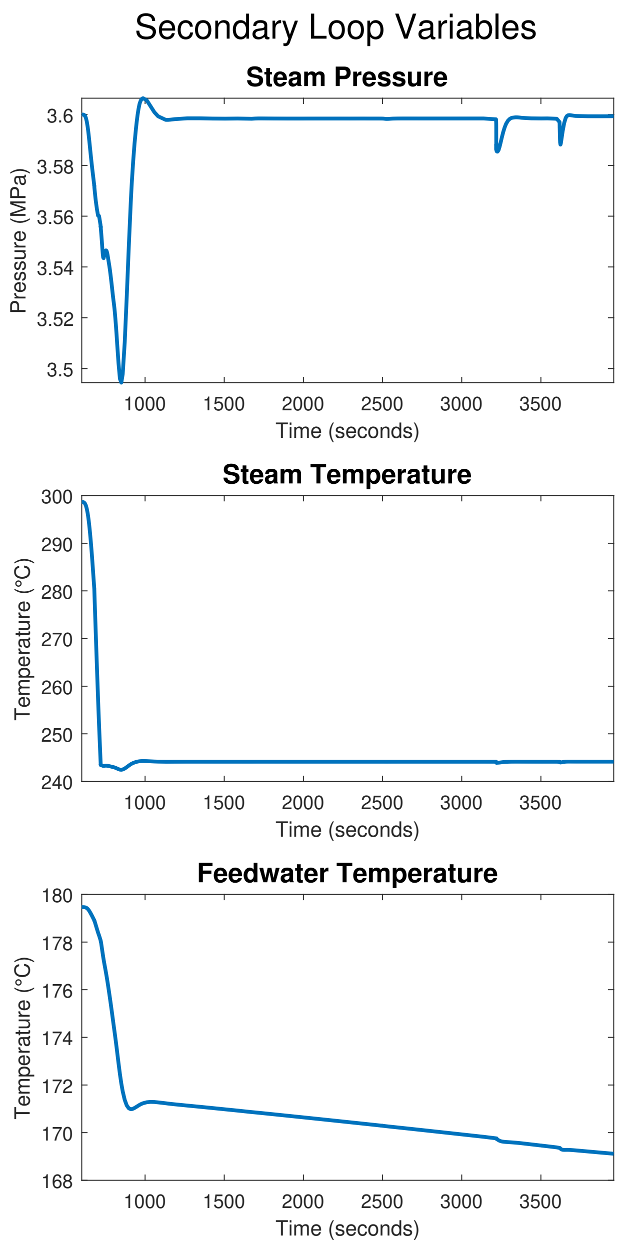

Figure 4.10: The steam pressure falls during the transient and experiences a . The steam temperature falls rapidly and subsequently stabilizes while the feedwater temperature falls quickly during the rapid reactivity insertion and then declines slowly due to the negative reactivity of xenon dominating the total reactivity in the core.

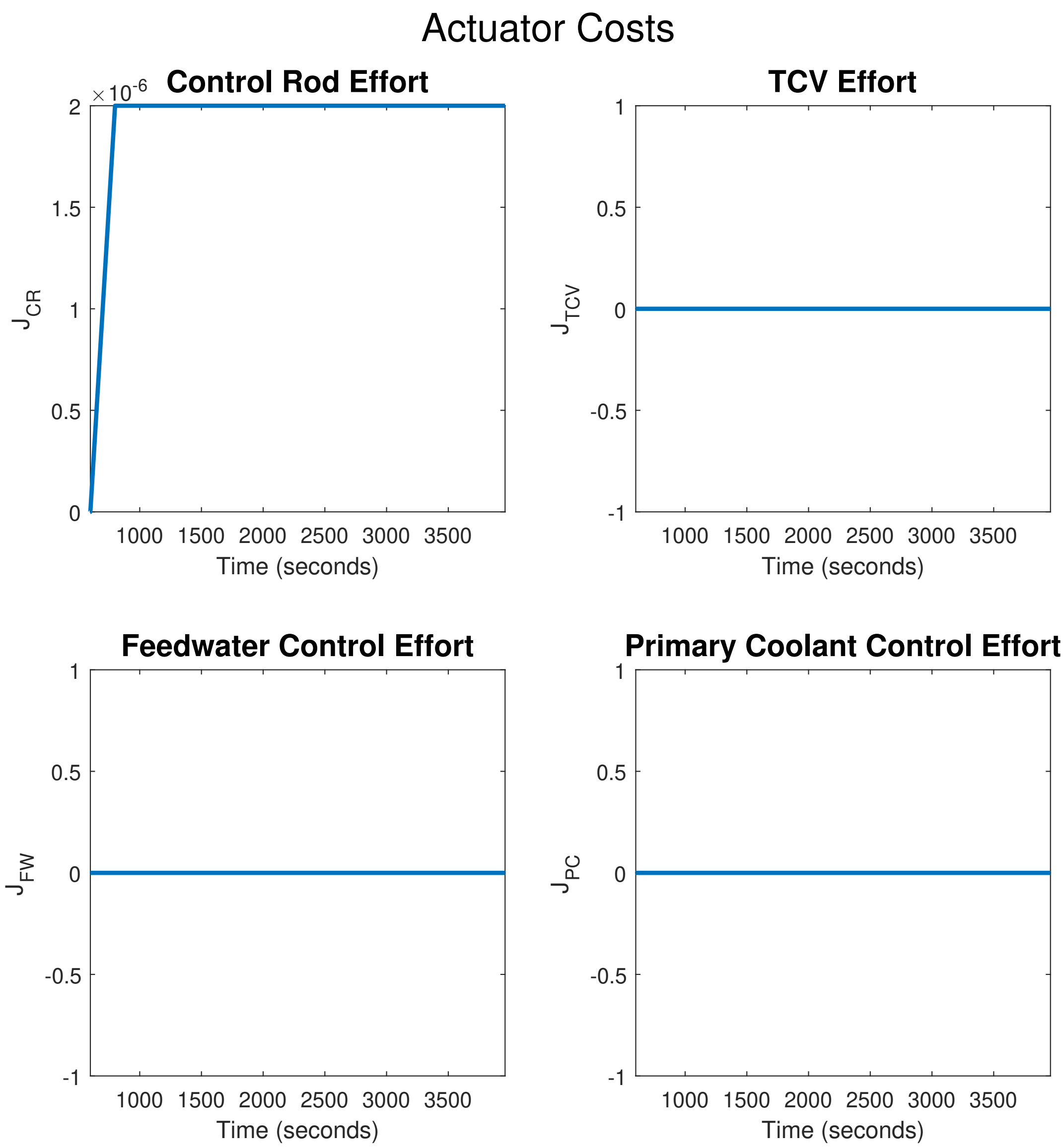

Figure 4.11: The actuator costs for the -2000 pcm ramp. Only the control rods are moved during this action.

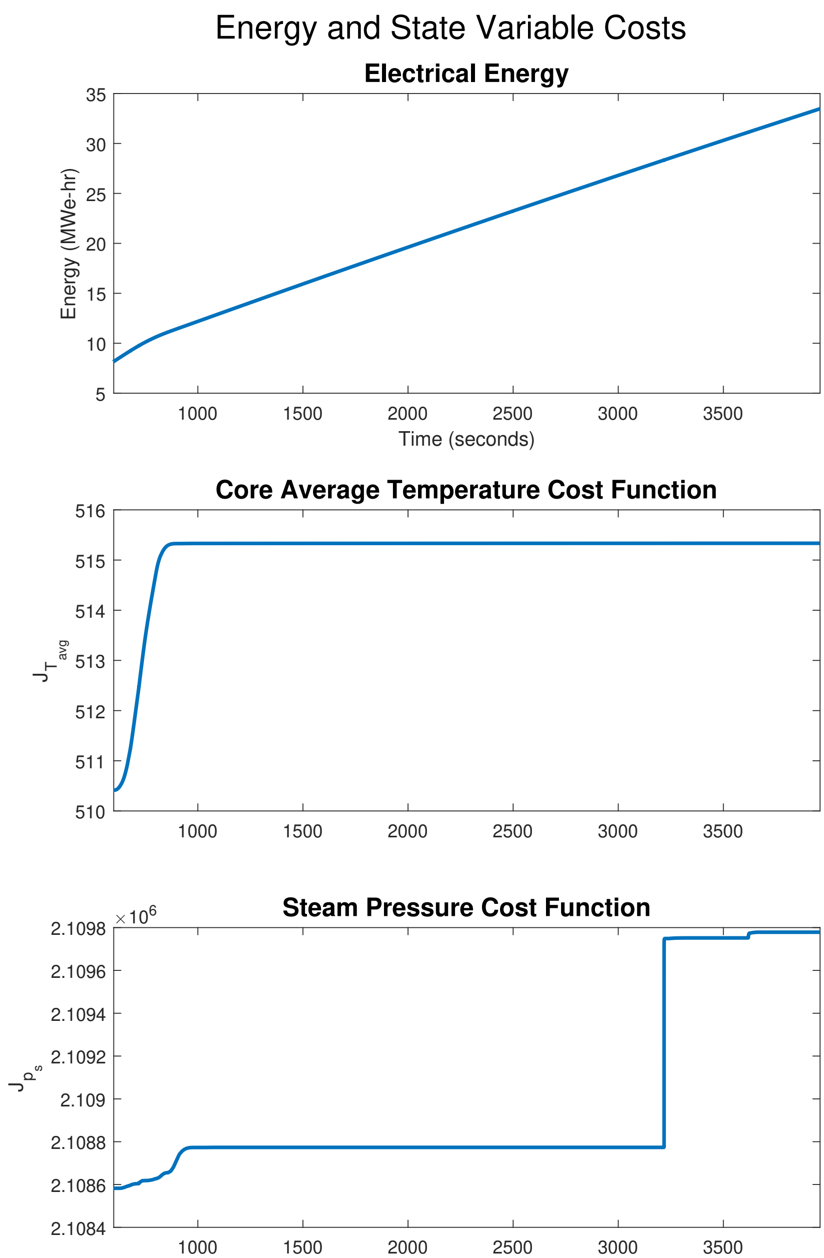

Figure 4.12: The energy produced and system costs/penalties associated with a -2000 pcm insertion. The large drop in core temperature implies a significant penalty to a control rod maneuver without consideration of maintaining the temperature in the primary circuit. There is a similarly large penalty for the steam pressure, but it stabilizes relatively quickly.

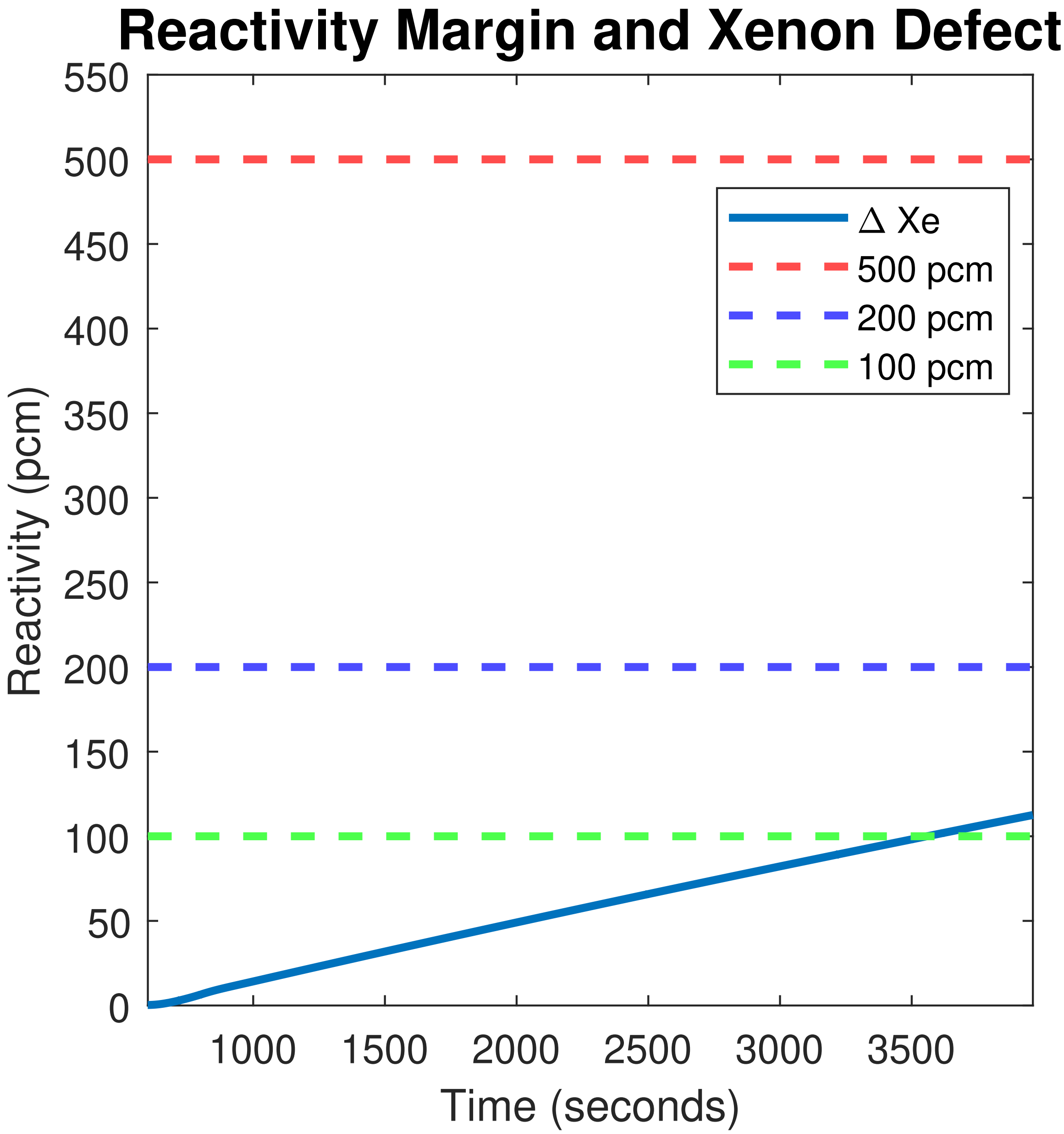

Figure 4.13: The xenon defect increases significantly due to the large drop in power level. Late in the core life cycle the xenon can exceed the excess reactivity even a short time following a power drop.

pressure experiences a small transient before stabilizing close to its nominal value while the steam temperature falls dramatically and feedwater temperature declines slightly. Figures 4.17 and 4.18 feature the effect of the primary pump control action on the actuator costs and system energy/costs, respectively. Xenon increases only slightly in the simulation in Figure 4.19.

4.5.3 Feedwater Mass Flow Rate

The feedwater mass flow rate was perturbed from its nominal value at 100% power demand to evaluate the effect on both reactor power and turbine power and plant performance generally. Both the reactor and turbine-generator power are relatively sensitive to changes in the feedwater mass flow rate. Altogether controlling the heat removal rate from primary is promising due to this sensitivity and close to linear response in the power (it is common for feedwater mass flow controllers to use feedforward 1-D interpolation programs), but with lower thermal feedback coefficients this control approach implies large temperature penalties.

10% Nominal Ramp of Feedwater Mass Flow Rate

A small ramp perturbation of -10% was made to the feedwater mass flow rate going into the steam generator in the secondary coolant loop. The results of this perturbation appear in Figures 4.20-4.25. In Figure 4.20 the reactor thermal power falls from 160 MWth to 149.5 MWth with a small positive thermal reactivity feedback at the end of the feedwater mass flow rate ramp action; the electrical power falls from 49.2 MWe to 45.5 MWe. The axial offset increases only slightly to a new short term stable level while the pressurizer level increases dramatically before falling off linearly. The pressurizer pressures evolves similarly but experiences a smaller change in relative terms. In Figure 4.21 it is apparent that this moderate change in the feedwater mass flow rate has a dramatic effect on the core's thermal behavior. This is commensurate with our understanding of use changes in the heat removal rate in the secondary loop to induce power level changes in the primary loop. In Figure 4.22 the behavior of the secondary loop steam variables in response to the feedwater mass

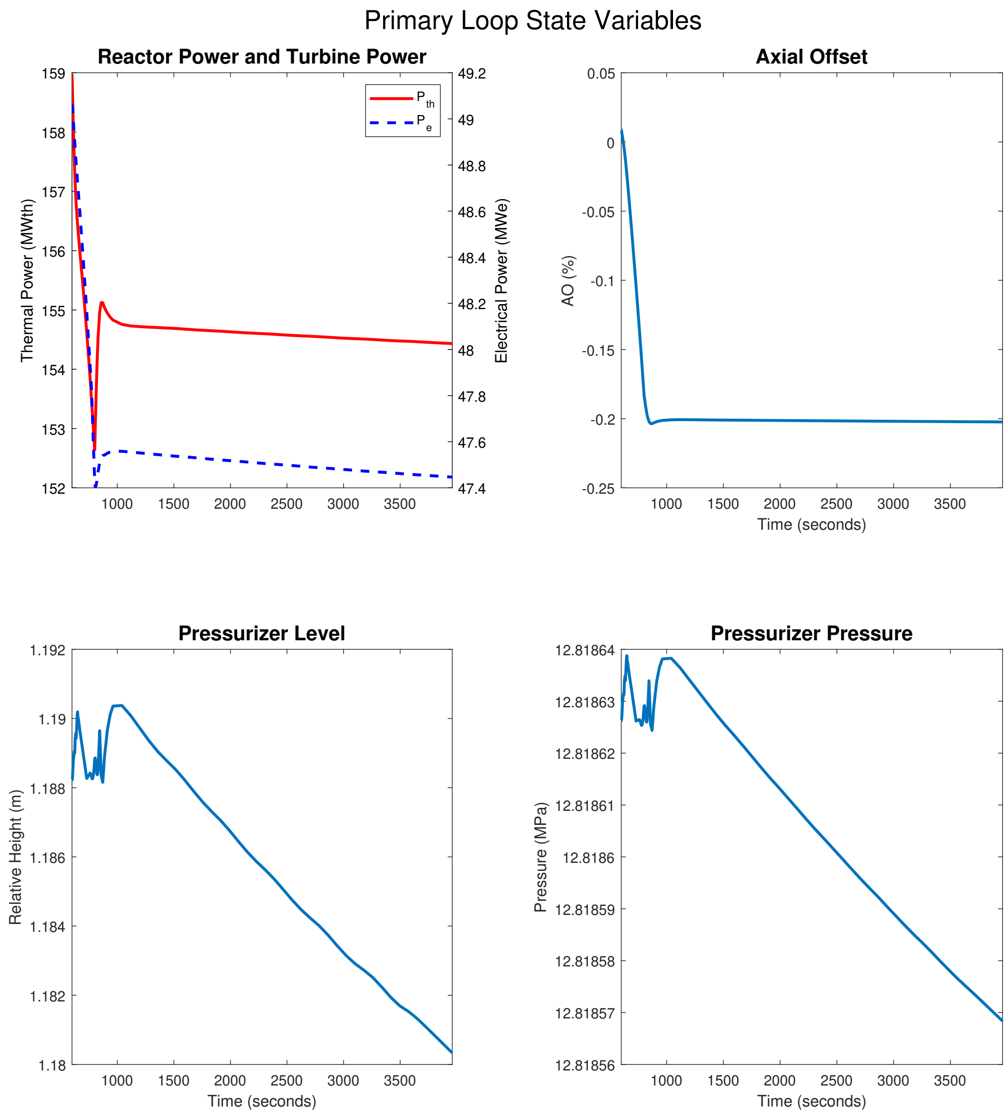

Figure 4.14: The plant state variables of interest are plotted here. Note the feedback in the thermal power and sharp steam pressure transient at the end of the primary pump mass flow rate ramp action.

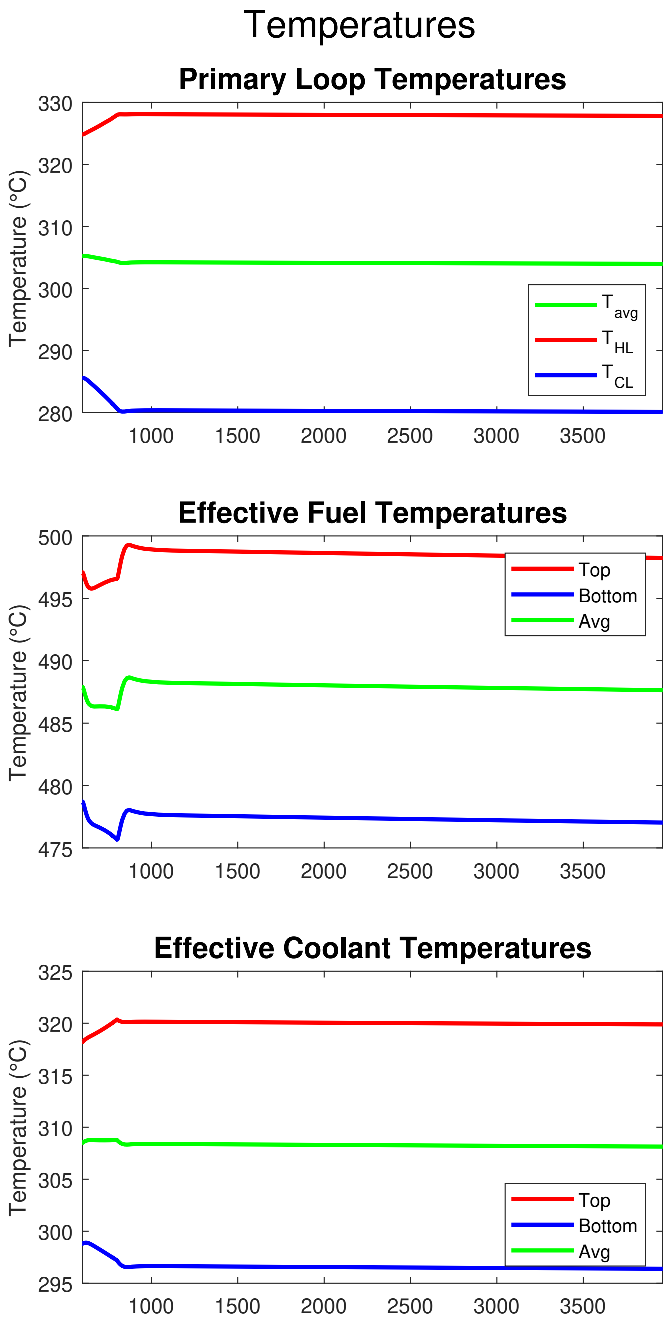

Figure 4.15: The delta T through the core increases somewhat while the average temperature changes very little.

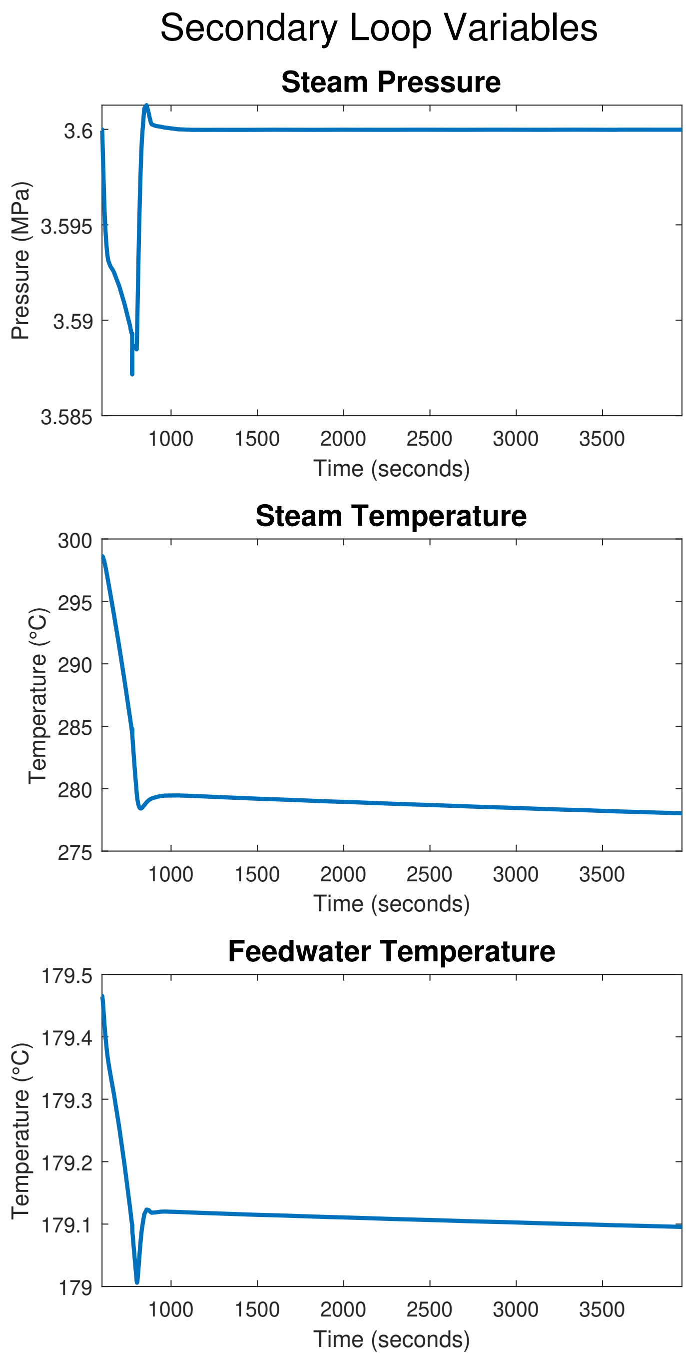

Figure 4.16: Response in the secondary loop due to ramp decrease in primary coolant mass flow rate.

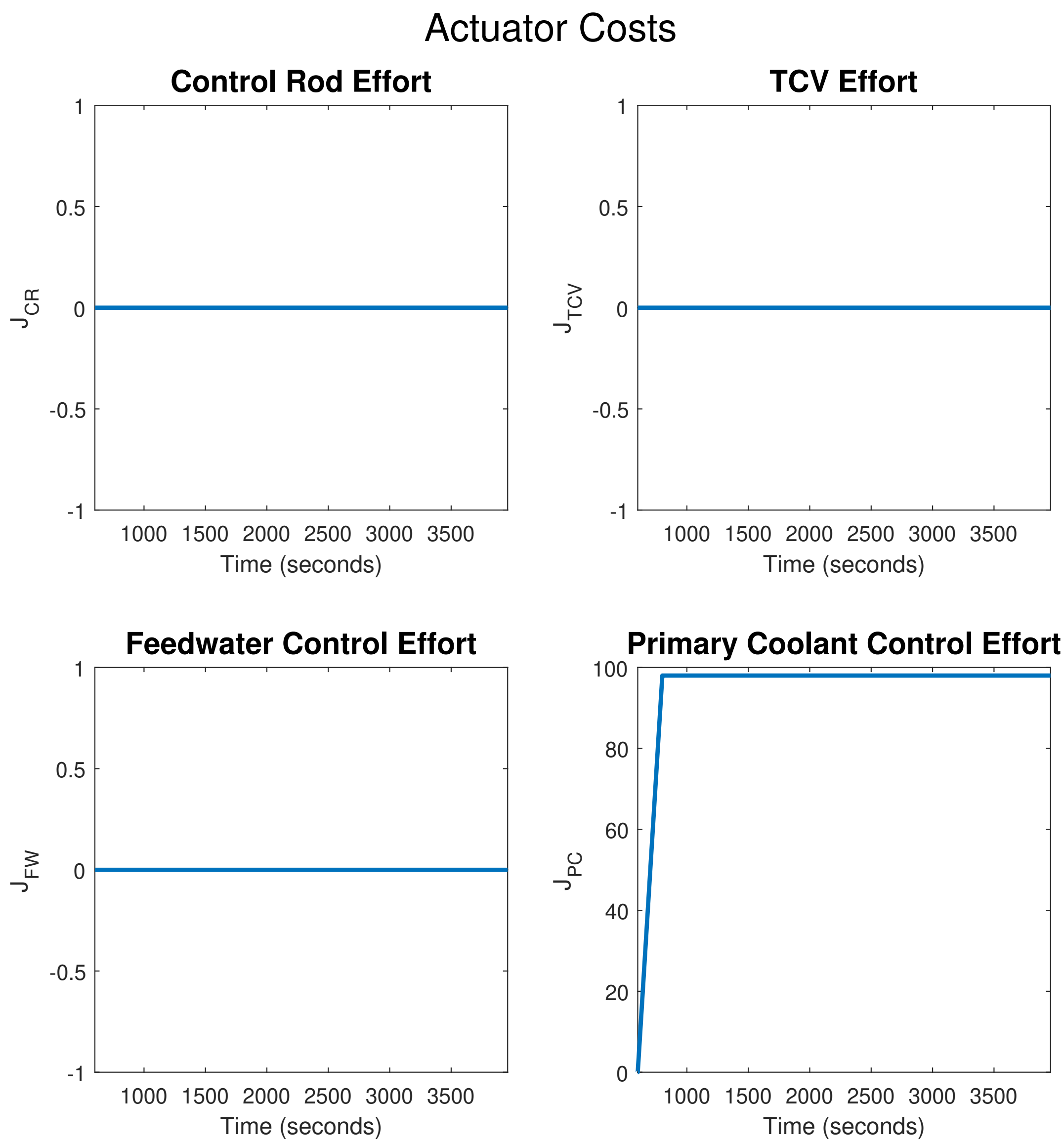

Figure 4.17: The cost of actuation for the primary coolant ramp maneuver is plotted here. Since this is solely a primary pump maneuver, only this cost evolves over the simulation.

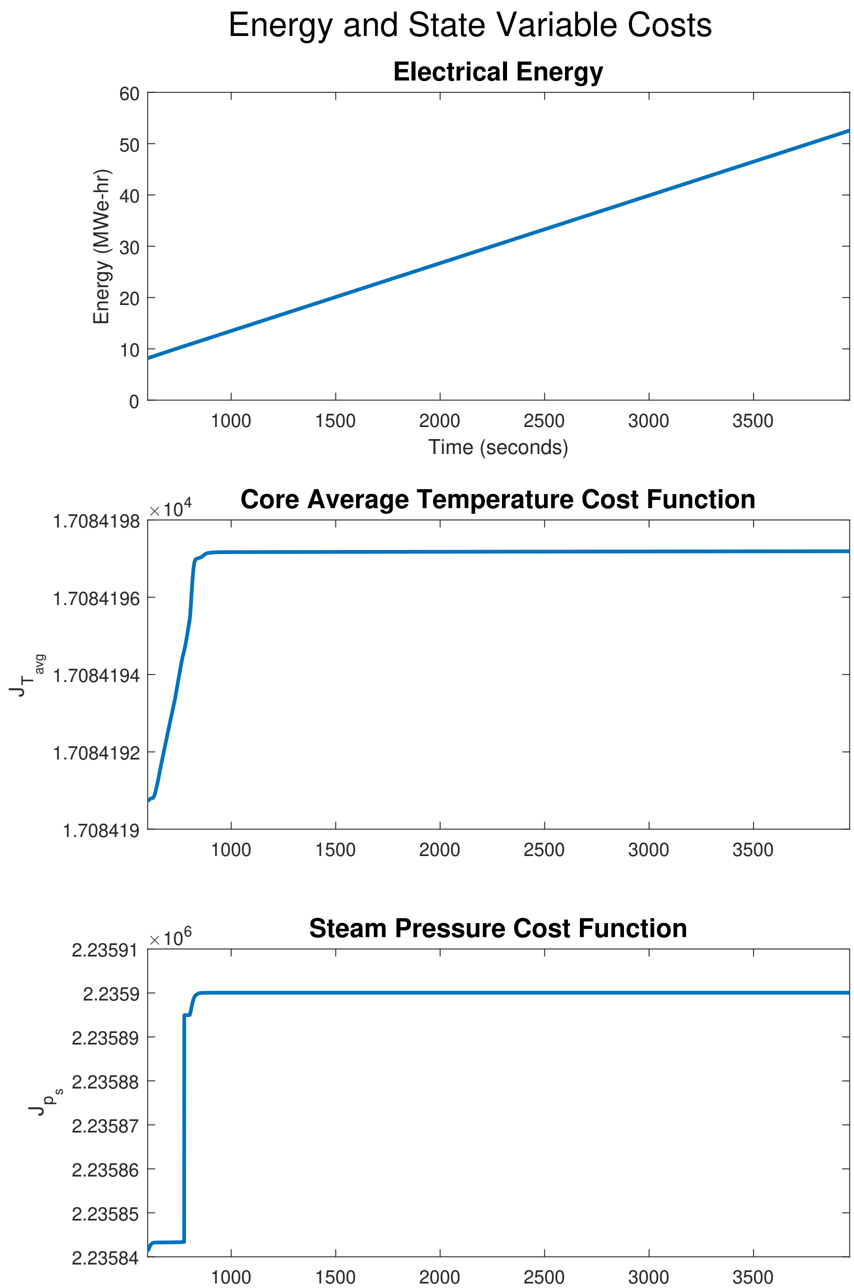

Figure 4.18: Energy production grows approximately linearly while the steam and temperature costs grow modestly with the primary pump change.

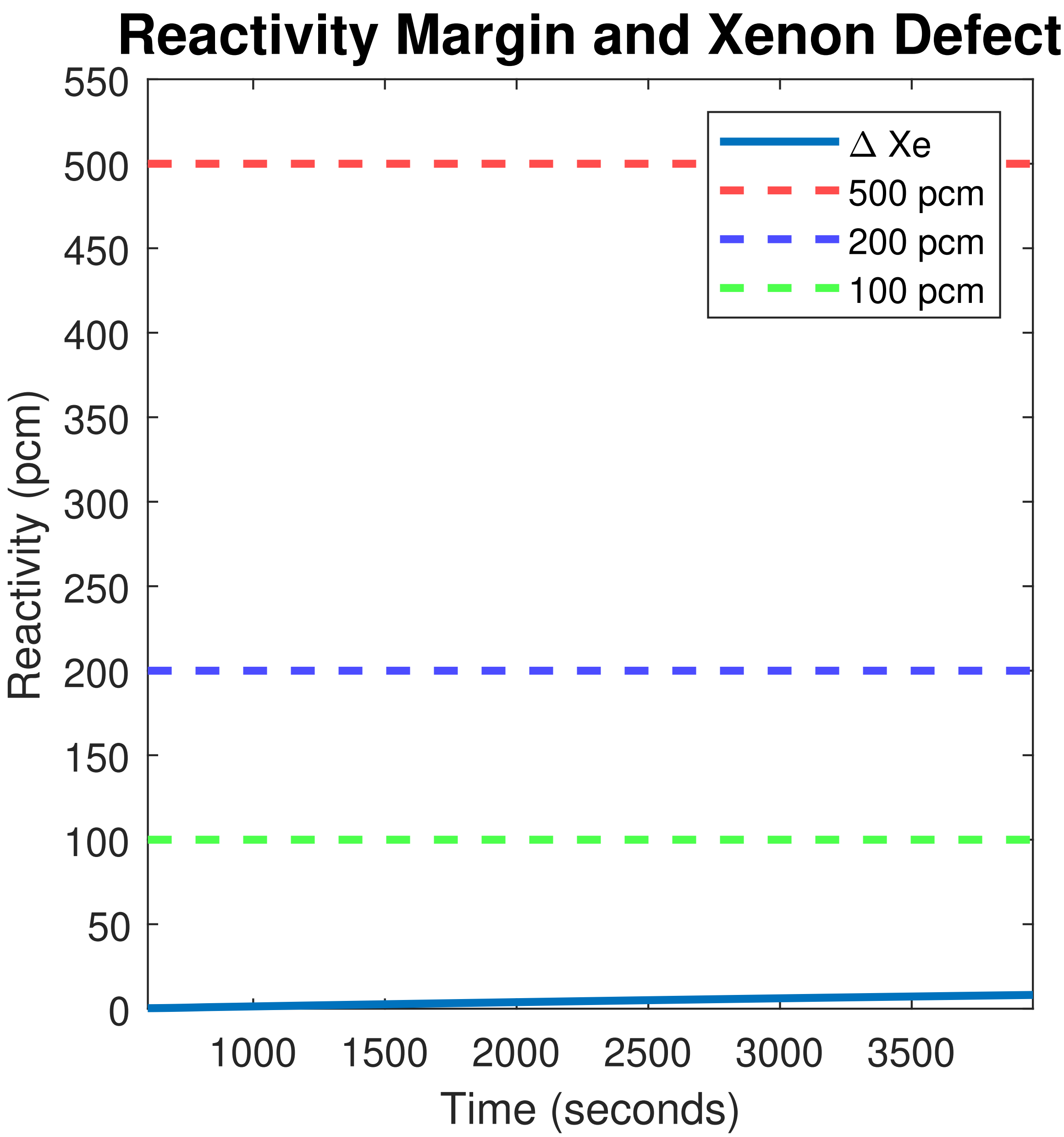

Figure 4.19: Xenon reactivity relative to low excess reactivities for the primary pump action.

flow rate drop can be seen, with the steam pressure dropping from 3.5 to 3.15 MPa. The steam temperature also rises markedly while the feedwater temperature falls from 179.5 C to a little over 176 C. In Figures 4.23 and 4.24 the actuator costs, state variable costs, and energy produced are plotted. Lastly the xenon reactivity evolution from the feedwater and power level drop appears in Figure 4.25. Overall these results suggest feedwater control is a good actuator for load following albeit not completely linear in response with respect to the thermal and electrical power generated.

50% Nominal Ramp of Feedwater Mass Flow Rate

A larger ramp perturbation of -50% is made to the feedwater mass flow rate going into the steam generator in the secondary coolant loop. The results of this dramatic reduction in feedwater flow rate appear in Figures 4.26-4.31. In Figure 4.26 the thermal power falls from its nominal rating to 90 MWth, and the electrical power falls from its nominal to 25 MWe. It is worth noting this electrical power change is close to 50%, the same as the feedwater mass flow rate ramp decrease. The axial offset rises to 0.45%, and the pressurizer level rises dramatically before falling at the end of the ramp with the pressure behaving similarly. In Figure 4.27 the coolant temperatures rise significantly while the fuel temperatures have a correspondingly large decrease. In Figure 4.28 the steam pressure falls precipitously during the ramp, as does the feedwater temperature while the steam temperature rises well above its nominal value. In Figures 4.29 and 4.30 the actuator and state variable costs and energy produced are plotted for the -50% feedwater ramp simulation. The steam pressure cost associated with the control action is quite large as expected due to the large drop in steam pressure in the earlier Figure 4.28. In Figure 4.31 it is clear that even for the short duration of this simulation that the xenon reactivity has changed enough to pose a problem for ramping and power management for a reactor that has low excess reactivity.

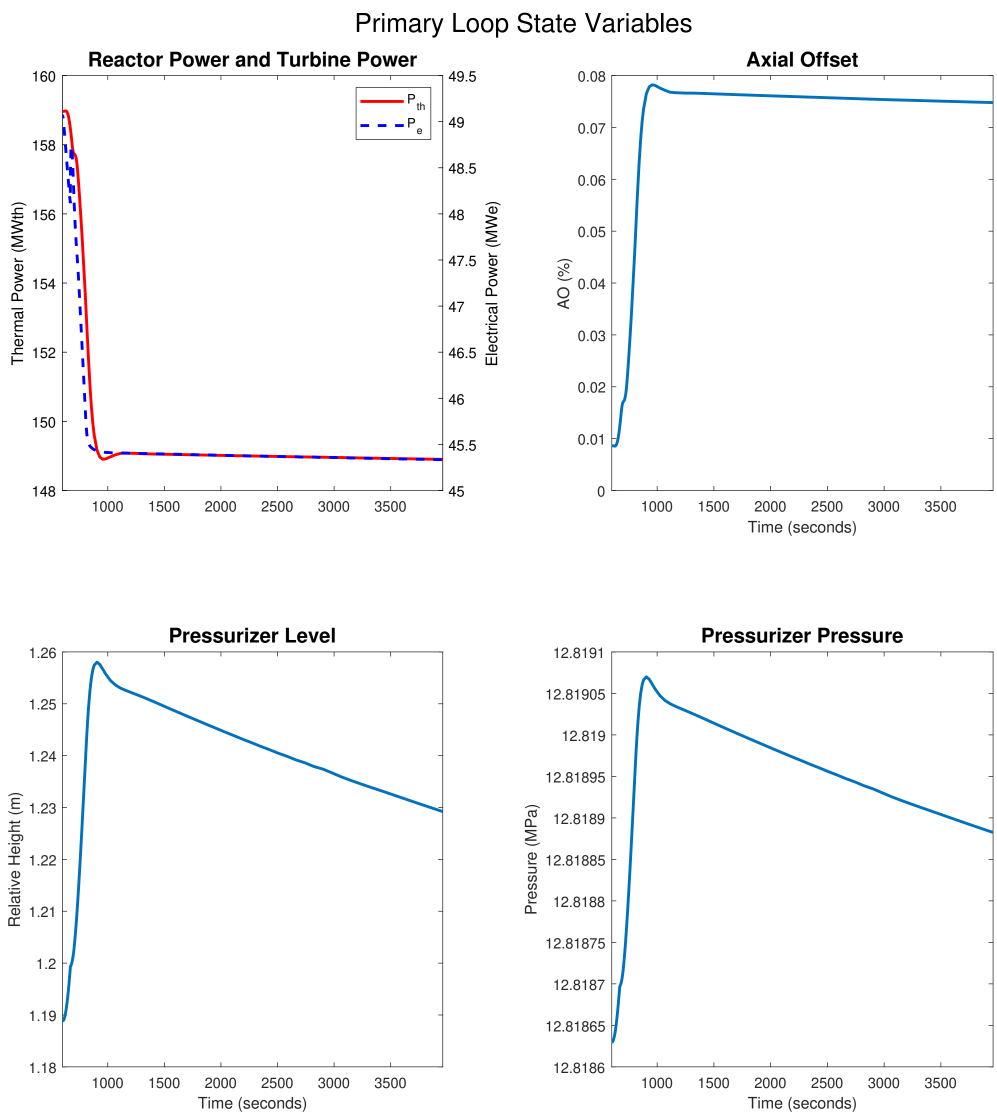

Figure 4.20: The plant state variables of interest for the -10% feedwater ramp are plotted here.

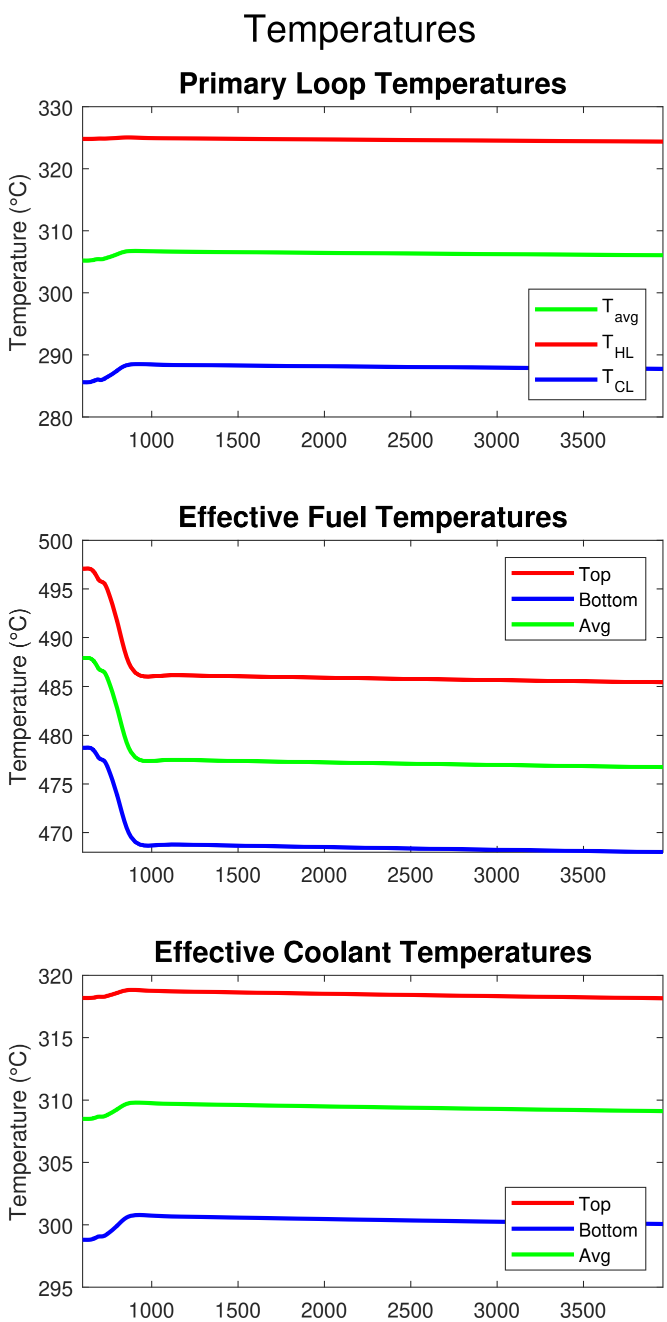

Figure 4.21: The primary loop temperature profiles associated with the -10% feedwater ramp are presented here. Note the dramatic drop in effective fuel temperatures. Note the dramatic drop in fuel temperature.

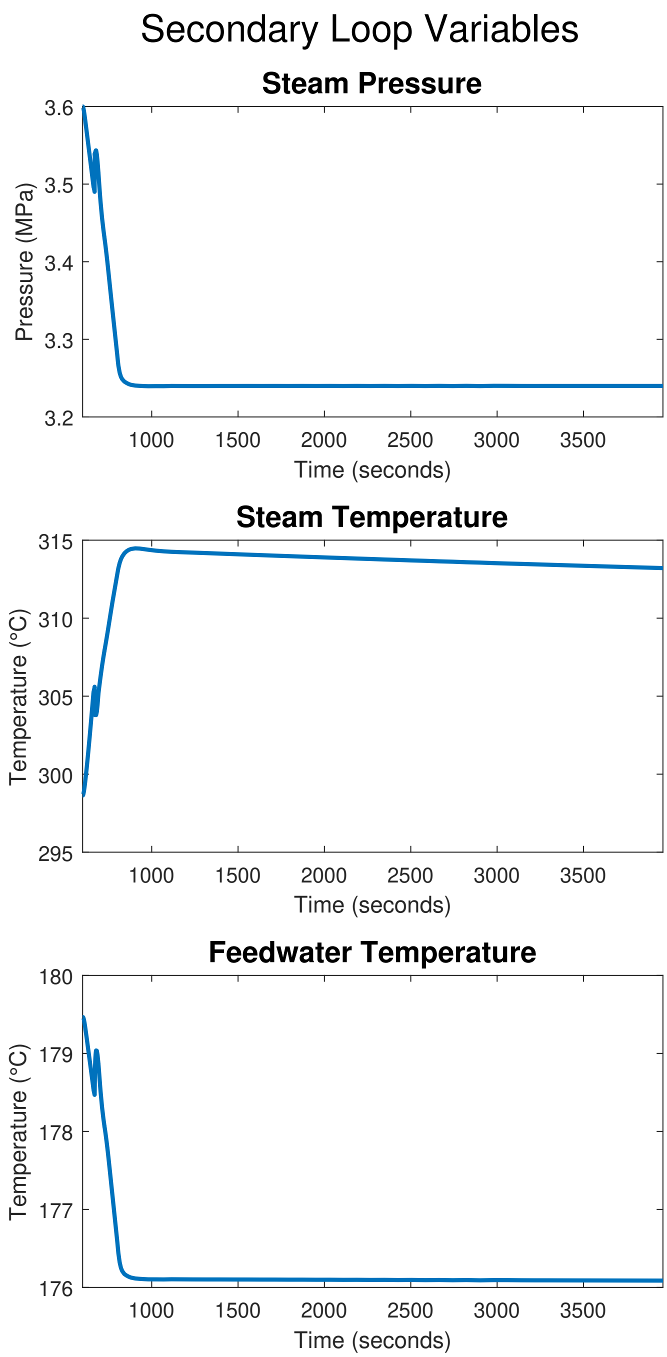

Figure 4.22: Secondary loop state variables for the -10% feedwater ramp are presented here. Note the dramatic drop in steam pressure and not insignificant increase in steam temperature.

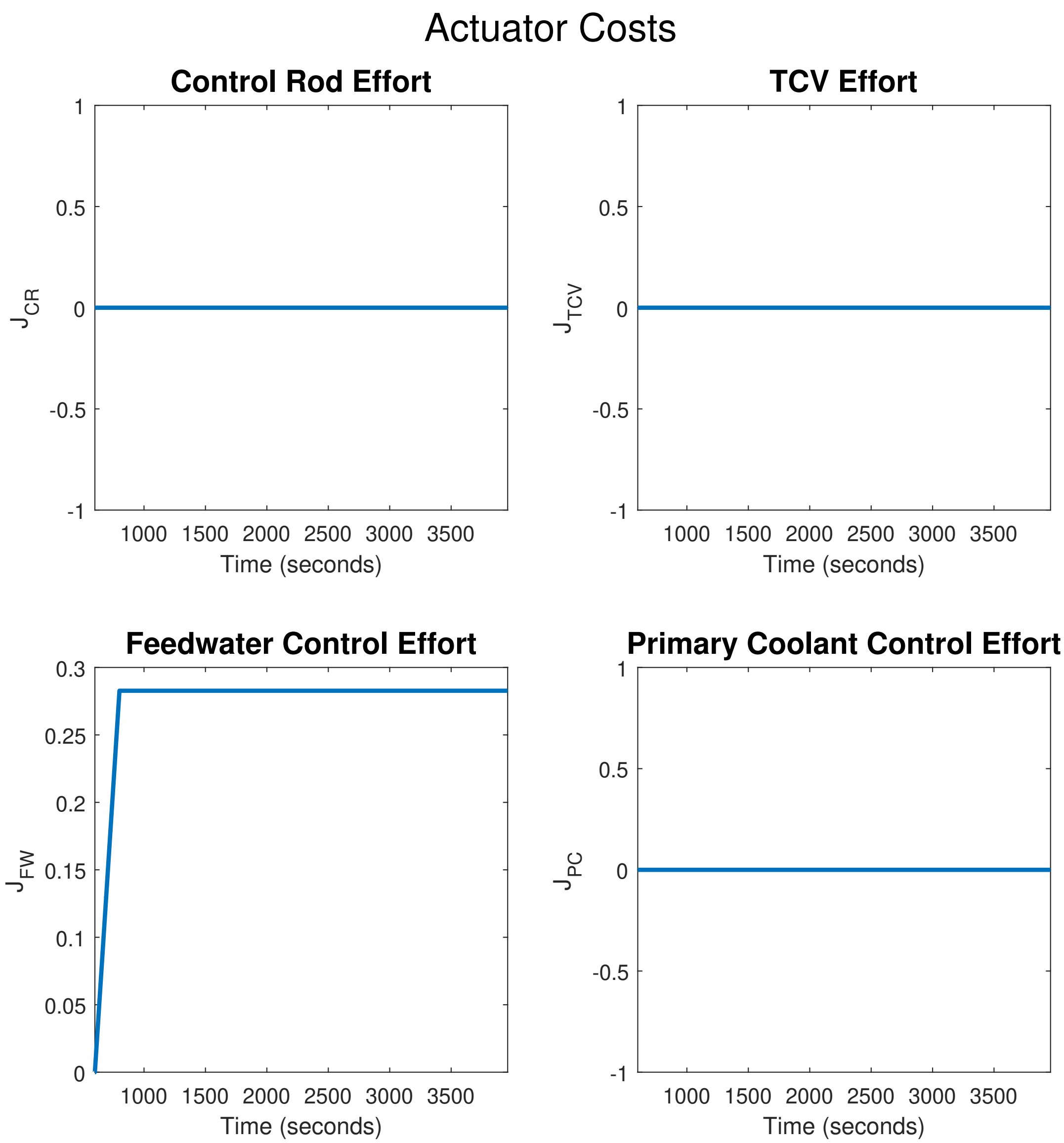

Figure 4.23: The cost of actuation for the -10% feedwater ramp maneuver is plotted here. Since this is solely a feedwater pump maneuver, only the feedwater cost evolves over time.

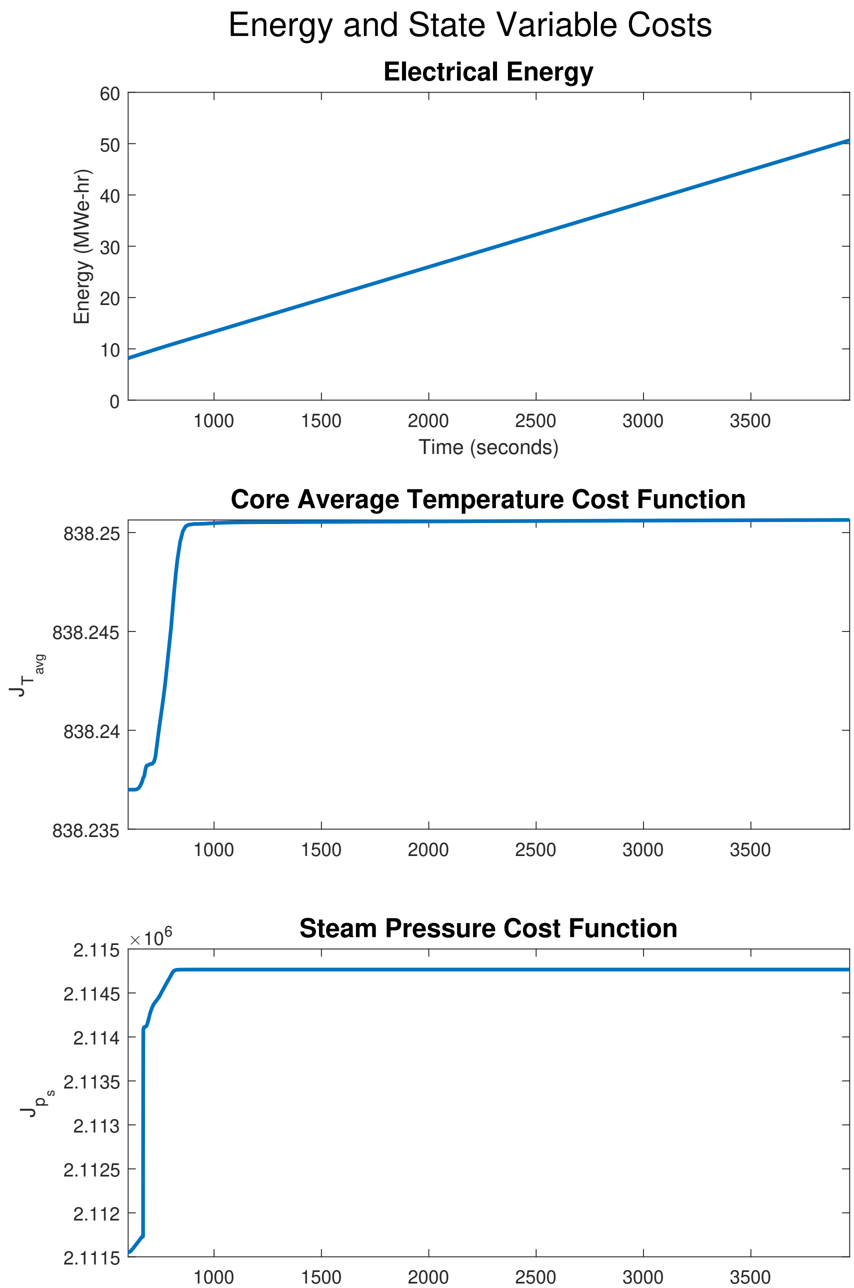

Figure 4.24: State variable costs and energy production associated with the -10% feedwater drop.

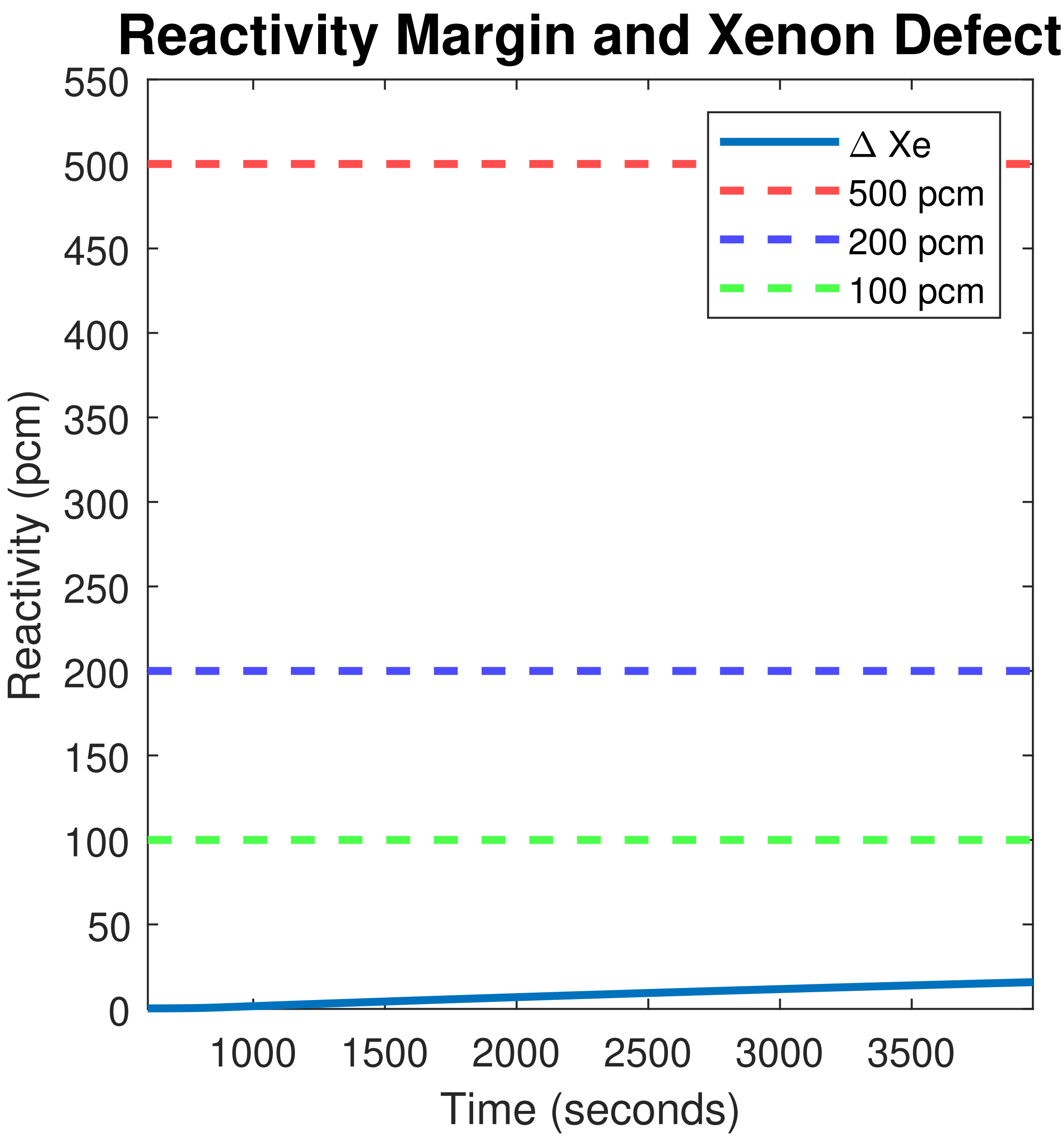

Figure 4.25: Xenon reactivity has a small but noticeable increase due to a moderate drop in power level even in a shorter simulation.

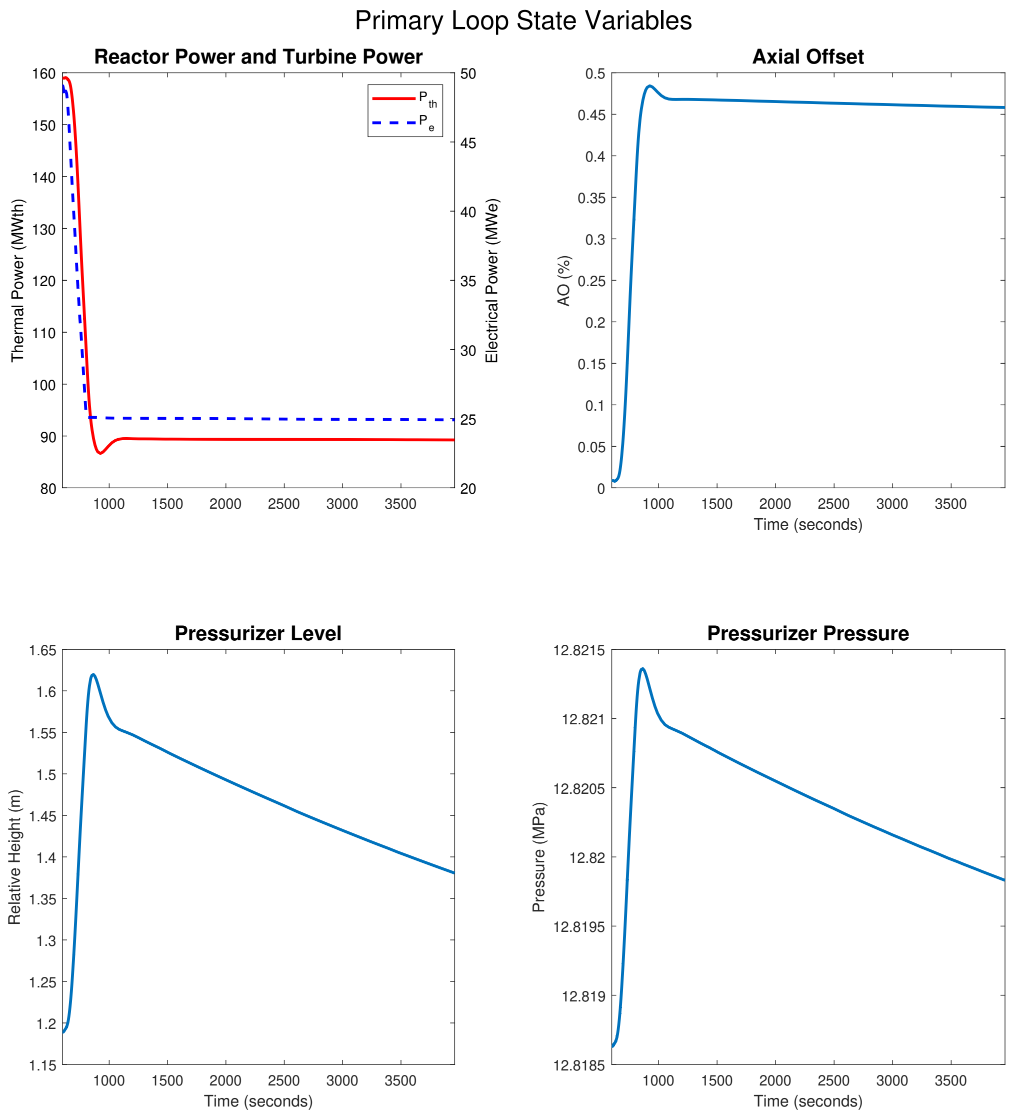

Figure 4.26: The plant state variables associated with the -50% feedwater drop.

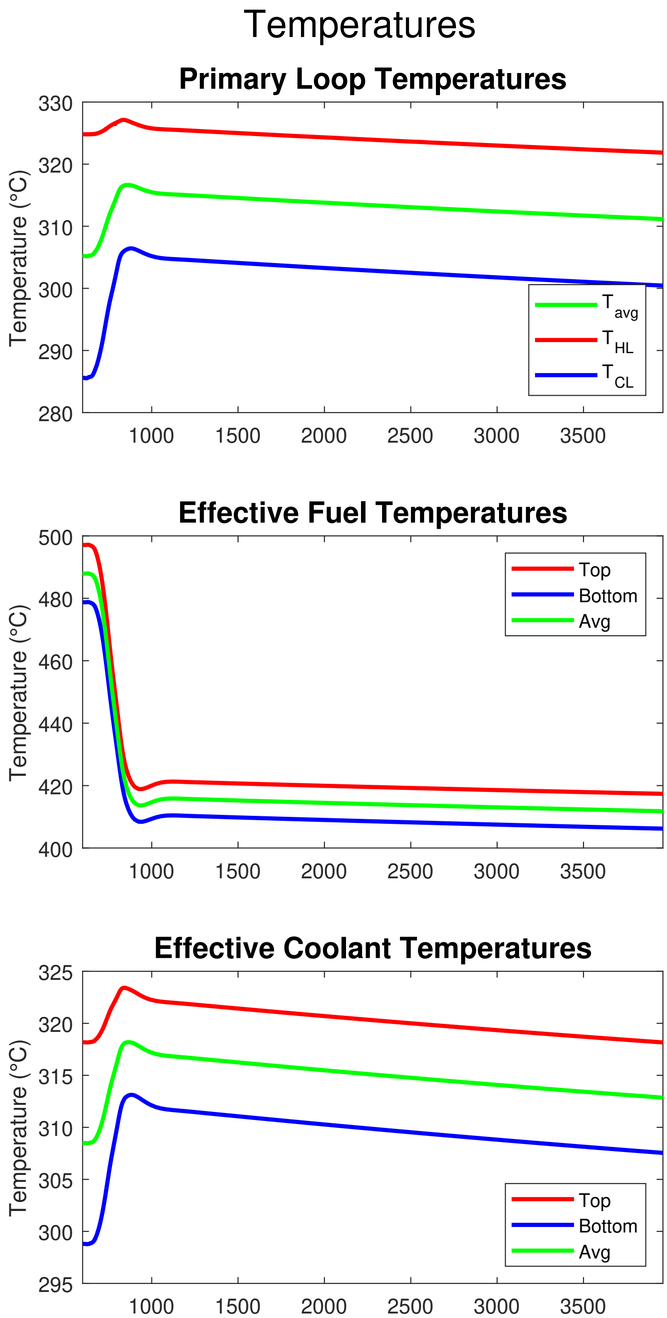

Figure 4.27: Temperatures associated with the -50% feedwater drop. The fuel temperature decrease is very large, and the coolant temperature increases are significant in magnitude.

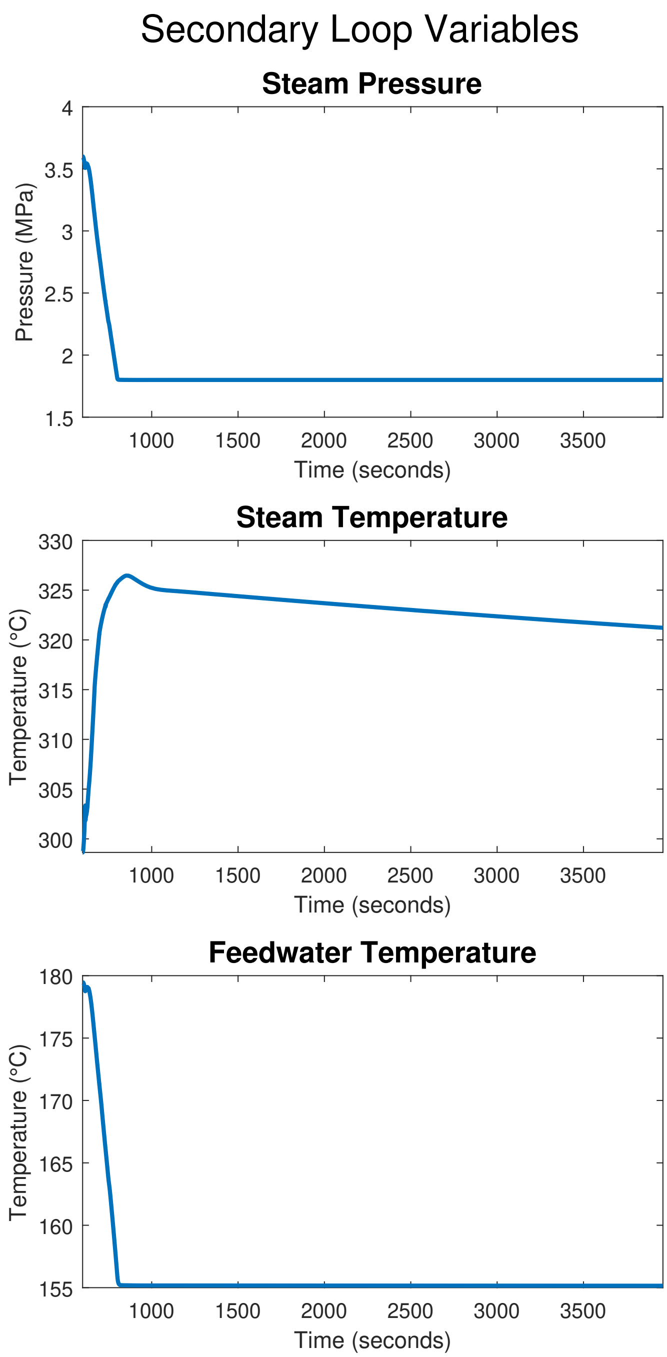

Figure 4.28: Evolution of the secondary loop variables of interest arising from the -50% feedwater mass flow rate ramp. Steam pressure and feedwater temperature fall dramatically while the steam temperature rises 25 C before starting to decline.

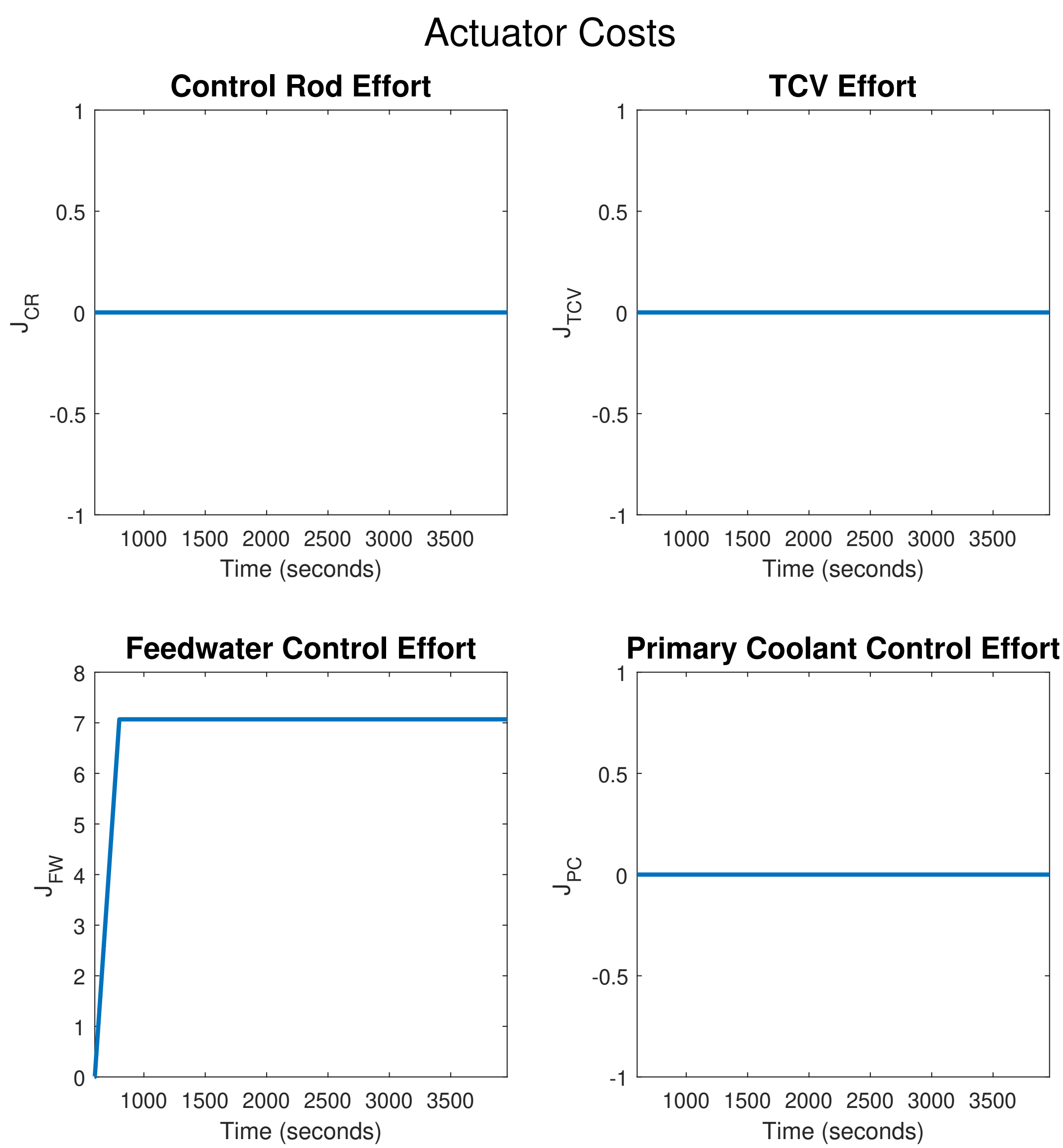

Figure 4.29: Actuator effort arising from the -50% feedwater drop.

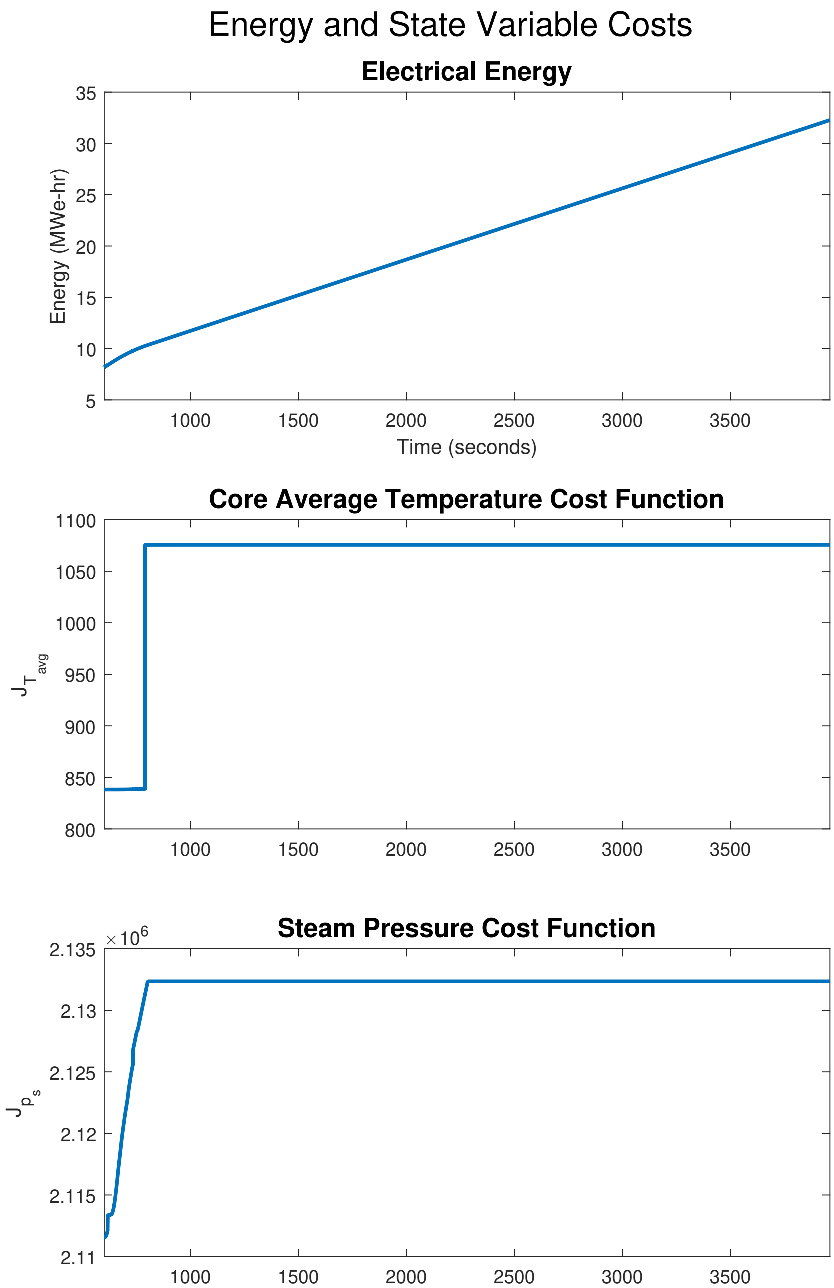

Figure 4.30: State variable costs and energy produced during the simulation with the -50% feedwater drop.

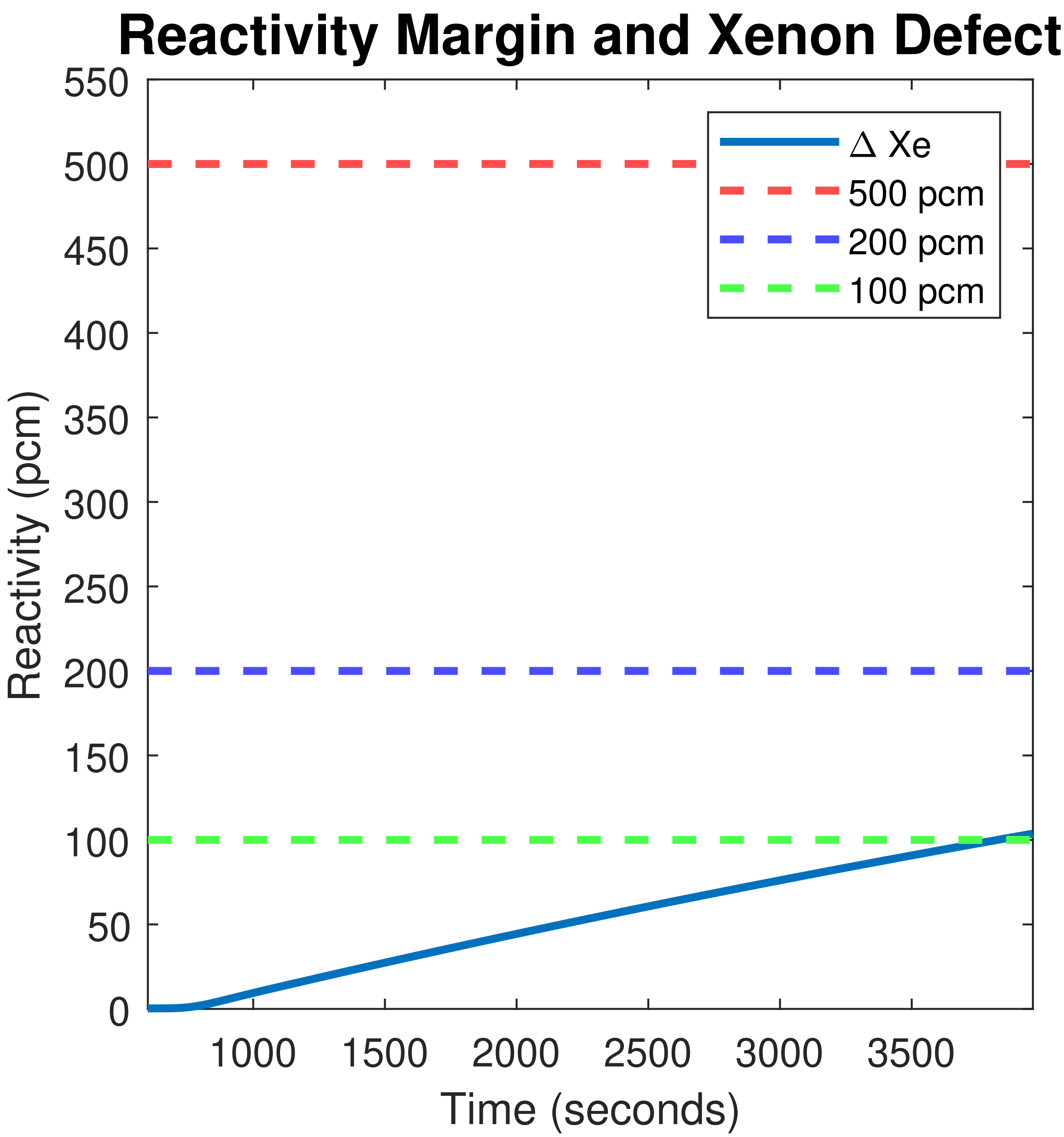

Figure 4.31: The power level drop is enough for the xenon reactivity differential to exceed the 100 pcm excess reactivity margin in less than 50 minutes after the 50% feedwater ramp.

4.5.4 Turbine Control Valve

The turbine control valve (TCV) position was adjusted in the following perturbation studies. The results suggest that, for this model and the given valve parameters, turbine admission control is not a promising actuator for load balancing but may have a place in other control strategies and concerns relevant to the stable and safe operation of the balance of plant components. A TCV strategy would be useful for the previously examined feedwater control actions due to the penalties they impose on steam pressure and temperature, and turbine valve admission is used in older synchronous generators with governors, including existing PWR plants.

50% TCV position ramp

A moderate (50%) reduction in the valve opening is made, from 100% to 50%, over a period of 200 s. The results appear in Figures 4.32-4.37. In Figure 4.32 the powers, axial offset, and pressurizer level and pressure decrease very slightly. In Figure 4.33 the temperatures change little in response to the partial TCV closure. In Figure 4.34 the expected changes in the steam properties of pressure and temperature occur for an isenthalpic valve. The feedwater temperature also decreases slightly followed by a small rebound at the end of the TCV closure motion. In Figures 4.35 and 4.36 the actuator costs, state variable costs, and electrical energy for the half-closure are plotted. The main variable of note is the steam pressure cost arising from the valve aperture shrinking. In Figure 4.37 the xenon reactivity is virtually unchanged as expected.

90% TCV position ramp

A large (90%) reduction in the valve opening is made, from 100% to 10%, over a period of 200 s. The results appear in Figures 4.38-4.43. In Figure 4.38 the reactor thermal and electrical powers fall slightly while axial offset rises slightly. The pressurizer level and pressure rise slightly before falling again. In Figure 4.39 the fuel temperatures fall markedly while the coolant temperatures rise slightly. In Figure 4.40 the pressure rises significantly as expected

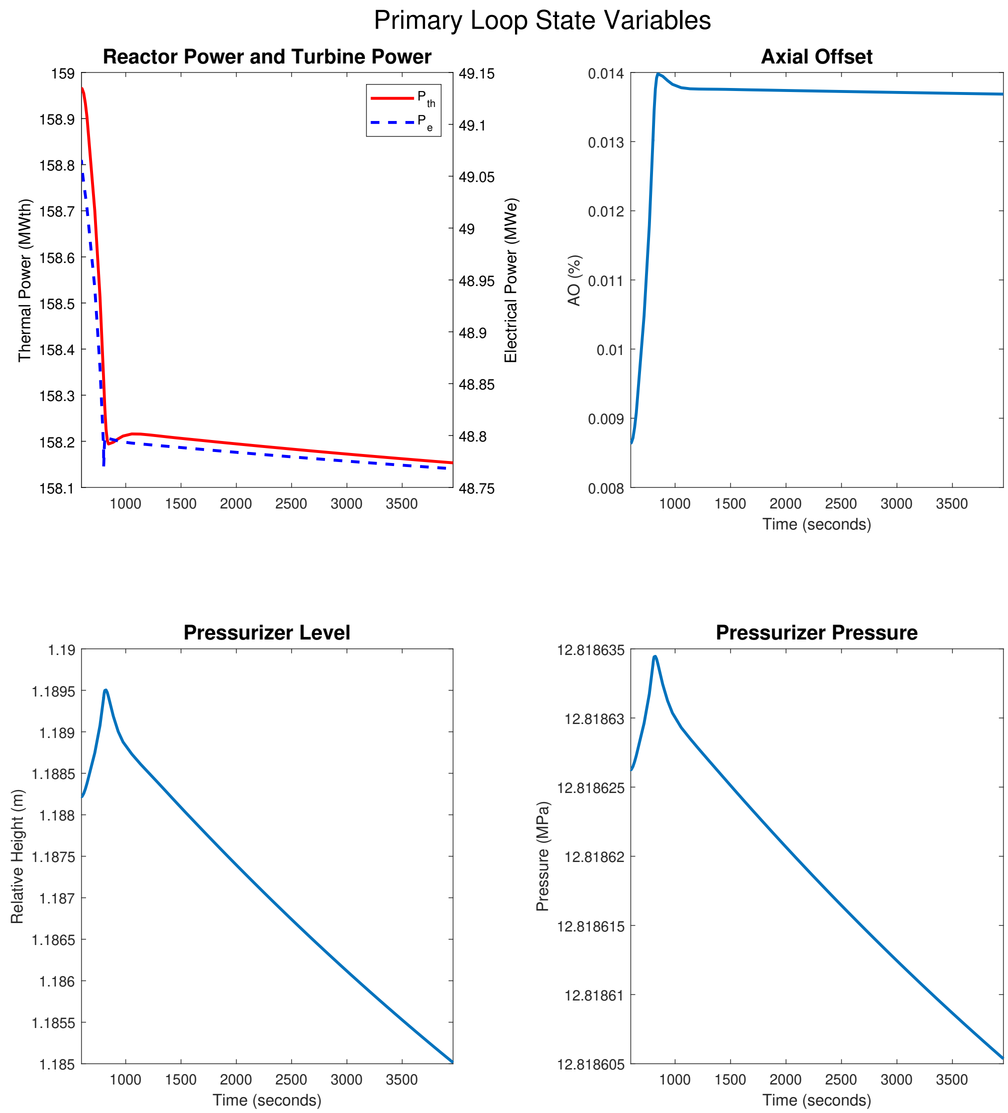

Figure 4.32: The primary system variables change little in response to closing the valve opening by half.

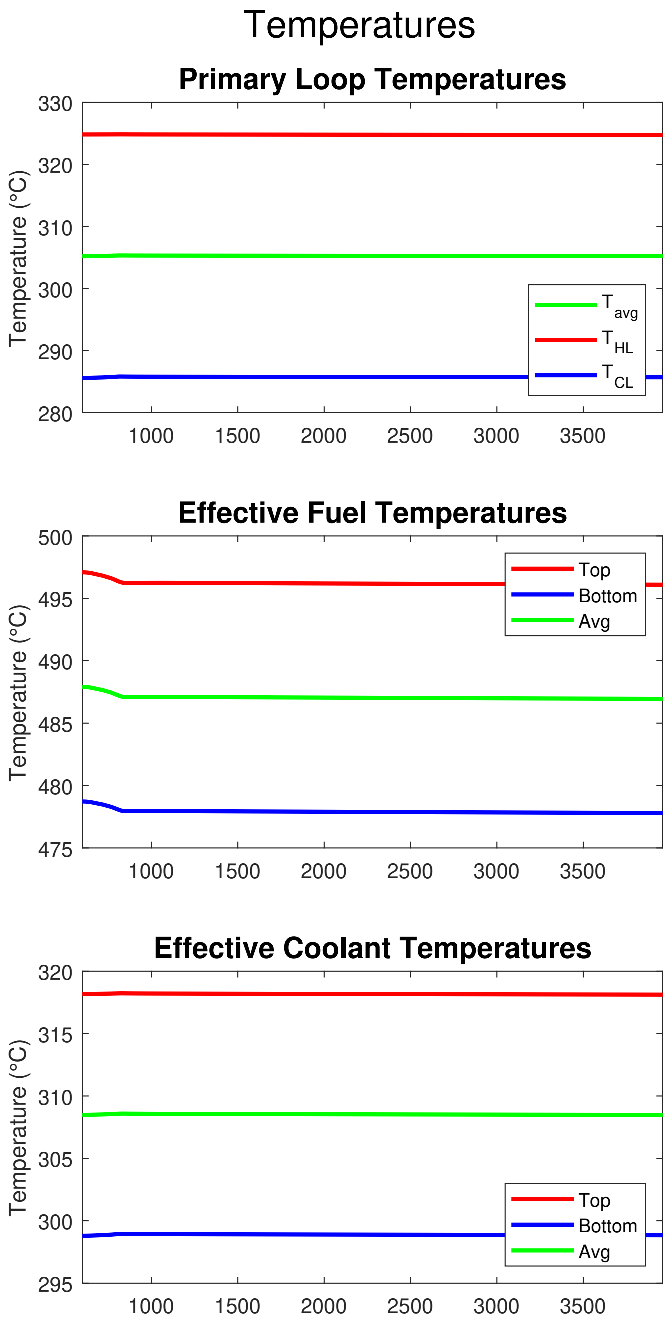

Figure 4.33: The coolant temperatures change negligibly in response to the -50% TCV action, and the fuel temperatures decrease slightly.

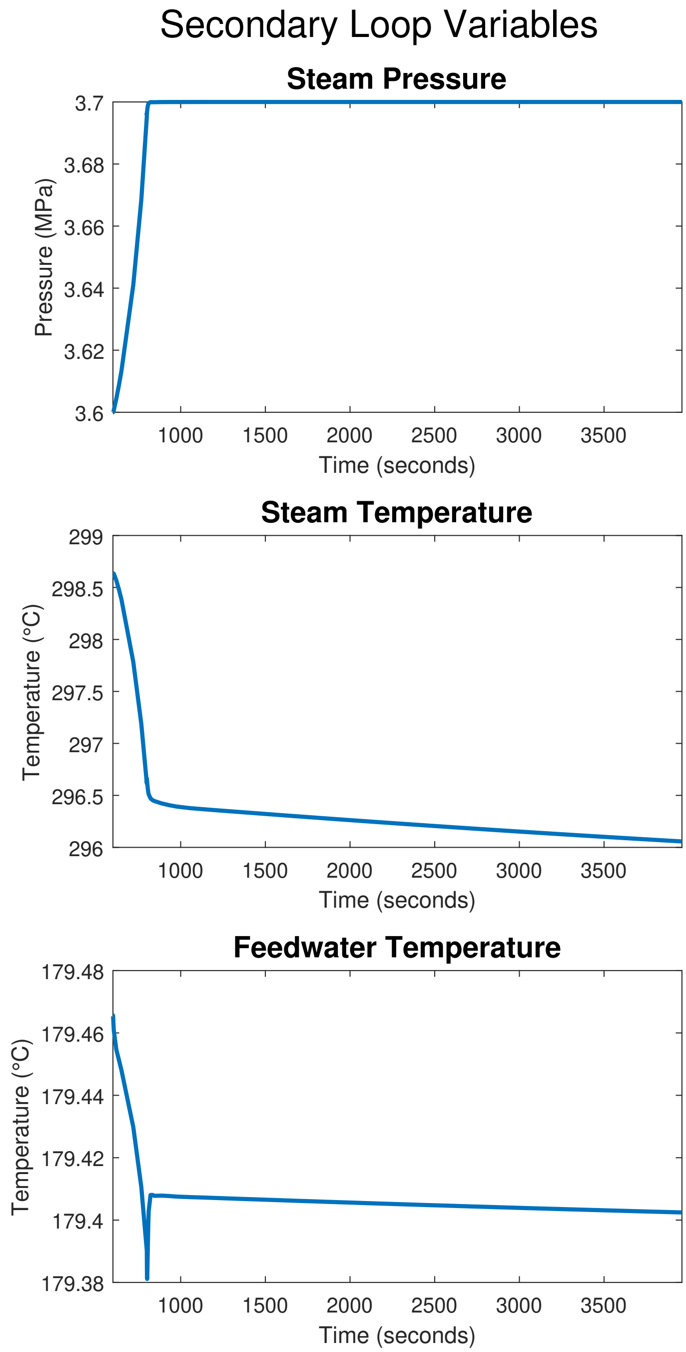

Figure 4.34: The steam pressure increases somewhat as expected while the steam and feedwater temperatures fall slightly.

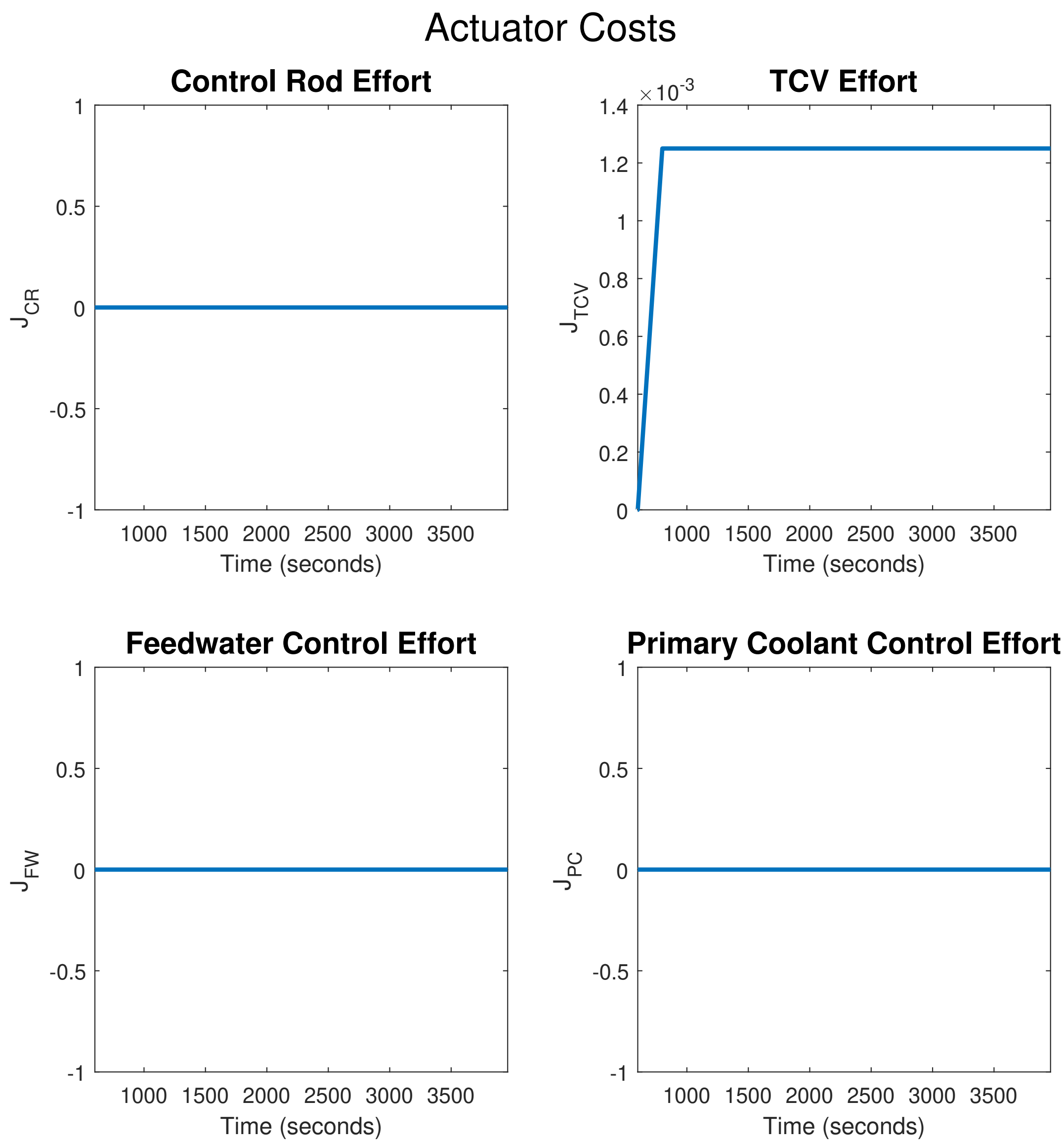

Figure 4.35: The actuator costs due to the -50% valve closure are plotted above.

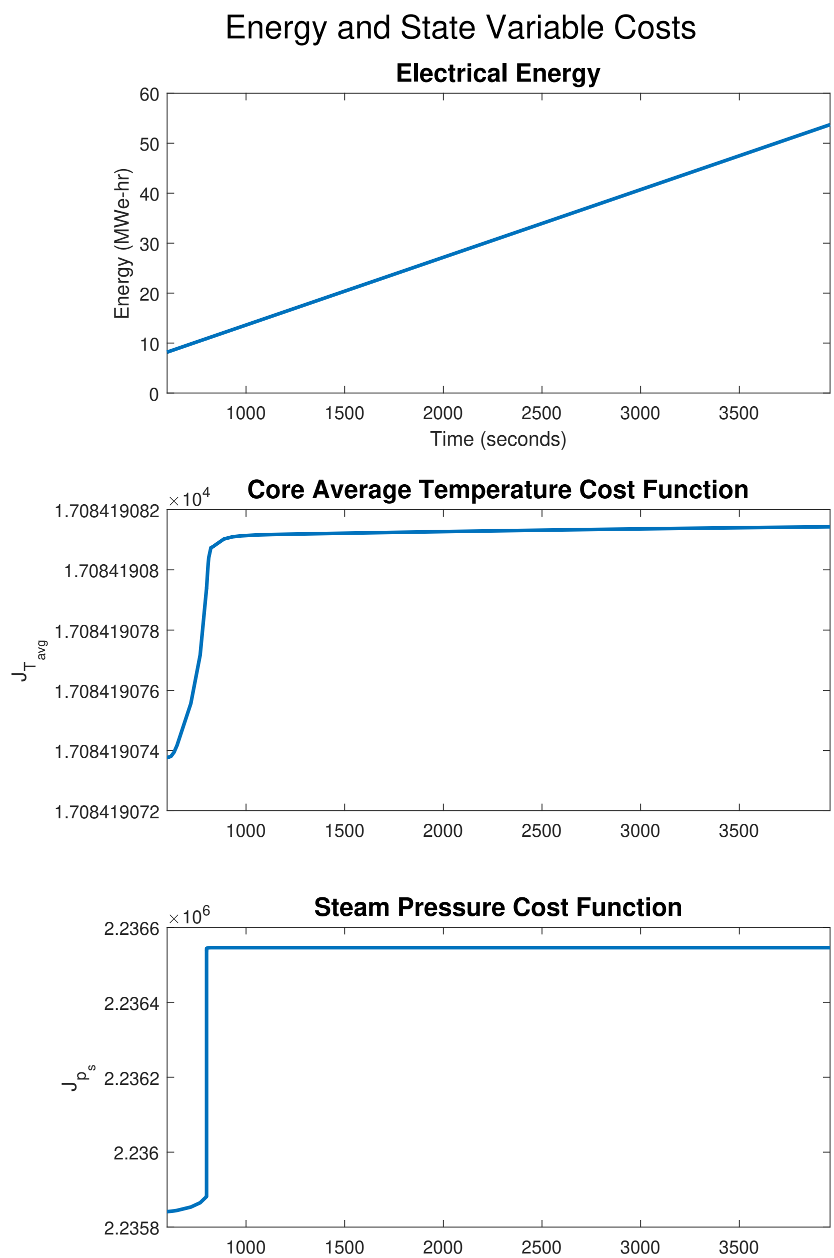

Figure 4.36: The total energy generated is not much different from full power operation. The core temperate cost barely changes in response to the valve closure while the steam cost increases noticeably.

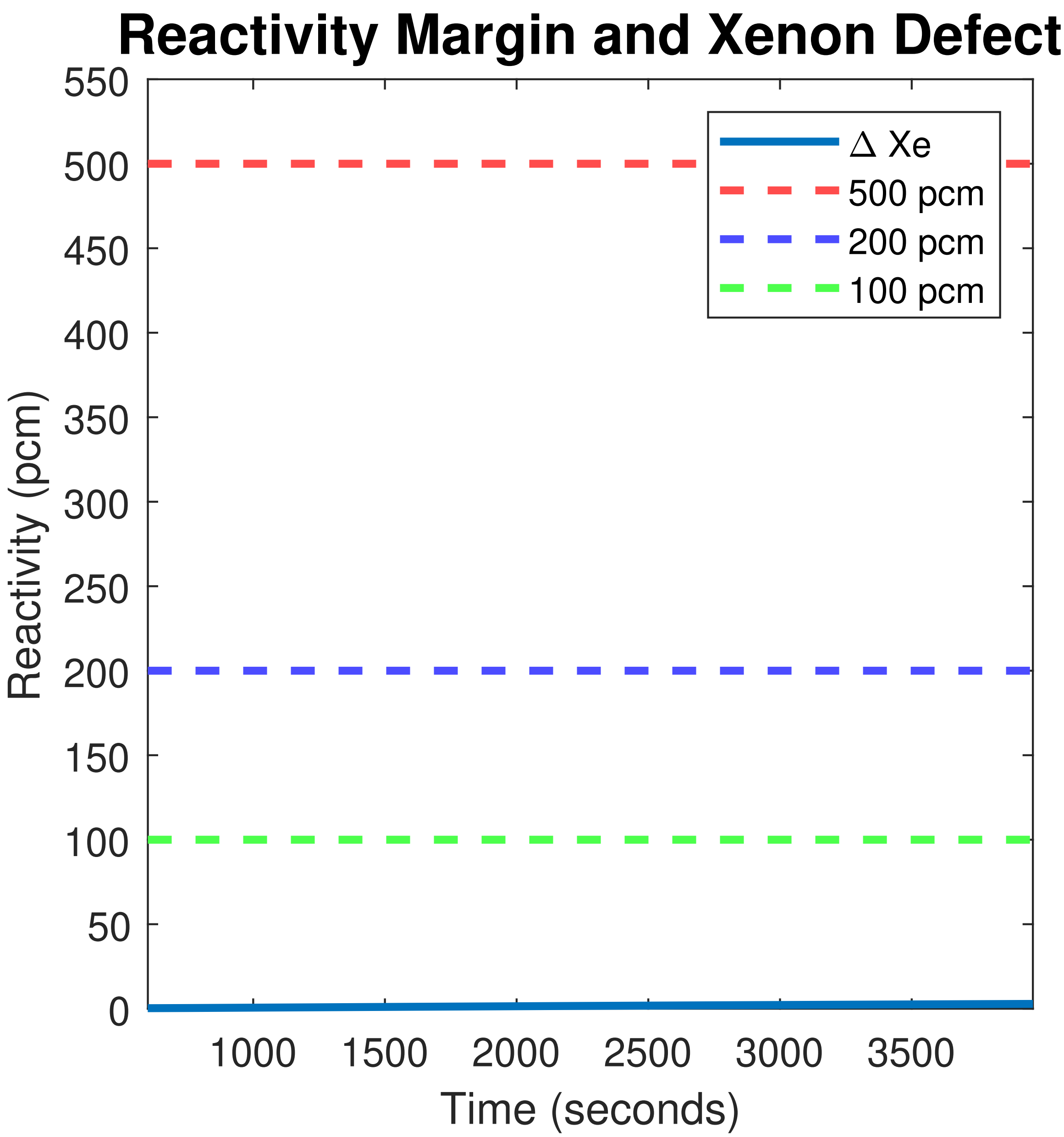

Figure 4.37: The xenon reactivity hardly changes since the power level decreased very little.

of valve throttling while the steam and feedwater temperatures decrease. In Figures 4.41 and 4.42 the actuator and state variable costs are plotted along with electrical energy. Of note among these plots is the rise in the steam pressure cost function stemming from the throttling. In Figure 4.43 the xenon reactivity defect evolves only slightly due to the small power drop.

4.6 Effect of Xenon on Operation and Load Following Capability

4.6.1 Available Ramp

This figure of merit is of particular interest for load balancing operation. The electrical ramp that a thermal generator can provide is required to solve the unit commitment-economic dispatch problem or estimate the ramping services that can be provided. Due to the strongly nonlinear, complex, and power history-dependent behavior of the plant model, there is not a straightforward way to calculate ramp rate availability *a priori*. While the reactor can always be ramped down until it reaches its minimum power (5%/min under EPRI guidelines), it cannot be readily ramped back up immediately to previous higher power levels due to the parasitic absorption of neutrons by poisons, principally xenon-135. In some cases it is required for the poison to be burned out over several hours; this has significant consequences for very large downward ramps or reactor trips [37]. An adjusted approach for ramp rate estimation from Ponciroli et al. [14] is used that accounts for the and slightly relaxes its strict condition on the available reactivity margin and sampling timing. The concept from Ponciroli et al. is illustrated in Figure 4.44. The xenon-135 concentration and reactivity rise in accordance with the Bateman equations for itself and its parent iodine-135 following a downward maneuver.

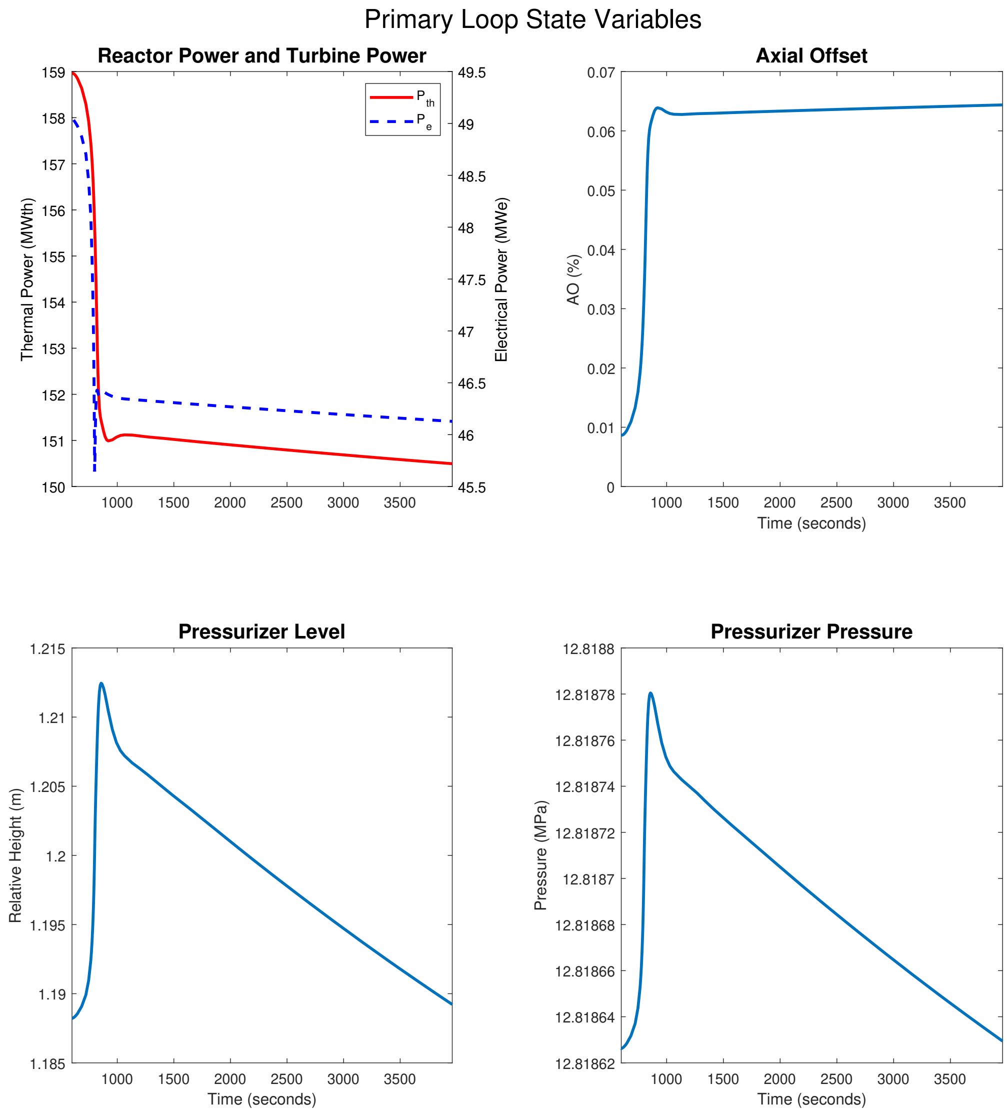

Figure 4.38: The primary loop has a moderate response to this large -90% valve motion, with a power drop of roughly 9 MWth/3 MWe.

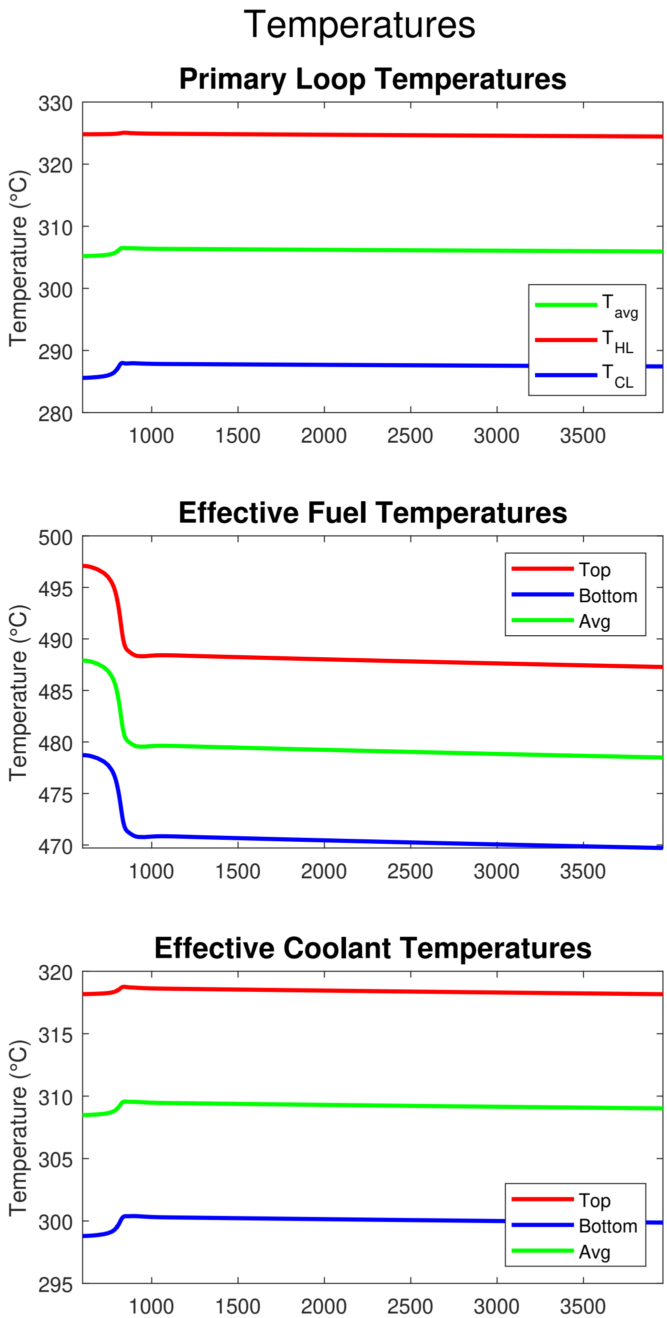

Figure 4.39: The fuel temperatures fall in response to the -90% valve throttle while the coolant temperatures rise only slightly.

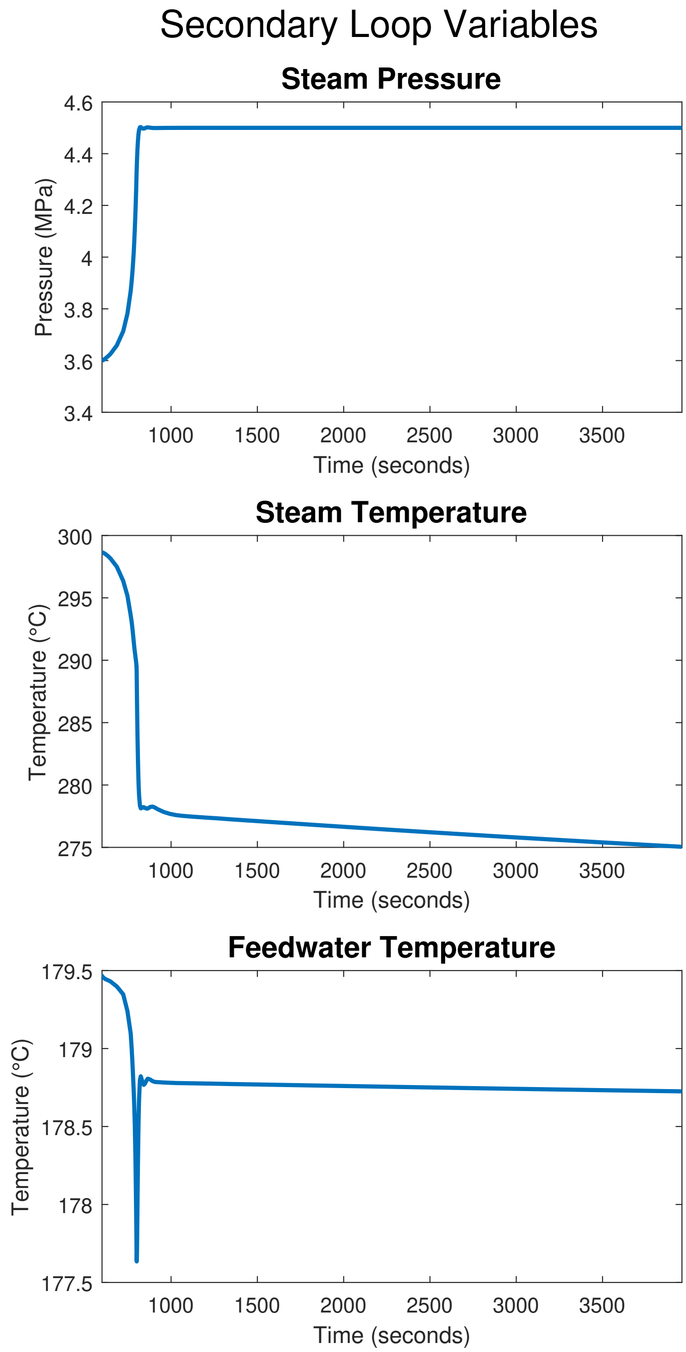

Figure 4.40: The steam pressure increases significantly while the steam temperature falls correspondingly. The feedwater temperature falls slightly with a small rebound.

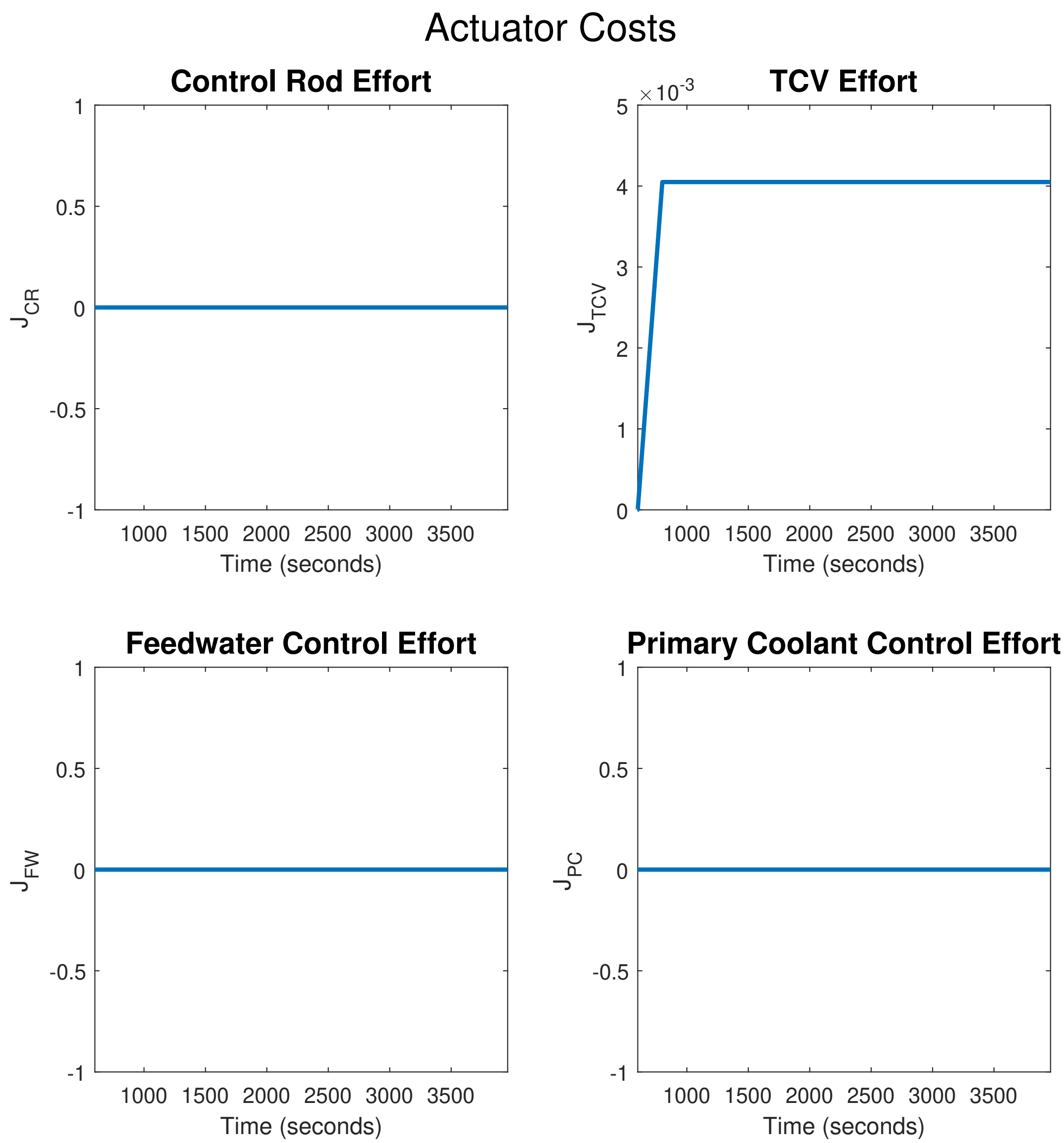

Figure 4.41: The actuator costs for the -90% valve throttle. Only the TCV effort is nonzero.

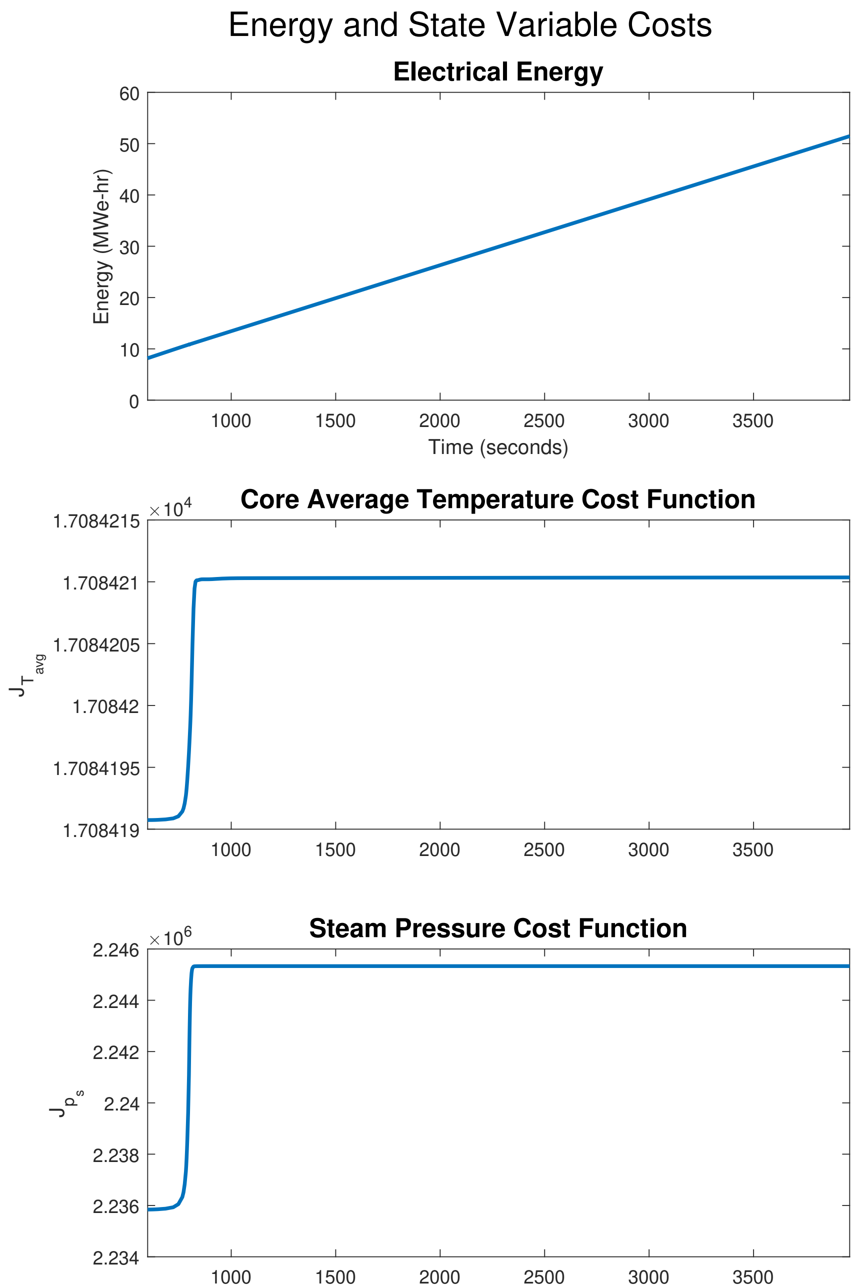

Figure 4.42: State variable costs and energy generated during the simulation with a -90% valve closure. The steam pressure cost rises due to the pressure rise from throttling.

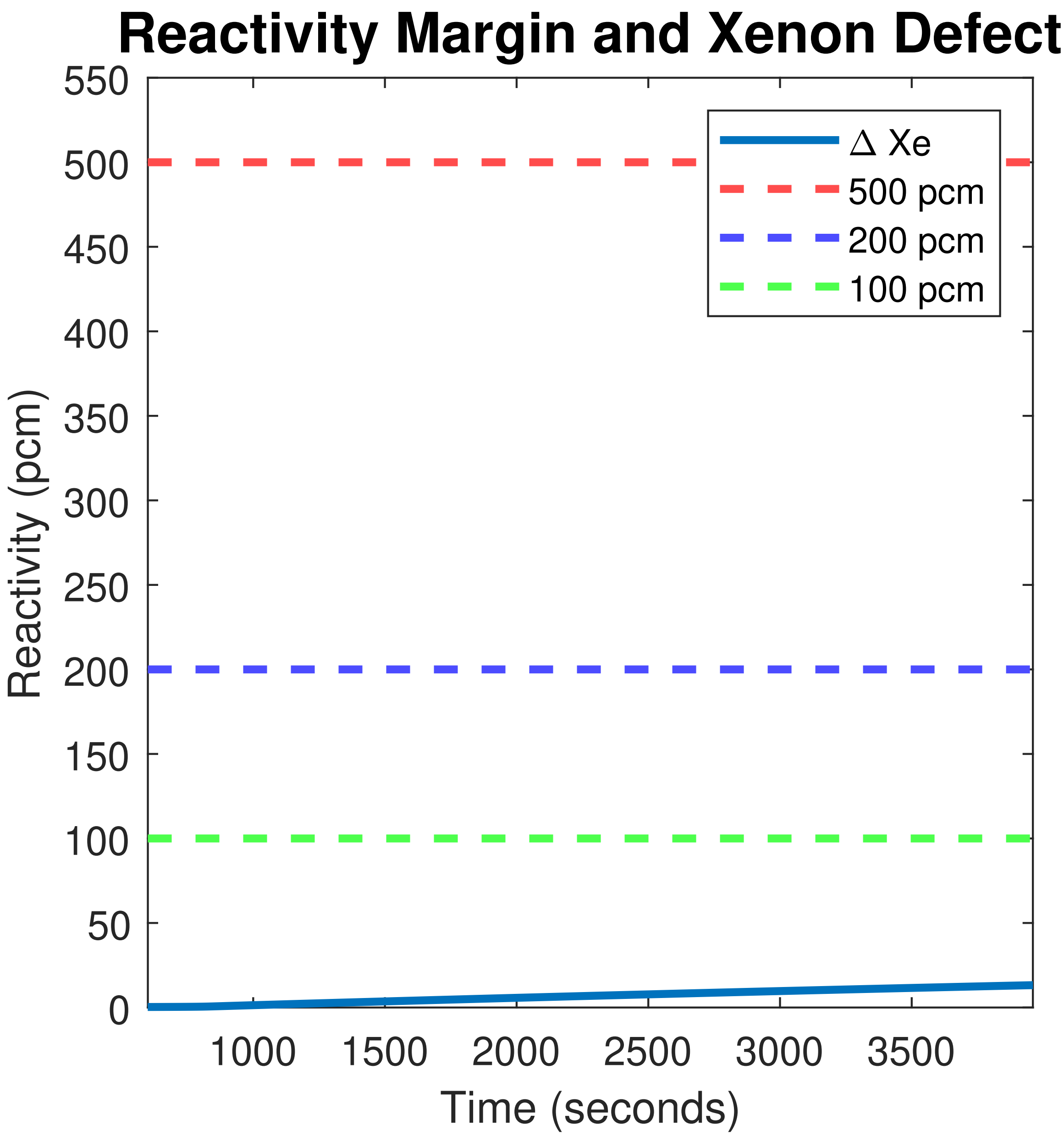

Figure 4.43: The xenon reactivity defect rises only slightly from the small power drop during the throttle.

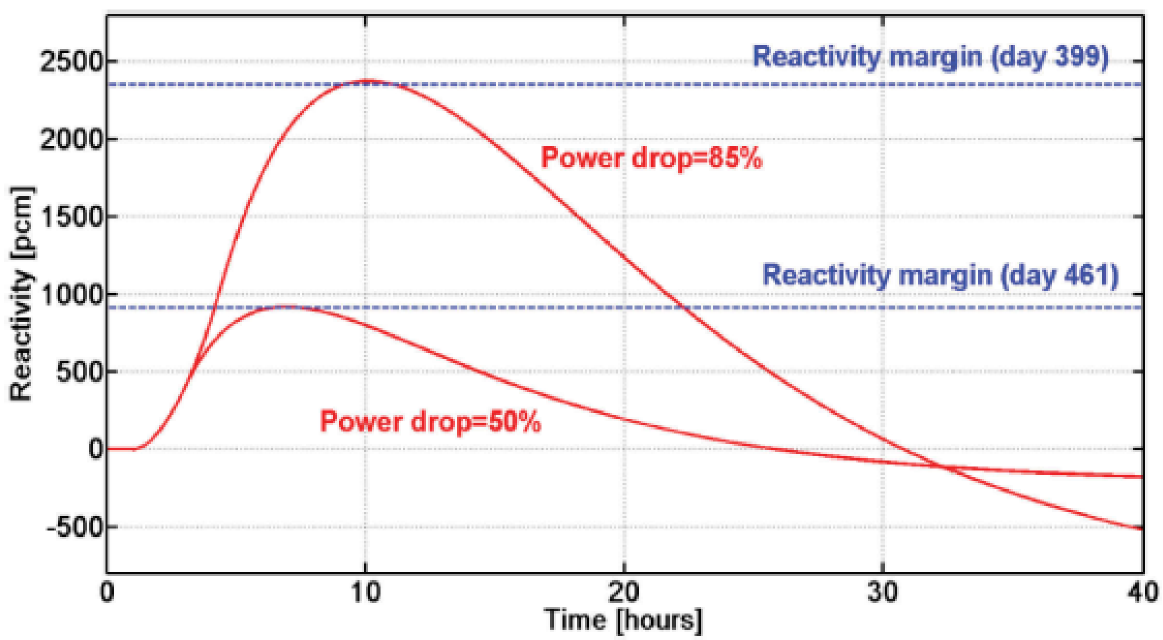

(a)

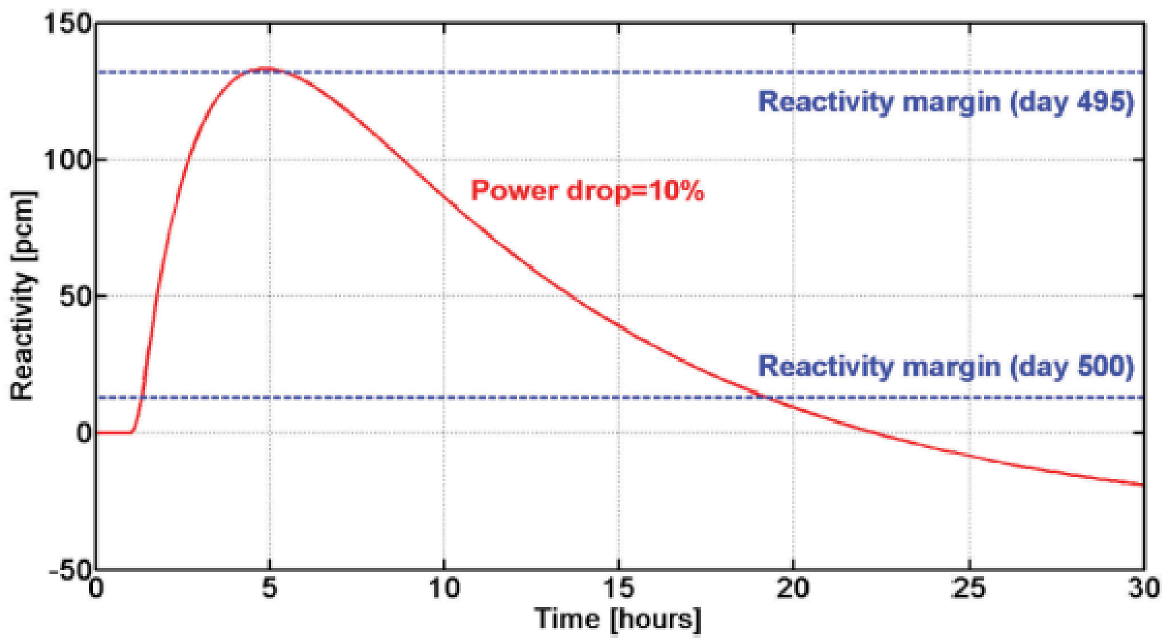

(b)

Figure 4.44: Evolution of xenon over time due to different downward ramps with excess reactivity margin comparisons as in [14].

Xenon Poisoning and Stage of Cycle Analysis

The burnup of the core between refuelings has implications for control due to the loss of excess reactivity as well as the decrease of the U-235 fraction and increase of the Pu-239 fraction in the fuel. This can manifest as changes in the neutronics parameters, i.e., the reactor period, the delayed neutron fraction, and the individual precursor group fractions and decay times. Toward the end of reactor life cycle, reactors in France have reduced load follow capability due to loss of excess reactivity [15]. Because the excess reactivity of the fuel decreases during the reactor core life cycle, it is worthwhile to explore to what degree ramp rates are limited for IPWRs late in the cycle due to a combination of this lower excess reactivity and xenon buildup from prolonged operation at low power levels. A burnup-dependent analysis is conducted to quantify and evaluate the ramping capability by evaluating excess reactivity relative to the xenon defect during operation.

The simulations in Figures 4.45 and 4.46. A 1000 pcm insertion leads a drop from nominal power to 115 MWth before thermal feedback returns the power level to 130 MWth; for 2000 pcm this change is from nominal to 70 MWth and back to 90 MWth. The incipient xenon temporal oscillation that adds negative reactivity and pushed the reactor thermal power level down can also be seen in the figures. This oscillation must be compensated to avoid unwanted changes in the power level and temperature of the reactor. Control strategies for LWRs typically involve a core temperature controller, which helps preserve the integrity of the fuel cladding, assemblies, and core components. However, this also limits the flexibility by choice. Without enough excess reactivity or sufficient thermal feedback, whether due to limited core temperature transients or low reactivity feedback coefficients, xenon can limit ramping [59] [14]. A simple relationship can be derived relating the xenon reactivity defect, excess reactivity, and thermal feedback.

$$\Delta\rho_X \geq \rho_0 + \rho_{fb} = \rho_0 + \alpha_C \Delta T_C + \alpha_F \Delta T_F \tag{4.12}$$

If this inequality condition is satisfied, then the core is xenon-constrained. The results of Figures 4.45 and 4.46 demonstrate that for the power level changes associated with those

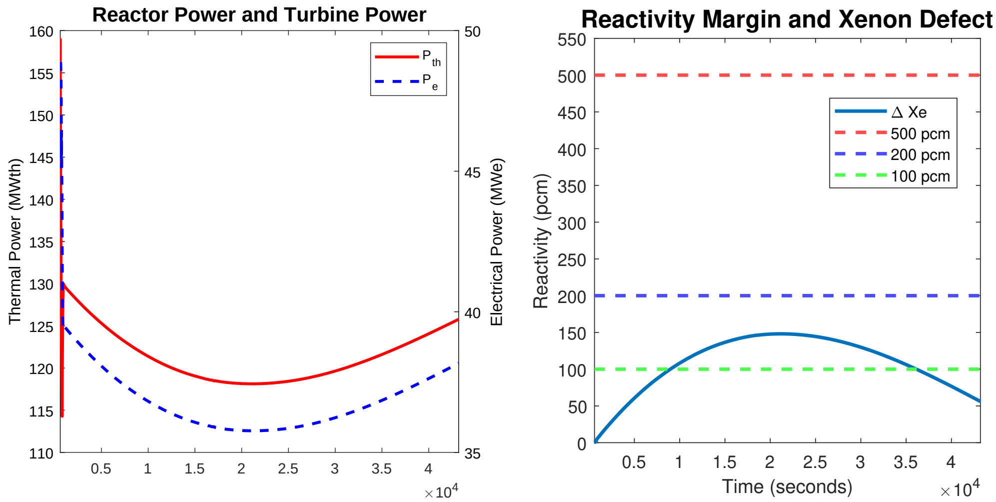

Figure 4.45: Power and xenon defect response due to 1000 pcm insertion

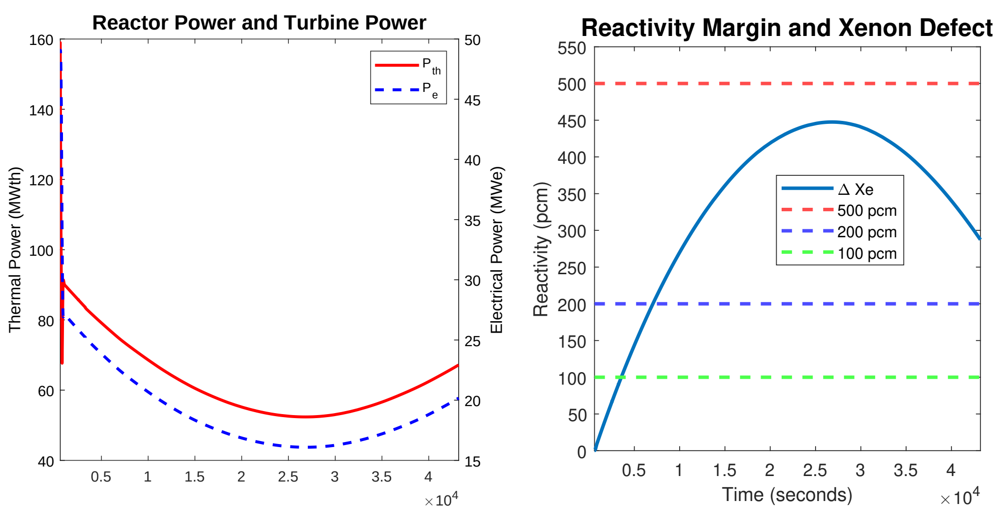

Figure 4.46: Power and xenon defect response due to 2000 pcm insertion

insertions, the core becomes constrained for the delineated 100 pcm and 200 pcm levels, respectively, if the core temperature is fixed. In principle, for a linearized core model, the operationally free or constrained surfaces may be derived analytically and plotted for reactivity insertions or flux changes of arbitrary sizes. The constraints imposed by control laws may be prohibitive, especially those that explicitly use thermally dependent "inherent" load following strategies as presented by Zarei [64].

4.6.2 Linear Stability Analysis of PWR with Xe feedback

It is known that xenon feedback results in instability at low flux levels and can be demonstrated using traditional methods for a linearized core kinetics system with feedback [65] [66]. The axially-smeared system of equations for the primary system heat transfer model for the rod and coolant envelope are the following.

$$C_{F1}\dot{T_{F1}} = q'''V_{F1} - h_{F12}(T_{F1} - T_{F2}) \tag{4.13}$$

$$C_{F2}\dot{T_{F2}} = q'''V_{F2} + h_{F12}(T_{F1} - T_{F2}) - h_{F23}(T_{F2} - T_{F3}) \tag{4.14}$$

$$C_{F1}\dot{T_{F1}} = q'''V_{F3} + h_{F23}(T_{F2} - T_{F3}) - h_{FG}(T_{F3} - T_{G1}) \tag{4.15}$$

$$C_{G1}\dot{T_{G1}} = h_{FG}(T_{F3} - T_{G1}) - h_{G12}(T_{G1} - T_{G2}) \tag{4.16}$$

$$C_{G2}\dot{T_{G2}} = h_{G12}(T_{G1} - T_{G2}) - h_{G23}(T_{G2} - T_{G3}) \tag{4.17}$$

$$C_{G3}\dot{T_{G3}} = h_{G23}(T_{G2} - T_{G3}) - h_{GC}(T_{G3} - T_{C1}) \tag{4.18}$$

$$C_{C1}\dot{T_{C1}} = h_{GC}(T_{G3} - T_{C1}) - h_{C12}(T_{C1} - T_{C2}) \tag{4.19}$$

$$C_{C2}\dot{T_{C2}} = h_{C12}(T_{C1} - T_{C2}) - h_{C23}(T_{C2} - T_{C3}) \tag{4.20}$$

$$C_{C3}\dot{T_{C3}} = h_{C23}(T_{C2} - T_{C3}) - h_{CW}(T_{C3} - T_{W}) \tag{4.21}$$

$$C_{W}\dot{T_{W}} = h_{CW}(T_{C3} - T_{W}) - \frac{\dot{m}_W}{m_W}(T_W - T_{in}) \tag{4.22}$$

The C_{ij} terms are the heat capacitances of the nodes, T_{ij} terms are temperatures, q''' is the volumetric fission power density, the V_{ij} terms the active fuel node volumes, and the h_{ij} terms are the coefficients of heat transfer, all for their respective regions and interfaces. This system of heat balances can be simplified using an overall heat transfer coefficient treatment between the fuel and coolant. The weighted fuel temperature with overall heat transfer coefficient between fuel and coolant is

$$\bar{T}_f = T_{cool} + \frac{q}{2\pi}[\frac{1}{4k_f} + \frac{1}{R_0 h_{gap}} + \frac{\ln(R_W/R_0)}{2k_C} + \frac{1}{R_W h_{film}}] \tag{4.23}$$

Here q is the fission power in the rod, and the term in brackets constitutes the effective heat transfer coefficient between the fuel and coolant. The W subscript is used to distinguish the coolant from the cladding subscript C. This relation can be used for the heat balances in the system and lead to the simplified thermal hydraulics and feedback common in the modeling literature. The approach from Kale et al. [66] is reproduced for this reactor. The averaged heat balances, one-group kinetics equations, and normalizations for the Laplace transform are

$$\frac{dP}{dt} = \frac{\rho - \beta}{\Lambda} P + \lambda C \tag{4.24}$$

$$\frac{dC}{dt} = \frac{\beta}{\Lambda} P - \lambda C \tag{4.25}$$

$$\frac{dT_F}{dt} = \frac{P}{m_F C_F} - \frac{h_{eq} A_{eq}}{m_F C_F}(T_F - T_W) \tag{4.26}$$

$$\frac{dT_W}{dt} = \frac{h_{eq} A_{eq}}{m_W C_W}(T_F - T_W) - \frac{2\dot{m}_W}{m_W}(T_W - T_{in}) \tag{4.27}$$

$$x = \frac{P - P_0}{P_0} \tag{4.28}$$

$$y = \frac{C - C_0}{C_0} \tag{4.29}$$

$$G(s) = \frac{x(s)}{\rho(s)} = \frac{s + \lambda}{s\Lambda(s + \lambda + \frac{\beta}{\Lambda})} \tag{4.30}$$

This simplification is justified as additional thermal hydraulic detail and larger numbers of precursor groups have virtually no impact on the system stability calculation [66]. The condition for linear system stability, i.e., that the poles must be in the left-hand side of the plane, requires the denominator of the transfer function, $D(s) = 1 - G(s)H(s)$, to be equal to 0. The denominator function in the frequency domain for the simplified model is calculated from the $H(s)$ transfer functions for the fuel temperature, coolant temperature, and xenon concentrations.

$$H_f(s) = \frac{z_f(s)}{x(s)} \qquad H_c(s) = \frac{z_c(s)}{x(s)} \qquad H_X(s) = \frac{z_X(s)}{x(s)} \tag{4.31}$$

$$H_f(s) = \frac{a_1(a_3 + a_4 + s)}{s^2 + s(a_2 + a_3 + a_4) + a_2 a_4} \frac{P_0}{T_{f0}} \tag{4.32}$$

$$H_c(s) = \frac{a_1 a_3}{s^2 + s(a_2 + a_3 + a_4) + a_2 a_4} \frac{P_0}{T_{c0}} \tag{4.33}$$

$$H_X(s) = \frac{-\left[a_5 \lambda_I + (a_6 + a_7 \rho_{X0})(s + \lambda_I)\right]}{(s + \lambda_I)(s + \lambda_X + a_7 P_0)} \frac{P_0}{\rho_{X0}} \tag{4.34}$$

Then the overall function feedback $H(s) = \delta\rho_{fb}(s)/x(s)$ is the feedback calculated from the previous functions

$$H(s) = \alpha_f T_{f0} H_f(s) + \alpha_c T_{c0} H_c(s) + \rho_{X0} H_X(s). \tag{4.35}$$

Given the overall plant transfer function $Tr(s)$ is

$$Tr(s) = \frac{G(s)}{1 - G(s)H(s)}, \tag{4.36}$$

the denominator function $D(s)$ of the transfer function then is

$$D(s) = 1 - G(s)H(s) \tag{4.37}$$

$$= 1 - \frac{x(s)}{\rho(s)}\frac{\delta\rho_{fb}(s)}{x(s)} \tag{4.38}$$

$$= 1 - \frac{(s+\lambda)}{s\Lambda(s+\lambda+\dfrac{\beta}{\Lambda})}[\alpha_f T_{f0} H_f(s) + \alpha_c T_{c0} H_c(s) + \alpha_X T_{X0} H_X(s)]. \tag{4.39}$$

The zeros of this polynomial can be computed easily in MATLAB. The zeros for this system are $-406.3, -3.023, -0.1592, -0.02645, 1.306 \times 10^{-5}, 3.247 \times 10^{-4}$. The two positive roots demonstrate that the system is unstable with xenon feedback.

Chapter 5

Control System Implementation and Dynamic Simulation Results

The material of this chapter concerns the implementation of the fuzzy logic control system for the IPWR power plant. The background and motivation for the selection of fuzzy logic control from Subsection 2.1.3 are recapitulated and discussed further in Section 5.1. A fuzzy logic inference system and controller are implemented in MATLAB using the Fuzzy Logic Toolbox and its integration with Simulink. The results of fuzzy logic control systems for reactor-leading, turbine-leading, and coordinated control operation for achieving trapezoidal load profiles and a synthetic load profile derived from CAISO time series data for June 30, 2020, are presented.

5.1 Fuzzy Logic Control

The benefit of implementing fuzzy logic control specifically in this work is to have a system of control that is straightforward to implement, readily intelligible to a human operator, and whose safety is convincing to that operator or a regulator [29]. Besides the conventional PWR applications of FLC from Chapter 2 in articles from Hah and Lee [25], Akin and Altin [23], and Ruan [20], fuzzy logic control has been applied to a variety of other simulated reactor models as well as research reactors, such as the University of New Mexico AGN-201M reactor, for power level and power tracking operation [29]. In applications such as the power tracking outlined in [29], the linguistic rules for power level regulation that are used in lieu of more common PID control and feedforward program control strategies follow from a conceptual understanding of the reactor physics, the thermal hydraulics, and the coupling between these two. An increase in reactivity will increase the power level, and a decrease in reactivity will decrease the power level. Larger values of these inputs will elicit a larger response in the power or can counteract an undesirable evolution of similar magnitude. It is this sort of language upon which a fuzzy controller is predicated and can be formalized and implemented for models in software suites like MATLAB.

5.2 Fuzzy Logic Rule Base

Following from the discussion in the prior section, it is clear that power level tracking of the kind described in the cited fuzzy logic control literature is desirable for continuous load balancing operation of an IPWR plant. The reactivity insertion and feedwater mass flow rate results from Chapter 4 motivate those actuators for such a control system and have the underlying physics, the intuitive behavior, and the demonstrated input-output response that make FLC both feasible and desirable for the objectives of load balancing operation. A fuzzy inference system (FIS) is constructed from the qualitative size of the power error and rate of increase/decrease of the power error–large negative (LN), negative (N), zero (Z), postive (P), and large positive (LP). The proportional and derivative rules are as follows in Table 5.1 and Table 5.2. There are 25 (5×5) linguistic rules altogether for each of the power error input, the time derivative of the power error input, the reactivity control output, and the feedwater mass flow output. A Mamdani FIS is used to fuzzify the inputs, and a centroid algorithm is used to defuzzify the outputs.

5.3 Control Studies of SMR Model

The results of the closed loop fuzzy logic control simulations for each control strategy–reactor-leading, turbine-leading, and coordinated control–are presented and discussed in turn for the trapezoidal profile. The CAISO simulation was conducted only for the coordinated control due to the apparent benefits in power tracking of such a system.

5.3.1 Case Study: Trapezoidal Profile

A simple sequence of ramp maneuvers was conducted by constructing a trapezoidal reactor power demand (100%-90%-90%-100% nominal). This load profile was simulated for a reactor-leading strategy, a turbine-leading strategy, and a coordinated control strategy, with the control rod speed and feedwater mass flow rate speed moving in concert to the common relative power error signal and its derivative in % and %/s, respectively.

Reactor-Leading Operation

Here the desired power profile is achieved through the addition and subtraction of reactivity from the reactor core via control rod motion. The results of this external reactivity fuzzy logic control strategy appear in Figures 5.8-5.13. The FLC creates a reactivity output based on the rules in Table 5.1. In Figure 5.8 the reactor power and turbine power evolve as expected and desired based on the Chapter 4 results for feedforward action with the control rods. The axial offset and pressurizer level and pressure behave similarly. The thermal power level is tracked well aside from the anomalous spike and an unexpected kink in the power curve when the demand profile starts to rise again at 2400 seconds. The turbine power evolves in response to thermal transients and thus lags the reactor power evolution, a feature typical of reactor-leading operation. The state variables in Figures 5.9 and 5.10 respond follow and lag the reactor thermal power as expected from the perturbation simulations for reactivity in Chapter 4. Reactor-leading operation with the developed fuzzy logic controller is an effective strategy for achieving desired load profiles, but the turbine power lags several seconds. Large penalties are also associated with the control rod effort, core temperature

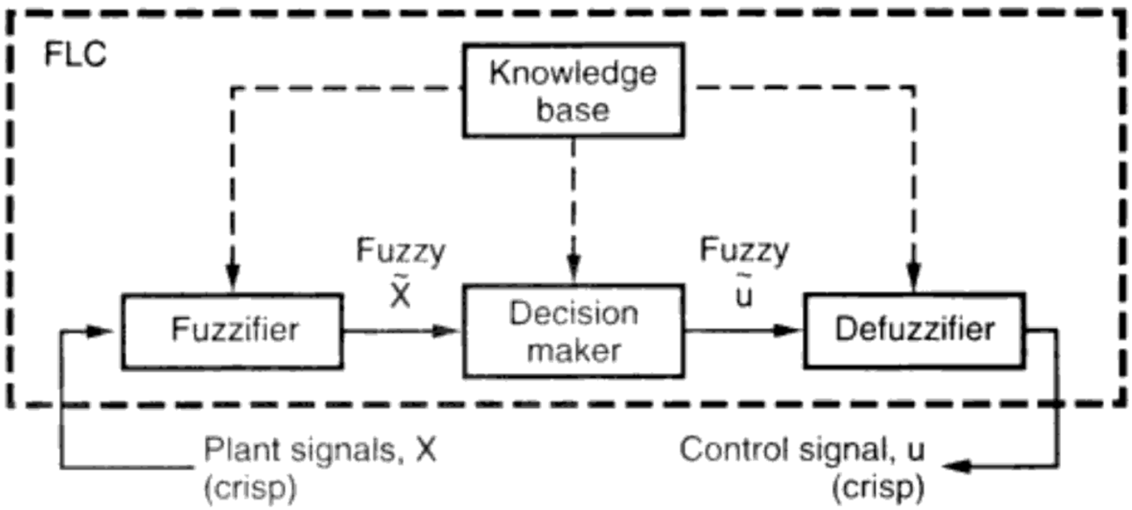

Figure 5.1: Generic diagram of a fuzzy logic controller from Heger et al. [29]. The fuzzy membership rule sets constitute the knowledge base of the controller. The fuzzification-decision making-defuzzification algorithm produces a crisp output from a crisp input.

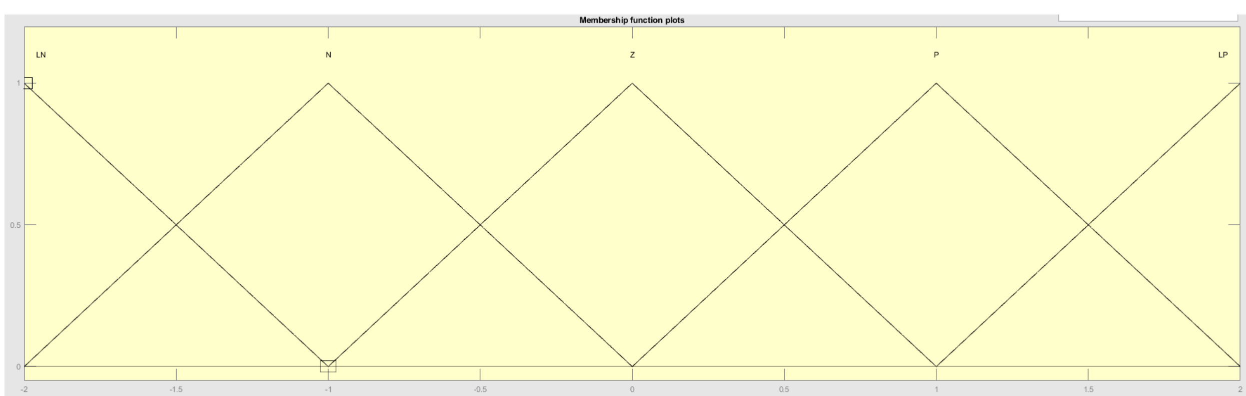

Figure 5.2: The five membership functions for the relative power error–large negative (LN), negative (N), "zero" (Z), positive (P), and large positive (LP).

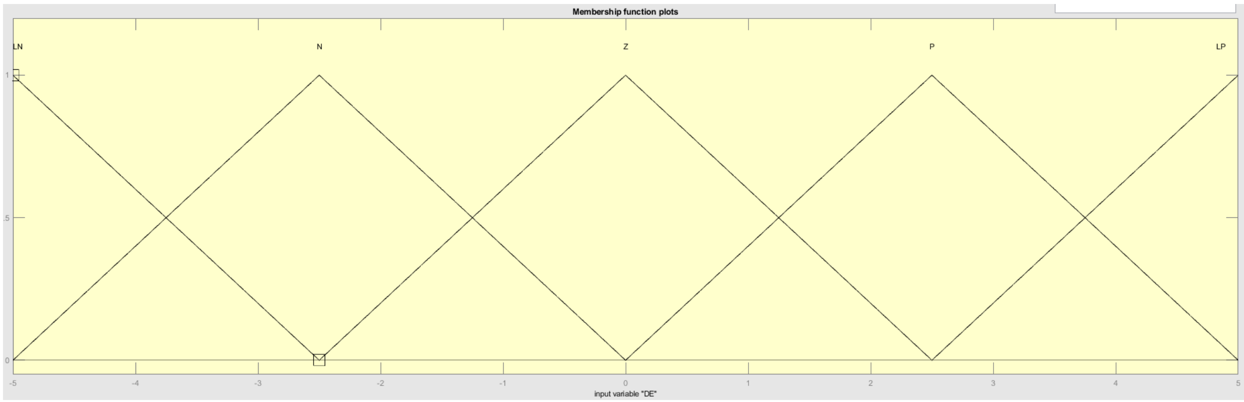

Figure 5.3: The five membership functions for the time derivative of relative power error–large negative (LN), negative (N), "zero" (Z), positive (P), and large positive (LP).

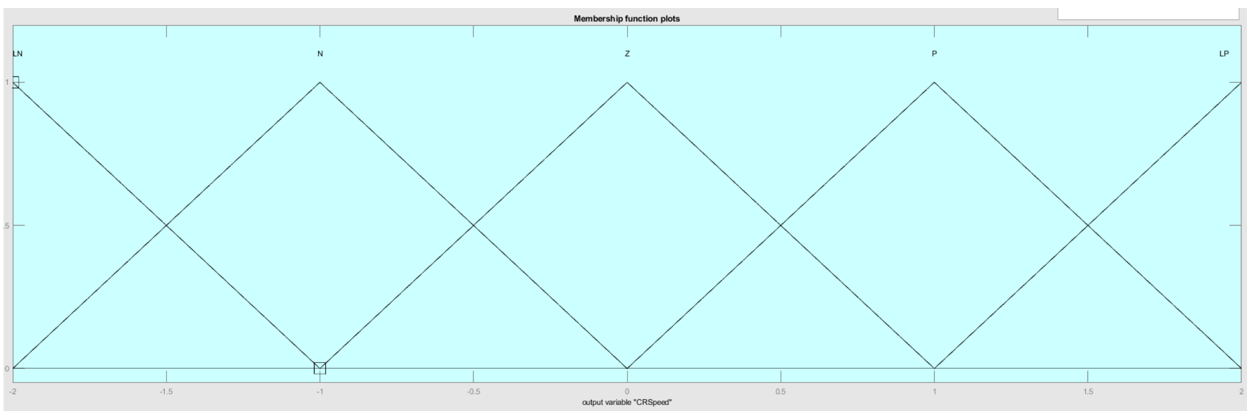

Figure 5.4: The five membership functions for the control rod reactivity rate input–large negative (LN), negative (N), "zero" (Z), positive (P), and large positive (LP).

Table 5.1: Fuzzy Logic Rule Base for Control Rod Reactivity Insertion

DE \E	LN	N	Z	P	LP
LN	LP	LP	Z	N	N
N	LP	P	Z	N	N
Z	P	P	Z	N	N
P	P	P	Z	N	LN
LP	P	P	Z	LN	LN

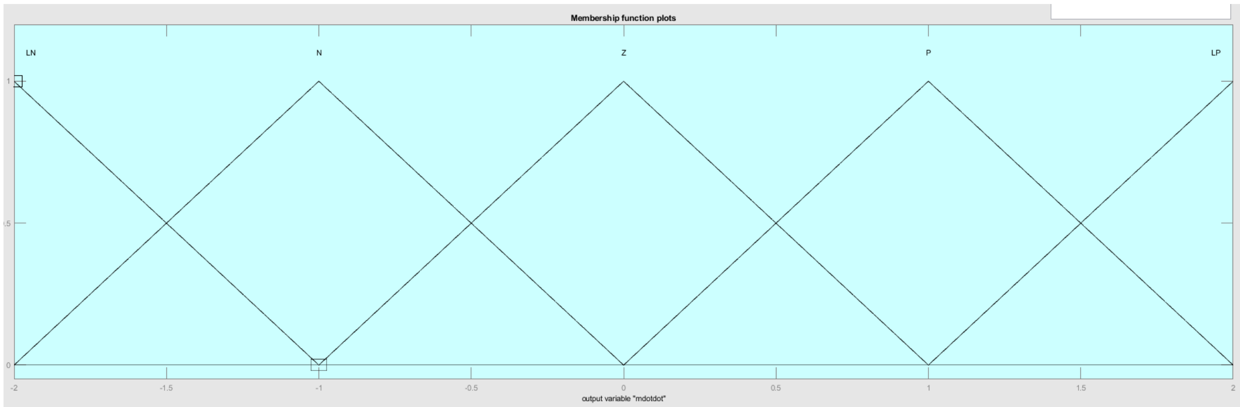

Figure 5.5: The five membership functions for the time derivative of feedwater mass flow rate–large negative (LN), negative (N), “zero” (Z), positive (P), and large positive (LP).

Table 5.2: Fuzzy Logic Rule Base for Feedwater Mass Flow Rate Control

DE \E	LN	N	Z	P	LP
LN	LP	LP	Z	N	N
N	LP	P	Z	N	N
Z	P	P	Z	N	N
P	P	P	Z	N	LN
LP	P	P	Z	LN	LN

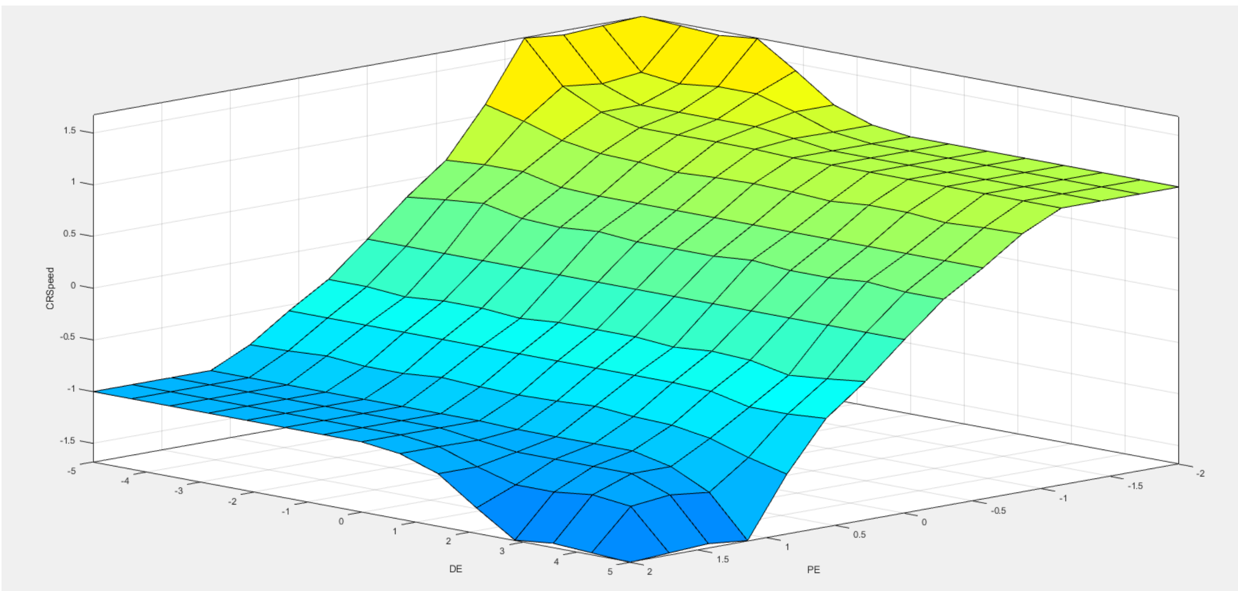

Figure 5.6: This is the rules output surface for the control rod insertion speed fuzzy inference system. The left axis denotes the derivative error in percent per second while the right axis denotes the proportional error in percent. It is identical to the rules surface of the feedwater FIS, but the output is adjusted by a different gain to scale with the dimensions of the reactivity in pcm.

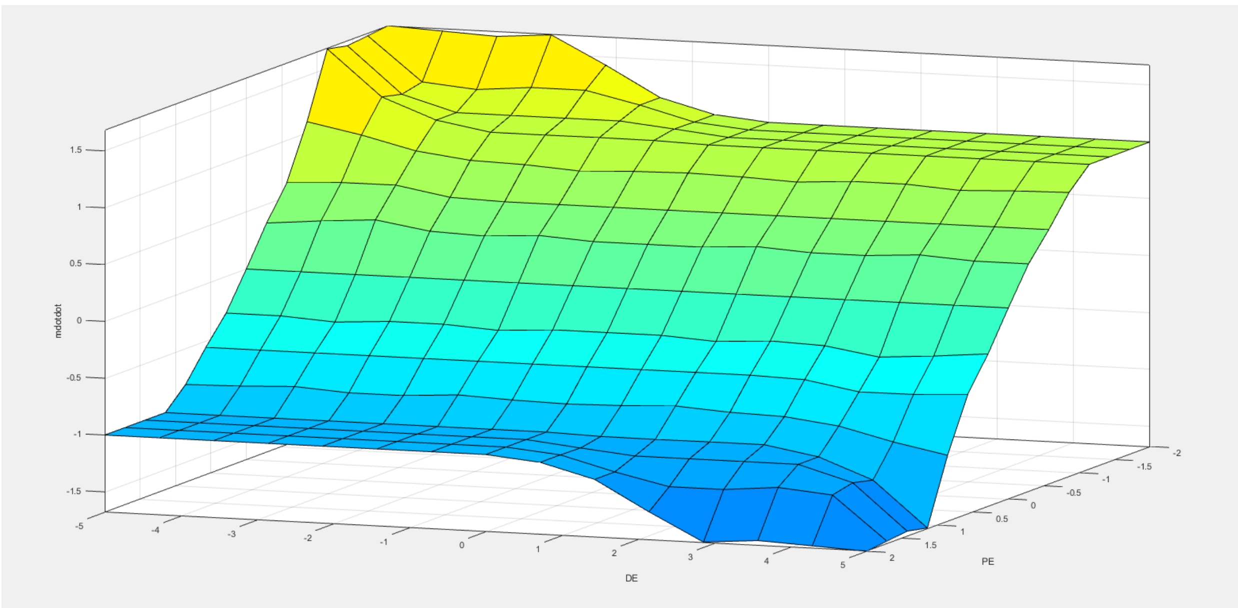

Figure 5.7: This is the rules output surface for the feedwater mass flow rate speed ($\ddot{m}$) fuzzy inference system. The left axis denotes the derivative error in percent per second while the right axis denotes the proportional error in percent. It is identical to the rules surface of the control rod FIS, but the output is adjusted by a different gain to scale with the dimensions of the mass flow rate.

cost, and steam pressure cost, which may have consequences for component degradation, maintenance scheduling, and development of vibrations in secondary and tertiary systems. Xenon does not increase enough to have any meaningful consequences for this gentle profile, as is apparent in Figure 5.13.

Turbine-Leading Operation

Here the desired power profile is achieved through the addition and subtraction of heat removal from the reactor core via changing the feedwater mass flow rate. The FLC control for the feedwater mass flow rate uses the rule set previously defined in Table 5.2 to calculate the fuzzified output and appear in Figures 5.14-5.19. In Figure 5.14 the reactor power and turbine power evolve as expected and close to the desired trajectory based on the Chapter 4 results for feedforward action with feedwater mass flow rate. However, relying solely upon feedwater control involves slower thermal phenomena compared to controlling the neutron population more directly with absorbers like control rods. The primary loop temperatures do not evolve quite as dramatically for turbine-leading operation, especially the coolant temperatures, but the fuel temperatures still experience significant changes in temperature in Figure 5.15. In Figure 5.16 the secondary temperatures and steam pressure behave similarly but with pronounced excursions near 1000 s and 3700 s, which is not observed in the reactor-leading or coordinated-control simulations. These small excursions do not have a noticeable effect on the feedwater control effort in Figure 5.17, which is affected mostly by the demand profile rather than other system disturbances. These short, sharp shocks cause a large increase in the steam pressure cost at these times in Figure 5.18 as expected, while the core temperature cost follows a trajectory qualitatively similar to the feedwater control. These facts suggest that steam evolution in the secondary side are the cause of these small disturbances rather than coolant evolution in the primary. A strategy that relies too heavily on feedwater control is likely to have significant consequences and costs for secondary system component health and degradation due to fast changes in the steam mass inventory and enthalpy in a once-through

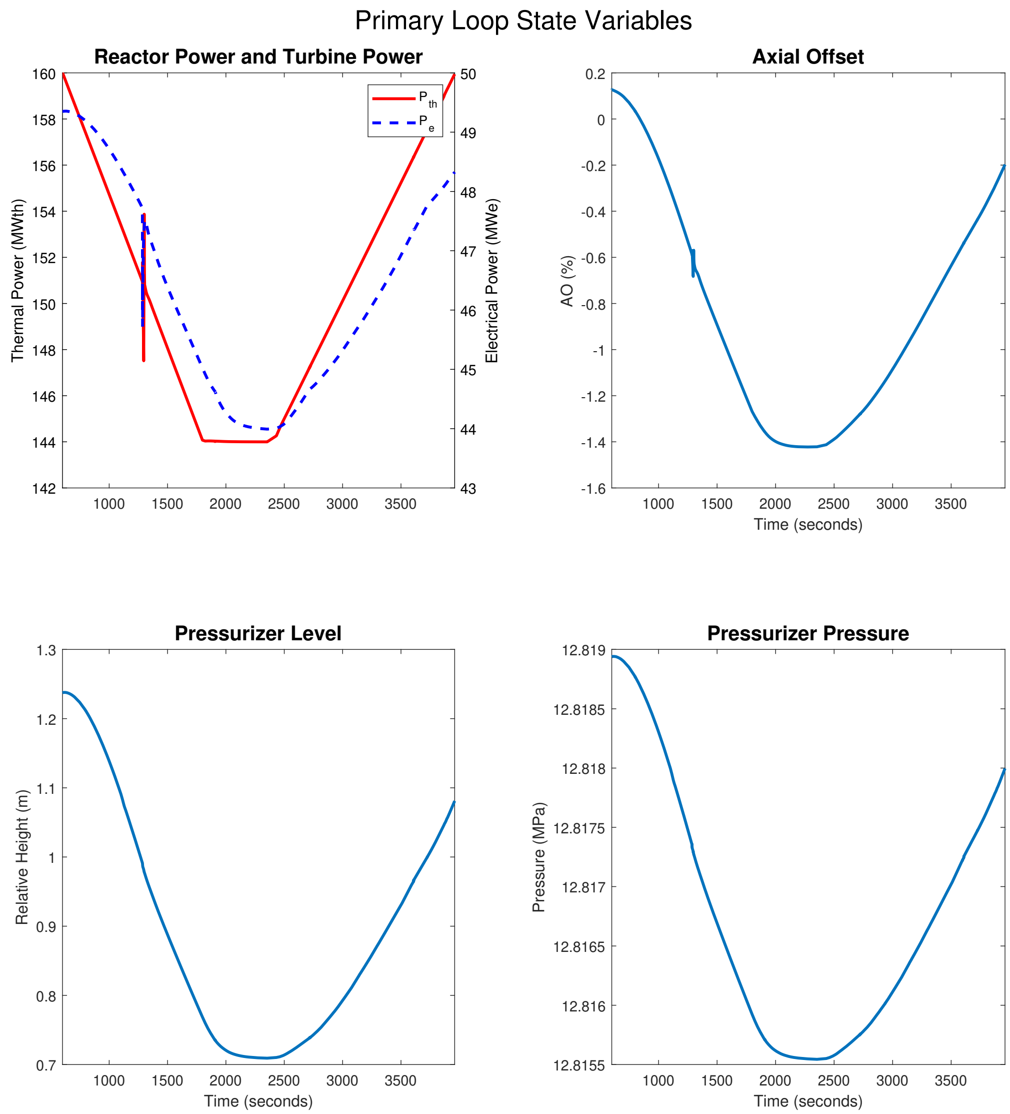

Figure 5.8: The primary state variables for the trapezoidal profile and reactor-leading control system appear here. There is an anomalous transient near 1200 s, but this is most likely a mathematical artifact due to the solver.

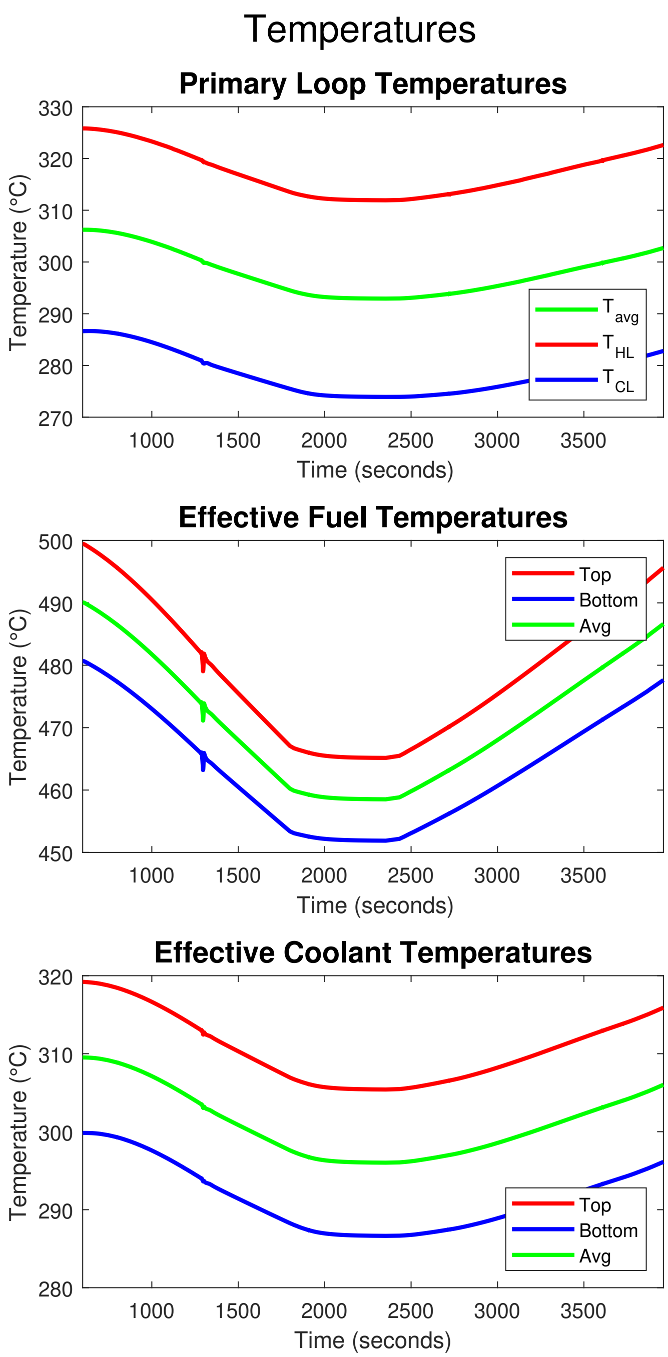

Figure 5.9: The primary system temperatures also follow a generally trapezoidal shape.

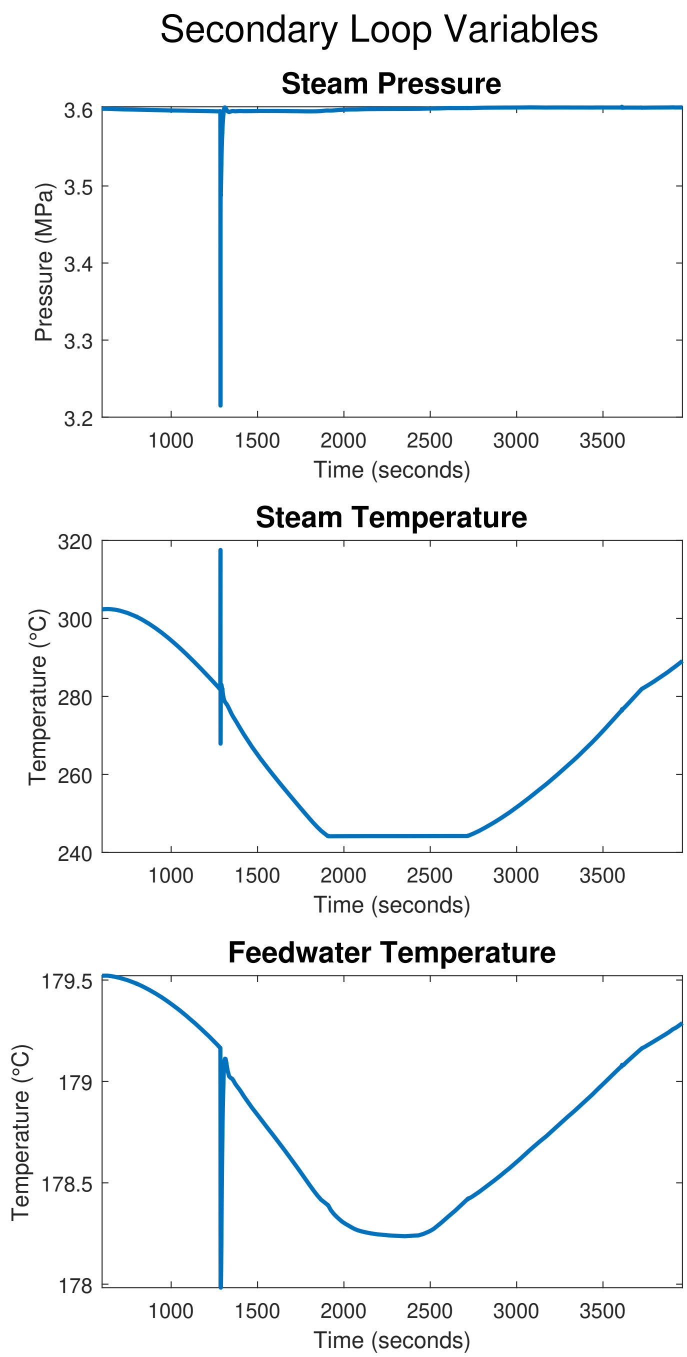

Figure 5.10: The steam pressure hovers near a constant value while the steam and feedwater temperatures follow a generally trapezoidal shape in time. Again an anomalous transient appears, but this is likely a mathematical artifact due to the solver.

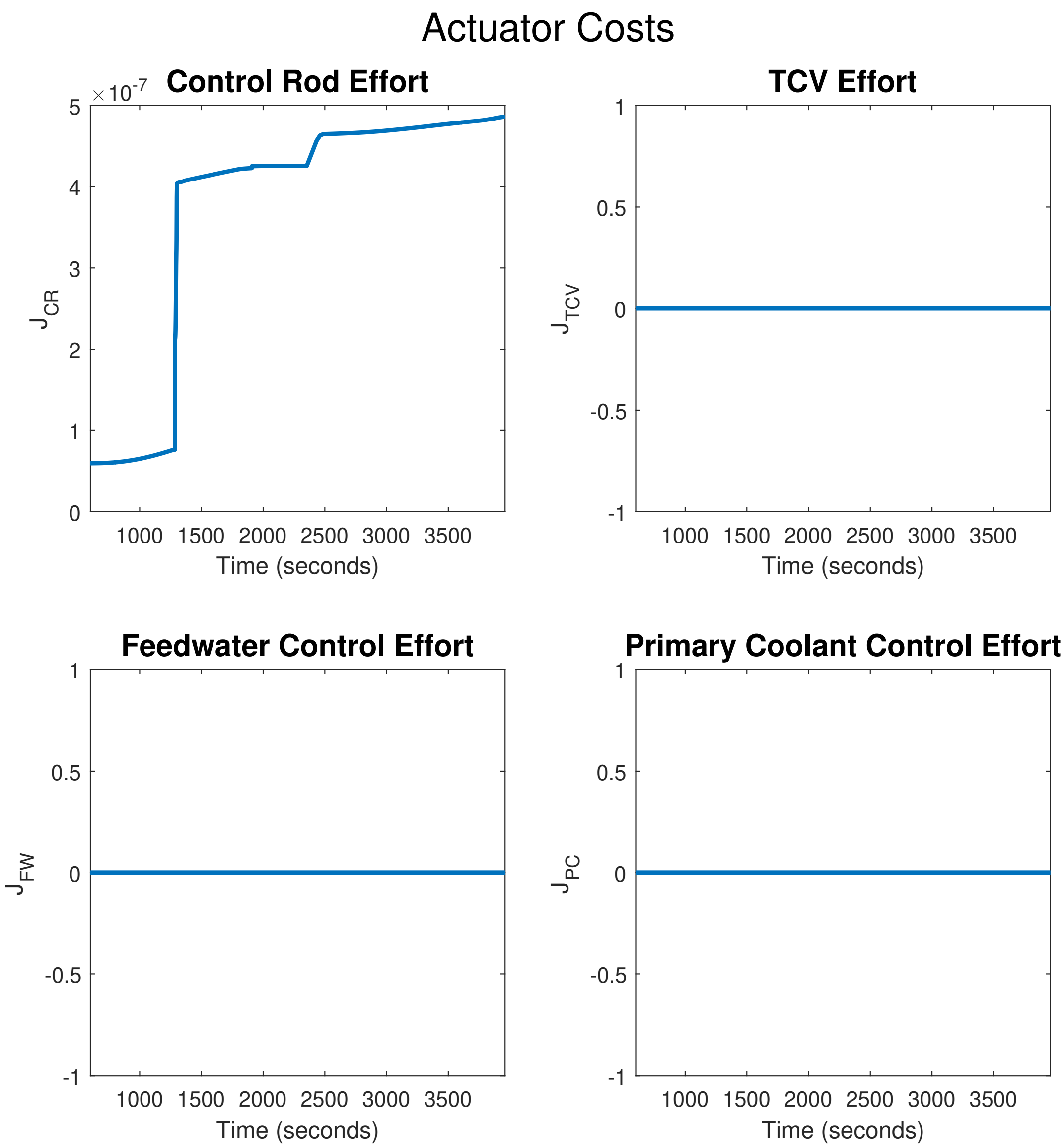

Figure 5.11: This is the actuator effort for the trapezoidal demand met with the reactor-leading strategy. The effort rises dramatically to compensate the anomalous spike and evolves more smoothly during the remainder simulation.

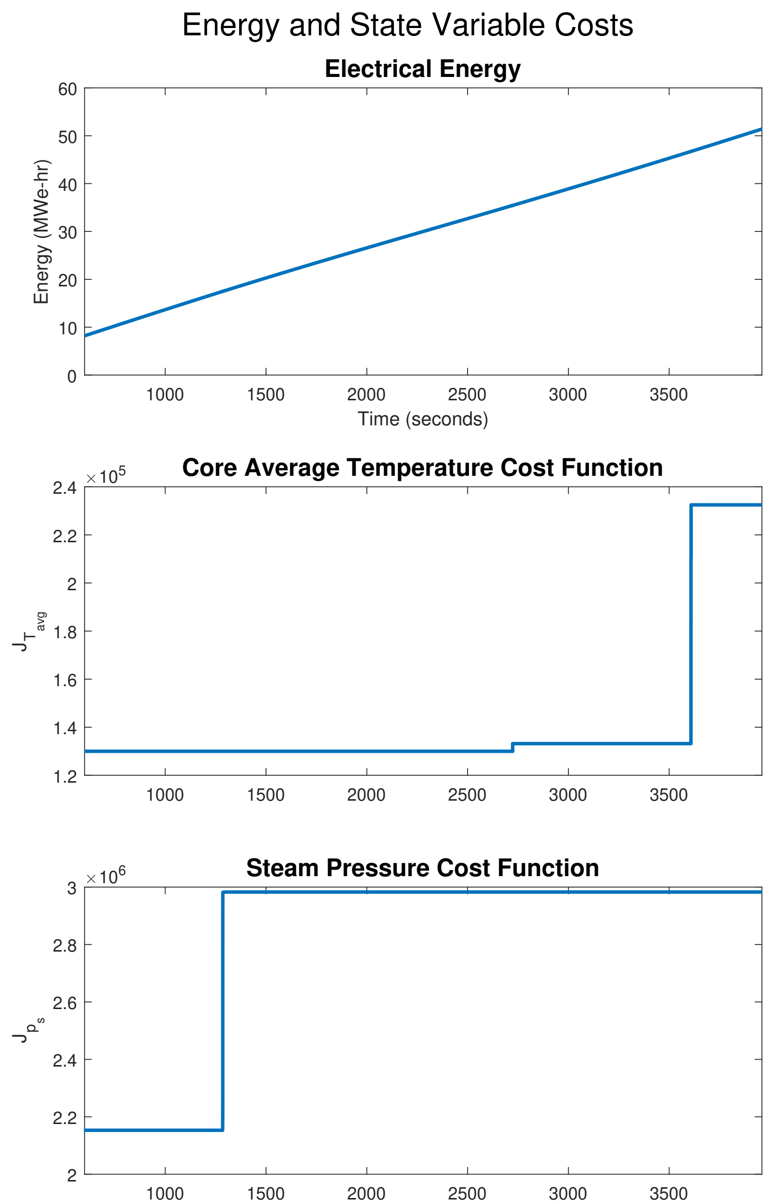

Figure 5.12: The energy generated over the simulation is not particularly interesting, but the state variable costs for the reactor-leading trapezoidal simulation have a dramatic evolution. The steam pressure cost rises almost step-wise during the anomalous spike while the core temperature cost evolves smoothly until the latter part of the simulation.

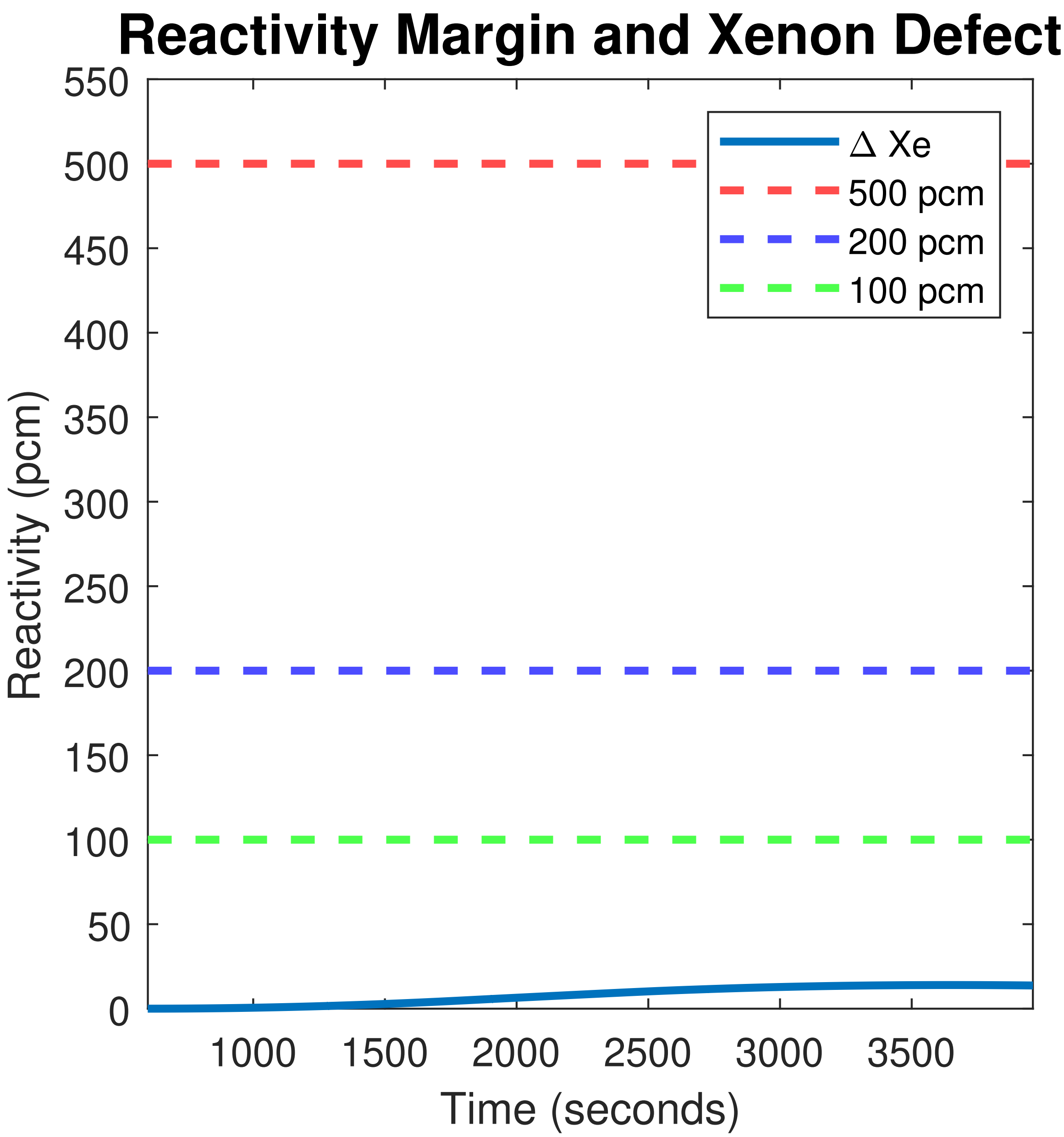

Figure 5.13: The xenon reactivity defect evolves slightly during the reactor-leading trapezoidal simulation since the maneuver is much slower than the time constants associated with the net generation of xenon in a thermal spectrum reactor.

steam generator. The xenon evolution in Figure 5.19 is similarly not consequential for this profile and strategy as it was for the reactor-leading simulations.

Coordinated Control Operation

The results for the coordinated control appear in Figures 5.20-5.25. The control rod reactivity speed program and the feedwater mass flow rate speed program share a common defuzzified output while the gains for each are scaled properly to their physical dimensions. The feedwater gain is scaled to have a smaller effect due to possible power level under/overshoot arising from slower thermal feedback phenomena. The control rod action and its influence dominate the control and evolution of the plant for this coordinated control system. The thermal power response in Figure 5.20 is somewhat smoother compared to the reactor-leading and turbine-leading simulations, although the turbine power still lags due to the explicitly selected dominance of the control rod influence. The primary system temperatures and secondary loop variables in Figures 5.21 and 5.22 behave most similarly to those of the reactor-leading simulations. The actuator cost curves in Figure 5.23 exhibit rather different qualitative behavior as the duty of meeting the load profile falls between the two actuators rather than upon one alone. Both rise steeply during the ramp down and rise gently during the ramp up. In Figure 5.24 the steam pressure cost evolves significantly due to small but rapid excursions in the steam pressure that are visible in Figure 5.22. This suggests that the feedwater mass flow rate constantly shifting, even with modest relative magnitude, can have a measurable deleterious effect on the secondary components if one takes the functional cost formulation to be an accurate proxy for component health. The core temperature cost experiences a dramatic rise at the end of the simulation, but this is likely a numerical artifact due to solver convergence for the simulation ending time step. As is the case for the previous control simulations, the xenon in Figure 5.25 does not change enough to constrain the system.

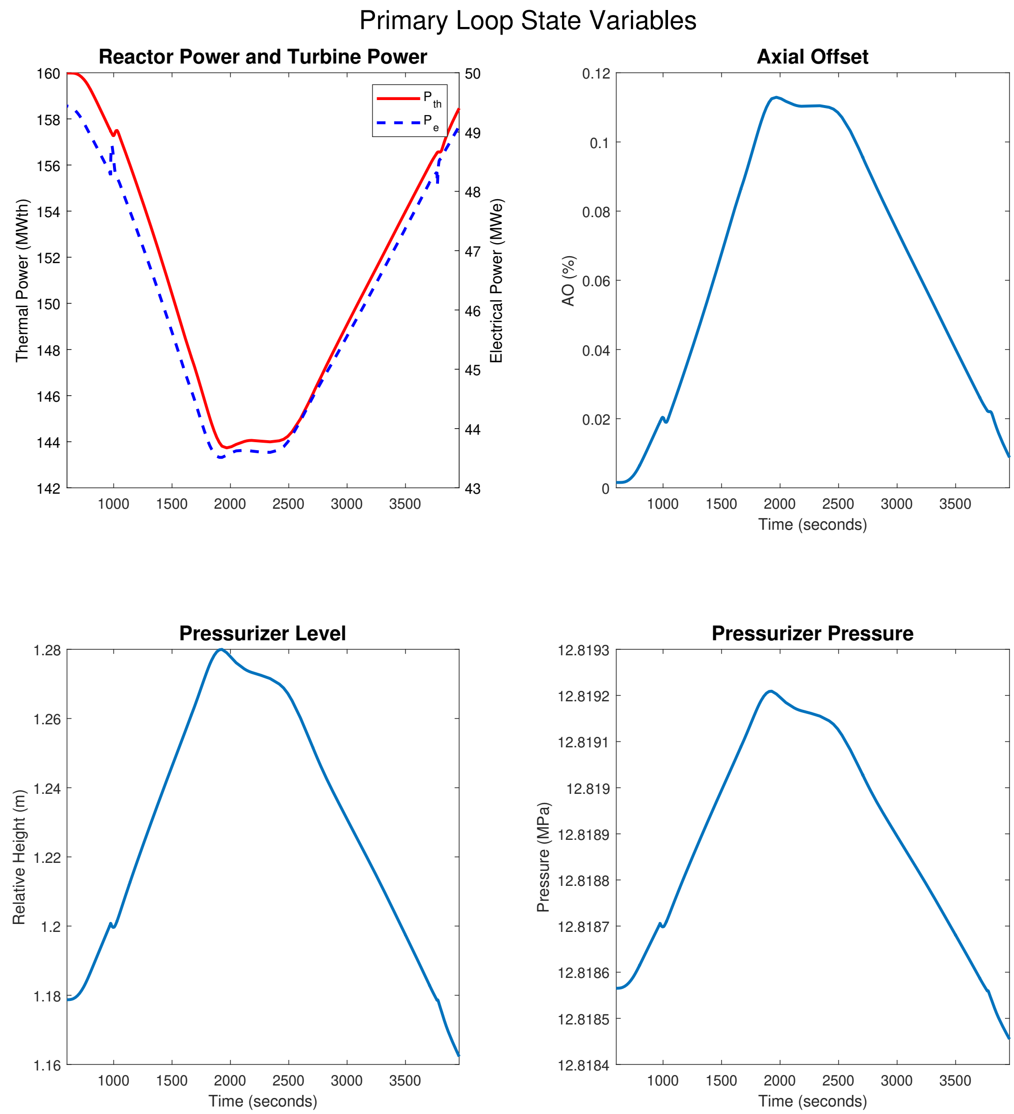

Figure 5.14: The primary state variables for the trapezoidal profile and turbine-leading control system appear here. Note the somewhat slower response compared to the control rod-only reactor-leading approach.

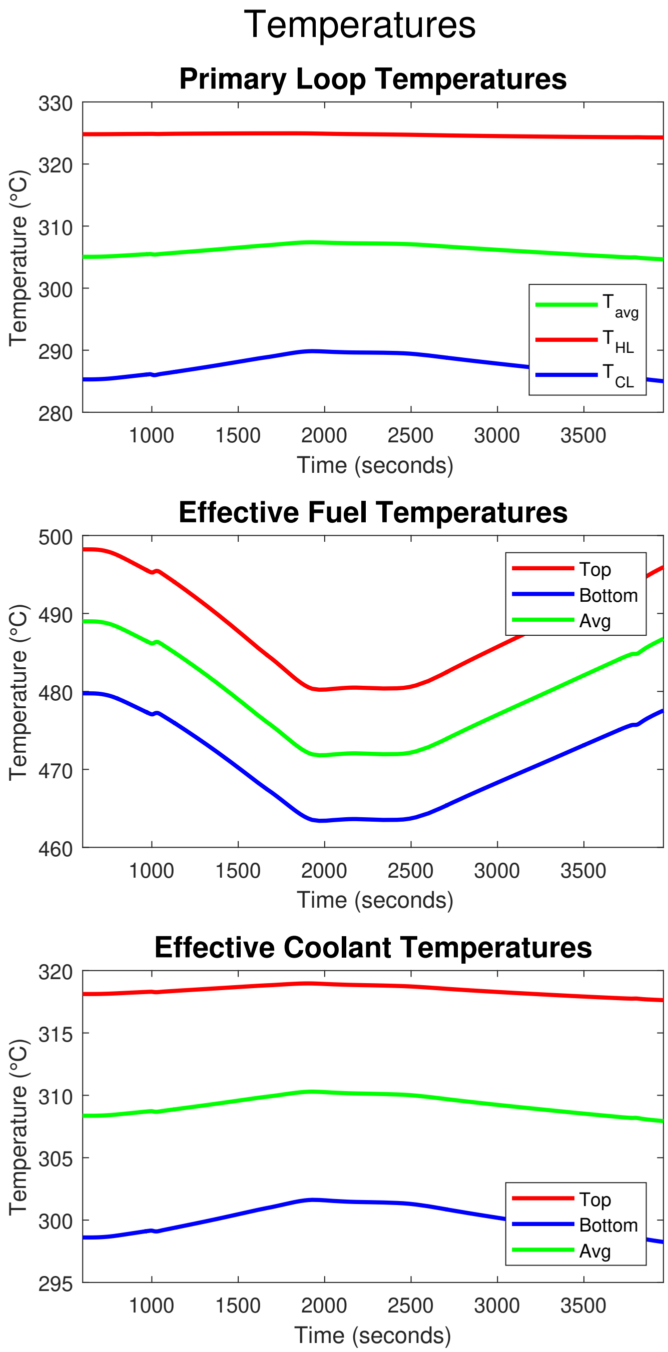

Figure 5.15: The primary system temperatures for the turbine-leading trapezoidal simulation. The fuel temperatures change significantly during the simulation.

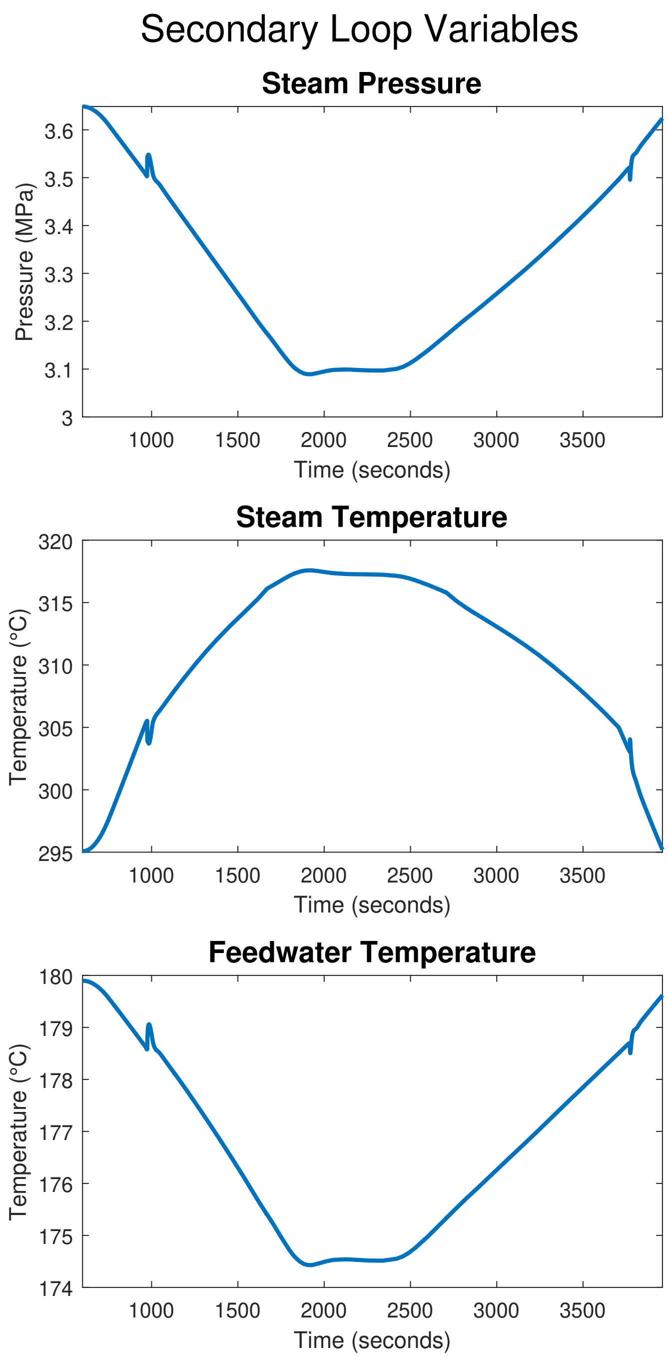

Figure 5.16: The steam temperature evolves in a fashion different from the pressure and feedwater temperature.

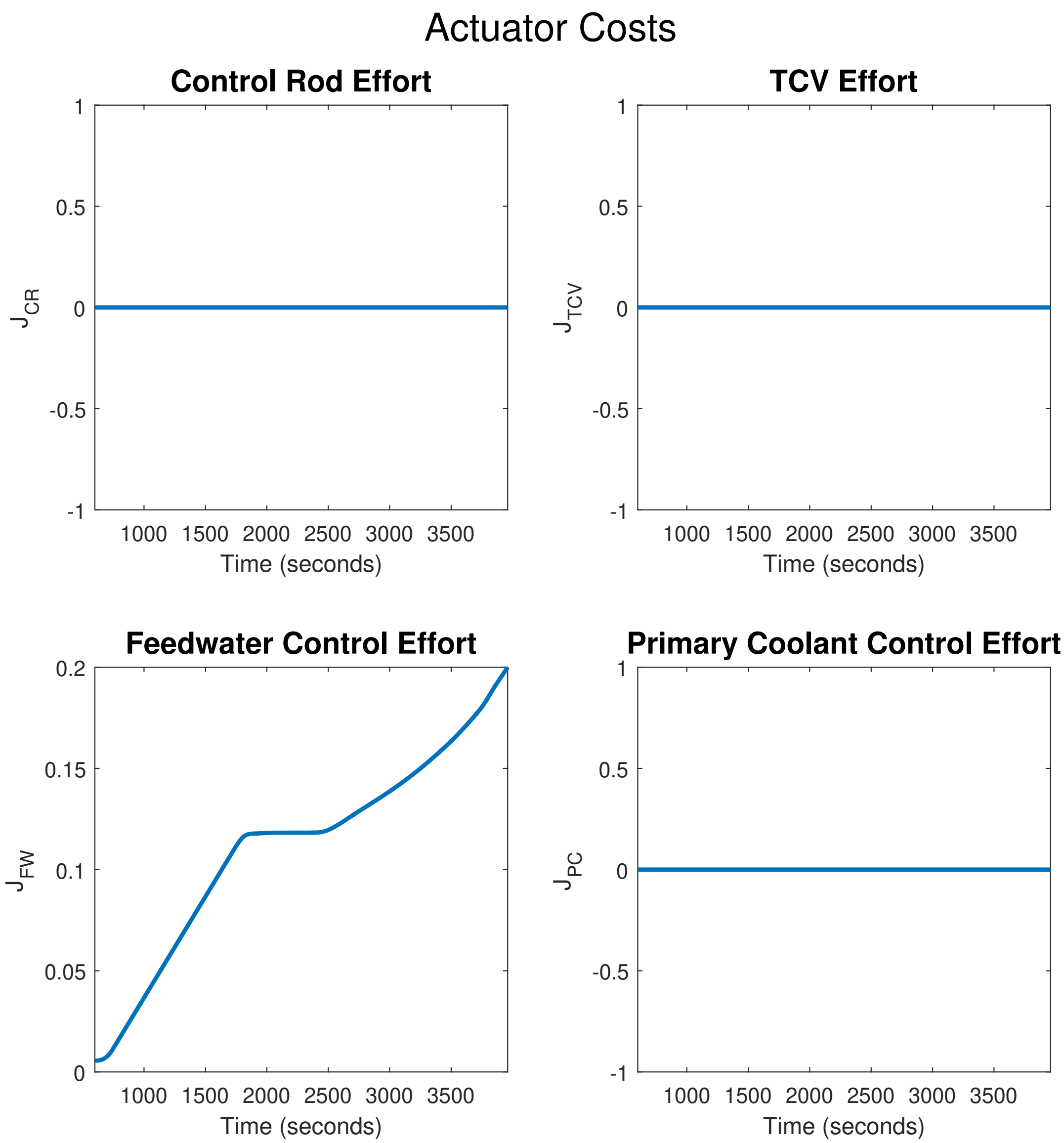

Figure 5.17: The actuator costs for the turbine-leading trapezoidal simulation.

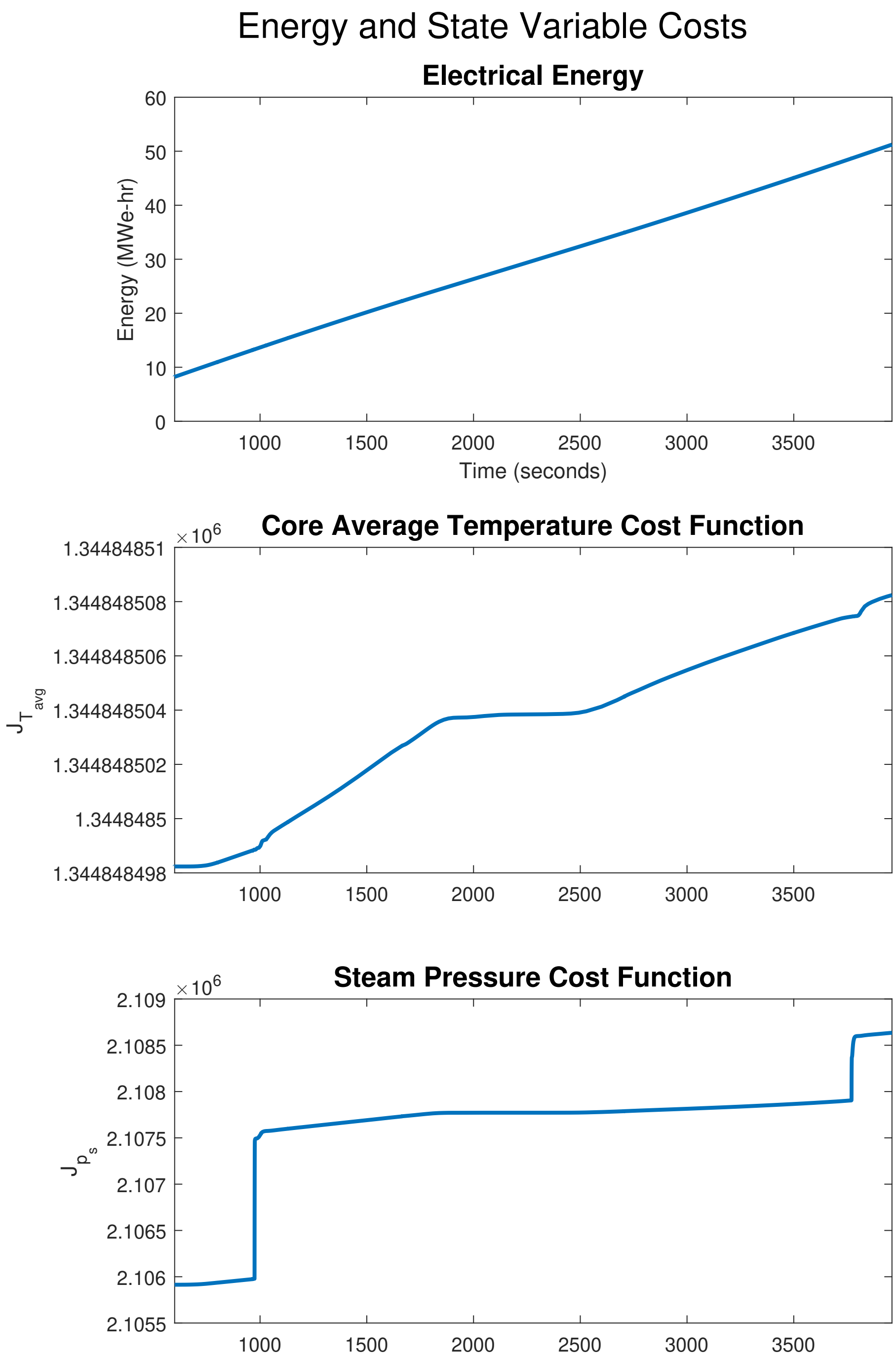

Figure 5.18: The energy and system costs for the turbine-leading trapezoidal simulation.

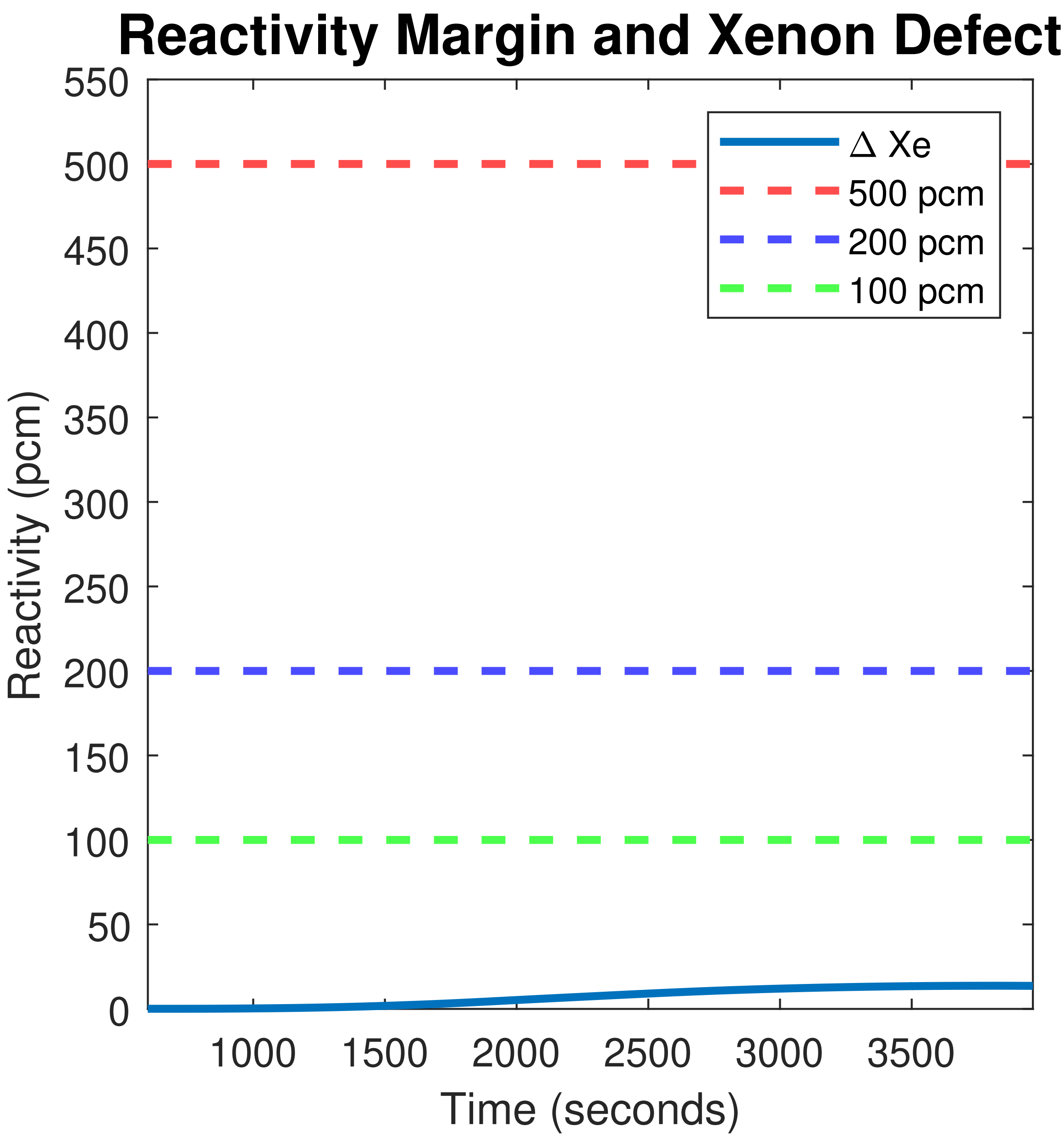

Figure 5.19: The xenon reactivity defect evolves only modestly as expected and in a fashion similar to the reactor-leading simulation.

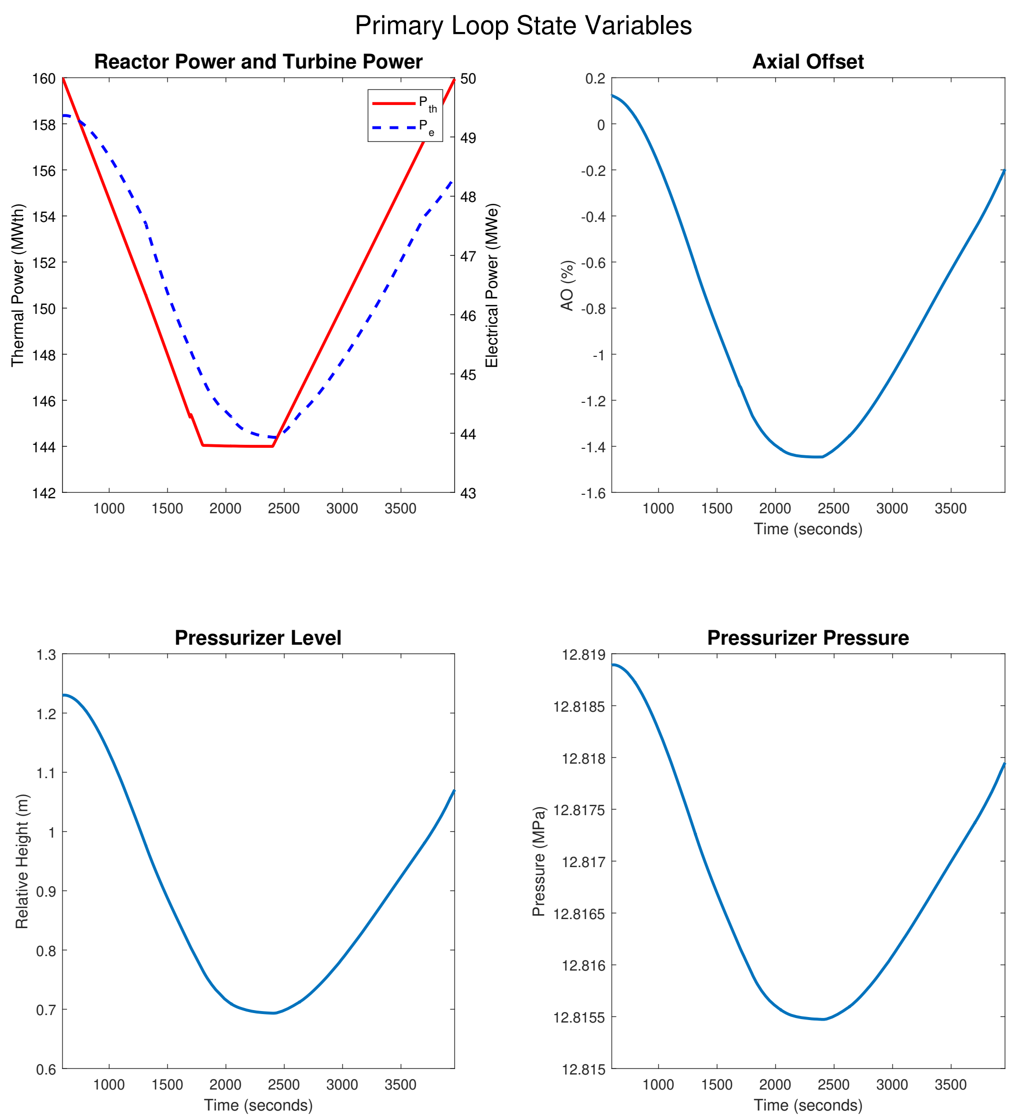

Figure 5.20: The primary states for the coordinated control trapezoidal simulation.

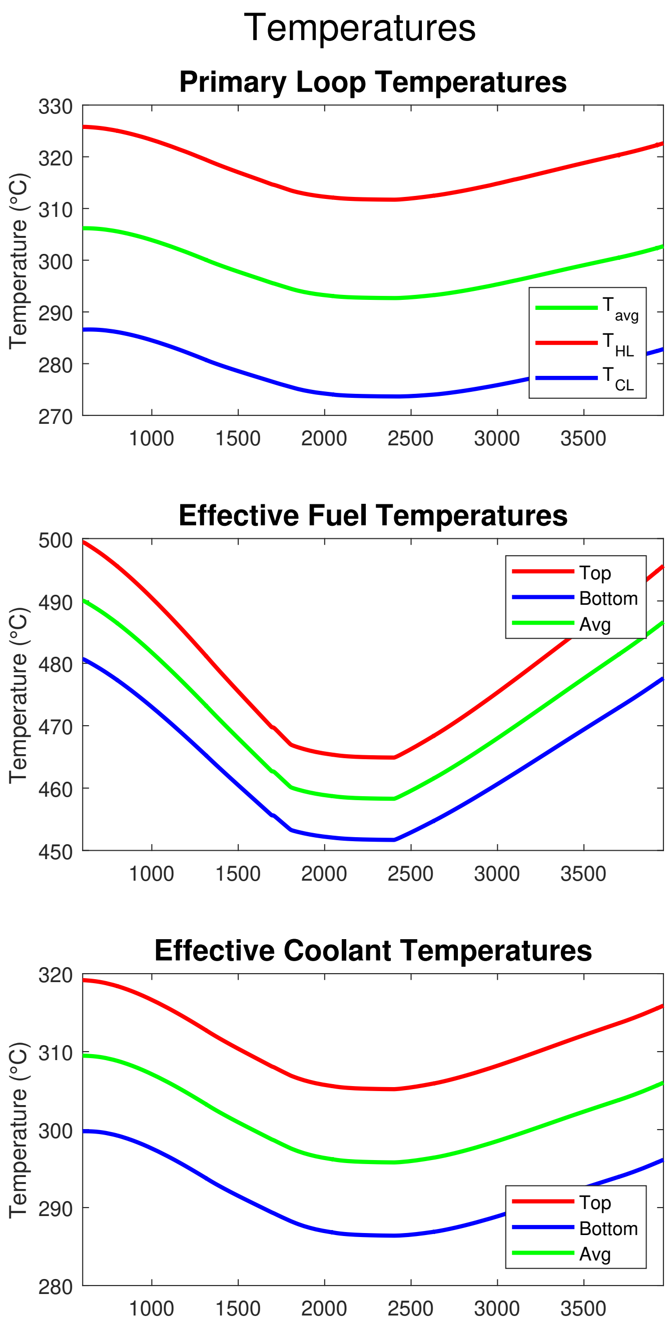

Figure 5.21: The primary system temperatures for the coordinated control trapezoidal simulation.

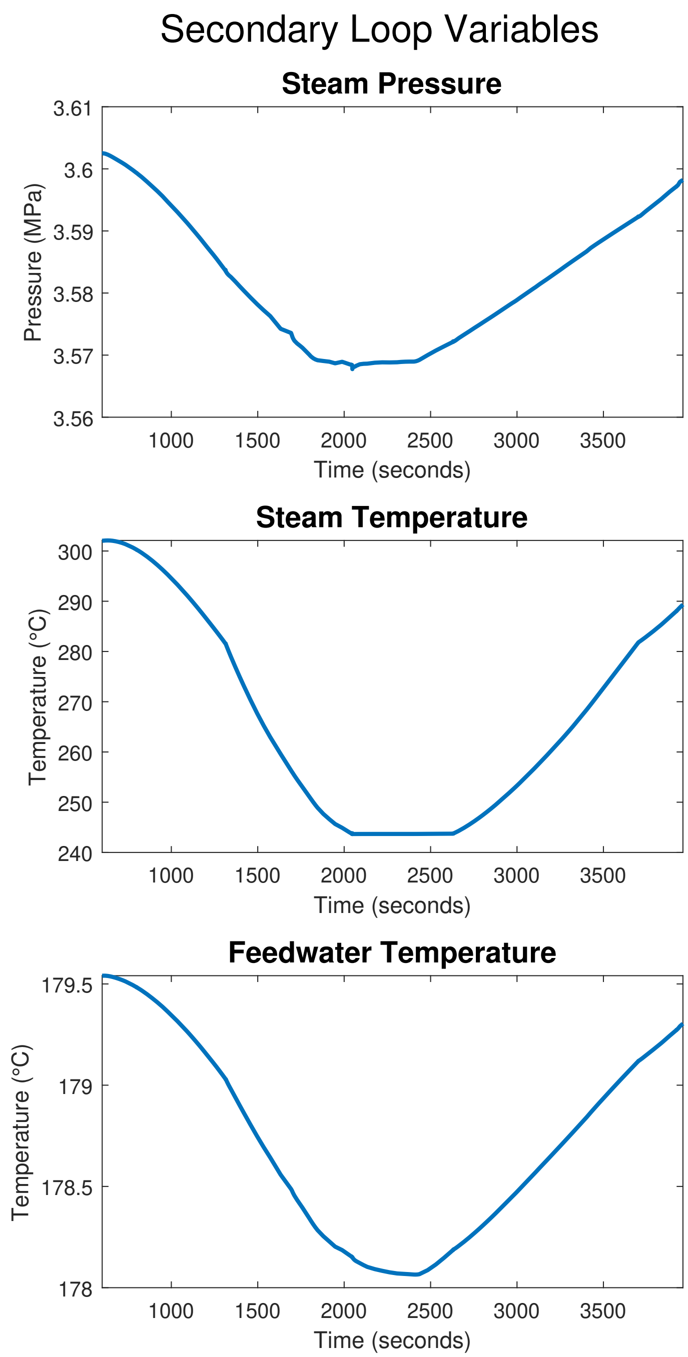

Figure 5.22: The secondary loop states for the coordinated control trapezoidal simulation.

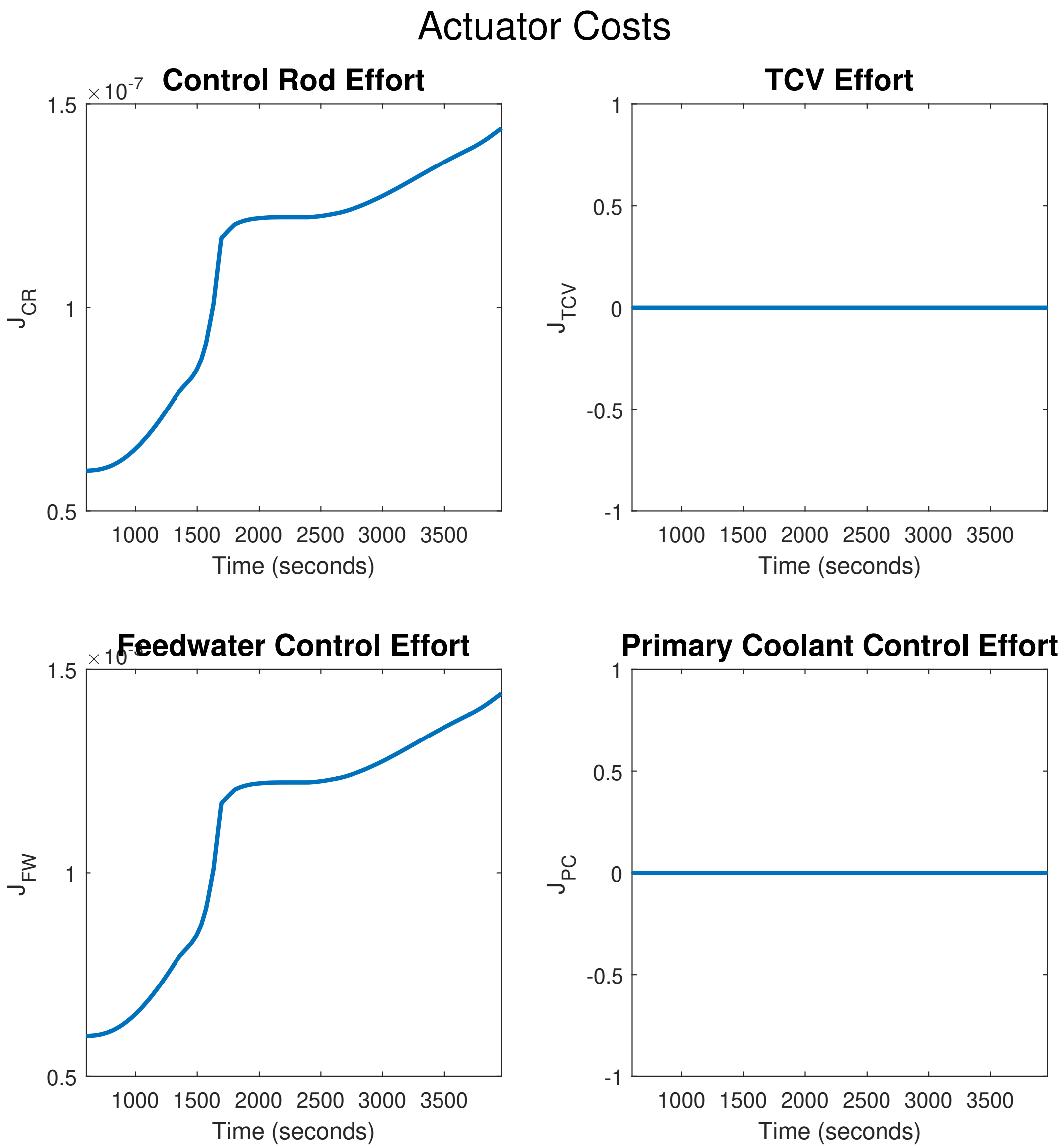

Figure 5.23: The actuator costs for the coordinated control trapezoidal simulation. Significant effort for both control rod and feedwater control are exerted.

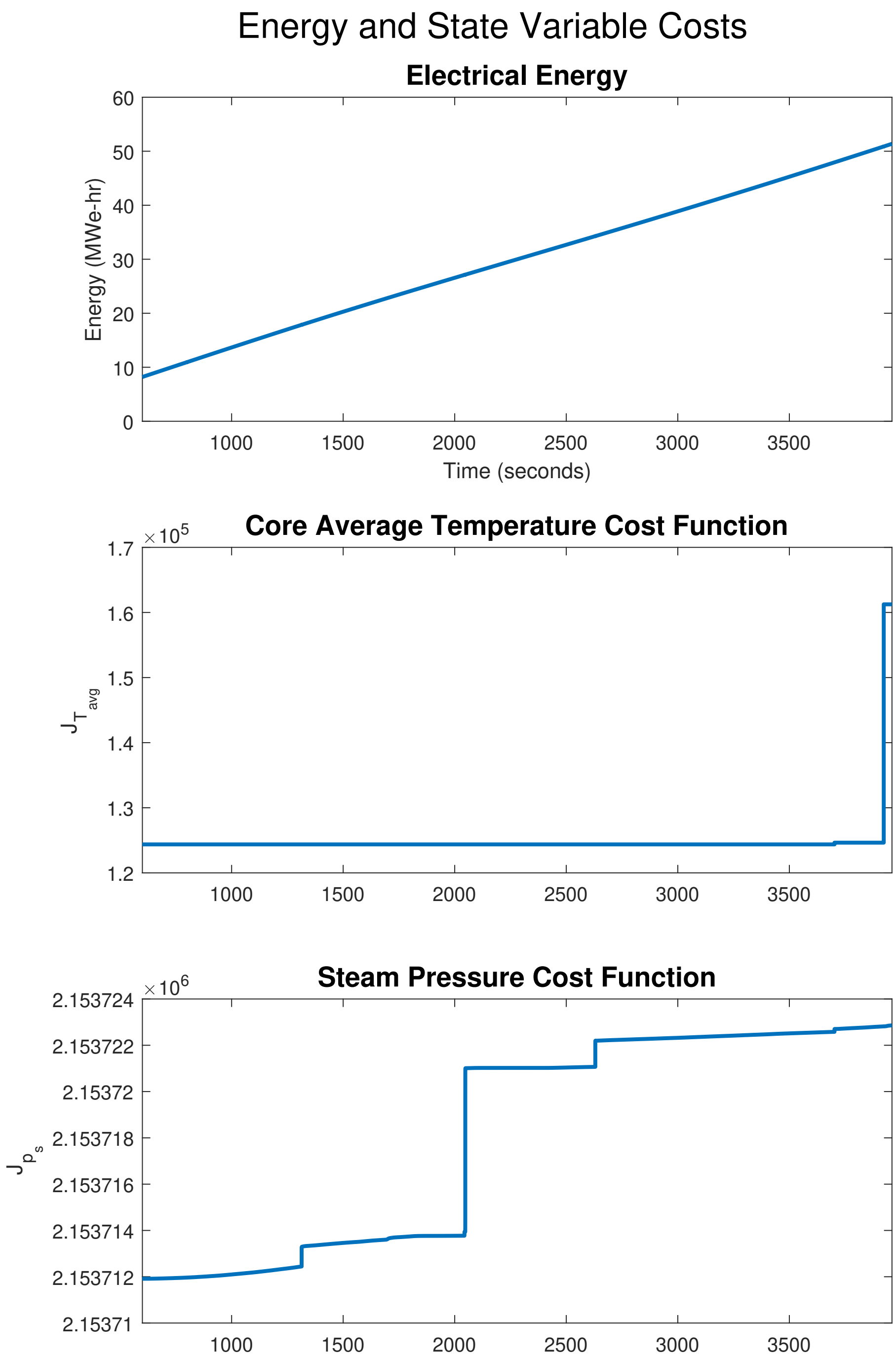

Figure 5.24: Energy and state variable costs for the coordinated control trapezoidal simulation.

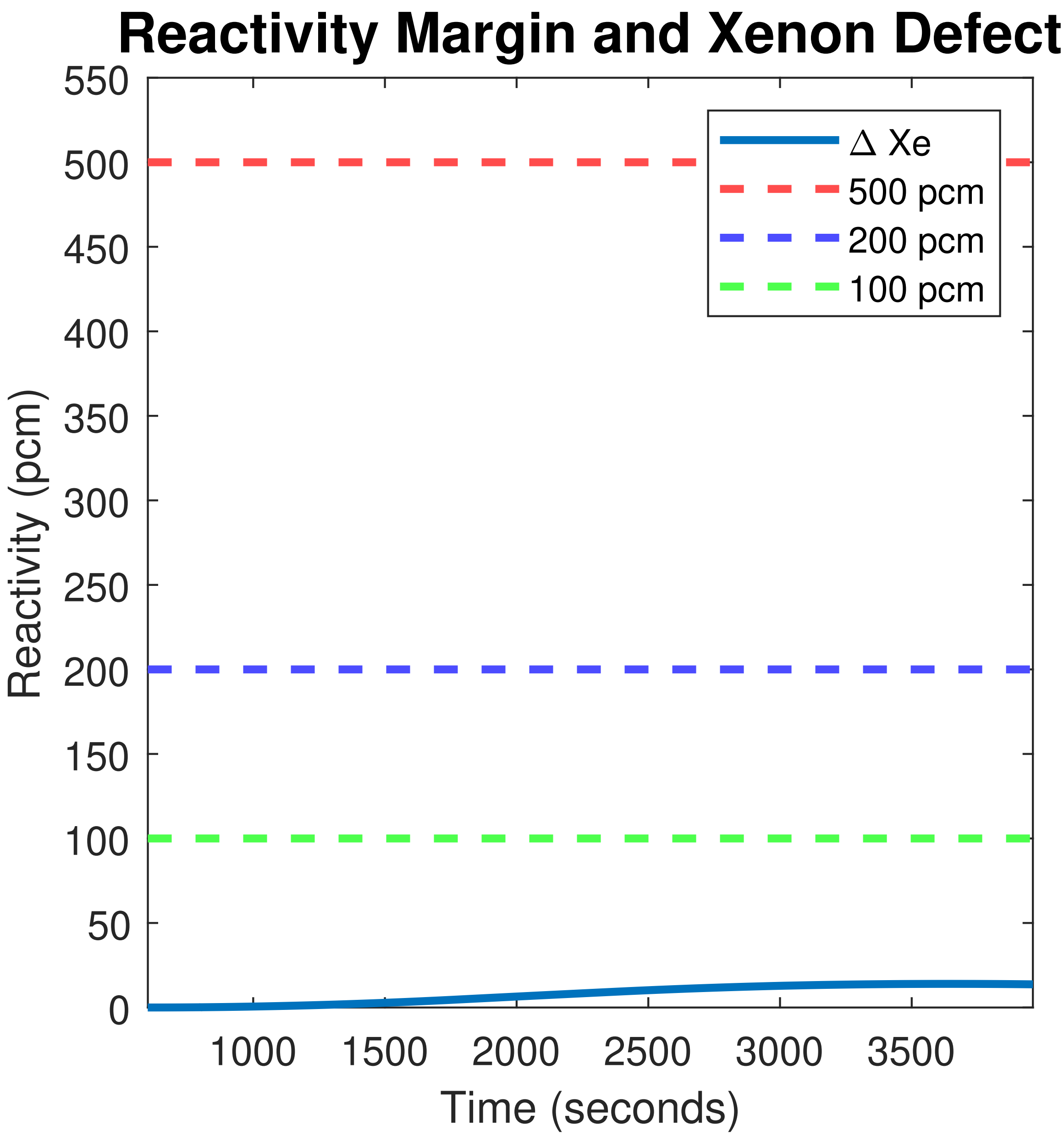

Figure 5.25: The xenon reactivity defect evolves similarly to the previous trapezoidal load simulations.

5.3.2 Grid Demonstration: Synthetic CAISO Profile

Two approaches have been under consideration for the integration of renewables into the model. The first is aggressive load following in a distributed generation system like that in the UAMPS and NuScale studies evaluating load following and performance of a 50 MWe module in tandem with the Horse Butte wind farm [2]. This scenario was useful for the purpose of demonstrating plant flexibility using different control strategies, especially steam bypass, but it is likely somewhat more aggressive than a power plant would be expected to operate in larger electrical system. Instead the generating profile of an independent system operator (ISO), specifically California ISO (CAISO), was used to develop a reference profile as being more representative of what load following IPWRs may face in a high renewables energy system like that of California on a sunny day.

A synthetic load profile is constructed from the 5-minute data of CAISO energy supply for the day of June 30, 2020 and appears in Figure 5.27. Publicly available power five minute time series data from CAISO were used [67] and appear in Figure 5.26. The load profile is constructed from the non-VRE net demand of CAISO generation. This is further adjusted and smoothed heuristically to the profile below because a real load following reactor in the US would likely not operate around these short variations in net demand, but rather, follow a load shape over several hours and only adjust every half-hour at most. The IPWR system is initialized to nominal power and fluctuates with the smoothed demand. The results of this appear in Figures 5.28-5.33 below. The power generation profiles for the reactor and turbine follow the derived demand curve very closely, although the lag in the turbine power is still apparent even at this time scale in Figure 5.28. Additional controls, such as anticipatory feedforward control, could ameliorate the turbine lag. There is still significant evolution of the primary temperatures and secondary loop variables in Figures 5.29 and 5.30. The costs associated with actuator effort and state variable evolution in Figures 5.31 and 5.32 show that ramping the power level back up has an outsized contribution to the stress on the system compared to ramping down. This is due in part to the need to compensate for the xenon that built up during the initial ramp down.

Most interestingly the xenon reactivity defect in Figure 5.33 increases enough to constrain a system with the low excess reactivity levels one would expect in the last weeks or days of a LEU LWR. This offline analysis implies that, at least late in a reactor core fuel cycle, this kind of load following operation typical of a grid with moderate VRE penetration would not be possible as discussed in Ponciroli et al. [14]. Allowances would need to be made for this late cycle consideration, whether it is migrating to a multimodular strategy where freshly loaded modules undergo larger power variations or simply restricting the ramping and forgoing the revenue of some ramping and frequency control services. Overall the results demonstrate the feasibility of load following operation in an energy system with significant renewables penetration, although the temperature and steam cost responses suggest this control approach has a nontrivial penalty on plant component health.

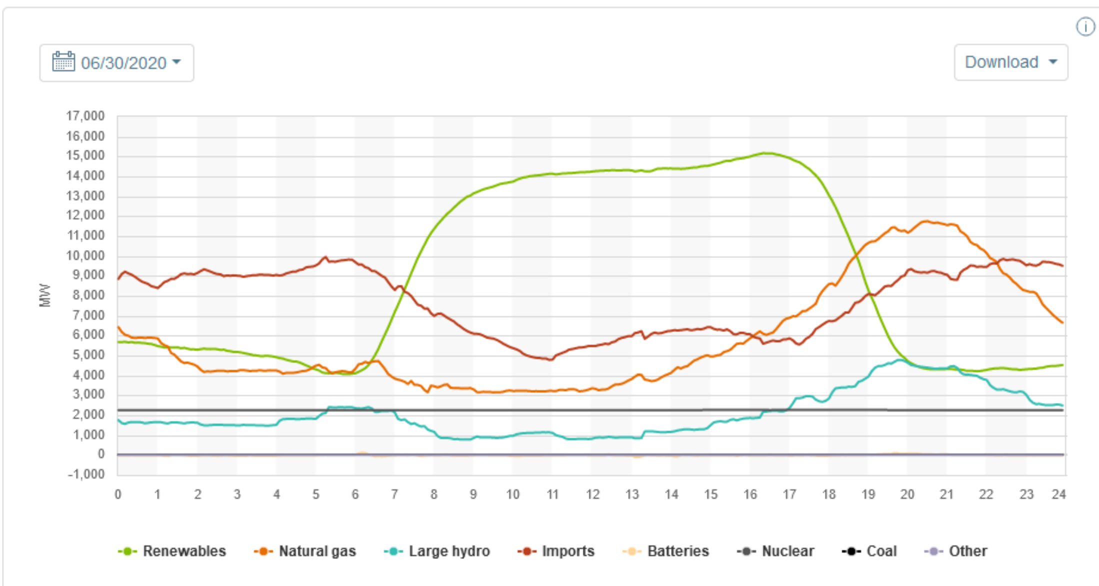

Figure 5.26: CAISO generation (in MWe) five minute time series data as they appear on CAISO's webpage for June 30, 2020 [67]. Note the rapid increase in solar generation in the morning, persistent and high supply during the day, and the rapid decrease in the evening.

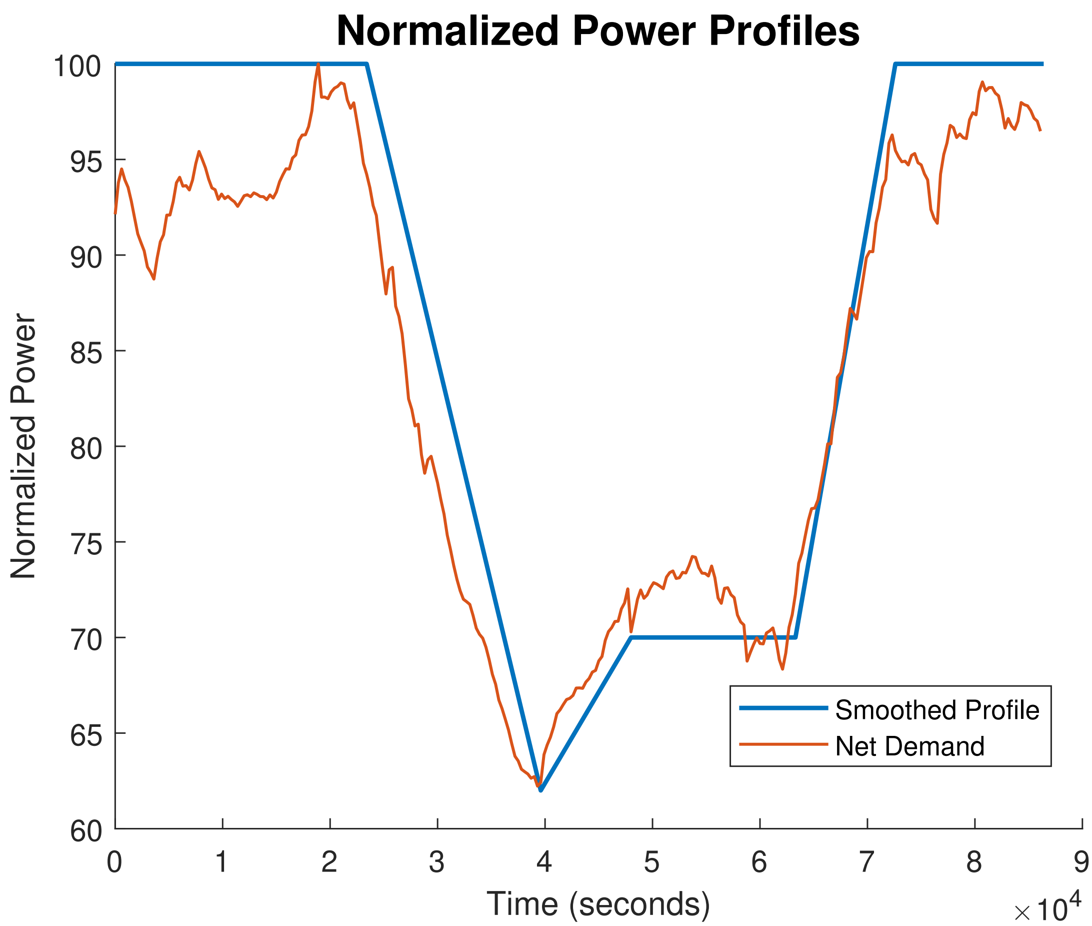

Figure 5.27: Derived power demand for the June 30, 2020 CAISO generation data.

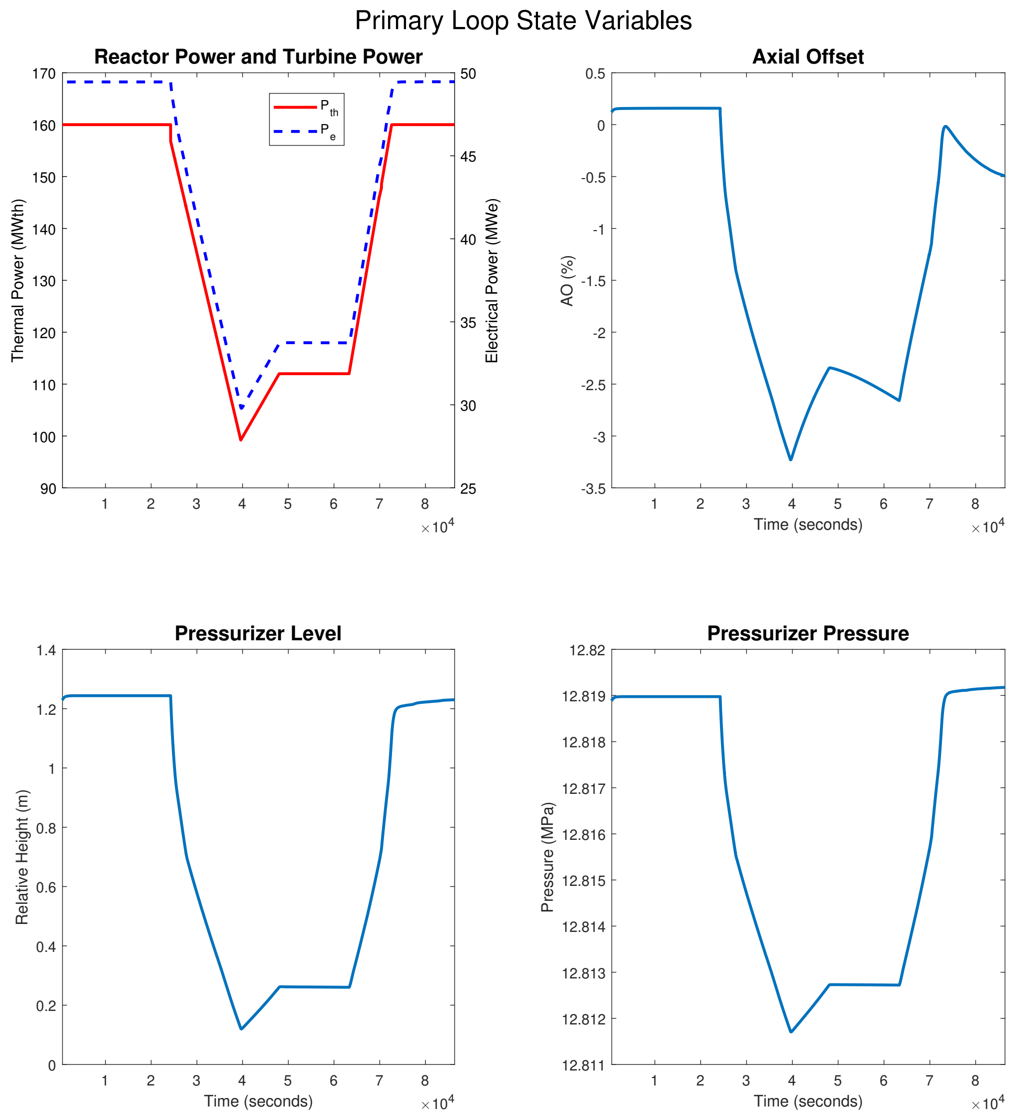

Figure 5.28: The primary state variables for the coordinated control CAISO simulation.

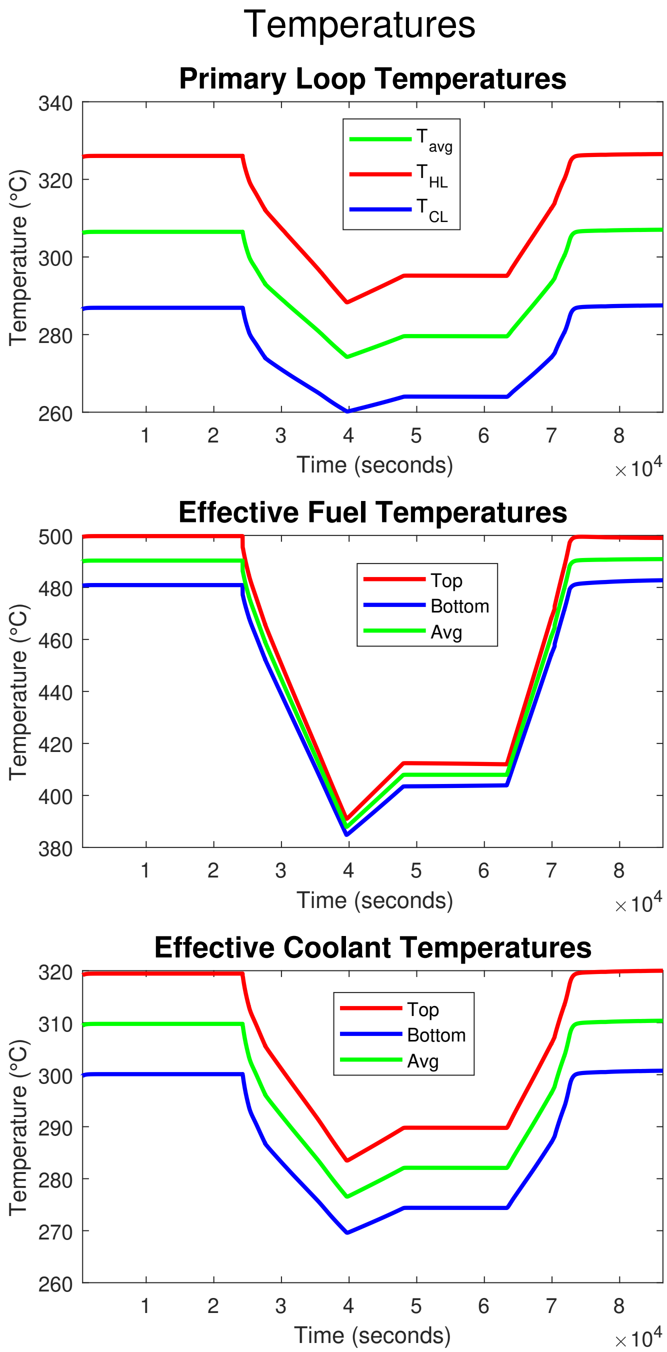

Figure 5.29: The primary system temperatures for the coordinated control CAISO simulation.

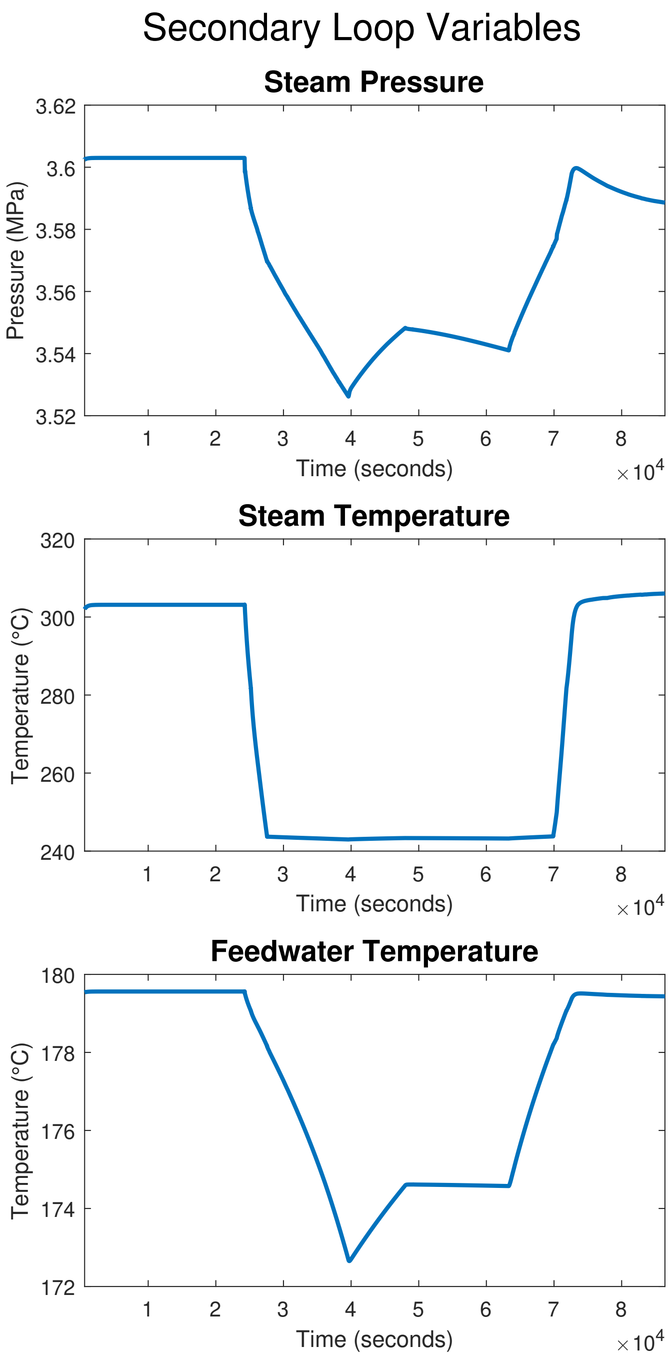

Figure 5.30: The secondary system state variables for the coordinated control CAISO simulation.

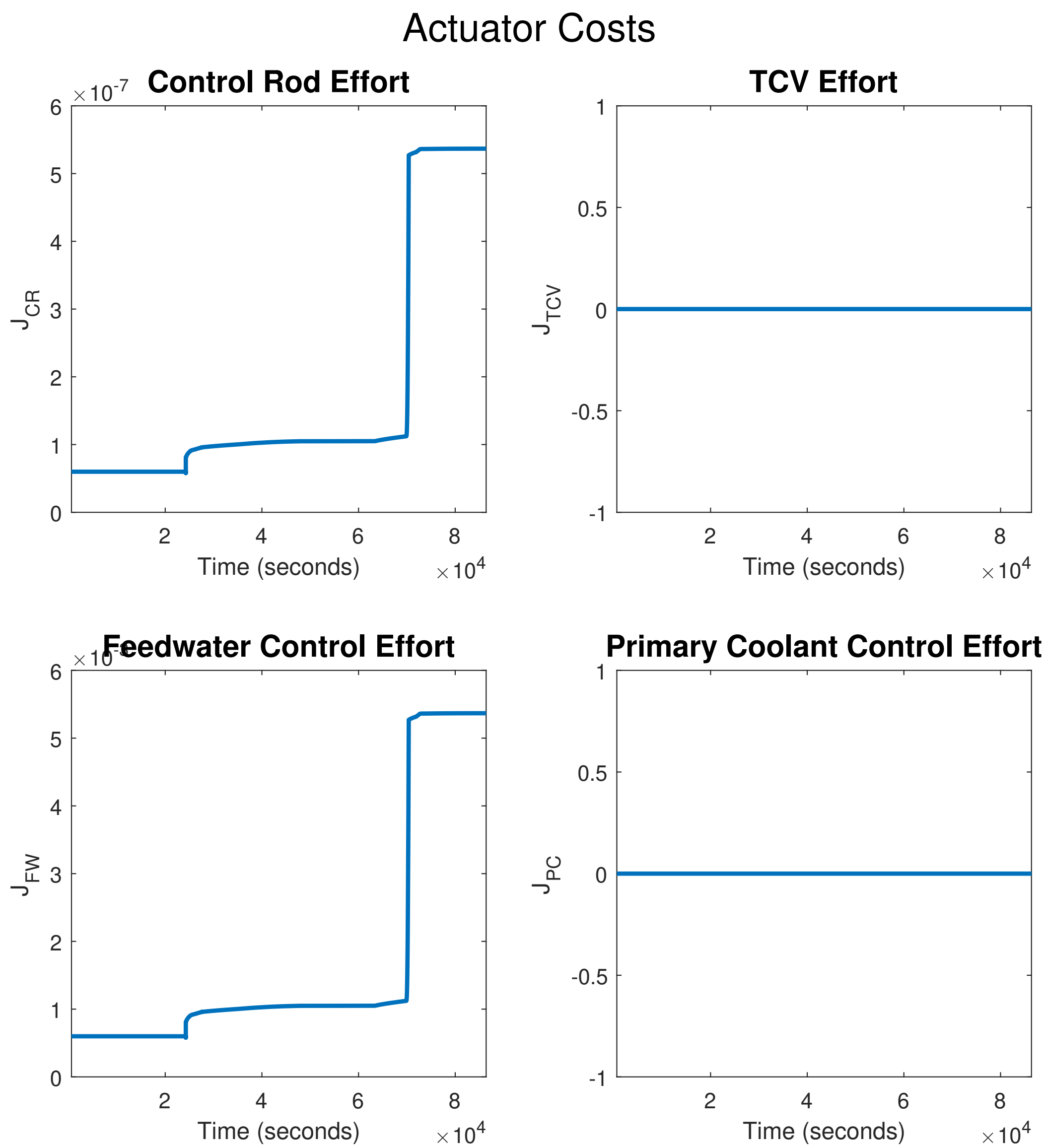

Figure 5.31: The actuator costs for the coordinated control CAISO simulation. The dramatic night ramp imposes a significant cost increase in terms of actuator effort.

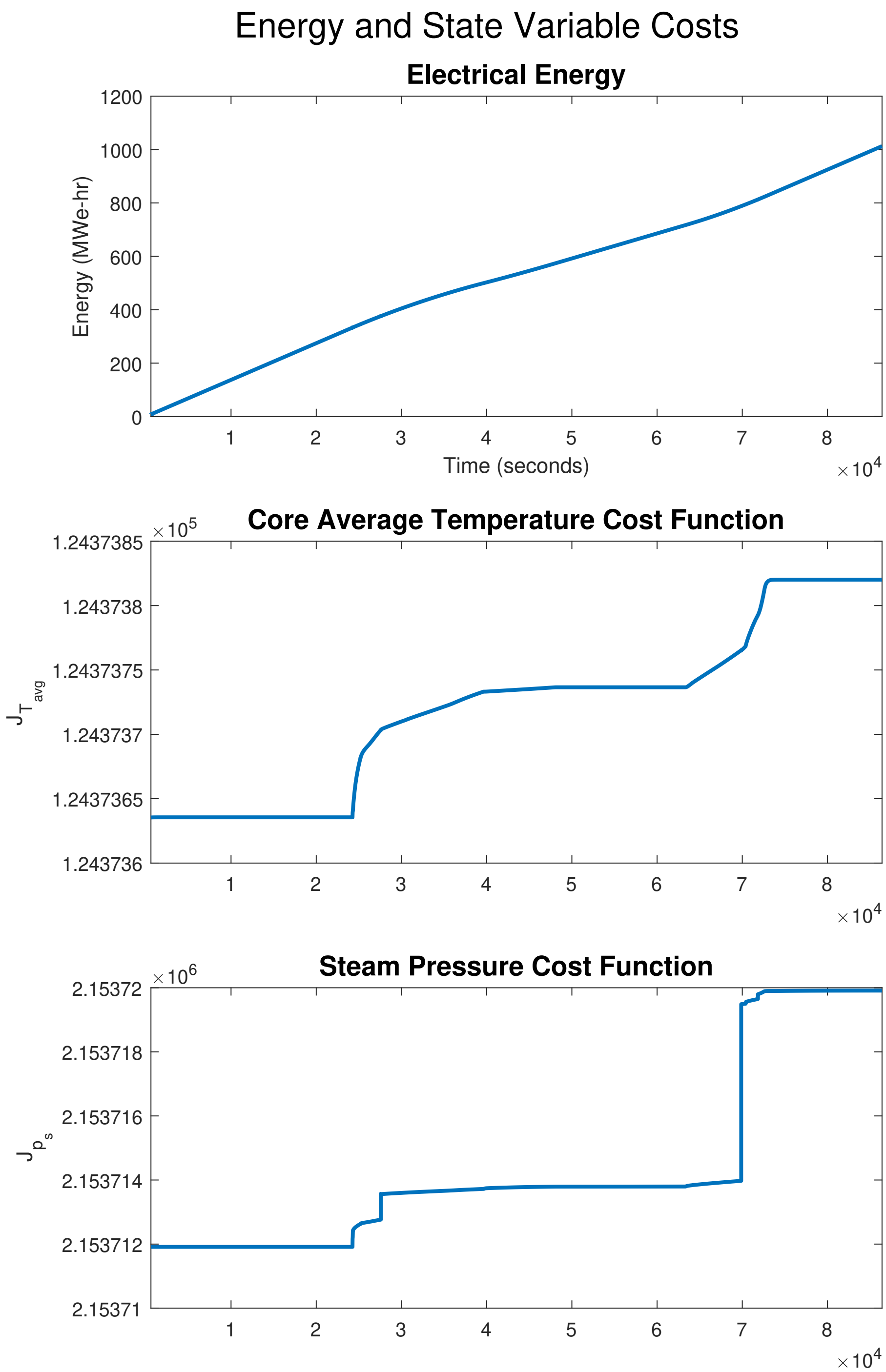

Figure 5.32: Energy and state variable costs for the coordinated control CAISO simulation.

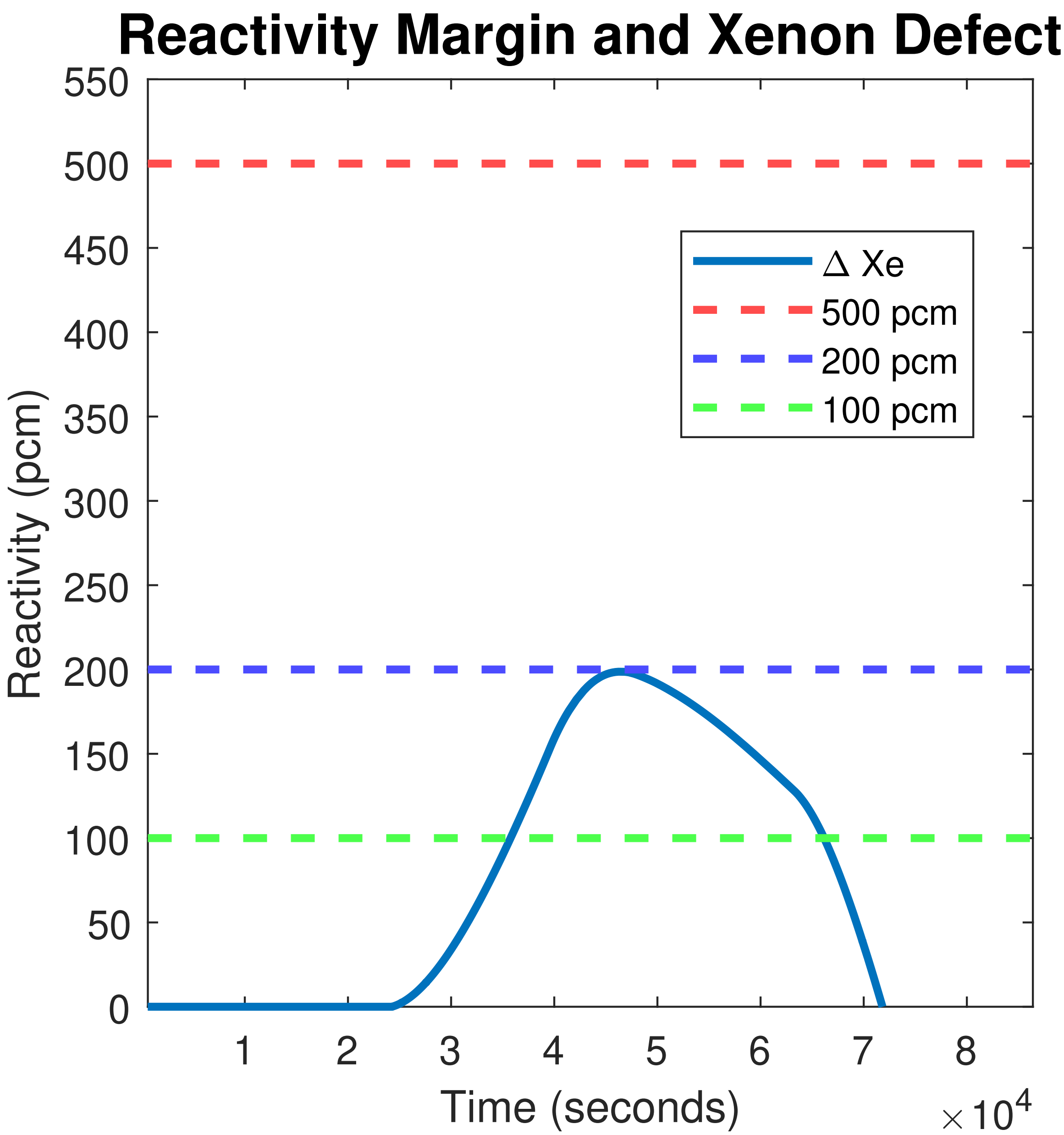

Figure 5.33: The power level falls enough during the CAISO simulation to cause the xenon reactivity defect to reach 200 pcm at its nadir. It is possible to simply withdraw the rods and burnout xenon during ramp up, but this has implications for plant operation for systems that may rely on a passive form of load late in the core loading time when excess reactivity is only a few hundred pcm.

Chapter 6

Conclusions and Future Work

6.1 Conclusions

The flexible operation of novel nuclear power plants for a future high renewables grid requires operational concepts distinct from those used in traditional baseload operation. In this work an SMR IPWR power plant was modeled and simulated with feedforward and feedback controls deemed appropriate for a nonlinear system. The performance of this system and control actions were evaluated qualitatively and quantitatively, specifically through the development and application of figures of merit such as actuator effort and a quantification of a notion of penalty for changes in state variables.

The results and studies of several ramp perturbations of four different candidate actuators–the reactor core reactivity, primary coolant mass flow rate, feedwater mass flow rate, and turbine control valve position–suggested the first two would be the only reasonably effective means to operate in a load following mode in a high renewables grid for this model and thus control systems were designed for those two. They do, however, come with a meaningful notional cost associated with the core temperature and steam pressure, which reflects the degradation, the increased maintenance cost/frequency, and/or increased failure rates of components that may occur with aggressive load balancing operation of an IPWR power plant.

The xenon defect was shown to become large enough for large power drops to impose restrictions on systems that lack sufficient reactivity margin to overcome the penalty imposed by the xenon reactivity defect. This is especially relevant for IPWR concepts that don't rely on boron control as dilution is entirely absent or ineffective as a strategy for mitigating xenon buildup or burnup following a power drop. Significant temperature variations are allowed in these simulations, but this would likely not be the case for a real world reactor due to thermomechanical considerations for the fuel cladding, rod banks, and instrumentation as well as the deleterious effect on the quality of steam entering the turbine. The change in xenon defect was shown to be significant enough for a more aggressive load balancing scenario to impose a power constraint on the module very late in the fuel cycle when the excess reactivity available to a core is low. Thus, at least late in the reactor core cycle, xenon must be considered in the unit commitment and economic dispatch of these modules in conjunction with any thermally-dependent control strategy implemented.

A reactor-leading operational concept with a fuzzy logic controller for the control rod reactivity insertion was developed and its efficacy in meeting a simple trapezoidal demand profile demonstrated. This strategy had the virtue of rapidly meeting a thermal profile demand given it, but the turbine response lagged by several seconds. The thermal and steam pressure penalties were also significant. The turbine-leading operational concept with a fuzzy logic controller for the feedwater mass flow rate achieved somewhat faster turbine performance for a trapezoidal demand profile, although the thermally-dependent response was a demerit that led to overshooting the profile. Finally the fuzzy logic coordinated control was demonstrated as capable of meeting a simple trapezoidal power profile as well as a load profile representative of a generating mix with significant renewables penetration. This coordinated control involved actuator effort in terms of both the control rod action and feedwater mass flow action, but, at least for the trapezoidal demand, this resulted in slightly improved reactor power tracking performance. The coordinated control system performance for the CAISO derived demand profile demonstrated the feasibility of the control system for power tracking, and the challenges and costs of such operation were quantified by figures of merit as proxies for additional costs imposed on the plant during continuous load balancing operation.

At the most essential level, the load balancing capability of an SMR IPWR power plant with a coordinated control between the primary and secondary loop was demonstrated in a general sense. An SMR module was maneuvered to match load profiles of varying degrees of aggressiveness and realism. The state variable error, the control effort, and the limitations imposed on flexible operation by xenon poisoning and fuel burnup were documented and evaluated. The relative merits of reactor leading operation, turbine leading operation, and coordinated control were investigated and discussed.

6.2 Candidate Pathways for Future Work

This dissertation work provides a possible foundation for the exploration of the operation of SMR IPWRs for load balancing and potentially new nuclear technology in general that can be operated flexibly. There are a number of promising ways to iterate and improve upon the work of this dissertation, most likely in improving model fidelity, expanding the toolset for evaluation and performance evaluation, implementing other control schemes that are suitable for nonlinear systems, and, perhaps most immediately useful and meaningful, improving direct integration with grid and electricity market models to understand more deeply and rigorously the interaction between the flexible operation of SMRs and a high renewables grid and the constraints and challenges imposed on both.

6.2.1 Model Augmentation

The model presented here is adequate for the concerns of this work, but others may wish to develop higher fidelity models for the purposes of validation or increased realism. Two reactor core nodes were deemed sufficient for capturing the relevant axial phenomena, in particular the axial offset of the reactor thermal power, but increasing model granularity by increasing the number of nodes in either the radial or axial direction may lead to interesting results for the core profile which could be compared to high fidelity neutronics codes or such codes coupled to thermal hydraulics codes for particularly ambitious efforts. The pressurizer here is also simple as it is a generic tank volume with liquid and vapor phases. It may be desirable for anyone particularly interested in pressurizer behavior in an SMR module to use that considers its actual geometry and incorporate the heater, spray, and relief valve control systems.

The balance of plant used in this model is also relatively simple. The turbine is only divided into a high pressure stage and a low pressure stage with steam extraction to a feedwater heater from the HP stage. The feedwater heater itself is an open mixed volume as well. In comparison, the NuScale design certification document regarding the steam system features a diagram with 10 turbine stages and 6 feedwater heaters as of this writing [54]. Anyone interested in the complex interaction between multiple feedwater heating systems during operational transients may find it beneficial to develop such a high fidelity model of the turbine and feedwater heater systems.

6.2.2 Multi-objective Optimization of Figures of Merit

There are many figures of merit one could develop and select to evaluate the flexible operation of a nuclear plant. A quadratic form of power error and actuator cost were employed because of their obvious and meaningful applicability to the evaluation of controlling a system and the existence of analogous figures of merit are common in the general study of and literature on control systems. One could construct other figures of merit that measure plant fatigue and actuator effort appropriate for whatever reactor design, model fidelity, and control scheme used. Another figure of merit that might be useful could be the extreme value of a state variable for a system to be optimized under a multi-objective framework with tradeoffs between the extreme variable value, quadratic costs of the aforementioned types, and others relevant in control of systems such as settling time or overshoot. For instance, it is possible in principle to adjust the membership functional forms and intervals of the fuzzy logic rulesets in this work with global optimization techniques to improve a metric of interest to the control designer. Ramp rate availability in this work is calculated in a very conservative and *ad hoc* sense within the framework of the full nonlinear model and online simulation. It may be worth exploring other formulations of the ramp rate availability problem with model linearization around several operating points offline.

The quadratic figures of merit defined in the work are amenable to standard optimization techniques like gradient descent. It may be desirable to explore optimization of one or more figures of merit for both synthetic and real historical load profiles. Such case studies could lead to development of generalizable operational concepts and/or control parameters and gains. The ramp rate availability is also defined in a somewhat narrow way. The calculation can be further relaxed by tracking the entirety of the power history and reactivity history instead of just the most recent power change used for online simulation. The consequence of this relaxation would become apparent in load profiles that gradually ramp down over several hours at even moderate levels of fuel burn up.

6.2.3 Multi-modular Power Plant Operation

The work of this dissertation only concerned itself with the modeling and simulation of a single module. Statements regarding plant operation assumed identical operation of identical modules, with power and ramp rates simply scaling linearly with the total number of modules. However, it is likely that individual modules would be installed at different times, have different refueling schedules, and have different operating and fault histories. For these reasons load demands and control actions may be distributed different across different modules, especially if one is shutdown for maintenance or refueling. Future work in multi-modular operation might also look at ranking decisions based on figures of merit like the cost functions laid out in this work or implementing control strategies that involve a more complex sequence of actions such as different ramps across modules at different time intervals or steam bypass.

6.2.4 Alternate Actuators and Control Schemes

Fuzzy logic control need not be the only form of nonlinear or intelligent control applied to this particular nuclear power plant system or such systems generally. Fuzzy logic control was chosen for its ability to "behave" like an expert operator and its more relaxed linguistic approach to controller design [68]. Model predictive control is an option increasingly used in process engineering and autonomous vehicles. Linearization around multiple operating points can assist with the implementation of model predictive control, but the power history dependence of xenon may complicate this control design effort.

There may also be other actuators available to the modeler depending on the secondary systems coupled to the reactor module, as in low grade steam applications, or the level of fidelity added to the model, such as additional valves for the balance of plant, or sprays and heaters for the pressurizer. Multi-modular operation of more than one IPWR, as would be expected at an SMR power plant, may lead to further insight into the operation and control of IPWRs as systems coupled to each other as well as the grid.

6.2.5 Augmentation of Grid Integration

The load profile demonstrations whereby the reactor thermal power is maneuvered to match a predetermined demand, often a closed form function like a trapezoid, are common in the literature on "load following" of nuclear power plants. However, this is a somewhat artificial approach that neglects the reality of operating in an electrical grid. A higher fidelity model should consider the ability of the turbine-generator to match the grid frequency (nominally 60 Hz), which could be supplied from real historical data from an ISO.

There is also no interface with a grid model or electricity market models. Such models would be of keen interest for anyone who wanted to evaluate the economic impact of flexible operation of a nuclear power plant. Having such integration would improve the validity of any results produced from simulating flexible operation in a high renewables grid. Coupling would allow one to investigate the effect of flexible nuclear operation on grid stability, system cost, and the prices of electricity and ancillary services. Direct coupling to a UC-ED model may be challenging due to the very different time domains involved. The reactor neutronics evolve on the order of microseconds, the thermal phenomena on the order of seconds, and the grid optimization is on the order of several minutes or hours. For this reason, it may be desirable to use a parametric approach where ramp rate availability is supplied to a UC-ED optimization problem, an addition to the model over the case of nuclear generators being treated as inflexible must-take baseload plants.

Bibliography

[1] K. KELEHER, "New nuclear power plant coming to Idaho Falls," *KIFI* (2018). 1

[2] D. T. INGERSOLL et al., "Can nuclear power and renewables be friends?," *Proc. Proceedings of ICAPP 2015*, May, 2015. xi, 2, 12, 21, 23, 140

[3] A. LOKHOV, "Technical and Economic Aspects of Load Following with Nuclear Power Plants," Nuclear Energy Agency OECD (2011). 2, 3, 4, 11, 12, 56

[4] J. FANDRICH et al., "Non-baseload Operation in Nuclear Power Plants: Load Following and Frequency Control Modes of Flexible Operation," IAEA (2018). 3

[5] F. REITSMA, M. H. SUBKI, J. C. LUQUE-GUTIERREZ, and S. BOUCHET, "Advances in Small Modular Reactor Technology Developments," IAEA (2020). xi, 4, 6, 8

[6] M. D. CARELLI et al., "The design and safety features of the IRIS reactor," *Nuclear Engineering and Design*, **230**, *1–3*, 151 (2004). 4

[7] J. W. HINES et al., "Advanced Instrumentation and Control Methods for Small and Medium Reactors with IRIS Demonstration," Report 1, University of Tennessee (2011). 4, 17

[8] M. S. GREENWOOD, "TRANSFORM-Library: A Modelica based library for modeling thermal hydraulic energy systems and other multi-physics systems," Report, Oak Ridge National Laboratory (2020). 4, 16, 24, 167

[9] R. WOOD, C. BRITTAIN, J. A MARCH-LEUBA, L. E CONWAY, and L. ORIANI, "A Plant Control System Development Approach for IRIS," (2003). xi, 5, 17

[10] International Atomic Energy Agency, "Modern Instrumentation and Control for Nuclear Power Plants," International Atomic Energy Agency (1999). 12, 13

[11] International Atomic Energy Agency, "Electric Grid Reliability and Interface with Nuclear Power Plants," International Atomic Energy Agency (2012). 12

[12] P. MORILHAT, S. FEUTRY, C. L. MAITRE, and J. M. FAVENNEC, “Nuclear Power Plant Flexibility at EDF,” EDF (2019). 12, 13

[13] H. LUDWIG, T. SALNIKOVA, A. STOCKMAN, and U. WAAS, “Load cycling capabilities of German nuclear power plants (NPP),” *VGB PowerTech*, **91(5)**, 38 (2011). 12, 13

[14] R. PONCIROLI et al., “Profitability Evaluation of Load-Following Nuclear Units with Physics-Induced Operational Constraints,” *Nuclear Technology*, **200**, *3*, 189 (2017). xvi, 13, 56, 98, 105, 106, 141

[15] J. D. JENKINS et al., “The benefits of nuclear flexibility in power system operations with renewable energy,” *Applied Energy*, **222**, 872 (2018). 13, 106

[16] International Atomic Energy Agency, “Non-baseload Operation in Nuclear Power Plants: Load Following and Frequency Control Modes of Flexible Operation,” 2017. 13

[17] G. LI, “Extension for load-follow operation of PWR core by using single- or multi-variable control of state-feedback,” *Annals of Nuclear Energy*, **68**, 183 (2014). 13, 29

[18] G. LI et al., “Modeling and control of nuclear reactor cores for electricity generation: A review of advanced technologies,” *Renewable and Sustainable Energy Reviews*, **60**, 116 (2016). 13, 14, 29

[19] M. ZAREI, “A multi-point kinetics based MIMO-PI control of power in PWR reactors,” *Nuclear Engineering and Design*, **328**, 283 (2018). 13, 29

[20] D. RUAN, “Fuzzy logic in the nuclear research world,” *Fuzzy Sets and Systems*, **74**, *1*, 5 (1995). 14, 112

[21] C. LIU, J.-F. PENG, F.-Y. ZHAO, and C. LI, “Design and optimization of fuzzy-PID controller for the nuclear reactor power control,” *Nuclear Engineering and Design*, **239**, *11*, 2311 (2009). 14

[22] R. SUTTON, "Monitoring and control of nuclear plant using fuzzy logic," *Proc. IEE Colloquium on Two Decades of Fuzzy Control - Part 1*, p. 9/1–913, May, 1993. 14

[23] H. L. AKIN and V. ALTIN, "Rule-based fuzzy logic controller for a PWR-type nuclear power plant," *IEEE Transactions on Nuclear Science*, **38**, *2*, 883 (1991). 14, 112

[24] M. N. KHAJAVI, M. B. MENHAJ, and A. A. SURATGAR, "Fuzzy adaptive robust optimal controller to increase load following capability of nuclear reactors," *Proc. PowerCon 2000. 2000 International Conference on Power System Technology. Proceedings (Cat. No.00EX409)*, volume 1, p. 115–120 vol.1, 2000. 14

[25] Y.-J. HAH and B.-W. LEE, "Fuzzy Power Control Algorithm for a Pressurized Water Reactor," *Nuclear Technology*, **106**, *2*, 242 (1994), Publisher: Taylor & Francis _eprint: https://doi.org/10.13182/NT94-A34979. 14, 19, 112

[26] M. S. FODIL, P. SIARRY, F. GUELY, and J. L. TYRAN, "A fuzzy rule base for the improved control of a pressurized water nuclear reactor," *IEEE Transactions on Fuzzy Systems*, **8**, *1*, 1 (2000). 14, 18, 19, 49

[27] D. RUAN, "Online experiments of controlling nuclear reactor power with fuzzy logic," *Proc. Fuzzy Systems Conference Proceedings, 1999. FUZZ-IEEE '99. 1999 IEEE International*, volume 3, p. 1712–1717 vol.3, Aug., 1999. 14

[28] H. M. EMARA, A. ELSADAT, A. BAHGAT, and M. SULTAN, "Power stabilization of nuclear research reactor via fuzzy controllers," *Proc. Proceedings of the 2002 American Control Conference (IEEE Cat. No.CH37301)*, volume 6, p. 5066–5071 vol.6, May, 2002. 14

[29] A. HEGER, N. K. ALANG-RASHID, and M. JAMSHIDI, "Application of Fuzzy Logic in Nuclear Reactor Control Part I: An Assessment of State-of-the-Art," *Nuclear Safety*, **36**, *1*, 109 (1995). xvii, 15, 112, 113, 115

[30] F. LI, *Dynamic Modeling, Sensor Placement Design, and Fault Diagnosis of Nuclear Desalination Systems*, PhD thesis, University of Tennessee, 2011. 15

[31] K. FRICK, D. DOSTER, J., and S. M. BRAGG-SITTON, "Control Strategies for Coupling Thermal Energy Storage Systems with Small Modular Reactors," *Proc. Transactions of the American Nuclear Society*, June, 2017. 15

[32] Frick, Konor and Doster, J. Michael, "Coupling of Thermal Energy Storage with Small Modular Reactors," *Proc. Transactions of the American Nuclear Society*, Nov., 2016. 15

[33] K. FRICK, C. T. MISENHEIMER, J. M. DOSTER, S. D. TERRY, and S. BRAGG-SITTON, "Thermal Energy Storage Configurations for Small Modular Reactor Load Shedding," *Nuclear Technology*, **202**, *1*, 53 (2018), Publisher: Taylor & Francis _eprint: https://doi.org/10.1080/00295450.2017.1420945. 15

[34] K. FRICK, J. M. DOSTER, and S. BRAGG-SITTON, "Design of a Sensible Heat Peaking Unit for Small Modular Reactors," *Proc. Transactions of the American Nuclear Society*, Nov., 2017. 15

[35] Fugate, David L. et al., "Nuclear Hybrid Energy System FY16 Modeling Efforts at ORNL," Report, Oak Ridge National Laboratory (2016). 16

[36] K. FRICK and S. BRAGG-SITTON, "Development of the NuScale Power Module in the INL Modelica Ecosystem," *Nuclear Technology*, **0**, *0*, 1 (2020), Publisher: Taylor & Francis _eprint: https://doi.org/10.1080/00295450.2020.1781497. 16, 38

[37] J. J. DUDERSTADT and L. J. HAMILTON, *Nuclear Reactor Analysis*, Wiley, Hoboken, NJ (1976). 17, 26, 27, 49, 98

[38] M. WINOKUR and L. TEPPER, "Extension of Load Follow Capability of a PWR Reactor by Optimal Control," *IEEE Transactions on Nuclear Science*, **31**, *2*, 932 (1984). 18, 29

[39] F. FRANCESCHINI and B. PETROVIC, "Advanced operational strategy for the IRIS reactor: Load follow through mechanical shim (MSHIM)," *Nuclear Engineering and Design*, **238**, *12*, 3240 (2008). 18

[40] H. SONG, J. WAN, R. LUO, and F. ZHAO, "Dynamic simulation and control studies of CPR1000 reactor core with advanced MSHIM control strategy," *Progress in Nuclear Energy*, **105**, 29 (2018). 18

[41] G. R. ANSARIFAR and S. SAADATZI, "Nonlinear control for core power of pressurized water nuclear reactors using constant axial offset strategy," *Nuclear Engineering and Technology*, **47**, *7*, 838 (2015). 18

[42] M. A. D. S. MAGALHãES, C. A. B. D. O. LIRA, M. A. B. D. SILVA, J. D. L. BEZERRA, and F. R. D. A. LIMA, "Boron transient effects on the behavior of IRIS reactor using dynamic modeling," *Progress in Nuclear Energy*, **69**, 44 (2013). 18, 19

[43] P. S. LONDHE, B. M. PATRE, and A. P. TIWARI, "Design of Single-Input Fuzzy Logic Controller for Spatial Control of Advanced Heavy Water Reactor," *IEEE Transactions on Nuclear Science*, **61**, *2*, 901 (2014). 19

[44] P. S. LONDHE, B. M. PATRE, and A. P. TIWARI, "Fuzzy-like PD controller for spatial control of advanced heavy water reactor," *Nuclear Engineering and Design*, **274**, 77 (2014). 19

[45] R. K. MUNJE, B. M. PATRE, P. S. LONDHE, A. P. TIWARI, and S. R. SHIMJITH, "Investigation of Spatial Control Strategies for AHWR: A Comparative Study," *IEEE Transactions on Nuclear Science*, **63**, *2*, 1236 (2016). 19

[46] R. T. WOOD and T. L. WILSON, "Inherent reactor power controller for a metal-fueled ALMR," *IEEE Transactions on Nuclear Science*, **37**, *2*, 1032 (1990). 19

[47] R. PONCIROLI, A. CAMMI, A. DELLA BONA, S. LORENZI, and L. LUZZI, "Development of the ALFRED reactor full power mode control system," *Progress in Nuclear Energy*, **85**, 428 (2015). 20, 53

[48] R. PONCIROLI, A. CAMMI, S. LORENZI, and L. LUZZI, "Control approach to the load frequency regulation of a Generation IV Lead-cooled Fast Reactor," *Energy Conversion and Management*, **103**, 43 (2015). 20

[49] G. XIA, P. MINJUN, and D. XUE, "Analysis of load-following characteristics for an integrated pressurized water reactor," *International Journal of Energy Research*, **38**, *3*, 380 (2014). 20

[50] X. DU, G. XIA, and L. HE, "Operation characteristic of Integrated Pressurized Water Reactor under coordination control scheme," *Annals of Nuclear Energy*, **75**, 658 (2015). 20

[51] International Atomic Energy Agency, "Instrumentation and Control Systems for Advanced Small Modular Reactors," International Atomic Energy Agency (2017). 21

[52] S. SHIMJITH, A. TIWARI, B. BANDYOPADHYAY, and R. PATIL, "Spatial stabilization of Advanced Heavy Water Reactor," *Annals of Nuclear Energy*, **38**, *7*, 1545 (2011). 29

[53] P. F. WANG, Y. LIU, B. T. JIANG, J. S. WAN, and F. Y. ZHAO, "Nodal dynamics modeling of AP1000 reactor for control system design and simulation," *Annals of Nuclear Energy*, **62**, 208 (2013). 29

[54] "NRC: Application Documents for the NuScale Design,". 38, 153

[55] S. E. ARDA and K. E. HOLBERT, "Nonlinear dynamic modeling and simulation of a passively cooled small modular reactor," *Progress in Nuclear Energy*, **91**, 116 (2016). xii, 42, 43, 46

[56] B. POUDEL, K. JOSHI, and R. GOKARAJU, "A Dynamic Model of Small Modular Reactor Based Nuclear Plant for Power System Studies," *IEEE Transactions on Energy Conversion*, **35**, *2*, 977 (2020), Conference Name: IEEE Transactions on Energy Conversion. xii, 42, 44, 45

[57] Q. MA, X. WEI, J. QING, W. JIAO, and R. XU, "Load following of SMR based on a flexible load," *Energy*, **183**, 733 (2019). xii, 42, 46

[58] D. BOSE et al., "An Interval Approach to Nonlinear Controller Design for Load-Following Operation of a Small Modular Pressurized Water Reactor," *IEEE Transactions on Nuclear Science*, **64**, *9*, 2474 (2017). 50, 53

[59] W. J. GARLAND, *The Essential CANDU*, UNENE (2017). xiii, 51, 52, 53, 106

[60] A. CAMMI, F. CASELLA, M. RICOTTI, and F. SCHIAVO, "Object-Oriented Modelling for Integral Nuclear Reactors Dynamic Simulation," *Proc. Proceedings for International Conference on Integrated Modeling & Analysis in Applied Control & Automation 2004*, p. Nu–02, Jan., 2004. 53

[61] L. E. WEAVER, *Reactor Dynamics and Control*, American Elsevier Publishing Company, Inc. (1968). 54, 55

[62] M. A. SCHULTZ, *Control of nuclear reactors and power plants*, Number 462 p. in McGraw-Hill series in nuclear engineering, McGraw-Hill, New York (1961). 54

[63] Lokhov, A., "Load-following with nuclear power plants," *NEA News*, **29(2)**, 18 (2011). 56

[64] M. ZAREI, "On the inherent load following features of a small modular nuclear reactor," *Nuclear Engineering and Design*, **370**, 110896 (2020). 108

[65] D. L. HETRICK, *Dynamics of Nuclear Reactors*, American Nuclear Society (1993). 108

[66] V. KALE, R. KUMAR, K. OBAIDURRAHMAN, and A. GAIKWAD, "Linear stability analysis of a nuclear reactor using the lumped model," *Nuclear Technology and Radiation Protection*, **31**, 218 (2016). 108, 109, 110

[67] "California ISO - Supply,". xix, 140, 142

[68] N.-J. NA and Z.-G. BIEN, "A Fuzzy Controller for the Steam Generator Water Level Control and Its Practical Self-Tuning Based on Performance," *Nuclear Engineering and Technology*, **27**, *3*, 317 (1995), Publisher: Korean Nuclear Society. 155

[69] T. BERGMAN, A. LAVINE, and F. INCROPERA, *Fundamentals of Heat and Mass Transfer, 7th Edition*, John Wiley & Sons, Incorporated (2011). 169, 171

[70] "McAdams - Thom - Chen's Correlation - Nucleate Boiling,". xx, 174

Appendices

A TRANSFORM Models

This appendix lays out in greater detail the energy balances and heat transfer models for the reactor core and steam generator heat exchange models mentioned in Chapter 3. The energy balance/heat transfer problems are treated as 2D node centered or 1D node centered finite difference problems. For both the fuel and steam generator, flows are treated as azimuthally symmetric and thus neglected in the modeling. The energy balances use externally specified boundary conditions for the heat transfer.

$$\frac{dE}{dt} = q_r + q_{r+dr} + q_z + q_{z+dz} + q'''V \tag{1}$$

$$q = -\lambda A \frac{dT}{dx} \tag{2}$$

Here λ is an overall heat transfer coefficient, A is the cross section area of transfer, and x is the normal coordinate (not necessarily rectilinear) direction of heat transfer. The energy balances for discrete node ij take the general form

$$\rho_{ij} C_{p_{ij}} V_{ij} \frac{dT_{ij}}{dt} = q_{i-1/2,j} + q_{i+1/2,j} + q_{i,j-1/2} + q_{i,j+1/2} \tag{3}$$

The j subscripts are dropped for the 1D energy balance and heat transfer [8].

$$\rho_i C_{p_i} V_i \frac{dT_i}{dt} = q_{i-1/2} + q_{i+1/2} \tag{4}$$

Reactor Core Heat Transfer Model

The reactor core heat transfer model is a 2D finite difference discretization of the azimuthally symmetric cylindrical heat equation for the fuel, gap, and clapping regions of the fuel rod. The diagram level model of the fuel heat transfer model as it appears in Dymola is featured in Figure 1. Each region in Figure 1 has the following discretization for equal dimension nodes ij:

$$V_{ij} = 2\pi r_i \Delta r_i \Delta z_j \tag{5}$$

$$\begin{aligned}
\rho_{ij} C_{p_{ij}} V_{ij} \frac{dT_{ij}}{dt} = &-\frac{(\lambda_{i,j} + \lambda_{i-1,j}) 2\pi (r_i - 0.5\Delta_r) \Delta z_j (T_{i,j} - T_{i-1,j})}{2\Delta r} \\
&- \frac{(\lambda_{i,j} + \lambda_{i+1,j}) 2\pi (r_i + 0.5\Delta r) \Delta z_j (T_{i,j} - T_{i+1,j})}{2\Delta r} \\
&- \frac{2(\lambda_{i,j} + \lambda_{i,j-1}) \pi (r_i \Delta r)(T_{i,j} - T_{i,j-1})}{\Delta z} \\
&- \frac{2(\lambda_{i,j} + \lambda_{i,j+1}) \pi (r_i \Delta r)(T_{i,j} - T_{i,j+1})}{\Delta z} \\
&+ q''' V_{ij}.
\end{aligned} \tag{6}$$

The boundary q_{ij} heat flows are the heat flows between radial and axial nodes. The q''' represents the heat generation density in the volume. For the fuel itself, this is the heat of the fission reaction. For the gap and cladding, $q''' = 0$; no heat generation is assumed. This discretization is repeated for the gap region and cladding region.

The 1D nodalization for the heat transfer from the fuel cladding to the coolant is approached similarly. This level of the model appears in Figure 2. The temperature calculated from the outer most fuel cladding node in the 3-region fuel heat transfer model is supplied to another effective heat transfer model between the cladding and the primary coolant. These equations are

$$\alpha_j = \frac{\mathrm{Nu}_j \, \lambda_j}{L_{char_j}} \tag{7}$$

$$\mathrm{Nu} = 0.023 \mathrm{Re}^{0.8} \mathrm{Pr}^{0.4} \tag{8}$$

$$q_j = -\alpha_j A (T_{clad_j} - T_{coolant_j}). \tag{9}$$

Here Re and Pr are the Reynolds number and Prandtl number, respectively. The Nusselt number (Nu) is calculated using a laminar flow or Dittus-Boelter correlation for turbulent flow, λ is the thermal conductivity of the fluid, and L_{char} is the characteristic length, which is just the wetted perimeter of the j-th node in the coolant channel [69]. The heat from the rod is transferred to the surrounding coolant using a 1D discretization. The energy balance for the coolant surrounding the fuel rod is the following.

$$\rho_j C_{p_j} V_j \frac{dT_j}{dt} = q_j + \dot{m}_{j-1} h_{j-1} - \dot{m}_j h_j \tag{10}$$

Here $\dot{m}_{j-1}$, $\dot{m}_j$, h_{j-1}, h_j are the inlet and outlet mass flow rates and enthalpies, respectively.

Steam Generator Heat Transfer Model

The steam generator for the IPWR is modeled as a straight OTSG. The diagram level model of the steam generator model as it appears in Dymola is featured in Figure 3. The heat transfer model is a 1D discretization between the shell and tube wall, and between the tube wall and secondary fluid in the tube. The heat transfer to the shell side (primary) of the steam generator is developed using the same scheme as in Equation 10 because both are the single phase highly pressurized liquid phase light water coolant. The heat transfer for the wall and tube differ from this but ultimately interact as effective 1D models, as shown in 3.

$$q_r = -\lambda A \frac{dT}{dr} \tag{11}$$

The discretization of the tube wall is then

$$q_r = q_i = \frac{(\lambda_{i,j} + \lambda_{i+1,j}) A_i (T_{i+1,j} - T_{i,j})}{2\Delta r} \tag{12}$$

$$q_z = q_j = \frac{(\lambda_{i,j} + \lambda_{i,j+1}) A_j (T_{i,j} - T_{i,j})}{2\Delta z} \tag{13}$$

The cross section areas A_i and A_j are distinguished since a different cross sectional area is presented for radial heat transfer and axial heat transfer. The steam generator tube wall has two radial nodes and ten axial nodes. The tube secondary fluid and shell primary fluid

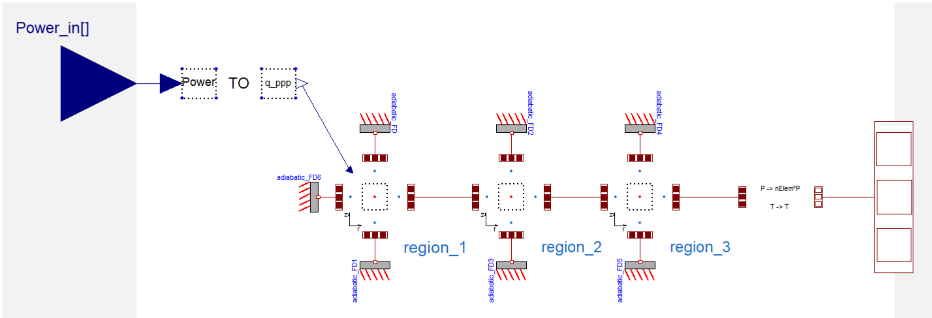

Figure 1: Three region heat transfer model from the TRANSFORM library as it appears in the Dymola environment.

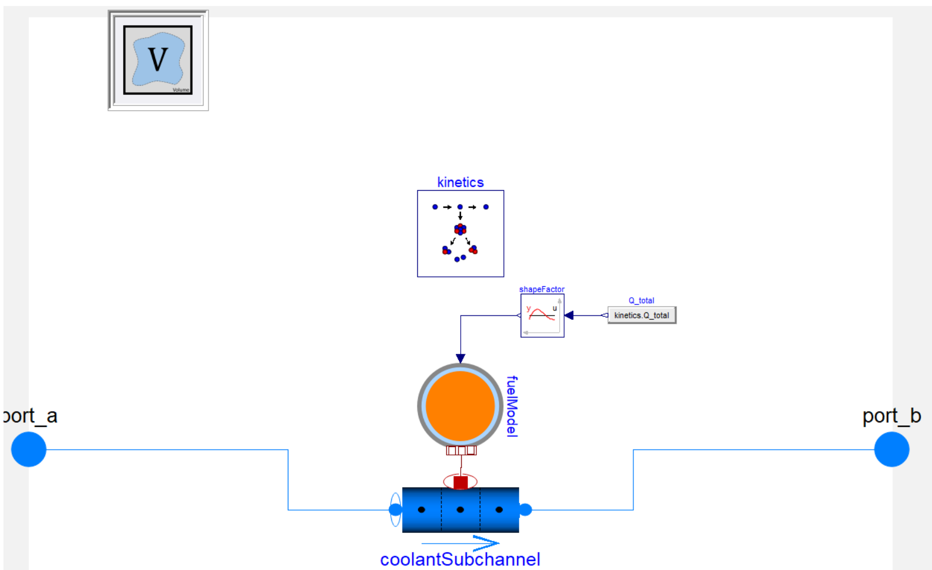

Figure 2: Subchannel model coupling fuel heat transfer to coolant, coolant fluid model, and reactor kinetics.

regions are also divided into ten axial nodes. The heat transfer model between the tube wall and the secondary fluid is a two-phase flow, three region model. These three regions are the subcooled water region, the saturated two-phase region, and the superheated steam region. The single phase regions (subcooled water and superheated steam) use a Dittus-Boelter correlation while the two-phase region uses Chen's correlation [69]. All the relevant equations for the Chen's correlation calculation appear below.

$$X_{tt} = (\frac{x}{1-x})^{0.9}(\frac{\rho_{fsat}}{\rho_{gsat}})^{0.5}(\frac{\mu_{gsat}}{mu_{fsat}})^{0.1} \tag{14}$$

$$F = (\frac{1}{X_{tt}} + 0.213)^{0.736} \tag{15}$$

$$S = \frac{1}{1 + (2.53 \times 10^{-6})\mathrm{Re}_{tp}^{1.17}} \tag{16}$$

$$\alpha_f = \frac{\lambda_{fsat}}{D}\mathrm{Nu} \tag{17}$$

$$\alpha_{FZ} = 0.00122\frac{(\lambda_{fsat}^{0.79}C_{pfsat}^{0.45}\rho_{fsat}^{0.49}g^{0.25})\Delta T_{sat}^{0.24}\Delta p_{sat}^{0.75}}{\sigma^{0.5}\mu_{fsat}^{0.29}h_{fg}^{0.24}\rho_{gsat}^{0.24}} \tag{18}$$

$$\alpha = \alpha_f F + \alpha_{FZ} S \tag{19}$$

The effective heat transfer then is a composite of the Dittus-Boelter and Chen correlations. The heat transfer energy balance equations between the tube wall and primary coolant loop as well as between the tube wall and secondary coolant loop have the same form as the heat transfer between the fuel cladding and the primary coolant, i.e., one dimensional in the radial direction. The heat transfer between the tube wall and primary coolant loop uses the single phase correlation models only while the heat transfer between the tube wall and secondary coolant uses the correlations associated with the phase on the secondary side.

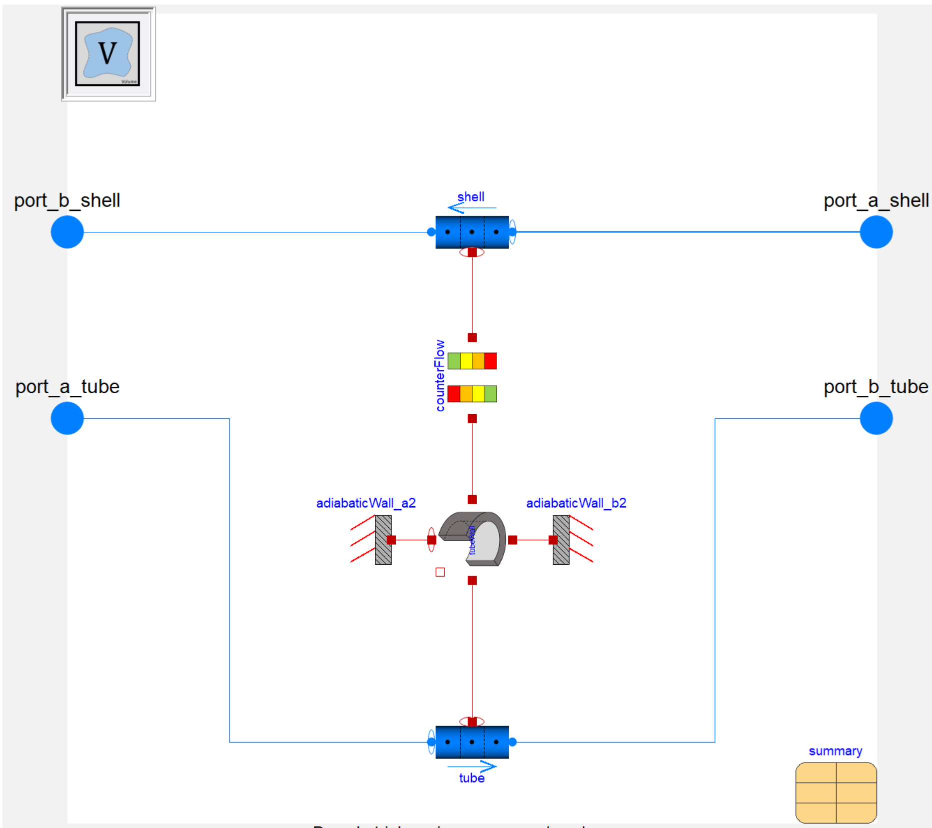

Figure 3: Diagram level model of the TRANSFORM steam generator heat exchanger model in Dymola IDE.

$$q_j = -\alpha_j A(T_{wall_j} - T_{coolant_j}). \tag{20}$$

$$\rho_j C_{p_j} V_j \frac{dT_j}{dt} = q_j + \dot{m}_{j-1} h_{j-1} - \dot{m}_j h_j \tag{21}$$

Chen's Correlation

$$h_{tp} = h_{FZ}S + h_l F$$

$$h_{tp} = S \underbrace{\frac{k_l^{0.79} c_l^{0.45} \rho_l^{0.49} g_c^{0.25} \Delta T^{0.24} \Delta P^{0.75}}{\sigma^{0.5} \mu_l^{0.29} H_{fg}^{0.24} \rho_v^{0.24}}}_{\substack{\text{nucleate pool boiling} \\ \text{Forster – Zuber}}} + \underbrace{F Re_l^{0.8} Pr_l^{0.4} k_l / De}_{\substack{\text{forced convection} \\ \text{Dittus – Boelter}}}$$

where:

h_{tp} - two-phase heat transfer coefficient

S - the nucleate boiling suppression factor; 0.00122 for FZ correlation

F - two-phase multiplier; correction factor, which is defined as the ratio of the true two-phase Reynolds number to the single-phase

k_l - thermal conductivity of liquid

c_l - specific heat of liquid

g_c - gravitational conversion factor

ΔT - wall superheat

ΔP - difference in saturation and wall superheat pressures

σ - surface tension

μ_l – viscosity

H_{fg} – enthalpy of vaporization

De – equivalent diameter

$$S = \frac{1}{1 + 0.00000253\,Re_{tp}^{1.17}}$$

$$F = \left(\frac{1}{X_{tt}} + 0.213\right)^{0.736}$$

Figure 4: Heat transfer coefficient formula with nucleate boiling and forced convection [70]

B MATLAB Scripts for Linear Stability Analysis

Xenon stability calculation script

```
clc; clear;
syms s lambda L beta
syms a1 a2 a3 a4 a5 a6 a7 alphaf alphac Tf0 Tc0 P0 rhox0 lambdaI lambdaX;
G = (s+lambda)/(s*L*(s+lambda+(beta/L)));
syms zf zc zx;

% Make sure  these expressions are actually correct
Hf = ((a1*(a3+a4+s))/(s^2+(a2+a3+a4)*s+a2*a4))*((P0/Tf0));
Hc = ((a1*a3)/(s^2+(a2+a3+a4)*s+a2*a4))*((P0/Tc0));
% Hx = -((a5*lambdaI+(a6+a7*rhox0)*(s+lambdaI))/
% ((s+lambdaI)*(s+lambdaX+a7*P0)))*(P0/rhox0);
HxNum = -(a5*lambdaI+(a6+a7*rhox0)*(s+lambdaI))*(P0/rhox0);
HxDen = (s+lambdaI)*(s+lambdaX+a7*P0);
Hx = HxNum/HxDen;
H = alphaf*Tf0*Hf + alphac*Tc0*Hc + rhox0*Hx;
% H = alphaf*Tf0*Hf + alphac*Tc0*Hc;
Tr = G/(1 - G*H);
[nf, df] = numden(Tr);
D = 1-G*H;
expr1 = collect(D,s);
expr2 = collect(df,s); % coefficients in terms of s
Ds1 = simplify(expr1==0);
Ds2 = simplify(expr2==0);
Ds1 = collect(Ds1);
Ds2 = collect(Ds2);
cs = coeffs(Ds1,s); % coefficients of s
% substitute neutronics parameters
cs = subs(cs,{L beta lambda lambdaI lambdaX},...
    {16e-6 0.0065 0.0812 2.94e-5 2.1e-5});
```

```
% substitute initial temps and feedbacks/power
cs = subs(cs,{Tc0 Tf0},{573 790});
% substitute or use for parameters, might need to be mindful of sign of alphas
cs = vpa(cs,3);
cs = subs(cs,{a1 a2 a3 a4 a5 a6 a7},...
    {6.67e-8 0.142 0.169 2.865 8e-15 7.77e-16 2.91e-13});
% use Kale constant -> linear scaling and similar materials
%% parameterization
cs = vpa(cs,3)
cs = subs(cs,P0,1.6e8);
cs = subs(cs,{alphac alphaf rhox0},{-2e-4 -2e-5 -0.026});
cs = vpa(cs,3)
% Cannot seem to extract coefficients as in MATLAB documentation, so pulling
% them out by hand gives the coefficients (from highest to lowest power of s)
%% symbolic coefficients extracted manually in terms of P0 and alphas
cs6 = 1.6e-5;
cs5 = (4.66e-18*P0 + 0.00655);
cs4 = (2.68e-15*P0 + 2.91e-13*P0*rhox0 + 0.0207) - 6.67e-8*P0*alphaf;
cs3 = (8.54e-15*P0 + 9.48e-13*P0*rhox0 + 0.00265) - ...
    (6.67e-8*P0*(0.169*alphac + 3.03*alphaf) +...
    alphaf*(5.42e-9*P0 + 6.67e-8*P0*(2.91e-13*P0 + 2.1e-5)));
cs2 = (1.29e-15*P0 + 1.93e-13*P0*rhox0 + 1.33e-7) -...
    ((5.42e-9*P0 + 6.67e-8*P0*(2.91e-13*P0 + 2.1e-5))...
    *(0.169*alphac + 3.03*alphaf) +...
    alphaf*(1.59e-13*P0 + 5.42e-9*P0*(2.91e-13*P0 + 2.1e-5)));
cs1 = (2.59e-17*P0 + 9.62e-15*P0*rhox0 + 1.63e-12) -...
    ((1.59e-13*P0 + 5.42e-9*P0*(2.91e-13*P0 + 2.1e-5))...
*(0.169*alphac + 3.03*alphaf) + 1.59e-13*P0*alphaf*(2.91e-13*P0 + 2.1e-5));
cs0 = 8.52e-21*P0 + 2.83e-19*P0*rhox0 ...
    - 1.59e-13*P0*(0.169*alphac + 3.03*alphaf)*(2.91e-13*P0 + 2.1e-5);
%%
% Now routh.m script can be invoked
coefficient_array = [cs6 cs5 cs4 cs3 cs2 cs1 cs0];
coefficient_array = vpa(coefficient_array,3);
```

```
disp(coefficient_array);
% 290 C, P0 = 1.6e8 W, rhox0 = -0.026?
% Get a's, some can be copied from paper given they are thermal neutronics
% parameters
routhArray = routh(coefficient_array);
RA1 = routhArray(:,1); % get first column of array for stability condition
RA1 = vpa(RA1,3);
disp(RA1);
% can parametrize this in terms of P0 or alphas, depending on interest
% Perhaps do this analysis without Xe feedback in the future
```

Routh array script

```
function [varargout] = RouthArray(varargin)

%ROUTHARRAY Generates the Routh array for the given polynomial
%
%   [ROUTH] = ROUTHARRAY(P) Generates the Routh array for the polynomial
%   described by the vector P.  P should be a vector of coefficients of s
%   in descending order.
%
%   For example, to represent the polynomial
%
%       3*s^3 + 2*s^2 - 3
%
%   P = [3 2 0 -3]
%
%   For more information, see
%   http://www.chem.mtu.edu/~tbco/cm416/routh.html.
%
%INPUT:     -P:     vector of coefficients of s in descending order
%
%OUTPUT:    -ROUTH: Routh array
%
%Christopher Lum
%lum@uw.edu

%Version History
%11/17/12: Created
%05/08/19: Updated documentation
%05/09/19: Updated documentation
%06/06/20: Updated documentation

%----------------------OBTAIN USER PREFERENCES-----------------------------
```

```
switch nargin
    case 1
        %User supplies all inputs
        P = varargin{1};

    otherwise
        error('Invalid number of inputs');
end


%-----------------------CHECKING DATA FORMAT-------------------------------
if(~isvector(P))
    error('P should be a vector')
end

% if(~isreal(P))
%       error('P should be a real vector')
% end



%-------------------------BEGIN CALCULATIONS-------------------------------
%Step 1: Build an empty Routh array
n = length(P)-1;
h = ceil((n+1)/2);

ROUTH = zeros(n+1,h);
ROUTH = sym(ROUTH);
%Step 2: Fill in the first two rows of the Routh array
row = 1;
col = 1;
for k=1:n+1
    ROUTH(row, col) = P(k);

    if(row==2)
```

```
        col = col + 1;
    end

    if(row==1)
        row = 2;
    else
        row = 1;
    end

end

%Step 3: Build the Routh array (rows 3 to n+1)
for k=3:n+1

    %Get row x and y
    y = ROUTH(k-1,:);
    x = ROUTH(k-2,:);

    %Compute z_ki
    for i=1:h
        if(i==h)
            z_ki = 0;
        else
            z_ki = (y(1)*x(i+1) - x(1)*y(i+1)) / y(1);
        end

        ROUTH(k,i) = z_ki;
    end
end

varargout{1} = ROUTH;
```

Vita

Richard Bisson was born in Nashville, TN, to two history professors on a hot summer day in 1988. From a fairly young age Richard knew he wanted to study science and flitted between astronomy, marine biology, and astrophysics as a youth. He attended Hume-Fogg Academic High School, from which he graduated in 2007. He earned his bachelor's in physics and math (Magna Cum Laude) from Vanderbilt University in May 2011. His long-standing interest in climate change and energy technology motivated him to return to school to earn an M.S. in Nuclear Engineering and Engineering Physics from the University of Wisconsin in May 2015 and complete a Ph.D. at the University of Tennessee. Richard would like to continue his work and pursue his interests in nuclear technology, energy economics, and climate policy well beyond his dissertation.